

CANADIAN THESES ON MICROFICHE

I.S.B.N.

THESES CANADIENNES SUR MICROFICHE



National Library of Canada
Collections Development Branch

Canadian Theses on
Microfiche Service

Ottawa, Canada
K1A 0N4

Bibliothèque nationale du Canada
Direction du développement des collections

Service des thèses canadiennes
sur microfiche

NOTICE

The quality of this microfiche is heavily dependent upon the quality of the original thesis submitted for microfilming. Every effort has been made to ensure the highest quality of reproduction possible.

If pages are missing, contact the university which granted the degree.

Some pages may have indistinct print especially if the original pages were typed with a poor typewriter ribbon or if the university sent us a poor photocopy.

Previously copyrighted materials (journal articles, published tests, etc.) are not filmed.

Reproduction in full or in part of this film is governed by the Canadian Copyright Act, R.S.C. 1970, c. C-30. Please read the authorization forms which accompany this thesis.

**THIS DISSERTATION
HAS BEEN MICROFILMED
EXACTLY AS RECEIVED**

AVIS

La qualité de cette microfiche dépend grandement de la qualité de la thèse soumise au microfilmage. Nous avons tout fait pour assurer une qualité supérieure de reproduction.

S'il manque des pages, veuillez communiquer avec l'université qui a conféré le grade.

La qualité d'impression de certaines pages peut laisser à désirer, surtout si les pages originales ont été dactylographiées à l'aide d'un [redacted] ou si l'université nous a fait parvenir une [redacted] de mauvaise qualité.

Les documents qui font déjà l'objet d'un droit d'auteur (articles de revue, examens publiés, etc.) ne sont pas microfilmés.

La reproduction, même partielle, de ce microfilm est soumise à la Loi canadienne sur le droit d'auteur, SRC 1970, c. C-30. Veuillez prendre connaissance des formules d'autorisation qui accompagnent cette thèse.

**LA THÈSE A ÉTÉ
MICROFILMÉE TELLE QUE
NOUS L'AVONS REÇUE**



National Library
of Canada

Bibliothèque nationale
du Canada

Canadian Theses Division

Division des thèses canadiennes

Ottawa, Canada
K1A 0N4

54041

0-315-06121-9

PERMISSION TO MICROFILM — AUTORISATION DE MICROFILMER

• Please print or type — Écrire en lettres moulées ou dactylographier

Full Name of Author — Nom complet de l'auteur

MATTHEW VINCENT RICHARD STAINER

Date of Birth — Date de naissance

1/9/54

Country of Birth — Lieu de naissance

GREAT BRITAIN

Permanent Address — Résidence fixe

268 London Rd., BOSTON, Lincs., ENGLAND

Title of Thesis — Titre de la thèse

STRUCTURAL INVESTIGATIONS OF METAL COMPLEXE
PART I - LANTHANIDE HYDROTRISPYRAZOLYLBORO
PART II - (Phosphine)(olefin) TRICARBONYL IRON
COMPLEXES.

University — Université

UNIVERSITY OF ALBERTA

Degree for which thesis was presented — Grade pour lequel cette thèse fut présentée

Ph. D.

Year this degree conferred — Année d'obtention de ce grade

1981

Name of Supervisor — Nom du directeur de thèse

Professor J. Takats

Permission is hereby granted to the NATIONAL LIBRARY OF CANADA to microfilm this thesis and to lend or sell copies of the film

The author reserves other publication rights, and neither the thesis nor extensive extracts from it may be printed or otherwise reproduced without the author's written permission.

L'autorisation est, par la présente, accordée à la BIBLIOTHÈQUE NATIONALE DU CANADA de microfilmer cette thèse et de prêter ou de vendre des exemplaires du film.

L'auteur se réserve les autres droits de publication; ni la thèse ni de longs extraits de celle-ci ne doivent être imprimés ou autrement reproduits sans l'autorisation écrite de l'auteur.

Date

6/7/81

Signature

MVA Stainer

THE UNIVERSITY OF ALBERTA

STRUCTURAL INVESTIGATIONS OF METAL COMPLEXES.

PART I - LANTHANIDE HYDROTRISPYRAZOLYLBORATES.

PART II - (PHOSPHINE) (OLEFIN) TRICARBONYLIRON
COMPLEXES.

by



MATTHEW VINCENT RICHARD STAINER

A THESIS

SUBMITTED TO THE FACULTY OF GRADUATE STUDIES AND RESEARCH
IN PARTIAL FULFILMENT OF THE REQUIREMENTS FOR THE DEGREE
OF Ph.D.

DEPARTMENT OF CHEMISTRY

EDMONTON, ALBERTA

FALL, 1981

THE UNIVERSITY OF ALBERTA

RELEASE FORM

NAME OF AUTHOR Matthew Vincent Richard Stainer

TITLE OF THESIS Structural Investigations of Metal
..... Complexes. Part I - Lanthanide Hydro-
..... trispyrazolylborates. Part II -
..... (Phosphine) (olefin) tricarbonyliron
..... Complexes.

DEGREE FOR WHICH THESIS WAS PRESENTED..... Ph.D.

YEAR THIS DEGREE GRANTED 1981

Permission is hereby granted to THE UNIVERSITY OF ALBERTA LIBRARY to reproduce single copies of this thesis and to lend or sell such copies for private, scholarly or scientific research purposes only.

The author reserves other publication rights, and neither the thesis nor extensive extracts from it may be printed or otherwise reproduced without the author's written permission.

(Signed)..... *M.V. Stainer*

PERMANENT ADDRESS:

268 London Road

Boston, Lincs., England

DATED June 26, 1981

THE UNIVERSITY OF ALBERTA
FACULTY OF GRADUATE STUDIES AND RESEARCH

The undersigned certify that they have read, and recommend to the Faculty of Graduate Studies and Research, for acceptance, a thesis entitled STRUCTURAL INVESTIGATIONS OF METAL COMPLEXES. PART I - LANTHANIDE HYDROTRISPYRAZOLYL-BORATES. PART II - (PHOSPHINE) (OLEFIN) TRICARBONYLIRON COMPLEXES submitted by MATTHEW VINCENT RICHARD STAINER in partial fulfilment of the requirements for the degree of Doctor of Philosophy in Chemistry.

Joseph J. Keats
.....
Supervisor

Robert C. Fay
.....

R. Heavell
.....

R. McNeil
.....

Marki Carre
.....

A. Baalsgaard
.....

Date *July 6* 1981.

TO
RUTH, DOUGLAS
CAROLINE, DAVID
and
JUDITH

ABSTRACT

The series of complexes $\text{Ln}(\text{HBPz}_3)_3$ ($\text{Ln} = \text{Sm}, \text{Tb}, \text{Dy}, \text{Ho}, \text{Er}, \text{Tm}, \text{Yb}, \text{Lu}$) have been investigated by a variety of physical techniques with the aim of elucidating their solid and solution state structures. The complexes of the lanthanides lighter than Dy are isostructural in the solid state while those of the complexes heavier than Dy are assigned a different solid state structure. The X-ray crystal structure of $\text{Yb}(\text{HBPz}_3)_3$ has been determined. The ytterbium is eight coordinate and the coordination polyhedron about the metal is best described as a bicapped trigonal prism (BCTP). The point group symmetry of the molecule is close to C_3 . The ^1H , ^{13}C and ^{11}B NMR spectra of the paramagnetic Yb complex exhibit 21, 18 and 3, well separated resonances, respectively. These patterns are consistent with a solution structure close to the solid state structure where the approximate C_3 symmetry is now rigorous. The nuclei have large paramagnetic shifts and the geometric information from the X-ray structure allows a fit of calculated to observed ^1H shifts for the complexes, $\text{Ln} = \text{Dy}, \text{Ho}, \text{Er}, \text{Tm}, \text{Yb}$. The ^1H isotropic shifts are essentially free of contact shift contributions while, with exception of those in the Yb complex, the ^{13}C nuclei have detectable contact shifts.

Signals from a second isomer of the Dy, Ho and Er complexes are seen in the ^1H NMR spectra. This isomer is

postulated to have a square antiprismatic (SAP) coordination geometry and is in slow equilibrium with the BCTP isomer. Values of ΔH° and ΔS° for the isomerization have been obtained from variable temperature NMR experiments.

The SAP isomer undergoes a rapid intramolecular rearrangement process. A possible mechanism for this process is presented. Attempts to model the ^1H isotropic shifts for this isomer met with limited success. The averaging process does not result in effective axial symmetry and non-axial contributions to the pseudocontact shifts may be important for some nuclei.

The X-ray crystal structures of $\text{Fe}(\text{CO})_3(\text{PPh}_3)(\text{olefin})$ (olefin = diethylfumarate, diethylmaleate) have been determined.

Both molecular structures are based on the trigonal bipyramid with the olefin coordinated equatorially, as is expected by electronic considerations. The phosphine occupies an axial site in the maleate complex while in the fumarate complex, it coordinates in the electronically less favoured equatorial site. The difference between the two complexes is assigned to steric effects caused by the different olefin geometries.

ACKNOWLEDGMENTS

The author wishes to thank:

Professor J. Takats for his instruction, guidance and extreme patience throughout the course of this work.

Professor M. Cowie for assistance with the crystallographic studies.

Professor R.E.D. McClung for furnishing computer programs and many helpful discussions.

Glen Bigam for his expertise in recording the NMR spectra.

Members of the group for a variety of reasons:

Drs. J.L. Martin, A.P. Masino, A. Arduini, J.G.A.A.M. "Hansje Pansje" Reuvers and J.T. Malito; Messr. D.T. Martin, L. Ramsay and Ms. S. Gittawong who provided the crystals of the (phosphine)(olefin)tricarbonyl-iron complexes.

Judith for a multitude of reasons including particularly frank discussions concerning the use of lanthanide ions.

The University of Alberta and ultimately the taxpayers of Canada for providing financial support.

Jacki Jorgensen for her considerable help in the preparation of this presentation.

TABLE OF CONTENTS

	Page
Dedication	iv
Abstract	v
Acknowledgements	vii
List of Tables	xi
List of Figures	xv
List of Abbreviations	xvii
CHAPTER I INTRODUCTION	1
General Considerations	1
Lanthanide Complexes	3
CHAPTER II PHYSICAL CHARACTERIZATION OF $\text{Ln}(\text{HBPz}_3)_3$ COMPLEXES	6
Introduction	6
Solid State Studies	9
Solution Studies	14
The Singular Case of $\text{Ho}(\text{HBPz}_3)_3$	18
CHAPTER III THE SOLID STATE STRUCTURE OF $\text{Yb}(\text{HBPz}_3)_3$	22
Introduction	22
Data Collection	29
Solution and Refinement of the Structure	32
Results and Discussion	35
Conclusion	59

	Page
CHAPTER IV NMR STUDIES OF Ln(HBPz₃)₃ COMPLEXES	
Ln = Dy, Ho, Er, Tm, Yb, Lu	60
Introduction	60
¹ H, ¹³ C and ¹¹ B Spectra of Lu(HBPz ₃) ₃ and Yb(HBPz ₃) ₃	73
¹ H Spectra of Ln(HBPz ₃) ₃ Ln = Dy, Ho, Er, Tm	98
¹³ C and ¹¹ B Spectra of Ln(HBPz ₃) ₃ Ln = Dy, Ho, Er, Tm	112
Detection and Characterization of a Second Isomer of Ln(HBPz ₃) ₃ Ln = Er, Ho, Dy	125
Improved Structural Modelling of the Second Isomer - Solid State Structure of Dy(HBPz ₃) ₃ ?	149
Variable Temperature NMR Studies	150
Conclusion	157
CHAPTER V EXPERIMENTAL PROCEDURE	160
General	160
Synthesis of Ln(HBPz ₃) ₃	160
Infrared Spectra	161
X-ray Powder Diffraction	161
NMR Spectra	163
CHAPTER VI CRYSTAL AND MOLECULAR STRUCTURES OF Fe(CO)₃(PPh₃)(DIETHYLFUMARATE) AND Fe(CO)₃(PPh₃)(DIETHYLMALEATE)	164
Introduction	164
Experimental	165
Data Collection	166

	Page
Solution and Refinement of the Structures	166
Description of the Structures	171
Site Preference in $\text{Fe}(\text{CO})_3(\text{PR}_3)\text{olefin}$ Complexes	178
Bond Distances in the $\text{Fe}(\text{CO})_3(\text{PPh}_3)$ Molecular Fragment	182
Geometry and Bond Distances in the Fe-olefin Molecular Fragment	186
REFERENCES	200
Appendix 1: Programs Used in Crystal Structure Solution, Refinement and Analysis	213
Appendix 2: Structure Factor Amplitudes for $\text{Yb}(\text{HBPz}_3)_3$	215
Appendix 3: Least-Squares Programs Used in the Analysis of NMR Spectra	219
Appendix 4: Supplementary Data for Crystal Structures of $\text{Fe}(\text{CO})_3(\text{PPh}_3)(\text{olefin})$ (olefin = fum, mal)	225
Rigid Group Parameters	225
Hydrogen Atom Postions	227
Structure Factor Amplitudes	228

LIST OF TABLES

Table		Page
1	Electronic Configuration and Radii for the Tripositive Ions	2
2	Solid State Infrared Spectra of $\text{Ln}(\text{HBPz}_3)_3$ Complexes	10
3	X-ray Powder Diffraction Patterns $\text{Ln}(\text{HBPz}_3)_3$ $\text{Ln} = \text{Sm, Tb, Dy}$	12
4	X-ray Powder Diffraction Patterns $\text{Ln}(\text{HBPz}_3)_3$ $\text{Ln} = \text{Ho, Yb}$	13
5	Solution Infrared Spectra $\text{Ln}(\text{HBPz}_3)_3$ Complexes	15
6	X-ray Powder Diffraction Pattern of Crude Product $\text{Ho}(\text{HBPz}_3)_3$	20
7	Normalized Edge Lengths For Reference Polyhedra	25
8	Summary of Crystal Data and Intensity Data Collection for $\text{Yb}(\text{HBPz}_3)_3$	30
9	Positional and Thermal Parameters for Non-Hydrogen Atoms of $\text{Yb}(\text{HBPz}_3)_3$	36
10	Idealized Positional and Thermal Parameters for the Hydrogen Atoms of $\text{Yb}(\text{HBPz}_3)_3$	38
11	Polyhedral Shape Parameters for $\text{Yb}(\text{HBPz}_3)_3$	44
12	Normalized Edge Lengths of Polyhedra With Bicapped Trigonal Prismatic Geometry	46
13	Bond Distances, Edge Lengths and Angles for the Coordination Polyhedron of $\text{Yb}(\text{HBPz}_3)_3$	49
14	Interatomic Distances and Angles in the Polypyrazol-1-yl Borate Ligand	51
15	Planes and Calculated Least-Squares Planes Within the $\text{Yb}(\text{HBPz}_3)_3$ Molecule	54

Table		Page
16	Paramagnetic Shift Parameters of Lanthanide Ions	65
17	^1H , ^{13}C and ^{11}B Chemical Shifts of $\text{Lu}(\text{HBPz}_3)_3$	76
18	Geometric Variables for $\text{Yb}(\text{HBPz}_3)_3$	84
19	Diamagnetic Reference Shifts	87
20	The Six Sets of Magnetic Parameters Obtained from the Observed Shifts of H(13), H(43) and H(73)	89
21	Observed and Calculated ^1H Shifts for $\text{Yb}(\text{HBPz}_3)_3$	91
22	Magnetic Parameters from Least-Squares Refinements of Pseudocontact Shifts of $\text{Yb}(\text{HBPz}_3)_3$	92
23	Observed Isotropic and Calculated Pseudocontact ^{13}C and ^{11}B Shifts for $\text{Yb}(\text{HBPz}_3)_3$	97
24	Observed and Calculated ^1H Shifts for $\text{Tm}(\text{HBPz}_3)_3$	100
25	Observed and Calculated ^1H Shifts for $\text{Er}(\text{HBPz}_3)_3$	101
26	Observed and Calculated ^1H Shifts for $\text{Ho}(\text{HBPz}_3)_3$	102
27	Observed and Calculated ^1H Shifts for $\text{Dy}(\text{HBPz}_3)_3$	103
28	Magnetic Parameters from Least-Squares Refinements of ^1H Isotropic Shifts of $\text{Ln}(\text{HBPz}_3)_3$	104
29	Restrained and Unrestrained Least-Squares Refinements ^1H Pseudocontact Shifts	105
30	Observed Isotropic and Calculated Pseudocontact ^{13}C and ^{11}B Shifts for $\text{Tm}(\text{HBPz}_3)_3$	115
31	Observed Isotropic and Calculated Pseudocontact ^{13}C and ^{11}B Shifts for $\text{Er}(\text{HBPz}_3)_3$	116

Table		Page
32	Observed Isotropic and Calculated Pseudocontact ^{13}C and ^{11}B Shifts for $\text{Ho}(\text{HBPz}_3)_3$	117
33	Observed Isotropic and Calculated Pseudocontact ^{13}C and ^{11}B Shifts for $\text{Dy}(\text{HBPz}_3)_3$	118
34	Differences Between Observed Isotropic and Calculated Pseudocontact Shifts for $\text{Ln}(\text{HBPz}_3)_3$ $\text{Ln} = \text{Yb, Tm, Er, Ho, Dy}$ - Possible Contact Shifts	119
35	^1H Chemical Shifts and Isotropic Shifts for Second Isomer of $\text{Ln}(\text{HBPz}_3)_3$ $\text{Ln} = \text{Er, Ho, Dy}$	129
36	Geometric Factors for BCTP(2) Model of $\text{Ln}(\text{HBPz}_3)_3$	136
37	Results of Least-Squares Fit for BCTP(2) Model $\text{Ho}(\text{HBPz}_3)_3$	138
38	Results of Least-Squares Fit for BCTP(2) Model $\text{Dy}(\text{HBPz}_3)_3$	139
39	Magnetic Parameters and R_w Factors from Least-Squares Fit BCTP(2) Model $\text{Ln}(\text{HBPz}_3)_3$ $\text{Ln} = \text{Ho, Dy}$	141
40	Equilibrium Constants For the Isomerization of $\text{Ln}(\text{HBPz}_3)_3$ $\text{Ln} = \text{Ho, Dy}$	152
41	Analyses of $\text{Ln}(\text{HBPz}_3)_3$ Complexes	162
42	Summary of Crystal Data and Intensity Data Collection for $\text{Fe}(\text{CO})_3(\text{PPh}_3)$ (olefin) (olefin = fum, mal)	167
43	Positional and Thermal Parameters for Non-Group Atoms of $\text{Fe}(\text{CO})_3(\text{PPh}_3)$ (fum)	172
44	Positional and Thermal Parameters for Non-Group Atoms of $\text{Fe}(\text{CO})_3(\text{PPh}_3)$ (mal)	173
45	Bond Lengths and Bond Angles in $\text{Fe}(\text{CO})_3(\text{PPh}_3)$ (fum)	179
46	Bond Lengths and Bond Angles in $\text{Fe}(\text{CO})_3(\text{PPh}_3)$ (mal)	180

Table		Page
47	Metal Carbonyl Bond Lengths for Some Trigonal Bipyramidal Iron Carbonyl Complexes	184
48	Angles Describing the Geometry of the Coordinated Olefin	190
49	Fe-C(olefin) and C-C Double Bond Lengths in Fe(CO) ₄ (olefin) and Fe(CO) ₃ (PPh ₃)(olefin) Complexes	196
50	1.0 x (F _O vs. F _C) for Yb(HBPz ₃) ₃	215
51	Rigid Group Parameters Fe(CO) ₃ (PPh ₃)(fum)	225
52	Rigid Group Parameters Fe(CO) ₃ (PPh ₃)(mal)	226
53	Hydrogen Atom Positions Fe(CO) ₃ (PPh ₃)(fum)	227
54	Hydrogen Atom Positions Fe(CO) ₃ (PPh ₃)(mal)	227
55	10 x (F _O vs. F _C) Fe(CO) ₃ (PPh ₃)(fum)	228
56	10 x (F _O vs. F _C) Fe(CO) ₃ (PPh ₃)(mal)	233

LIST OF FIGURES

Figure		Page
1	Solid State Infrared Spectra of $\text{Ln}(\text{HBPz}_3)_3$ Ln = Ho, Dy	11
2	Solution Infrared Spectra $\text{Ln}(\text{HBPz}_3)_3$, Ln = Tb, Dy, Yb	17
3	Solid State Infrared Spectra of $\text{Ho}(\text{HBPz}_3)_3$ a) Solid Residue From CH_2Cl_2 Recrystallization; b) Crude Product	19
4	Reference Polyhedra for Eight Coordination	24
5	Cell Packing Diagram $\text{Yb}(\text{HBPz}_3)_3$	39
6	Stereoview of the $\text{Yb}(\text{HBPz}_3)_3$ Molecule	40
7	$\text{Yb}(\text{HBPz}_3)_3$ Atom Numbering Scheme	41
8	View of $\text{Yb}(\text{HBPz}_3)_3$ Molecule Perpendicular to the Non-Crystallographic Mirror Plane	43
9	Numbering Scheme for BCTP Polyhedral Edges	44
10	Coordination Polyhedron of $\text{Yb}(\text{HBPz}_3)_3$	45
11	200 MHz ^1H NMR Spectrum of $\text{Lu}(\text{HBPz}_3)_3$	74
12	50.33 MHz ^{13}C NMR Spectrum of $\text{Lu}(\text{HBPz}_3)_3$	75
13	200 MHz ^1H NMR Spectrum of $\text{Yb}(\text{HBPz}_3)_3$	77
14	50.33 MHz ^{13}C NMR Spectrum of $\text{Yb}(\text{HBPz}_3)_3$	79
15	64.23 MHz ^{11}B NMR Spectrum of $\text{Yb}(\text{HBPz}_3)_3$	80
16	Coordinate System Defining Geometric Variables r , θ and k for a nucleus N	83
17	Contour Map of Pseudocontact Shifts in $\text{Yb}(\text{HBPz}_3)_3$ Molecule	93
18	Scheme Showing Interconversion of Two Possible Conformations of the Bidentate Ligand in $\text{Yb}(\text{HBPz}_3)_3$	95

Figure		Page
19	Plot of Observed vs. Theoretical Magnetic Susceptibility Anisotropies, D_1 and D_2	108
20	Plot of Observed vs. Theoretical Magnetic Susceptibility Anisotropies, D_2	109
21	50.33 MHz ^{13}C NMR Spectrum of $\text{Tm}(\text{HBPz}_3)_3$	113
22	50.33 MHz ^{13}C NMR Spectrum of $\text{Er}(\text{HBPz}_3)_3$	114
23	Plot of Observed Contact Shift vs. $g_J(g_J-1)J(J+1)$ for C(14) of $\text{Ln}(\text{HBPz}_3)_3$	121
24	Plot of Observed Contact Shift vs. $g_J(g_J-1)J(J+1)$ for C(15) of $\text{Ln}(\text{HBPz}_3)_3$	122
25	200 MHz ^1H NMR Spectrum $\text{Ho}(\text{HBPz}_3)_3$ ($\delta 250$ to -200 ppm)	126
26	200 MHz ^1H NMR Spectrum $\text{Ho}(\text{HBPz}_3)_3$ ($\delta 25$ to -25 ppm)	127
27	BCTP(2) Structural Model for Second Isomer of $\text{Ln}(\text{HBPz}_3)_3$ with Bicapped Trigonal Prismatic Geometry	132
28	Variable Temperature 200 MHz ^1H NMR Spectra of $\text{Ho}(\text{HBPz}_3)_3$	151
29	Plot of $\ln K$ vs. $1/T$ for the Isomerization of $\text{Ho}(\text{HBPz}_3)_3$ and $\text{Dy}(\text{HBPz}_3)_3$	154
30	Cell Packing Diagram for $\text{Fe}(\text{CO})_3(\text{PPh}_3)$ (fum)	174
31	Cell Packing Diagram for $\text{Fe}(\text{CO})_3(\text{PPh}_3)$ (mal)	175
32	Perspective View of $\text{Fe}(\text{CO})_3(\text{PPh}_3)$ (fum)	176
33	Perspective View of $\text{Fe}(\text{CO})_3(\text{PPh}_3)$ (mal)	177

ABBREVIATIONS

acry	methyl acrylate
dpa	pyridine-2,6-dicarboxylate
dpf	diphenylfulvene
dpm	dipivalomethanato(2,2,6,6-tetramethylheptane-3,5-dionato)
Et	ethyl
fum	diethylfumarate
Ln	lanthanide
mal	diethylmaleate
pic	picoline
Ph	phenyl
PY	pyridine
PYR	pyrazine
pz	pyrazolyl $C_3N_2H_3$
^t Bu	tert-butyl
tcne	tetracyanoethylene
THF	tetrahydrofuran
THF-d ₈	C_4D_8O
TMS	tetramethylsilane
toluene-d ₈	C_7D_8

CHAPTER I

INTRODUCTION

General Considerations

The lanthanides, the 14 elements that follow lanthanum in the periodic table, form the longest continuous series of chemically similar elements found in the periodic table.^{1,2} The series may be described as being somewhat enigmatic, their close chemical similarities making isolation and purification difficult until the advent of ion exchange chromatography in the 1940's.

The series corresponds to the progressive filling of the 4f orbitals from La ($[\text{Xe}] 5d^1 6s^2$) to Lu ($[\text{Xe}] 4f^{14} 5d^1 6s^2$). The 4f orbitals lie buried deep below the outermost shells and essentially play no part in the bonding in lanthanide compounds. The 3+ oxidation state dominates and provides the consistent theme of the chemistry of the series. The subtle differences and trends that are encountered when traversing the series are principally due to the changes in the ionic radii of the 3+ cations. The radii of the 3+ ions are given in Table 1. The dramatic decrease in size from La^{3+} to Lu^{3+} , the lanthanide contraction, is the result of the relatively imperfect mutual shielding of the 4f electrons.¹

TABLE 1. Electronic Configuration and Radii for the
Tripositive Ions

Element	Symbol	Electronic Configuration M^{3+}	M^{3+} Ionic Radii ^{a,b}	
			CN 6	CN 8
Scandium	Sc	[Ar]	.745	.870
Yttrium	Y	[Kr]	.900	1.019
Lanthanum	La	[Xe]	1.032	1.160
Cerium	Ce	4f ¹ ^c	1.01	1.143
Praseodymium	Pr	4f ²	.99	1.126
Neodymium	Nd	4f ³	.983	1.109
Promethium	Pm	4f ⁴	.97	1.093
Samarium	Sm	4f ⁵	.958	1.079(1.27) ^d
Europium	Eu	4f ⁶	.947(1.17) ^d	1.066(1.25) ^d
Gadolinium	Gd	4f ⁷	.938	1.053
Terbium	Tb	4f ⁸	.923	1.040
Dysprosium	Dy	4f ⁹	.912	1.027
Holmium	Ho	4f ¹⁰	.901	1.015
Erbium	Er	4f ¹¹	.890	1.004
Thulium	Tm	4f ¹²	.880	.994
Ytterbium	Yb	4f ¹³	.868(1.02) ^d	.985(1.14) ^d
Lutetium	Lu	4f ¹⁴	.861	.977

^aReference 4.

^bValues for coordination numbers six and eight; CN 6 and CN 8 respectively.

^cOnly those electrons outside the closed rare gas shell are indicated.

^dRadii for M^{2+} ions.

The predominance of the 3+ oxidation state is simply due to the balance between solvation energies or lattice energies and ionization potentials which combine to make those compounds in which the metal appears as M^{III} the most stable. Oxidation states other than 3+ are found. Most notable are Ce^{IV} , Eu^{II} and Yb^{II} which result from the special stability associated with the $4f^0$, $4f^7$ and $4f^{14}$ electronic configurations.

Lanthanide Complexes

Lanthanide complexes lack many of the features that characterize the chemistry of d-block transition metal complexes.^{2,3} They more closely resemble the complexes of the heavier group IIA alkaline earth cations Ca^{2+} , Ba^{2+} , Sr^{2+} . The interaction between metal ion and ligand is electrostatic. All the lanthanide ions present the same empty 6s and 6p valence shell to coordinating ligands. The partially filled 4f shell lies deeper in the atom and takes effectively no part in covalent bond formation. Consequently the influence of the ligand field on the 4f orbitals is very much smaller than in the d-block complexes where ligand field stabilization energies contribute greatly to the stability of complexes.

Plots of formation constant and heats of formation of lanthanide complexes against atomic number frequently

show inflections at or near Gd^{3+} . Since this corresponds to the f^7 electronic configuration a crystal field stabilization might be suggested. However, the fact that the "gadolinium break" does not always occur exactly at gadolinium has resulted in the view that the "breaks" are the result of structural changes^{2,3} associated with the change in size of the $3+$ ion. There is support for this view when the structures of the seven coordinate complexes $Yb(acac)_3H_2O$ ⁵ and $Lu(dpm)_3(3-pic)$ ⁶ are compared with the corresponding eight coordinate $Y(acac)_3(H_2O)_2$ ⁷ and $Ho(dpm)_3(4-pic)_2$ ⁸. The smaller Yb^{3+} and Lu^{3+} exhibit the lower coordination number. Similarly NMR studies of the dithiophosphate $Ln(S_2P(OR)_2)_4^-$ complexes⁹ indicate a change in the solution structure between the dysprosium and the holmium complexes.

The generally weaker, electrostatic, non-directional bonding in lanthanide complexes as compared to d-block complexes results in facile ligand exchange processes. Both intermolecular and intramolecular reactions appear to be important when these complexes are studied in solution.

The lanthanide ions are typical A type cations in the Ahrland-Chatt-Davies scheme¹⁰ or "hard acids" in the Pearson sense.¹¹ By far the majority of isolable complexes involve oxygen donor ligands or mixed oxygen-nitrogen chelate ligands. The ligands are commonly anionic and

multidentate as typified by β -diketonate, dicarboxylate and amine-carboxylate ligands. However, it should not be imputed that lanthanide bonding with other donor atoms is necessarily weak. For a complex to be stable in aqueous media requires that the ligand compete with H_2O , which is a good ligand towards lanthanide ions and is also available in great abundance, and OH^- which forms insoluble hydroxides. Use of non-aqueous and less strongly coordinating solvents has made possible the isolation of complexes containing ligands which are neutral oxygen donors¹² or simple nitrogen donors.¹³ Complexes where all the donor atoms in the complex are nitrogen such as the polydentate amine^{14,15} and terpyridyl^{16,17} ligands although few in number are now well characterized. A small number of complexes involving sulphur donor ligands, the dithiocarbamates $Ln(dtc)_4^-$ ^{18,19} and the dithiophosphinates $Ln[S_2P(OR)_2]_4^-$ ²⁰ have been synthesized as well.

More recently there has been considerable interest in the organometallic chemistry of the lanthanides.²¹⁻²⁴ Like the classical coordination complexes the bonding here also appears to be mostly electrostatic in nature.^{24,25}

CHAPTER II

PHYSICAL CHARACTERIZATION OF $\text{Ln}(\text{HBPz}_3)_3$ COMPLEXES

Introduction

The HBPz_3^- ligand is one of the family of poly(pyrazol-1-yl)borate ligands $(\text{R}_{4-n}\text{BPz}_n)^-$ ($n = 2, 3, 4$; Pz = 1-pyrazolyl; R = H, alkyl, aryl) first synthesized by Trofimenko.²⁶ These ligands have provided an extensive and varied range of coordination and organometallic complexes.^{27, 28, 29} The HBPz_3^- ligand is uninegative and when tridentate a six-electron donor. These features allow an analogy with the cyclopentadienide anion to be drawn and frequently the corresponding complex can be prepared where a RBPz_3 moiety is found in the place of an $\eta^5\text{-C}_5\text{H}_5$ group. As a general rule, complexes involving RBPz_3^- are more stable than the analogous C_5H_5^- complexes.

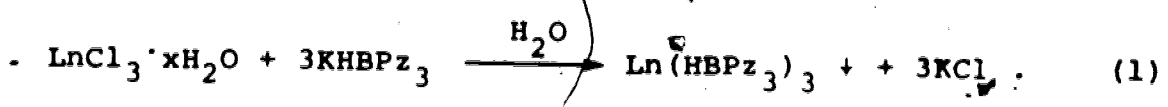
The $\text{HBPz}_3^- - \text{C}_5\text{H}_5^-$ analogy and interest in metallocene groups " $(\text{C}_5\text{H}_5)_2\text{M}$ " were to some extent responsible for the interest in the early transition metal poly(pyrazol-1-yl)borates. The complexes $(\text{C}_5\text{H}_5)(\text{HBPz}_3)\text{TiCl}_2$ ³⁰ and $(\text{HBPz}_3)\text{MCl}_3$ ³¹ ($\text{M} = \text{Ti}, \text{V}$) have been prepared. Similarly the prominence of C_5H_5^- in the organometallic chemistry of the lanthanides and actinides produced interest in the poly(pyrazol-1-yl)borate complexes of these metals. Bagnall et al. have prepared the complexes $\text{U}(\text{HBPz}_3)_4$ and

$UCl_2(HBPz_3)_2$.³² Interestingly the former is described as having a coordination number ≥ 8 , while in the latter the ligands are thought to be bidentate on the basis of the NMR spectra.³³ The mixed complexes $U(C_5H_5)_2(HBPz_3)_2$, $U(C_5H_5)_2Cl(HBPz_3)$ and $U(C_5H_5)Cl_2(HBPz_3)$ are also described.^{33,34} The stability of the latter complex is of note as the analogous $U(C_5H_5)_2Cl_2$ complex is unstable towards disproportionation. The complex $U(C_5H_5)(H_2BPz_2)Cl_2$ is similarly unstable. The thorium complexes have been synthesized as the N,N-dimethylacetamide adducts.³⁴ The $HBPz_3^-$ ligand appears, from the 1H NMR spectrum, to be bidentate in the $Th(C_5H_5)Cl_2(HBPz_3)(CH_3CON(CH_3)_2)_{1.5}$ and $U(C_5H_5)Cl_2(HBPz_3)(Ph_3PO)$ complexes while in $U(C_5H_5)Cl_2(HBPz_3)$ it is probably tridentate. The phosphine oxide adduct is prepared by stirring with Ph_3PO in THF. Interestingly, reaction of $U(C_5H_5)_3Cl$ with an equivalent of $HBPz_3^-$ did not give $U(C_5H_5)_3(HBPz_3)$ but resulted in the formation of small amounts of $U(C_5H_5)_2(HBPz_3)_2$ from the substitution of a C_5H_5 ring by $HBPz_3$ group.³⁴

The lanthanide complexes $Ln(HBPz_3)Cl_2 \cdot (THF)_{1.5}$ and $Ln(HBPz_3)_2Cl \cdot THF$ ($Ln = Y, Er, Yb$ and Lu) have been synthesized.^{35,36} The mixed sandwich derivatives $Ln(HBPz_3)(C_8H_8)$ were prepared by reaction of the dichloro-tris(pyrazol-1-yl)borate complex with $K_2C_8H_8$. However, reaction with various other organometallic reagents such

as $\text{Na}(\text{C}_5\text{H}_5)$, $\text{Mg}(\text{CH}_2\text{SiMe}_3)_2$ etc., gave the $\text{Ln}(\text{HBPz}_3)_3$ complexes as the only identifiable products.³⁶

The $\text{Ln}(\text{HBPz}_3)_3$ complexes can be readily prepared from aqueous media by the reaction of the hydrated lanthanide chlorides and KHBPz_3 .^{35,36}



Unlike the mixed ligand-chloro species they are stable towards hydrolysis in air as solids. The synthesis of an all nitrogen donor atom lanthanide complex in aqueous media, although surprising, is almost certainly made possible by its insolubility in H_2O . The remarkable stability of the complexes almost certainly is derived from the unique properties of the HBPz_3^- ligand and its ability to satisfy the high coordination numbers sought by lanthanide ions.

Initial investigations³⁶ of the complexes revealed that, although all can be prepared by reaction (1) and are insoluble in water, the complexes $\text{Ln} = \text{La}, \text{Pr}$ and Sm are also very sparingly soluble in all common organic solvents while the complexes $\text{Ln} = \text{Y}, \text{Er}, \text{Yb}$ and Lu are moderately soluble in THF, acetone and CH_2Cl_2 (up to 0.1 M for $\text{Yb}(\text{HBPz}_3)_3$ in CH_2Cl_2). This difference in the solubility properties between the complexes of the early and late lanthanides was assigned to a change in structure due to the change in the size of the lanthanide

ion. Differences in the IR spectra of the two sets of complexes were also noted. Particularly sensitive are the B-H stretching vibrations of these complexes at $\sim 2500 \text{ cm}^{-1}$.^{35,36}

This chapter describes the results of structural studies of the $\text{Ln}(\text{HBPz}_3)_3$ series of complexes, in the solid state and in solution using infrared spectroscopy and X-ray powder diffraction.

Solid State Studies

The infrared absorptions of the $\text{Ln}(\text{HBPz}_3)_3$, in the solid state as mineral oil mulls, in the region $2300\text{-}2600 \text{ cm}^{-1}$ are listed in Table 2. These are the absorptions arising from the B-H stretching vibrations. The spectra of the dysprosium and holmium complexes are shown in Figure 1. Table 2 and Figure 1 show that the complexes may be placed into two distinct groups on the basis of the pattern of their B-H stretching absorptions. The spectrum of $\text{Dy}(\text{HBPz}_3)_3$ is typical of those of the early lanthanide complexes while the $\text{Ho}(\text{HBPz}_3)_3$ spectrum is typical of the later lanthanide complexes.

The X-ray powder diffraction patterns of the samarium, terbium and dysprosium complexes are summarized in Table 3 and the patterns arising from the holmium and ytterbium complexes are given in Table 4. There is

Table 2. Solid State Infrared Spectra of $\text{Ln}(\text{HBPz}_3)_3$ Complexes. a,b,c

Sm	Tb	Dy	Ho	Er	Tm	Yb	Lu
2499	w	2501	w	2501	w		
2451 (sh)		2453 (sh)	s	2452 (sh)			
2442	s	2442	m	2442			
2412 (sh)		2413 (sh)	w	2413 (sh)			
2405	m	2406	w	2407			
2375	w	2376	vW	2375			
2367 (sh)		2367 (sh)		2368 (sh)			
2341	vW	2343		2344			
2521 (sh)		2520 (sh)		2522 (sh)		2524 (sh)	2526 (sh)
2491 (sh)		2493 (sh)		2491 (sh)		2490 (sh)	2490 (sh)
2484	w	2483	w	2484	w	2484	2484
2478	w	2478	w	2479	w	2480	2481
2464 (sh)		2464 (sh)		2464 (sh)		2465 (sh)	2465 (sh)
2459	m	2460	m	2460	m	2460	2461
2445	vW	2447 (sh)	vW	2447	vW	2447	2447
2433	m	2434	m	2434	m	2434	2435
2416 (sh)		2417 (sh)		2416 (sh)		2417 (sh)	2418 (sh)
2407	m	2408	m	2408	m	2408	2408
2389 (sh)				2394 (sh)		2395 (sh)	2394 (sh)
2375	vW	2376	vW	2376	vW	2376	2376

^a Spectra as mineral oil mulls. ^b Frequencies in cm^{-1} . ^c Abbreviations: s=strong, m=medium; w=weak, vW=very weak, sh=shoulder.

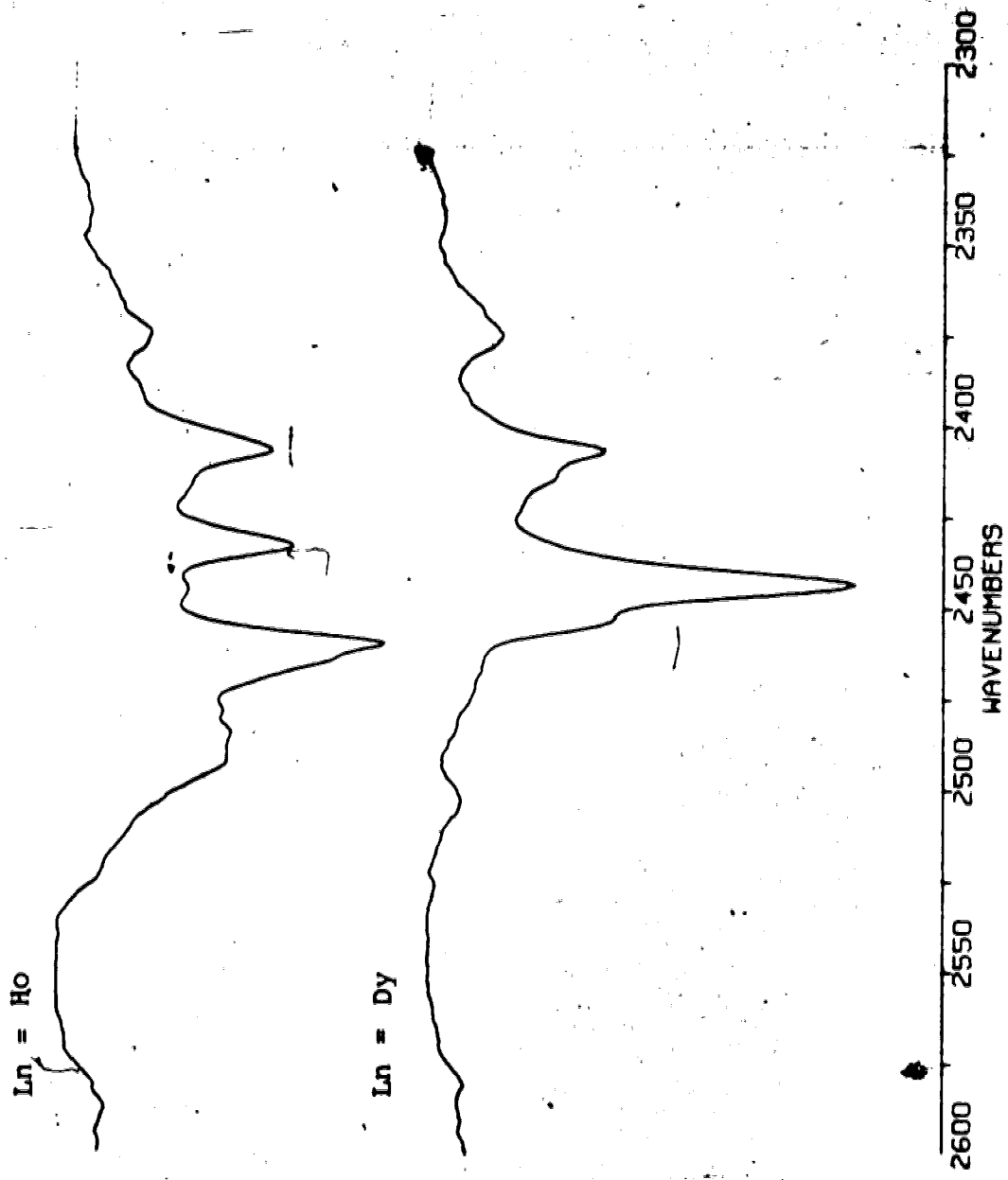


FIGURE 1. Solid State Infrared Spectra of $\text{Ln}(\text{HBPz})_3$, Ln = Ho, Dy.

Table 3. X-ray Powder Diffraction Patterns^a Ln(HBPz₃)₃

Ln = Sm, Tb, Dy

<u>Sm</u>	<u>Tb</u>	<u>Dy</u>
2θ ^b	2θ ^b	2θ ^b
8.55 s	8.65 s	8.55 s
10.7 vs	10.75 vs	10.65 vs
12.8 s	12.9 s	12.85 s
14.9 vw	14.0 vw	
15.5 m	15.55 m	15.5 m
17.2 w	17.4 w	17.3 w
18.4 vw	18.6 vw	18.4 vw
19.8 m	19.9 m	19.8 m
21.2 vw		21.2 vw
21.5 vw	21.7 vw	21.65 vw
22.9 m	23.1 s	22.95 s
23.8 m	24.0 s	23.85 s
24.5 s	24.65 s	24.6 s
26.0 s	26.0 m	26.05 s
26.3 w	26.2 s	26.4 w
	26.5 w	
27.4 w	27.4 w	27.4 w
29.1 vw	29.35 vw	29.2 vw
30.1 s	30.3 s	30.2 s
	31.1 vw	
32.1 w	32.35 w	32.1 w
32.9 m	33.1 m	33.0 m
33.9 vw	33.8 vw	33.8 vw
	34.35 vw	34.1 vw
34.9 vw	35.1 vw	34.95 w
35.6 vw		35.8 vw
36.0 vw	35.9 vw	36.1 vw
37.1 m	37.3 m	37.1 m
	38.5 vw	38.3 vw
	39.15 vs	38.9 vw
39.4 vw	39.3 vw	39.4 vw
40.3 w	40.4 w	40.3 w

^aRelative intensities: vs, very strong; s, strong; m, medium; w, weak; vw, very weak.

^bCuK_α Radiation λ = 1.5418 Å.

Table 4. X-ray Powder Diffraction Patterns^a Ln(HBPz₃)₃
Ln = Ho, Yb

<u>Ho</u>	<u>Yb</u>	<u>Ho</u>	<u>Yb</u>
2θ ^b	2θ ^b	2θ ^b	2θ ^b
8.15 vs	8.1 vs		27.0 w
10.15 vs	10.15 vs	27.15 w	27.2 vw
11.2 m	11.25 m		28.05 w
12.8 vs	12.9 vs	28.35 vw	28.35 w
13.7 vw	13.85 vw	28.5 w	28.6 w
15.2 m	15.3 m	29.1 w	29.1 w
15.85 m	16.0 w	29.9 m	29.95 m
16.45 w	16.5 w	30.3 w	30.4 w
17.05 m	17.1 m	30.85 vw	
17.4 w	17.5 m	31.4 w	31.5 m
17.7 vw	17.7 w	31.9 w	31.85 w
18.15 vw	18.7 vw	32.15 m	32.15 m
19.3 w	19.3 w		32.6 w
19.7 s	19.8 s	32.8 w	32.95 w
20.05 vw	20.1 vw	33.7 w	33.85 w
20.75 w	20.85 w		34.6 vw
21.7 m	21.8 m	34.85 w	34.9 m
22.0 m	22.05 m	35.35 vw	35.4 w
22.3 s	22.35 s		35.9 vw
23.0 w	23.05 w	35.9 m	36.1 m
23.45 s	23.6 s	36.65 w	36.7 w
24.25 vs	24.3 vs	37.0 w	37.05 w
24.8 vw	24.8 w		37.9 vw
25.1 m	25.2 m	38.9 w	39.0 w
25.45 s	25.5 s	39.2 w	39.25 w
25.85 s	25.9 s	39.55 m	39.65 m
26.1 m	26.2 m	39.9 vw	40.0 w
26.85 w	26.8 w		

^aRelative intensities: vs, very strong; s, strong; m, medium; w, weak; vw, very weak.

^bCuK_α Radiation λ = 1.5418 Å.

an obvious difference between the patterns of the holmium and dysprosium complexes. Therefore, from Table 2 and Tables 3 and 4 it can be concluded that the samarium, terbium and dysprosium complexes have one solid state structure while the holmium and ytterbium complexes have another.

The solubility properties of the complexes exhibit a change which parallels this change in the solid state structure. The complexes $\text{Ln}(\text{HBPz}_3)_3$ ($\text{Ln} = \text{La}, \text{Sm}, \text{Pr}, \text{Eu}, \text{Tb}$) are very sparingly soluble in CH_2Cl_2 and THF. The complexes of the lanthanides heavier than terbium and including yttrium are soluble in CH_2Cl_2 and THF. Thus, the solubility properties exhibit a terbium-dysprosium "break", in contrast to the infrared spectra and X-ray powder diffraction patterns which show a break between dysprosium and holmium.

Solution Studies

Results from the analysis of the NMR spectra of $\text{Yb}(\text{HBPz}_3)_3$ show that the molecular structure of the complex is the same in both the solid and solution states (this will be dealt with more fully in Chapters III and IV).

Table 5 gives the B-H stretching absorptions of the complexes in CH_2Cl_2 . Although $\text{Tb}(\text{HBPz}_3)_3$ has extremely

Table 5. Solution Infrared Spectra $\text{Ln}(\text{HBPz}_3)_3$
Complexes. ^{a,b,c}

Tb		Dy		Ho		Er		Tm
2484 (sh)		2484 (sh)		2486 (sh)		2486 (sh)		2487 (sh)
								2477 (sh)
2468 (sh)								
2462	m	2462	m	2463	m	2463	m	2464
								m
2380	w	2379	w	2379	w	2381	w	2378
								w
Yb		Lu						
2487 (sh)		2488 (sh)						
2477 (sh)		2477 (sh)						
2464	m	2464	m					
2380	w	2381	w					

^a CH_2Cl_2 solution spectra.

^b Frequencies in cm^{-1} .

^c Abbreviations: m=medium, w=weak, sh=shoulder.

limited solubility in CH_2Cl_2 it was possible to obtain an infrared spectrum using a Fourier transform spectrometer. Figure 2 shows the solution spectra of terbium, dysprosium and ytterbium complexes in the region 2300-2600 cm^{-1} . The absorptions are rather broad and not as well resolved as in the solid state spectra but the similarities between the spectra suggest that the molecular structure is the same for all the complexes in solution. This view is confirmed by the NMR spectra which show that the ytterbium and dysprosium complexes are isostructural in solution.

The implication therefore is that, if indeed the differences in the solid state infrared spectra reflect a difference in molecular structure rather than a change say in the packing of the molecules in the crystal, the dysprosium complex changes its molecular structure on dissolution.

The break in the properties of the $\text{Ln}(\text{HBPz}_3)_3$ complexes is clearly related to structural changes in the complexes. However, the break is not as abrupt as it appears from consideration of only the infrared spectra or only the solubility properties. The dysprosium complex seems to have a foot in both camps.

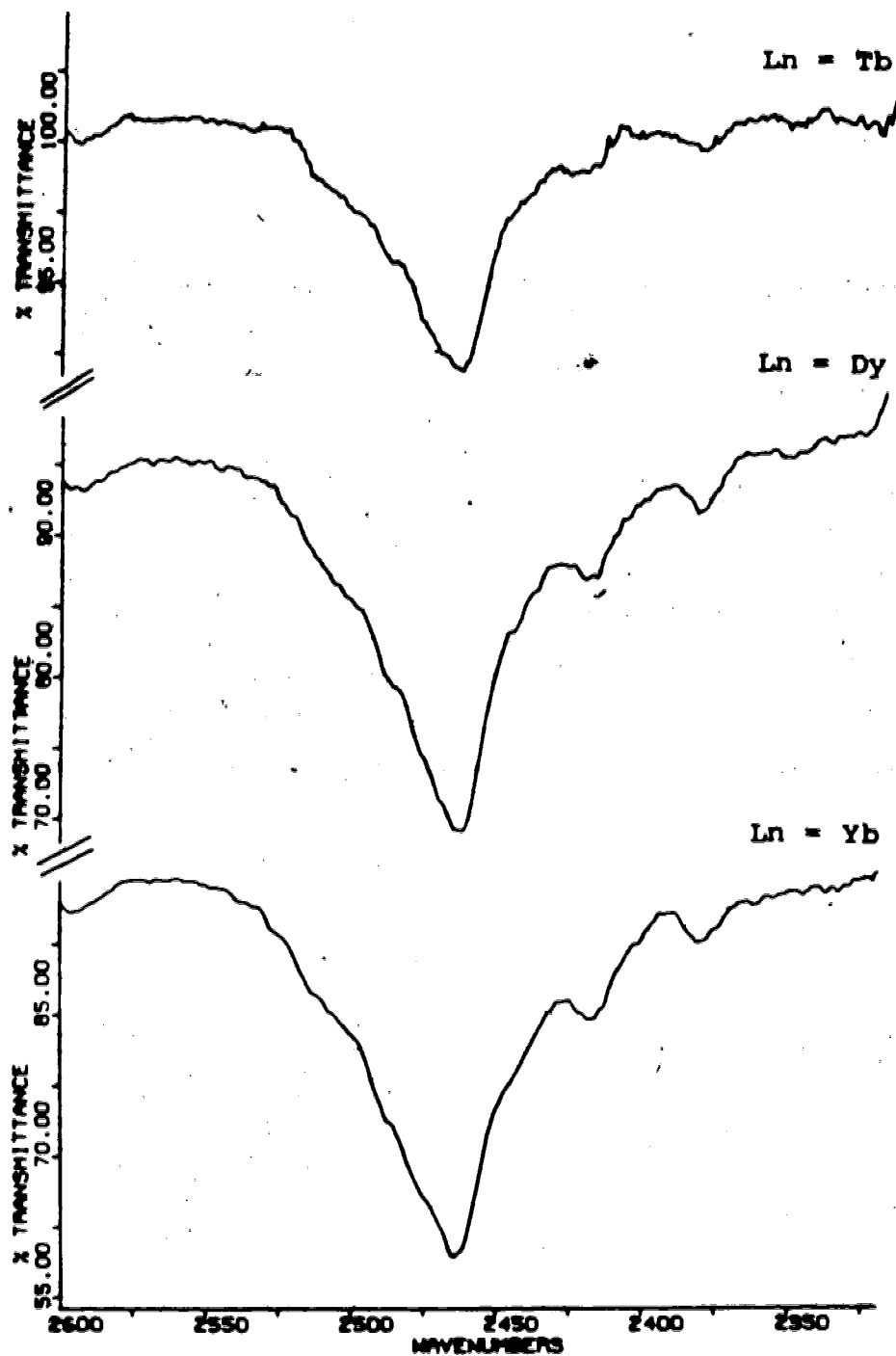


FIGURE 2. Solution Infrared Spectra $\text{Ln}(\text{HBPz}_3)_3$,
Ln = Tb, Dy, Yb.

The Singular Case of Ho(HBPz₃)₃

The infrared spectrum of Ho(HBPz₃)₃ shown in Figure 1 and the X-ray powder diffraction pattern in Table 4 are those from a recrystallized sample. Difficulty was sometimes encountered in completely dissolving Ho(HBPz₃)₃ samples in CH₂Cl₂ for recrystallization. The insoluble residue was recovered and its solid state infrared spectrum is shown in Figure 3. This spectrum is similar to those of Dy(HBPz₃)₃ and Tb(HBPz₃)₃ complexes and suggests that the Ho(HBPz₃)₃ can exist in both structural modifications. Preparation of Ho(HBPz₃)₃ by the standard method described in the experimental section gave crude product with ν(B-H) patterns which were different from both the Tb(HBPz₃)₃ and Yb(HBPz₃)₃ spectra. The exact pattern exhibited by the crude products was not reproducible. However, on recrystallization all gave solid samples with a pattern like that shown in Figure 1.

The infrared spectrum from one preparation is shown in Figure 3. This product was completely soluble in CH₂Cl₂ and its NMR spectrum in CD₂Cl₂ was indistinguishable from a recrystallized sample. It is tempting to assign the infrared spectrum to a mixture of Ho(HBPz₃)₃ with Tb(HBPz₃)₃-type structure and Yb(HBPz₃)₃-type structure. The X-ray powder diffraction pattern of this particular crude product is summarized in Table 6 and is unlike

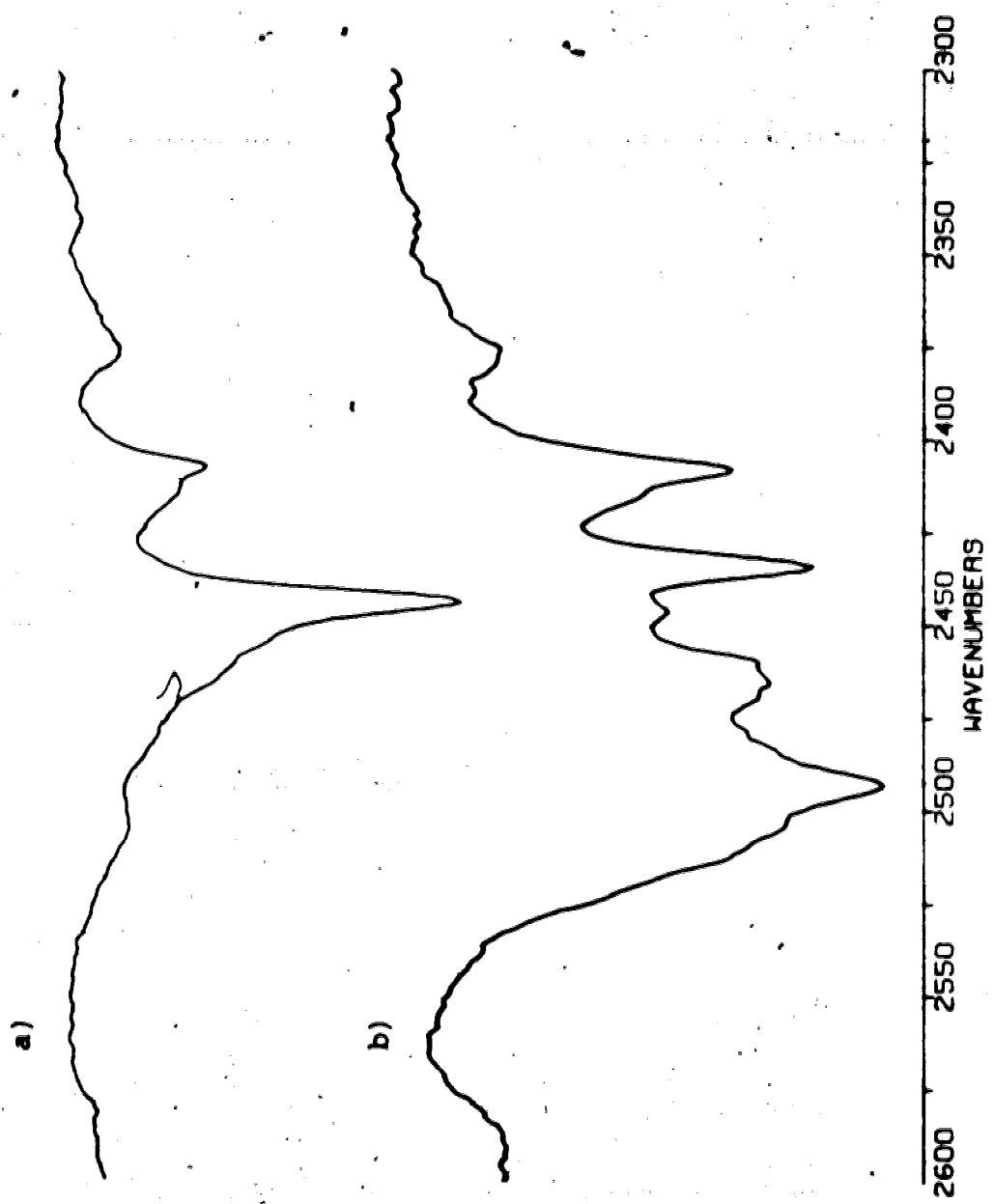


FIGURE 3. Solid State Infrared Spectra of $\text{Ho}(\text{HBPz}_3)_3$, a) solid residue from CH_2Cl_2 recrystallization; b) crude product.

Table 6. X-ray Powder Diffraction Pattern^a of Crude
Product $\text{Ho}(\text{HBPz}_3)_3$

$2\theta^b$		$2\theta^b$	
8.1	s	20.05	w
8.8	vw	20.9	m
10.0	vs	21.3	m
11.1	vw	22.4	w
11.85	vw	22.95	w
12.1	w	23.45	s
12.8	vs	24.25	s
13.7	m	24.7	m
15.2	w	25.1	m
15.85	w	25.5	m
16.4	m	25.9	m
17.1	vw	26.45	w
17.6	m	27.2	w
19.75	w	27.65	w

^aRelative intensities: vs, very strong; s, strong; m, medium; w, weak; vw, very weak.

^b $\text{CuK}\alpha$ Radiation $\lambda = 1.5418 \text{ \AA}$.

either those of $\text{Tb}(\text{HBPz}_3)_3$ or $\text{Yb}(\text{HBPz}_3)_3$.

The unpredictable behaviour of the holmium complex is perhaps slightly disconcerting, however, it firmly places the complex alongside the dysprosium complex in the grey area of structure between terbium and erbium.

CHAPTER III

THE SOLID STATE STRUCTURE OF $\text{Yb}(\text{HBPz}_3)_3$

Introduction

Lanthanide complexes typically have high coordination numbers. This feature and the lack of covalent directional bonding make structural studies of these complexes particularly interesting. The focus of this interest is the coordination polyhedron formed by the ligand atoms around the metal centre.

Coordination numbers of up to 12 are known with 8 being the most common. For one coordination number there may be two or more coordination geometries that are commonly found. The coordination geometry adopted by a complex is principally determined by the size of the central metal ion and the ligand geometry.

The structures of lanthanide complexes have been reviewed^{37,38} and there are several reviews of coordination numbers of 8 or greater.^{39,40,41} Hoard and Silverton⁴² have calculated the "most favoured polyhedra" for eight coordination by minimizing the repulsive energy between ligands, $\sum_{i \neq j} R_{ij}^{-n}$. R_{ij} is a function of the distance between ligating atoms i and j , and the value of n depends on the model from $n = 1$ (Coulombic repulsion) to $n = \infty$ (the hard sphere model where the atoms are considered to

be incompressible spheres).

Figure 4 shows the three major coordination polyhedra found in eight coordinate complexes, the D_{4d} square antiprism (SAP), the D_{2d} dodecahedron (DOD) and the C_{2v} bicapped trigonal prism (BCTP). The BCTP is much less common than both the DOD and SAP. The dimensions of the idealised polyhedra are listed in Table 7. The hard sphere model dimensions are calculated using a points on a sphere model with identical metal-ligand bond lengths. This takes no account of the possibility of different bond lengths arising from the symmetry non-equivalent sites in the DOD (A and B) and the three such sites in the C_{2v} BCTP.

An alternative eight coordinate geometry, the cube, has been calculated⁴² to have much less favourable ligand-ligand repulsions than the DOD and SAP. Only one example⁴³ of a lanthanide complex with this geometry is known. Cubic geometry appears to be preferred over square antiprismatic geometry for the complex, $La(bpy)_4^{3+}$ ($bpyo = 2,2'$ -bipyridine dioxide), because of the more favourable stacking of the pyridine rings about the metal.

Extension of the method of minimization of the repulsive energies reveals that the differences in energy between idealised polyhedra and the energy barriers along the pathways connecting them are small.⁴⁴⁻⁴⁸ The pathways by which the polyhedra may interconvert are

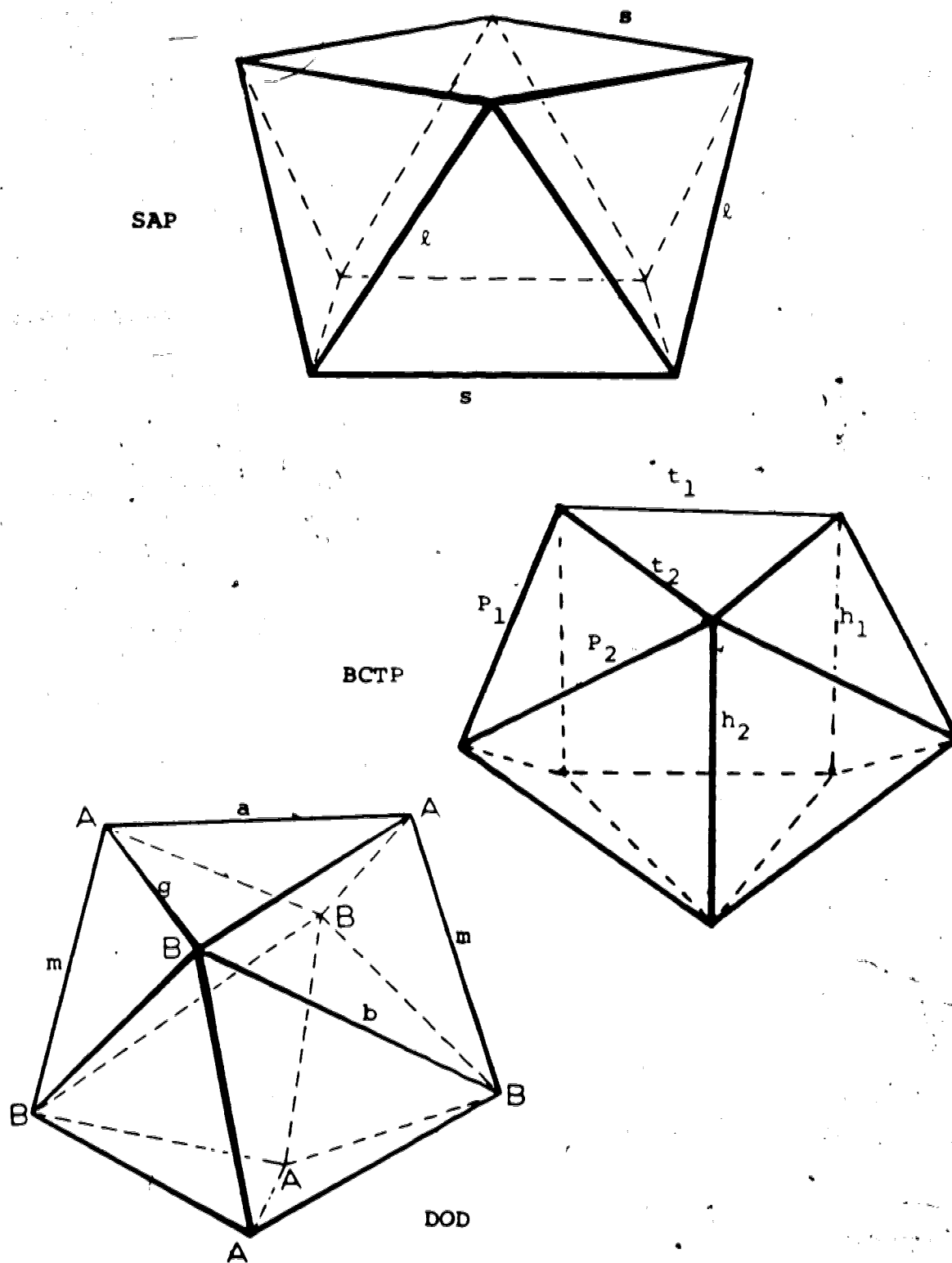


FIGURE 4. Reference Polyhedra for Eight Coordination.

Table 7. Normalised^a Edge Lengths For Reference Polyhedra.

DOD ^b		SAP ^b		BCTP ^c	
HSM ^d	MFP ^d	HSM	MFP	HSM	
a, m, g=1.119	a, m=1.17	l, s=1.215	l=1.258	t ₁ , t ₂ =1.115	
	g=1.24		s=1.190	P ₁ , P ₂ =1.115	
b=1.499	b=1.49			h ₁ , h ₂ =1.491	

^a Normalised edge lengths are the ratio of edge lengths to the central atom-ligand bond length.

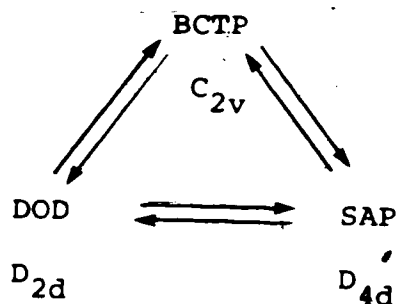
^b Data from reference 42.

^c Data from reference 50.

^d HSM, hard sphere model; MFP, most favoured polyhedron.

represented by the cycle shown in Scheme 1.

SCHEME 1:



The classic deformation modes^{49,50} involve the deformation of the b edges (those joining two B sites) of the DOD such that the triangular faces meeting at the edge form one square face of the SAP or BCTP. If two b edges are deformed simultaneously the SAP is formed, if only one b edge disappears the BCTP is obtained. Thus, there are two distinct routes connecting the SAP and the DOD, one is direct and the other is via the BCTP.

Often the coordination polyhedron observed for a complex does not correspond exactly to one definite idealised form. Several sets of parameters have been used to measure the deviations, both in direction and distance, from the idealised polyhedra. These include the angles between the metal ligand vectors and the principal axis of the polyhedron,⁴² the angle between the two BAAB trapezoids of the DOD⁵¹ and one^{52,41} method which uses the root mean square distance of the ligand atoms from the positions they would occupy in the reference polyhedron.

Probably the two most elegant methods are those of Porai-Koshits and Aslanov⁴⁹ and Muetterties and Guggenberger.⁵⁰ These authors define the shape parameters, δ , as the dihedral angles between faces meeting at the shape determining edges of the polyhedron. In the eight coordinate case these are the b edges of the DOD and the diagonals of the square faces of the SAP and BCTP. Porai-Koshits and Aslanov also used the angle ϕ which is a measure of the planarity of the two BAAB trapezoids.

Muetterties has noted that a description of the coordination geometry based on the polyhedral shape is generally superior in identifying distortions from the reference polyhedra than a description based on angles subtended by the ligand atoms and the central atom or normalised edge lengths.

A dramatic demonstration of the considerable advantages of using the δ shape parameters has been provided by Steffen and Fay⁵³ in their reinvestigation of the coordination geometries of the eight coordinate tetrakis acetylacetonate complexes, $M(\text{acac})_4$ ($M=\text{Zr, Ce, Th, U, Np}$). Two crystalline modifications of the complexes are known, α and β . The assignment of the β form as being close to square antiprismatic geometry is unambiguous. However, the δ and ϕ angles clearly show that the α - $M(\text{acac})_4$ are closest to BCTP geometry. These complexes had previously

been described in the literature as having both dodecahedral and square antiprismatic geometry.

Data Collection⁵⁴

Crystals suitable for X-ray diffraction were obtained from a sample of $\text{Yb}(\text{HBPz}_3)_3$, prepared by the method described in the experimental section (Chapter V) by slow crystallisation from CH_2Cl_2 /hexane solution.

A crystal of $\text{Yb}(\text{HBPz}_3)_3$ was mounted and sealed in a thin wall glass capillary. Preliminary Weissenberg and precession photographs showed systematic absences $h00$, $h = 2n+1$; $0k0$, $k = 2n+1$; $00l$, $l = 2n+1$; consistent with the space group $P2_1^2_12_1$.

The crystal was transferred to a Picker FACS I four circle automated diffractometer. Accurate cell parameters were obtained by a least-squares analysis of the setting angles of 12 carefully centred reflections chosen from diverse regions of reciprocal space ($50^\circ < 2\theta < 75^\circ$, Cu K_α radiation). Table 8 contains a summary of the crystal data and important features of the data collection. Intensity data were collected using a scintillation counter and pulse height analyser tuned to accept 90% of the Cu K_α peak. A θ - 2θ scan technique was used. Background counts were measured at both limits of each scan with stationary crystal and counter. Assuming approximate linearity of background, the intensity of the peak (I) is

Table 8. Summary of Crystal Data and Intensity Data Collection.

Compound	Yb(HBPz ₃) ₃			
Formula	YbN ₁₈ C ₂₇ B ₃ H ₃₀			
Cell Parameters				
a	13.729(2) Å			
b	21.465(3) Å			
c	11.461(1) Å			
Z	4			
Space Group	P2 ₁ 2 ₁ 2 ₁ (D ₂ ⁴ No. 19) ⁶⁰			
Crystal Volume	1.1 x 10 ⁻² mm ³			
Crystal Shape	Hexagonal Rod			
Faces and distances (in mm) from arbitrary origin within crystal	1	0	0	0.26
	1	0	0	0.26
	0	1	0	0.06
	0	1	0	0.06
	0	1	1	0.09
	0	1	1	0.09
	0	1	1	0.09
	0	1	1	0.09
Temperature	20°C			
Radiation	Cu K _α (Ni filtered)			
μ	55.62 cm ⁻¹			
Range in Absorption Correction Factors	0.282-0.550			
Receiving Aperture	3 mm x 3 mm, 30 cm from crystal			
Take off angle	3.1°			

continued...

Table 8 (continued)

Scan Speed	2° min ⁻¹ (4° ≤ 2θ ≤ 105°) 1° min ⁻¹ (105° < 2θ ≤ 122°)
Scan Range	0.95° below K _{α1} to 0.95° above K _{α2}
Background Counting Time	20 sec at each end of the scan for (4° ≤ 2θ ≤ 105°); 40 sec for (105° < 2θ ≤ 122°)
2θ limits	4.0° - 122.0°
p-factor ⁵⁶	0.04
Unique Data Collected	2959
Unique Data Used (F _o ² ≥ 2σ(F _o ²))	2662
Final number of parameters varied	313
Error in observation of unit weight. ⁵⁵	1.50
R	0.038
R _w	0.048

given by:

$$I = PK - (B_1 + B_2) \frac{tP}{tB}$$

where PK = peak count, tP = peak scan time, tB = the sum of the two background collection times and B₁ and B₂ are the background counts. Standard deviations in the intensity ($\sigma(I)$) were calculated using the equation:

$$\sigma(I) = [PK + \frac{tP^2}{tB^2} (B_1 + B_2) + p^2 I^2]^{1/2}$$

where p is an ignorance factor used to account for machine uncertainty.⁵⁶ The intensities of 3 standard reflections were measured automatically every 100 reflections (every 50 reflections for $2\theta > 105^\circ$) and showed no detectable decrease in intensity due to crystal decomposition during data collection.

The intensities of 2959 unique reflections were collected. 2662 were considered significantly above background ($I \geq 2\sigma(I)$) and were reduced to structure factor amplitudes and standard deviations in the structure factors by correction for Lorentz, polarisation and absorption effects.⁵⁷⁻⁶⁰

Solution and Refinement of the Structure.⁵⁴

The ytterbium atom position was located by a three dimensional Patterson⁶¹ synthesis. The remaining non-hydrogen atoms were located with some difficulty because

of the pseudo symmetry of the structure. The ytterbium lies very close to the position $0, y, 1/4$ and the molecule possesses approximate mirror symmetry, the mirror plane lying almost coplanar with the $0, y, z$ plane. The structure was slowly solved by successive full matrix least-squares refinements and difference Fourier syntheses. Only a few further non-hydrogen atoms being input into each least-squares - difference Fourier cycle to gradually break the pseudo symmetry. The function minimised during the least-squares refinement was $\sum w(|F_o| - |F_c|)^2$ where $|F_o|$ and $|F_c|$ are the observed and calculated structure amplitudes respectively, and w , is a weighting factor ($w = 1/\sigma(F)^2$). Atomic scattering factors were taken from Cromer and Wabers tabulations⁶² for all atoms except hydrogen for which the values of Stewart et al.⁶³ were used. Anomalous dispersion terms⁶⁴ for ytterbium were included in F_c . The hydrogen atom positions were calculated by a positioning program with C-H and B-H bond lengths of 0.95 \AA and were included in the refinement as fixed atoms with isotropic thermal parameters 1 \AA^2 greater than the atom to which they were attached. The large number of non-hydrogen atoms and the relatively small number of observed reflections resulted in only the ytterbium, nitrogen and boron atoms, and one carbon atom C(95) being refined with anisotropic thermal parameters. The remaining carbon atoms were refined with isotropic thermal parameters. C(95) was

refined anisotropically to resolve the ambiguity in the positions of C(95) and N(92) in the uncoordinated pyrazolyl group. Refinements were carried out with both possible dispositions of the atoms. In the arrangement finally chosen as being correct, the two atoms had thermal parameters roughly comparable, as viewed from ORTEP plots, to those of atoms N(91), B(3) and N(81). In the alternative arrangement N(92), refined as a carbon atom, and C(95), refined as a nitrogen, had thermal parameters which were noticeably smaller and larger, respectively than that of N(91).

The final model with 313 parameters varied refined to $R = 0.038$ and $R_w = 0.048$ where

$$R = \frac{\sum ||F_o| - |F_c||}{\sum |F_o|} \quad (2)$$

and

$$R_w = \left(\frac{\sum_w (|F_o| - |F_c|)^2}{\sum_w |F_o|^2} \right)^{1/2} \quad (3)$$

Refinement of the other enantiomer converged to a model with $R = 0.046$ and $R_w = 0.059$ indicating that the original choice of enantiomer is correct.

In the final difference Fourier synthesis the highest 20 peaks were in the vicinity of the isotropically refined carbon atoms ($0.46-0.35 \text{ e/\AA}^3$) and the ytterbium ion ($0.52-0.4 \text{ e/\AA}^3$). A listing of the observed and calculated structure amplitudes is given in Appendix 2.

Results and Discussion

The final positional and thermal parameters for the atoms with estimated standard deviations are listed in Table 9. The calculated positions of the hydrogen atoms are shown in Table 10.

The crystal structure consists of discrete molecular units. A molecular packing diagram is shown in Figure 5. A stereo view of the molecule is shown in Figure 6. The atom numbering scheme is described in Figure 7. The first digit of the number assigned to a nitrogen or carbon atom denotes the pyrazolyl ring (1 to 9) of which it is a member. The second digit denotes the position of the atom in the ring using the standard nomenclature for heterocyclic groups (N(X1) is attached to the boron atom). The carbon atoms have been omitted from Figure 7 for reasons of clarity. The hydrogen atoms are assigned the same number as the atom to which they are bonded. Thus, H(1) is attached to B(1) and H(44) to C(44).

The ytterbium is eight coordinate. Two ligands coordinate in a tridentate fashion while the third acts as a bidentate ligand. The molecular point group is close to C_8 . A noncrystallographic mirror plane bisecting the molecule contains three pyrazolyl rings (N(31)...C(35), N(61)...C(65), and N(91)...C(95)), the ytterbium atom and the three boron atoms. Figure 6 is a view along this

Table 9. Positional and Thermal Parameters for Non Hydrogen Atoms of Yb(HBPz₃)₃.

Atom	x ^a	y	z	U ^b ₁₁	U ₂₂	U ₃₃	U ₁₂	U ₁₃	U ₂₃
Yb	0.00604(3)	0.6860(2)	0.24151(3)	4.10(3)	3.68(2)	3.67(2)	-0.00(2)	-0.10(2)	0.36(2)
N(12)	-0.1062(6)	0.7673(4)	0.3092(8)	3.9(4)	6.1(6)	4.3(5)	-0.4(4)	0.2(4)	0.5(4)
N(11)	-0.0853(5)	0.8291(4)	0.3073(7)	4.2(4)	4.3(5)	4.2(4)	0.1(3)	0.4(3)	-0.9(3)
N(22)	0.1236(6)	0.7688(4)	0.2801(7)	4.8(4)	4.5(5)	3.8(5)	0.2(3)	0.2(4)	0.4(4)
N(21)	0.0988(5)	0.8305(4)	0.2852(7)	3.8(4)	6.0(6)	4.9(5)	-0.9(4)	0.5(3)	-0.5(4)
N(32)	-0.0092(7)	0.7753(3)	0.0839(5)	7.0(5)	3.7(3)	3.4(3)	0.3(5)	0.2(5)	0.1(3)
N(31)	-0.0103(7)	0.8365(3)	0.1108(5)	6.3(5)	3.6(3)	3.8(3)	-0.4(4)	0.8(4)	0.3(3)
N(42)	-0.0986(6)	0.6072(4)	0.3307(8)	5.3(5)	5.3(6)	5.8(6)	-1.7(4)	-0.6(4)	0.5(5)
N(41)	-0.0697(7)	0.5707(4)	0.4223(9)	5.6(6)	4.9(6)	7.2(6)	-0.9(4)	0.3(5)	1.5(5)
N(52)	0.1254(6)	0.6086(4)	0.3051(8)	5.0(5)	5.4(6)	5.6(5)	1.2(4)	0.0(4)	1.4(4)
N(51)	0.1121(6)	0.5739(4)	0.4044(8)	5.2(5)	5.1(5)	6.9(6)	0.7(4)	-0.6(5)	2.4(5)
N(62)	0.0260(6)	0.6982(3)	0.4615(6)	6.0(5)	5.3(4)	4.1(4)	0.1(4)	-0.3(3)	1.1(3)
N(61)	0.0251(7)	0.6478(4)	0.5348(6)	6.4(6)	6.0(5)	4.4(4)	0.8(5)	-0.3(4)	1.7(4)
N(72)	-0.1148(6)	0.6595(4)	0.1003(7)	5.3(5)	3.6(4)	4.0(4)	0.0(4)	-0.6(4)	0.3(3)
N(71)	-0.1002(6)	0.6134(4)	0.0177(8)	5.1(5)	3.7(5)	5.3(5)	-0.1(4)	-1.1(4)	0.9(4)
N(82)	0.1024(5)	0.6618(4)	0.0717(7)	4.6(4)	4.2(5)	4.0(4)	0.2(3)	0.8(3)	-0.6(3)
N(81)	0.0817(6)	0.6137(4)	0.0013(8)	5.5(5)	4.2(5)	4.8(5)	0.3(4)	0.3(4)	-0.7(4)
N(91)	-0.0132(7)	0.5177(3)	-0.0605(6)	7.5(6)	3.6(3)	4.1(3)	0.8(4)	-0.8(5)	0.2(3)
N(92)	-0.0201(7)	0.5254(3)	-0.1779(6)	10.5(7)	5.0(4)	3.6(4)	0.5(5)	-0.2(5)	0.1(3)
B(1)	0.0017(8)	0.8558(4)	0.2388(7)	5.3(5)	3.7(4)	4.6(5)	0.5(5)	-0.5(8)	-0.8(4)
B(2)	0.0249(11)	0.5821(6)	0.4831(11)	7.1(10)	5.3(7)	6.5(7)	1.3(7)	0.4(7)	2.4(6)
B(3)	-0.0065(13)	0.5723(4)	0.0248(8)	8.6(10)	4.1(5)	4.2(5)	-1.2(8)	1.0(8)	0.2(4)
C(99)	-0.0161(9)	0.4569(4)	-0.0328(8)	7.7(7)	3.3(4)	5.7(5)	-0.1(5)	-0.8(6)	0.6(4)

continued...

Table 9 (continued)

Atom	x	y	z	B(A ²)	Atom	x	y	z	B(A ²)
C(13)	-0.1884(7)	0.7620(5)	0.3714(9)	4.2(2)	C(94)	0.2515(8)	0.5440(6)	0.3224(12)	6.3(3)
C(14)	-0.2192(8)	0.8191(5)	0.4135(9)	5.0(2)	C(95)	0.1877(10)	0.5343(6)	0.4135(12)	6.2(3)
C(15)	-0.1531(8)	0.8590(5)	0.3704(9)	4.2(2)	C(83)	0.0268(8)	0.7479(4)	0.5287(8)	4.3(2)
C(23)	0.2137(8)	0.7661(5)	0.3200(10)	4.8(2)	C(64)	0.0286(9)	0.7299(5)	0.6463(10)	5.7(2)
C(24)	0.2481(8)	0.8252(5)	0.3530(9)	5.0(2)	C(65)	0.0259(8)	0.6670(5)	0.6459(9)	5.3(2)
C(25)	0.1743(8)	0.8644(5)	0.3289(9)	4.4(2)	C(73)	-0.2018(7)	0.6820(5)	0.0761(8)	4.2(2)
C(33)	-0.0242(7)	0.7717(4)	-0.0324(8)	4.3(2)	C(174)	-0.2446(8)	0.6545(5)	-0.0188(10)	5.5(2)
C(34)	-0.0341(8)	0.8317(5)	-0.0769(9)	5.2(2)	C(75)	-0.1768(8)	0.6118(5)	-0.0539(10)	5.2(2)
C(35)	-0.0250(8)	0.8706(4)	0.0147(8)	4.5(2)	C(83)	0.1830(7)	0.6883(5)	0.0322(8)	4.2(2)
C(43)	-0.1900(9)	0.5873(6)	0.3038(11)	5.6(3)	C(84)	0.2159(8)	0.6564(5)	-0.0687(9)	4.4(2)
C(44)	-0.2182(10)	0.5414(6)	0.3796(12)	6.6(3)	C(85)	0.1494(8)	0.6108(5)	-0.0863(9)	4.4(2)
C(45)	-0.1418(8)	0.5315(6)	0.4511(11)	5.8(3)	C(93)	-0.0246(7)	0.4688(5)	-0.2218(8)	4.8(2)
C(53)	0.2104(8)	0.5907(5)	0.2559(10)	5.2(2)	C(94)	-0.0243(8)	0.4246(5)	-0.1353(9)	5.0(2)

^aEstimated standard deviations in the least significant figure(s) are given in parentheses in this and all subsequent tables.

^bThe form of the thermal ellipsoid is:

$$\exp[-2\pi^2(a^2U_{11}h^2+b^2U_{22}k^2+c^2U_{33}l^2+2a^*b^*U_{12}hk+2a^*c^*U_{13}hl+2b^*c^*U_{23}kl)].$$

The quantities given in the table are the thermal coefficients $\times 10^2$.

Table 10. Idealised Positional and Thermal Parameters for the Hydrogen Atoms of



Atom	x	y	z	B(A ²)	Atom	x	y	z	B(A ²)
H(33)	-0.0278	0.7330	-0.0770	5.18	H(63)	0.0278	0.7903	0.5003	5.41
H(34)	-0.0446	0.8428	-0.1587	6.04	H(64)	0.0286	0.7566	0.7141	6.57
H(35)	-0.0276	0.9160	0.0125	5.43	H(65)	0.0281	0.6402	0.7132	6.17
H(13)	-0.2204	0.7229	0.3867	5.30	H(73)	-0.2324	0.7147	0.1208	5.29
H(14)	-0.2772	0.8284	0.4602	5.80	H(74)	-0.3065	0.6633	-0.0565	6.40
H(15)	-0.1522	0.9034	0.3835	5.21	H(75)	-0.1839	0.5840	-0.1196	6.17
H(23)	0.2517	0.7277	0.3254	5.79	H(83)	0.2153	0.7231	0.0689	5.20
H(24)	0.3122	0.8361	0.3815	6.11	H(84)	0.2715	0.6556	-0.1150	5.48
H(25)	0.1735	0.9088	0.3414	5.35	H(85)	0.1482	0.5819	-0.1509	5.34
H(43)	-0.2263	0.6019	0.2371	6.66	H(94)	-0.0262	0.3801	-0.1439	6.17
H(44)	-0.2809	0.5221	0.3873	8.19	H(93)	-0.0299	0.4592	-0.3038	5.68
H(45)	-0.1382	0.5012	0.5162	6.84	H(1)	0.0015	0.9005	0.2441	4.60
H(53)	0.2369	0.6086	0.1845	6.29	H(2)	0.0333	0.5532	0.5477	5.58
H(54)	0.3139	0.5214	0.3099	7.36	H(3)	-0.0007	0.5560	0.1036	5.17
H(55)	0.1950	0.5032	0.4771	7.50	H(95)	-0.0131	0.4392	0.0447	5.34

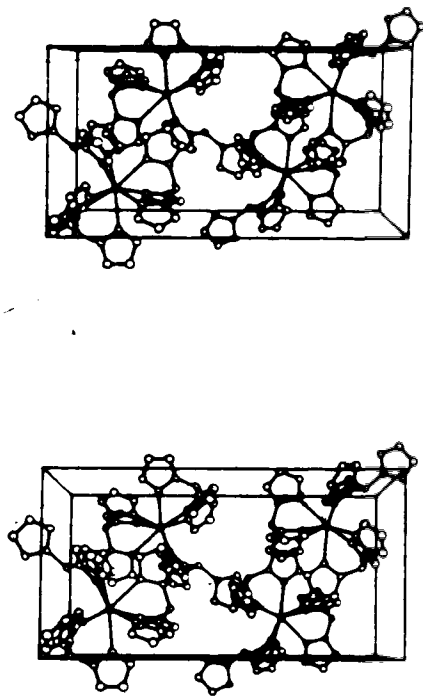


FIGURE 5. Cell Packing Diagram, $\text{Yb}(\text{HBPz}_3)_3$. The crystallographic a axis comes out of the page, the b axis runs from top to bottom and the c axis runs horizontal to the right.

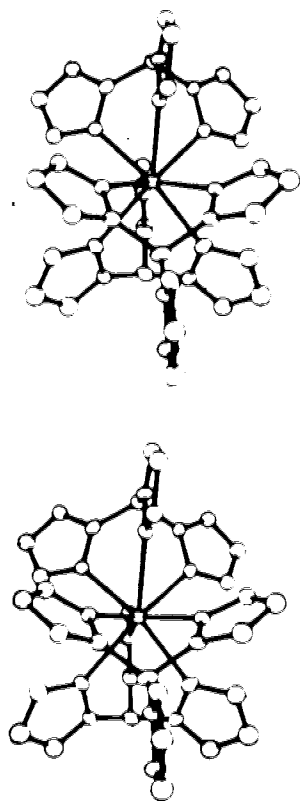


FIGURE 6. Stereoview of the Yb(HBPz)₃ Molecule.

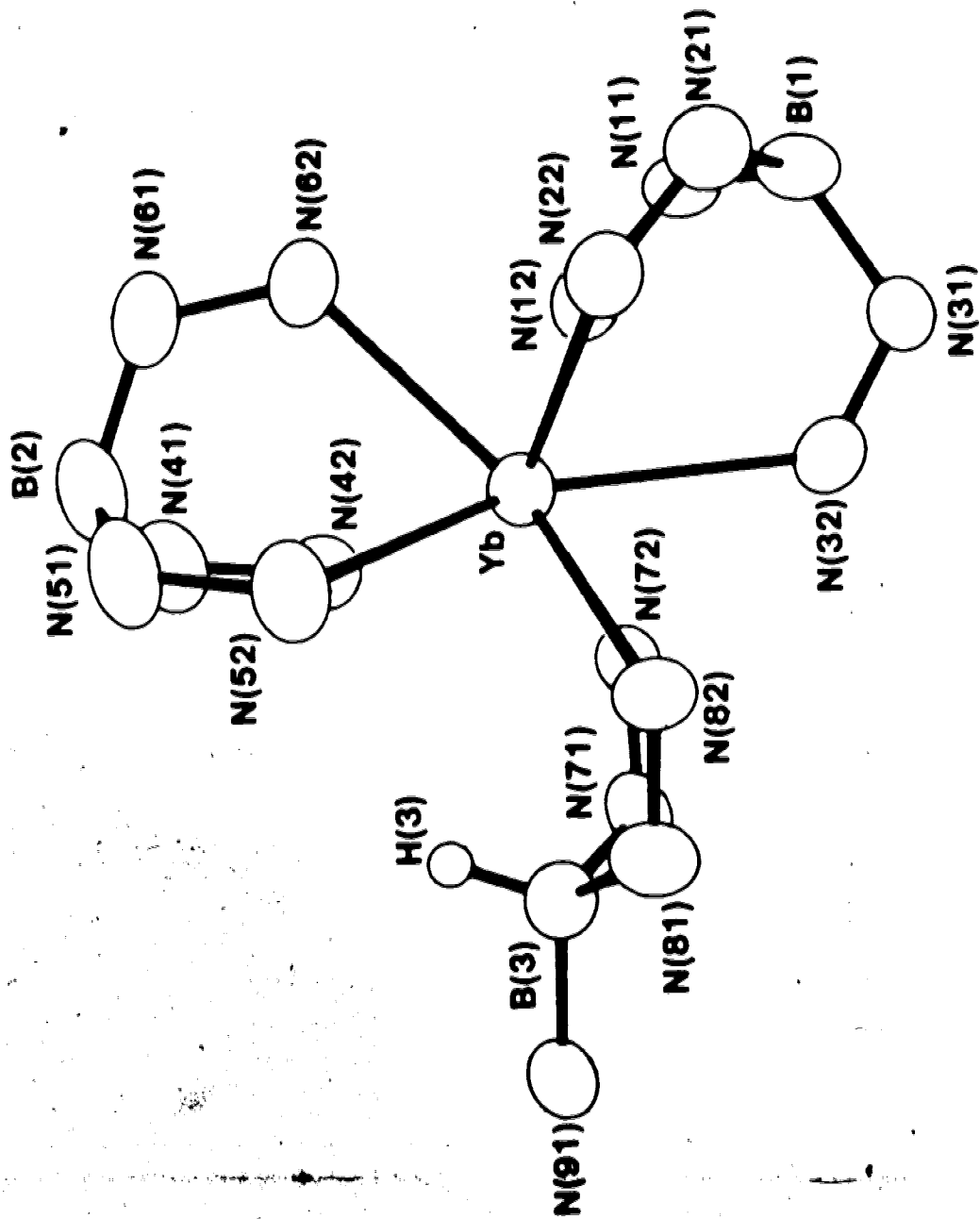


FIGURE 7. Yb(HBPz)₃ Atom Numbering Scheme.

plane while Figure 8 shows a view perpendicular to it.

The values of the shape parameter, δ and ϕ , for the $\text{Yb}(\text{HBPz}_3)_3$ complex are listed in Table 11 along with the values for the idealised polyhedra. Figure 9 shows the numbering scheme⁴¹ for the shape determining edges. 1(57)3 represents the edge between atoms 5 and 7 formed by the faces 157 and 573. The value of ϕ and the observation that only one of the δ angles is close to zero indicate that the coordination polyhedron formed by the eight nitrogen atoms is best described as a bicapped trigonal prism. A view of the coordination polyhedron emphasizing this origin is shown in Figure 10. The ligands are disposed such that each tridentate ligand bridges the height of the prism and caps a rectangular face of the prism. The bidentate ligand spans the remaining prism height. It is noteworthy that the configuration at B(3), the boron atom of the bidentate ligand, is such that H(3) is directed towards the ytterbium ion (for an assumed B-H bond length of 1.20 Å the hydrogen is 3.23 Å away from the metal atom). The uncoordinated pyrazolyl group is pointed away from the metal and thus has no opportunity to coordinate to the uncapped rectangular prism face to form a nine coordinate tricapped trigonal prismatic complex.

Table 12 gives the normalised edge lengths for the coordination polyhedron together with the idealised edge

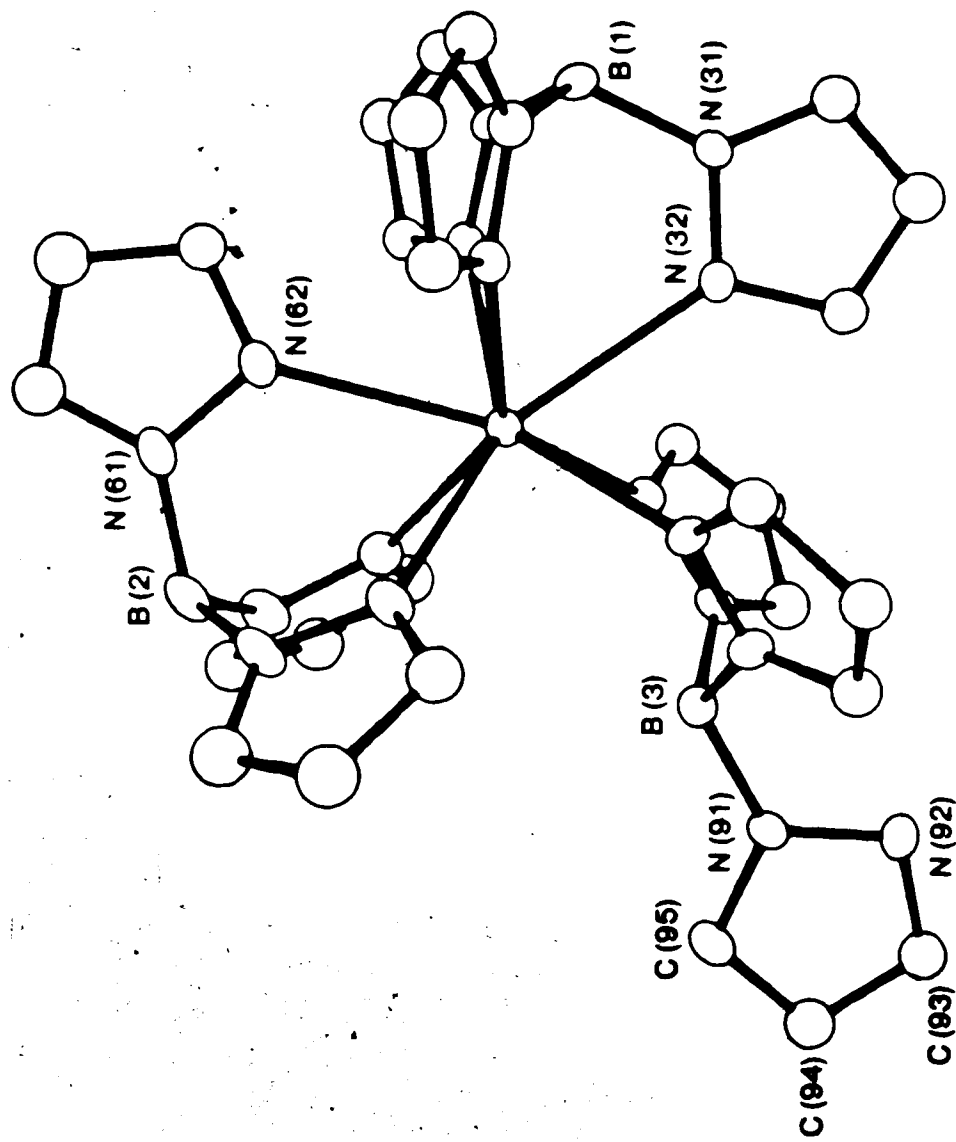


FIGURE 8. View of $\text{Yb}(\text{HBPz})_3$ Molecule Perpendicular to the Non-Crystallographic Mirror Plane.

TABLE 11. Polyhedral Shape Parameters for $\text{Yb}(\text{HBPz}_3)_3$ ^a

dihedral angle	$\text{Yb}(\text{HBPz}_3)_3$	DOD	BCTP	SAP
1(57)3	34.2	29.5	21.8	0.0
2(68)4	0.1	29.5	0.0	0.0
1(67)4	42.4	29.5	48.2	52.4
2(58)3	40.4	29.5	48.2	52.4
ϕ average	12.4	0.0	14.1	24.5

^aNumbering scheme for reference 41.

^bParameters for idealised polyhedra taken from reference 50.

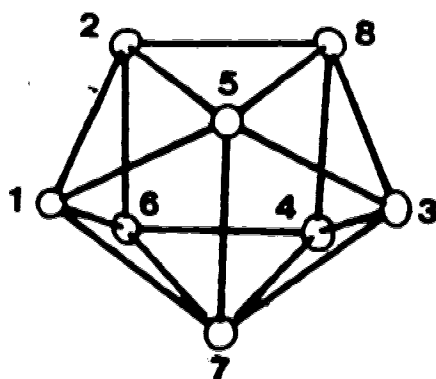


FIGURE 9. Numbering Scheme for BCTP Polyhedral Edges.

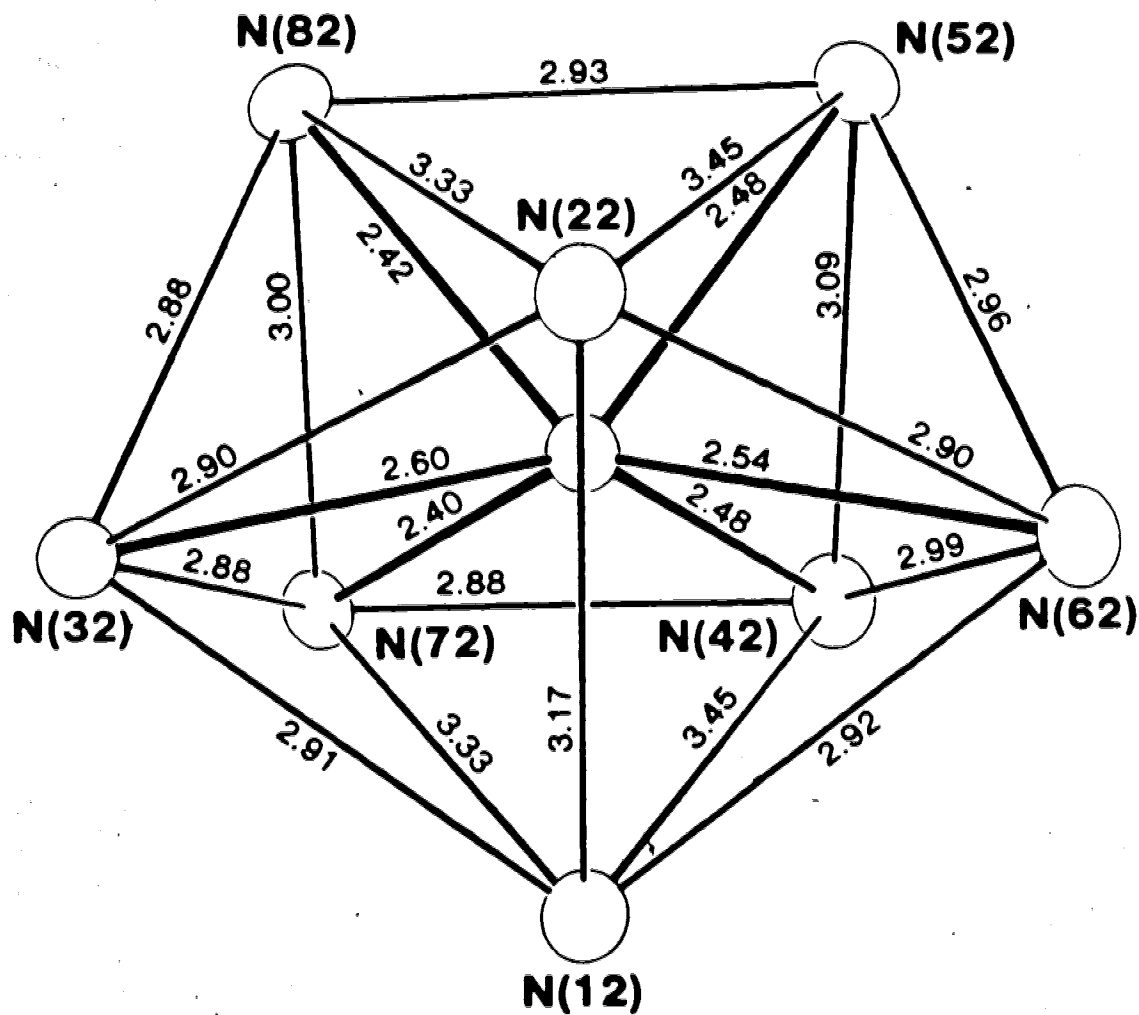


FIGURE 10. Coordination Polyhedron of $\text{Yb}(\text{HBPz}_3)_3$.

TABLE 12. Normalised Edge Lengths of Polyhedra With
Bicapped Trigonal Prismatic Geometry.

EDGE		HSM ^a	BCTP	MFP ^b	Yb(HBPz ₃) ^c
N(72)-N(82), N(42)-N(52)	h_1	1.491		1.25	1.22, 1.25
N(12)-N(22)	h_2	1.491		1.50	1.28
N(12)-N(72), N(22)-N(82)	t_2	1.155		1.36	1.35, 1.35
N(12)-N(42), N(22)-N(52)	t_2	1.155		1.36	1.40, 1.40
N(42)-N(72), N(52)-N(82)	t_1	1.155		1.13	1.17, 1.19
N(22)-N(32), N(12)-N(32)	p_2	1.155		1.18	1.17, 1.18
N(12)-N(62), N(22)-N(62)	p_2	1.155		1.18	1.18, 1.17
N(42)-N(62), N(52)-N(62)	p_1	1.155		1.21	1.21, 1.20
N(72)-N(32), N(82)-N(32)	p_1	1.155		1.21	1.17, 1.17

^aHard sphere model, reference 50.

^bMost favoured polyhedron, reference 41.

^cCalculated with average Yb-N bond length 2.47 Å

lengths of the reference polyhedron, reported by Muetterties⁵⁰ and Drew.⁴¹ In the latter study the prism is no longer constrained to rigorous trigonal symmetry. The agreement between the observed and the ESM dimensions is not good. The height of the prism, as represented typically by N(42)-N(52) (h_1), 3.09 Å although greater than N(42)-N(72) (t_1), 2.89 Å, is much shorter than N(12)-N(42) (t_2), 3.45 Å and N(12)-N(72) (t_2), 3.33 Å the remaining edges at the triangular faces of the prism. Drew has noted that, if the BCTP is produced from the D_{3h} tricapped trigonal prism by removal of a capping ligand from a rectangular prism face, contraction of that uncapped face and an opening out of the remaining four ligand atoms of the polyhedron would be expected. This effect is observed in this structure in the relative lengthening of the unique height of the prism, h_2 (the edge common to the two capped faces of the prism, N(12)-N(22) such that $h_2 > h_1$, and a relative shortening of the edges t_1 (formed by the triangular faces of the prism and the uncapped rectangular face, N(52)-N(82) and N(42)-N(72)), resulting in $t_2 > t_1$.

The dramatic difference in edge lengths at the triangular face of the prism, $t_2 > t_1$, also provides an explanation for the unexpectedly large value, 34.2°, for the δ angle at the N(12)-N(22) (1(57)3) edge. The value calculated by Muetterties for the idealised shape is 21.8°

where the prism was constrained to be trigonally symmetric. However, lengthening of t_2 relative to t_1 acts to increase this angle to its observed value. The idealised polyhedron shape despite these adjustments would still possess C_{2v} symmetry and this is the approximate symmetry of the coordination polyhedron of $Yb(HBPz_3)_3$.

The ytterbium-nitrogen bond lengths, the polyhedral edge lengths and the interbond angles at the ytterbium atom are shown in Table 13. The bond lengths range from 2.401(8) Å to 2.601(6) Å and are in agreement with those found in $Na_3Yb(dpa)_3$.⁶⁵ The coordination of the pyrazolyl groups within each tridentate ligand is not symmetrical. The capping pyrazolyl groups have a longer ytterbium-nitrogen bond length than those spanning the height of the prism. Additionally the ligand coordinating through N(12), N(22) and N(32) has a greater range of ytterbium-nitrogen bond lengths than the ligand with coordinating nitrogens N(42), N(52) and N(62). The differences between the longest and the shortest bond distances are 0.20 Å and 0.06 Å, respectively. Such variation is also observed in the bite distances. The difference between longest and shortest bite distances between N(12), N(22) and N(32) is 0.27 Å whereas for N(42), N(52) and N(62) it is only 0.11 Å. These distinct differences between the two tridentate ligands are almost

Table 13. Bond Distances, Edge Lengths and Angles for the
Coordination Polyhedron of $\text{Yb}(\text{HBPz}_3)_3$.

i) Bond distances (Å)			
Yb-N(12)	2.414(9)	Yb-N(42)	2.482(8)
Yb-N(22)	2.401(8)	Yb-N(52)	2.484(8)
Yb-N(72)	2.401(8)	Yb-N(32)	2.601(6)
Yb-N(82)	2.423(7)	Yb-N(62)	2.544(7)
ii) Edge Lengths (Å)			
N(12)-N(42)	3.446(12)	N(22)-N(52)	3.452(11)
N(12)-N(72)	3.331(12)	N(22)-N(82)	3.327(11)
N(42)-N(72)	2.879(12)	N(52)-N(82)	2.926(12)
N(12)-N(22)	3.173(11)	N(42)-N(52)	3.089(12)
		N(72)-N(82)	3.001(10)
N(32)-N(12)	2.910(11)	N(62)-N(12)	2.922(11)
N(32)-N(22)	2.898(11)	N(62)-N(22)	2.901(11)
N(32)-N(72)	2.884(11)	N(62)-N(42)	2.997(12)
N(32)-N(82)	2.881(11)	N(62)-N(52)	2.963(12)
iii) Angles at the Yb atom (degree)			
N(12)-Yb-N(42)	89.5(3)	N(22)-Yb-N(52)	89.9(3)
N(12)-Yb-N(72)	87.5(3)	N(22)-Yb-N(82)	87.2(3)
N(42)-Yb-N(72)	72.2(3)	N(52)-Yb-N(82)	73.2(3)
N(12)-Yb-N(22)	82.4(2)	N(42)-Yb-N(52)	76.9(3)
N(32)-Yb-N(62)	129.7(2)	N(72)-Yb-N(82)	76.0(2)
N(32)-Yb-N(12)	70.8(3)	N(62)-Yb-N(12)	72.2(3)
N(32)-Yb-N(22)	70.7(3)	N(62)-Yb-N(22)	71.8(3)
N(32)-Yb-N(72)	70.3(3)	N(62)-Yb-N(42)	71.2(3)
N(32)-Yb-N(82)	69.9(3)	N(62)-Yb-N(52)	72.2(3)

certainly due in part to the fact that the unique height of the prism bridged by N(12) and N(22) is longer than the other two heights. The bite distance of the bidentate ligand, N(82)-N(72) = 3.00(1) Å, lies in the range of bite distances exhibited by the tridentate ligands.

Although the significant variation in these distances detracts somewhat from the meaning of an average value, on the whole it appears that the bite distances are somewhat larger than those found in transition metal pyrazol-1-yl borate complexes (average values: Yb(HBPz₃)₃ 3.00 Å, Co(HBPz₃)₃⁶⁶ 2.89(11) Å).

The bond lengths and bond angles in the hydrotris-(pyrazol-1-yl)borate ligands are listed in Table 14 and are consistent with those found in structural studies of other complexes containing the poly(pyrazol-1-yl) borate ligands.^{29,66,67,68}

Each of the nine five-membered pyrazolyl rings are planar, the deviation of any atom from the calculated mean plane is less than 0.015 Å. The equations of these and some other important least-squares planes in the complex are given in Table 15.

The angle between the planes B(3), N(71), N(81) and N(71), N(81), N(72), N(82) in the bidentate ligand is 126.3°. Corresponding dihedral angles in the other two ligands, between B(1), N(11), N(21) and N(11), N(21), N(12), N(22), and B(2), N(41), N(51) and N(41), N(51), N(42), N(52)

Table 14. Interatomic Distances and Angles in Polypyrazol-1-yl Borate Ligand

1) Distances (Å)					
Yb-B(1)	3.589(8)	Yb-B(2)	3.600(11)	Yb-B(3)	3.526(11)
B(1)-N(11)	1.540(12)	B(2)-N(41)	1.495(16)	B(3)-N(71)	1.562(16)
N(1)-N(21)	1.547(12)	B(2)-N(51)	1.509(15)	B(3)-N(81)	1.532(15)
B(1)-N(31)	1.534(10)	B(2)-N(61)	1.530(15)	B(3)-N(91)	1.529(11)
N(11)-N(12)	1.358(11)	N(41)-N(42)	1.369(12)	N(71)-N(72)	1.384(11)
N(21)-N(22)	1.365(11)	N(51)-N(52)	1.372(12)	N(81)-N(82)	1.358(10)
N(31)-N(32)	1.349(8)	N(61)-N(62)	1.370(9)	N(91)-N(92)	1.359(9)
N(12)-C(13)	1.340(12)	N(42)-C(43)	1.362(14)	N(72)-C(79)	1.318(12)
N(22)-C(23)	1.319(13)	N(52)-C(53)	1.352(13)	N(82)-C(83)	1.324(11)
N(32)-C(33)	1.352(11)	N(62)-C(63)	1.315(11)	N(92)-C(93)	1.310(11)
C(13)-C(14)	1.383(14)	C(43)-C(44)	1.370(17)	C(73)-C(74)	1.370(14)
C(23)-C(24)	1.406(14)	C(53)-C(54)	1.380(16)	C(83)-C(84)	1.418(13)
C(33)-C(34)	1.391(13)	C(63)-C(64)	1.403(14)	C(93)-C(94)	1.372(13)
C(14)-C(15)	1.342(14)	C(44)-C(45)	1.348(17)	C(74)-C(75)	1.366(15)
C(24)-C(25)	1.345(14)	C(54)-C(55)	1.377(17)	C(84)-C(85)	1.353(13)
C(34)-C(35)	1.349(13)	C(64)-C(65)	1.350(14)	C(94)-C(95)	1.368(13)
C(15)-N(11)	1.342(12)	C(45)-N(41)	1.341(14)	C(75)-N(71)	1.335(13)
C(25)-N(21)	1.351(12)	C(55)-N(51)	1.347(15)	C(85)-N(81)	1.348(12)
C(35)-N(31)	1.339(11)	C(65)-N(61)	1.338(12)	C(95)-N(81)	1.343(10)

continued...

Table 14 (continued...)

ii) Angles in ligand chelate (degrees)			
N(11)-B(1)-N(21)	111.7(7)	N(41)-B(2)-N(51)	133.0(10)
N(11)-B(1)-N(31)	107.7(7)	N(41)-B(2)-N(61)	109.4(10)
N(21)-B(1)-N(31)	109.1(7)	N(51)-B(2)-N(61)	109.8(11)
B(1)-N(11)-N(12)	122.4(7)	B(2)-N(41)-N(42)	121.0(8)
B(1)-N(21)-N(22)	122.3(7)	B(2)-N(51)-N(52)	122.6(8)
B(1)-N(31)-N(32)	118.7(6)	B(2)-N(61)-N(62)	119.4(7)
N(11)-N(12)-Yb	122.9(6)	N(41)-N(42)-Yb	123.5(6)
N(21)-N(22)-Yb	122.8(6)	N(51)-N(52)-Yb	122.0(6)
N(31)-N(32)-Yb	122.6(4)	N(61)-N(62)-Yb	122.9(5)
iii) Angles within the pyrazolyl rings (degrees)			
C(15)-N(11)-N(12)	108.2(8)	C(45)-N(41)-N(42)	109.5(10)
C(25)-N(21)-N(22)	110.9(8)	C(55)-N(51)-N(52)	107.7(10)
C(35)-N(31)-N(32)	110.3(7)	C(65)-N(61)-N(62)	109.9(8)
N(11)-N(12)-C(13)	105.6(9)	N(41)-N(42)-C(43)	105.1(9)
N(21)-N(22)-C(14)	104.6(8)	N(51)-N(52)-C(53)	107.9(9)
N(31)-N(32)-C(15)	106.2(7)	N(61)-N(62)-C(63)	106.3(7)
N(12)-C(13)-C(14)	111.6(9)	N(42)-C(43)-C(44)	110.0(11)
N(22)-C(23)-C(24)	111.5(10)	N(52)-C(53)-C(54)	109.1(10)
N(32)-C(33)-C(34)	108.9(9)	N(62)-C(63)-C(64)	109.9(9)
N(71)-B(3)-N(81)	108.2(7)	N(71)-N(72)-C(73)	104.5(8)
N(71)-B(3)-N(91)	110.5(11)	N(81)-N(82)-C(83)	106.9(8)
N(81)-B(3)-N(91)	111.6(9)	N(91)-N(92)-C(93)	105.6(7)
B(3)-N(71)-N(72)	119.2(7)	N(72)-C(73)-C(74)	113.4(10)
B(3)-N(81)-N(82)	119.1(8)	N(82)-C(83)-C(84)	109.6(9)
B(3)-N(91)-N(92)	122.9(7)	N(92)-C(93)-C(94)	111.2(9)
N(71)-N(72)-Yb	123.1(6)		
N(81)-N(82)-Yb	124.1(6)		

(continued...)

Table 14 (continued...)

C(13)-C(14)-C(15)	103.4(9)	C(43)-C(44)-C(45)	106.2(12)	C(73)-C(74)-C(75)	103.3(10)
C(23)-C(24)-C(25)	104.9(9)	C(53)-C(54)-C(55)	105.6(12)	C(83)-C(84)-C(85)	104.9(9)
C(33)-C(34)-C(35)	106.2(9)	C(63)-C(64)-C(65)	105.7(10)	C(93)-C(94)-C(95)	105.7(9)
C(14)-C(15)-N(11)	111.2(9)	C(44)-C(45)-N(41)	109.0(11)	C(74)-C(75)-N(71)	109.8(10)
C(24)-C(25)-N(21)	108.0(9)	C(54)-C(55)-N(51)	109.6(12)	C(84)-C(85)-N(81)	108.9(9)
C(34)-C(35)-N(31)	108.3(8)	C(64)-C(65)-N(61)	108.2(9)	C(94)-C(95)-N(91)	107.0(8)

Table 15. Planes and Calculated Least-Squares Planes
Within the Yb(HBPz₃) Molecule.^{a,b}

Atom	Dev, Å	Atom	Dev, Å
Plane 1: Yb, B(1), B(2), B(3)			
Equation: (0.9965)X+(0.0150)Y+(-0.0825)Z-(0.0760)=0			
Yb	0.0000(4)		
B(1)	-0.003(11)		
B(2)	-0.005(15)		
B(3)	-0.004(2)		
Plane 2: N(71), N(81), N(41), N(51)			
Equation: (-0.0281)X+(-0.9206)Y+(-0.3894)Z-(-13.4365)=0			
N(71)	0.0005(77)		
N(81)	-0.0005(77)		
N(41)	-0.0007(92)		
N(51)	0.0007(92)		
Plane 3: N(81), N(21), N(51)			
Equation: (0.9930)X+(-0.0028)Y+(-0.1183)Z-(1.2589)=0			
Plane 4: N(71), N(11), N(41)			
Equation: (0.9970)X+(0.0253)Y+(-0.0736)Z-(-1.2986)=0			
Plane 5: N(31), N(32), C(33), C(34), C(35)			
Equation: (0.9872)X+(0.0454)Y+(-0.1528)Z-(0.4820)=0			
N(31)	0.002(10)	Yb	-0.1526(4)
N(32)	-0.002(9)	B(1)	-0.04(1)
C(33)	-0.002(10)	B(2)	-0.42(2)
C(34)	0.000(11)	B(3)	-0.06(2)
C(35)	0.002(10)		
Plane 6: N(11), N(12), C(13), C(14), C(15)			
Equation: (-0.5530)X+(0.1178)Y+(-0.8248)Z-(-0.1657)=0			
N(11)	-0.01(1)	Yb	-0.4219(4)
N(12)	0.005(8)	B(1)	0.059(9)
C(13)	0.012(10)		
C(14)	-0.008(10)		
C(15)	-0.002(10)		

(continued...)

Table 15 (continued)

Atom	Dev, Å	Atom	Dev, Å
Plane 7: N(21), N(22), C(23), C(24), C(25)			
Equation: (0.3570)X+(0.1328)Y+(-0.9246)Z-(-0.1683)=0			
N(21)	-0.004(8)	Yb	-0.3991(3)
N(22)	0.002(8)	B(1)	0.084(9)
C(23)	0.007(11)		
C(24)	-0.005(11)		
C(25)	0.001(10)		
Plane 8: N(41), N(42), C(43), C(44), C(45)			
Equation: (0.3696)X+(-0.6786)Y+(-0.6348)Z-(-11.7430)=0			
N(41)	-0.007(9)	Yb	-0.0130(4)
N(42)	0.005(9)	B(2)	-0.12(1)
C(43)	0.015(12)		
C(44)	-0.011(14)		
C(45)	0.001(13)		
Plane 9: N(51), N(52), C(53), C(54), C(55)			
Equation: (-0.4919)X+(-0.6854)Y+(-0.5369)Z-(-11.6821)=0			
N(51)	0.005(9)	Yb	0.0248(4)
N(52)	-0.006(9)	B(2)	-0.023(13)
C(53)	-0.003(11)		
C(54)	-0.003(13)		
C(55)	0.010(13)		
Plane 10: N(61), N(62), C(63), C(64), C(65)			
Equation: (0.9999)X+(-0.0147)Y+(-0.0084)Z-(0.0891)=0			
N(61)	0.003(8)	Yb	-0.2466(4)
N(62)	-0.000(9)	B(1)	-0.36(1)
C(63)	-0.009(10)	B(2)	0.02(2)
C(64)	0.012(12)	B(3)	-0.36(2)
C(65)	-0.006(11)		
Plane 11: N(71), N(72), C(73), C(74), C(75)			
Equation: (0.4244)X+(0.6775)Y+(-0.6007)Z-(8.2251)=0			
N(71)	0.007(8)	Yb	0.1619(4)
N(72)	-0.010(8)	B(3)	-0.11(1)
C(73)	-0.006(10)		
C(74)	-0.003(12)		
C(75)	0.013(11)		

(continued...)

Table 15 (continued)

Atom	Dev, Å	Atom	Dev, Å
Plane 12: N(81), N(82), C(83), C(84), C(85)			
Equation: $(-0.5460)X + (0.6146)Y + (-0.5693)Z - (7.4945) = 0$			
N(81)	0.000(8)	Yb	-0.0320(4)
N(82)	-0.003(9)	B(3)	-0.06(1)
C(83)	0.003(10)		
C(84)	-0.006(10)		
C(85)	0.006(10)		
Plane 13: N(91), N(92), C(93), C(94), C(95)			
Equation: $(0.9971)X + (-0.0411)Y + (-0.0644)Z - (-0.5987) = 0$			
N(91)	0.005(9)	Yb	-0.1047(4)
N(92)	-0.009(10)	B(1)	-0.31(1)
C(93)	-0.001(12)	B(2)	0.07(2)
C(94)	-0.008(12)	B(3)	-0.01(2)
C(95)	0.013(10)		
Plane 14: N(11), N(21), N(12), N(22)			
Equation: $(-0.1025)X + (0.0124)Y + (-0.9947)Z - (-3.1661) = 0$			
N(11)	0.004(8)		
N(21)	-0.004(8)		
N(12)	-0.004(9)		
N(22)	0.004(8)		
Plane 15: N(41), N(51), N(42), N(52)			
Equation: $(-0.0380)X + (-0.8213)Y + (-0.5693)Z - (-12.7972) = 0$			
N(41)	0.018(9)		
N(51)	-0.016(9)		
N(42)	-0.013(9)		
N(52)	0.013(9)		
Plane 16: N(71), N(81), N(72), N(82)			
Equation: $(-0.0834)X + (0.6613)Y + (-0.7455)Z - (8.6497) = 0$			
N(71)	0.020(9)		
N(81)	-0.021(9)		
N(72)	-0.014(8)		
N(82)	0.014(8)		

(continued...)

Table 15 (continued)

Atom	Dev, Å	Atom	Dev, Å
Plane 17: B(1), N(11), N(21)			
Equation: $(-0.0548)X + (-0.07649)Y + (-0.6419)Z - (-15.8080) = 0$			
Plane 18: B(2), N(41), N(51)			
Equation: $(-0.0472)X + (0.9667)Y + (-0.2517)Z - (10.6682) = 0$			
Plane 19: B(3), N(71), N(81)			
Equation: $(-0.0844)X + (-0.2123)Y + (-0.9735)Z - (-2.8770) = 0$			

Angles between planes (in degrees):

1-2	90.6	5-6	114.5
1-5	4.4	5-7	120.0
1-10	4.6	6-7	125.5
1-13	3.4	8-9	128.6
2-3	88.8	8-10	112.6
2-4	91.3	9-10	118.5
3-4	3.0	11-12	121.8
		14-17	129.4
		15-18	130.5
		16-19	126.3

^aPlanes defined as $C_1X + C_2Y + C_3Z + d = 0$ where $X = xa$, $Y = yb$, $Z = zc$, a , b , c are the orthorhombic unit cell dimensions and (x, y, z) the cell coordinates.

^bEstimated standard deviations in the least significant figures in parentheses.

are 129.4° and 130.5° , respectively. Thus, the boat conformation of the bidentate ligand is only very slightly "steeper" than would be expected from the geometries of the tridentate ligand. Similarly the dihedral angles between the pyrazolyl rings within each ligand range from 112.6° to 128.6° . The angle between the two coordinated pyrazolyl groups of the bidentate ligand is 121.8° .

Conclusion

The utility of the shape parameters, δ and ϕ , in succinctly describing polyhedral shapes is evidenced by the structure of $\text{Yb}(\text{HBPz}_3)_3$. The complex exhibits the less common form of eight coordination, the bicapped trigonal prism.

The observations of Drew concerning a compression of the uncapped rectangular prism face are also clearly seen. The normalised edge lengths of the $\text{Yb}(\text{HBPz}_3)_3$ polyhedron emphasise the fact that at least for the BCTP a description based on the polyhedral shape is immensely preferable to one based on idealized dimensions.

CHAPTER IV

NMR STUDIES OF $\text{Ln}(\text{HBPz}_3)_3$ COMPLEXES

$\text{Ln} = \text{Dy}, \text{Ho}, \text{Er}, \text{Tm}, \text{Yb}, \text{Lu}$

Introduction

With the exception of La^{3+} , with $4f^0$ and Lu^{3+} with $4f^{14}$ electronic configurations the tripositive lanthanide ions have unpaired $4f$ electrons. The resonances in the NMR spectra of the paramagnetic complexes are both shifted and line broadened relative to the resonances in the spectra of the corresponding diamagnetic complexes. The line broadening is caused by the more efficient relaxation mechanisms arising from the presence of the paramagnetic ion. Fortunately the very short electron spin-lattice relaxation times of the $4f$ electrons result in considerably less broadening of the resonances than is found in the NMR spectra of paramagnetic d -block transition metal complexes.

In 1969 Hinckley⁶⁹ introduced the lanthanide shift reagent $\text{Eu}(\text{dpm})_3(\text{py})_2$ and demonstrated its utility in the clarification of the proton NMR spectrum of chloesterol. The application of lanthanide shift reagents to a variety of chemical problems has been extensively reviewed.⁷⁰⁻⁷⁷

The isotropic shift, $(\Delta\nu/\nu_0)_{\text{iso}}$, caused by the paramagnetic lanthanide ion, is given by the equation:

$$\left(\frac{\Delta\nu}{\nu_0}\right)_{\text{iso}} = \left(\frac{\Delta\nu}{\nu_0}\right)_{\text{para}} - \left(\frac{\Delta\nu}{\nu_0}\right)_{\text{dia}} \quad (4)$$

where $(\Delta\nu/\nu_0)_{\text{para}}$ is the chemical shift in the paramagnetic complex and $(\Delta\nu/\nu_0)_{\text{dia}}$ is the chemical shift in the absence of paramagnetism. The latter is, of course, an unmeasurable quantity but it can be successfully approximated by the chemical shift of the resonance in the analogous La^{3+} or Lu^{3+} diamagnetic complexes.

The isotropic shift is a combination of shifts induced by two distinct mechanisms - a contact shift, $(\Delta\nu/\nu_0)_{\text{con}}$, and a dipolar (or pseudocontact) shift, $(\Delta\nu/\nu_0)_{\text{pc}}$.

$$\left(\frac{\Delta\nu}{\nu_0}\right)_{\text{iso}} = \left(\frac{\Delta\nu}{\nu_0}\right)_{\text{con}} + \left(\frac{\Delta\nu}{\nu_0}\right)_{\text{pc}}$$

The Fermi contact interaction⁷⁸ between electron spin and nuclear spin takes place only at the nucleus and thus requires the presence of spin density in an s orbital of the atom. The contact shift arises therefore by a "through bond" interaction.

An expression for the shift for a lanthanide ion has been developed by Lewis et al.:⁷⁹

$$\left(\frac{\Delta\nu}{\nu_0}\right)_{\text{con}} = \frac{2\pi\beta}{3kT} \cdot g_J(g_J-1)J(J+1) \cdot \frac{1}{\gamma_N} \cdot \frac{A}{h} \quad (5)$$

where J is the magnetic quantum number from the

Russell-Saunders spin-orbit angular momentum coupling, g_J is the Landé g factor, A/h is the electron nuclear hyperfine coupling constant in Hz and γ_N is the nuclear magnetogyric ratio. The contact shift is directly proportional to the term $g_J(g_J-1)J(J+1)$ and the term $A/h\gamma_N$. Values for the former, $\langle S_z \rangle$, have been calculated and tabulated by Golding and Halton.⁸⁰ A/h is dependent on the number and the nature of the bonds separating the nucleus and the lanthanide ion. The lack of covalency in the lanthanide-ligand bonding makes direct spin delocalisation from the lanthanide 4f electrons onto the ligand highly unlikely. However, spin density can be produced on the ligand atoms by the spin polarization mechanism described by Watson and Freeman,⁸¹ in which the 4f electrons polarize the outer filled 5s and 5p orbitals and this spin is then transferred, via an overlap or covalent mechanism, onto the ligand atoms. Values of A/h are thus smaller than those for paramagnetic transition metals. The hyperfine coupling constant is also dependent on the type of nucleus and theory predicts⁸² that the contact shifts for ^{13}C nuclei will be an order of magnitude greater than those for protons for an equivalent amount of spin density.

The dipolar interaction between a paramagnetic electron and the spin of the resonating nuclei is a

"through space" interaction and gives rise to the pseudocontact shift, $(\Delta\nu/\nu_0)_{pc}$. An expression for this shift was first given by McConnell and Robertson in terms of g value anisotropies.⁸³ Bleaney⁸⁴ has extended the description to lanthanide systems, (6).

$$\left(\frac{\Delta\nu}{\nu_0}\right)_{pc} = \frac{g_J^2 \beta^2 J(J+1)(2J-1)(2J+3)}{60(kT)^2} \left\{ D_z \left(\frac{3\cos^2\theta - 1}{r^3} \right) + (D_x - D_y) \left(\frac{\sin^2\theta \cos 2\Omega}{r^3} \right) \right\} \quad (6)$$

where

$$D_z = \langle r^2 \rangle A_2^0 \langle J || \alpha || J \rangle$$

$$D_x = \langle r^2 \rangle (A_2^2 - A_2^0) \langle J || \alpha || J \rangle$$

$$D_y = \langle r^2 \rangle (-A_2^2 - A_2^0) \langle J || \alpha || J \rangle$$

and r , θ and Ω are the polar coordinates of the NMR nucleus in the coordinate system defined by the magnetic axes of the complex, $\langle r^2 \rangle$ is the mean square of the electronic radius of the 4f electrons, A_2^0 and A_2^2 are energy coefficients related to the crystal field splitting of the 4f orbitals and $\langle J || \alpha || J \rangle$ is a numerical coefficient.

In a simplified form equation (6) can be written as:

$$\left(\frac{\Delta\nu}{\nu_0}\right)_{pc} = D_1 \frac{(3\cos^2\theta - 1)}{r^3} + D_2 \frac{(\sin^2\theta \cos 2\Omega)}{r^3} \quad (7)$$

where D_1 and D_2 are the molecular magnetic anisotropies which are expressed in terms of the principal magnetic susceptibilities X_x , X_y and X_z .

$$D_1 = \frac{1}{3N} (X_z - \frac{1}{2}(X_x + X_y))$$

$$D_2 = \frac{1}{2N} (X_x - X_y)$$

The magnetic susceptibilities are commonly expressed in Vvk mole^{-1} ($1\text{Vvk} = 10^{-6}$ c.g.s. units) while D_1 and D_2 , being properties of the complex are conveniently expressed in units of A^3 . For an isostructural series of lanthanide complexes $\langle r^2 \rangle$, A_2^0 and A_2^2 should remain effectively constant while from (6) it can be seen that the pseudocontact shifts will vary as the term

$g_J^2 J(J+1)(2J-1)(2J+3) \langle J || \alpha || J \rangle$. Table 16 lists the values of g_J , J , $\langle J || \alpha || J \rangle$, $g_J^2 J(J+1)(2J-1)(2J+3) \langle J || \alpha || J \rangle$ and $g_J(g_J-1)J(J+1)$ for the lanthanide ions.

The geometrical dependence of the pseudocontact shifts allows the use of this portion of the isotropic shifts to obtain solution structural information about the complex formed between a shift reagent and a substrate molecule. In the vast majority of this type of study the shift reagent substrate adduct is either observed or assumed to have axial symmetry (3-fold or greater). As a result $X_x = X_y$, $D_2 = 0$ and equation (7) reduces to (8).

Table 16. Paramagnetic Shift Parameters of Lanthanide Ions^a

Ion	J	g_J	$\langle J \alpha J \rangle$	$g_J^2 J(J+1)(2J-1) \langle J \alpha J \rangle$	$g_J(g_J-1)J(J+1)$
$4f^1$ Ce ³⁺	5/2	6/7	-0.0571 ^b	-11.8	-1.1
$4f^2$ Pr ³⁺	4	4/5	-0.0210	-20.7	-3.2
$4f^3$ Nd ³⁺	9/2	8/11	-0.00643	-8.08	-4.9
$4f^4$ Pm ³⁺	4	3/5	+0.00771	+4.28	-4.8
$4f^7$ Gd ³⁺	7/2	2	0		31.5
$4f^8$ Tb ³⁺	6	3/2	-0.0101	-157.5	31.5
$4f^9$ Dy ³⁺	15/2	4/3	-0.00635	-181	28.3
$4f^{10}$ Ho ³⁺	8	5/4	-0.00222	-71.2	22.5
$4f^{11}$ Er ³⁺	15/2	6/5	+0.00254	+58.8	15.3
$4f^{12}$ Tm ³⁺	6	7/6	+0.0101	+95.3	8.2
$4f^{13}$ Yb ³⁺	7/2	8/7	+0.0318	+39.2	2.6

^aData from reference 84.

$$\left(\frac{\Delta\nu}{\nu_0}\right)_{pc} = \frac{D_1(3\cos^2\theta-1)}{r^3} \quad (8)$$

Jesson has applied equation (8) to the NMR spectrum of $\text{Co}(\text{HBPz}_3)_2$, a truly axially symmetric molecule, and was able to obtain a separation of the pseudocontact and contact shifts.⁸⁵ The first application of (8) to a system involving a lanthanide shift reagent was reported by Briggs et al.^{86,87} They obtained a fit of observed to calculated shifts for the rigid substrate borneol. Since then the method has been extended to investigations of conformationally flexible substrates,⁷⁰⁻⁷⁶ particularly molecules of biological interest⁷⁷ including mononucleotides⁸⁸⁻⁹⁰ and small peptides.⁹¹

Several computer programs⁹²⁻⁹⁴ have been developed to produce a structural model of the lanthanide-substrate complex which is consistent with the observed pseudocontact shifts.

However, Sullivan⁹⁵ has noted that "it has been assumed that the correspondence between the observed lanthanide induced shift and those calculated based on a conformational model is a valid criterion for equating the actual conformation of the molecule in solution with the conformational model."

There are several assumptions frequently made when lanthanide ions are used as structural probes. These

have been listed by Horrocks.⁷⁴ We will consider here only the three that are most pertinent to the $\text{Ln}(\text{HBPz}_3)_3$ system:

- 1) The complex is magnetically axially symmetric or possesses "effective" axial symmetry.
- 2) The magnetic axis is colinear with the bond between the lanthanide and the ligating atom of the substrate.
- 3) The pseudocontact shifts can be successfully separated from the contact shift contribution to the isotropic shifts.

X-ray crystallographic structure determinations of shift reagent adducts^{6,8,96,97} have shown that these complexes possess at most two-fold symmetry. Also magnetic anisotropy measurements of the series of complexes $\text{Ln}(\text{dpm})_3(4\text{-picoline})_2$ in the solid state,⁹⁸ in agreement with the low symmetry seen in the X-ray structures, reveal large anisotropies with $D_2 > D_1$. Thus, the first assumption appears suspect, at least in certain cases, and should be treated with caution.

A common method to test for the presence of effective axial symmetry is to examine the shift ratios:

$$\frac{\left(\frac{\Delta\nu}{\nu_0}\right)_i^{\text{pc}}}{\left(\frac{\Delta\nu}{\nu_0}\right)_j^{\text{pc}}} = \frac{D_1}{D_1} \frac{(3\cos^2\theta_i - 1) r_j^3}{(3\cos^2\theta_j - 1) r_i^3} \quad (9)$$

The shift of the i^{th} nucleus, $(\Delta\nu/\nu_0)_i$ pc, is normalised to the isotropic shift for the j^{th} nucleus. The resulting shift ratios, (9), should be invariant for isostructural complexes if equation (8) is valid and can be applied to the system.

Several rationales for the observed effective axial symmetry have been proposed. Briggs et al.⁹⁹ have suggested that rapid exchange of the substrate between rotamers would average out the non-axial term containing D_2 . Horrocks¹⁰⁰ has derived the same result by assuming that "the lanthanide shift reagent adducts exist in solution as an ensemble of many rapidly interconverting geometrical isomers." The assumption that the unique magnetic axis lies along the lanthanide donor bond would appear to be intuitively correct if such a mechanism results in effective axial symmetry.

DeBoer et al.¹⁰¹ and Marinetti et al.¹⁰² have noted that if a small substrate molecule lies within a cone angle of $\sim 40^\circ$ about this unique axis then $3\cos^2\theta - 1 \gg \sin^2\theta$ and "apparent" axial symmetry will result even though the complex is magnetically non-axially symmetric and D_2 is of comparable magnitude to D_1 .

In several instances it has been found that equation (8) is not applicable and that the full form of the expression must be used to account for the observed

pseudocontact shifts. Cramer et al.^{103,104} have investigated the series of complexes $\text{Ln}(\text{dpm})_3\text{L}_2$ (L = pyridine, 4-picoline, 3-picoline and 3,5-lutidine) and have calculated the orientation of the magnetic axes and the parameters D_1 and D_2 . Catton et al.¹⁰⁵ have taken a similar approach to the NMR spectra of lanthanide crown ether complexes. Agresti et al.¹⁰⁶ have reexamined the shifts produced by the interaction of Ln^{3+} ions with lysozyme. Campbell, Dobson and Williams¹⁰⁷ had originally analysed the shifts using equation (8). However, the reexamination indicates that the induced shifts have considerable non-axial character.

Lee and Sykes¹⁰⁸ have studied the solution structure of the Ca^{2+} binding protein parvalbumin using Yb^{3+} as a structural probe. By consideration of the shifts of 3 resonances they were able to obtain sets of magnetic parameters for the lanthanide-protein complex, one of which successfully accounted for the shifts observed for six methyl groups in the protein.

In all of the studies involving non-axial symmetry mentioned above a preliminary knowledge of the structure of the species is required. This invariably is provided by X-ray crystallographic data. The lanthanide probe technique can therefore be regarded as an adjunct to X-ray crystallography to provide structural information

about the species in solution. Lee has noted¹⁰⁹ that the paramagnetic probe technique should in theory provide a more sensitive method for the structural determination of large molecules, such as proteins, than X-ray crystallography. The problem of contact shift contribution to the isotropic shifts is often important. The shift ratios $(\Delta\nu/\nu_0)_i/(\Delta\nu/\nu_0)_j$ should be constant for a series of lanthanide complexes if there are no contact contributions.

Observation of constant shift ratios has enabled many investigators to rule out contact shifts for certain nuclei. Typically these are protons well removed, in terms of bonds, from the lanthanide ion. Williams et al.¹¹⁰ have developed a method of separating the contact and pseudocontact shifts. Their approach is to use proton shifts which can be shown by shift ratios to be free of contact contributions and the theoretical coefficients $g_J(g_J-1)(J+1)J$ and $g_J^2J(J+1)(2J-1)(2J+3)\langle J||\alpha||J\rangle$ which determine the magnitude of the two different shifts. By this method they were able to obtain the ³¹P contact shifts in cytidene 5'-monophosphate. Pinkerton and Earl⁹ have used the same technique for the tetrakis dithiophosphate lanthanide complex, $\text{Ln}[\text{S}_2\text{P}(\text{OEt})_2]^-$. Reilley et al.^{111,112} have discussed the various methods available for the separation of the two types of shifts.

Desreux and Reiley¹¹³ have obtained a separation for the ^{13}C nuclei in the $[\text{Ln}(\text{dpa})_3]^{-3}$ complexes by a method which uses the two different temperature dependencies of the shifts. From Bleaney's theory $(\Delta\nu/\nu_0)_{\text{pc}}$ should follow a T^{-2} dependence while $(\Delta\nu/\nu_0)_{\text{con}}$ should follow a T^{-1} dependence. However, Sherry et al.¹¹⁴ failed to obtain a separation with this method and there has been much debate in the literature over the exact nature of the temperature dependencies that should be observed for the pseudocontact and contact shifts.¹¹⁵⁻¹¹⁷ DeBoer et al.¹⁰¹ have observed shifts which more closely follow T^{-1} than T^{-2} and Lee and Sykes¹¹⁸ have found the rather unusual T^{-3} dependence. It is clear from experiment that the observed temperature dependence is often not simple.

In general ^1H contact shifts are much smaller than those of other nuclei such as ^{13}C . In fact, by a judicious choice of lanthanide ion,¹¹⁹ specifically, Yb^{3+} , many investigators have been able to circumvent the problem of contact contributions to the ^1H isotropic shifts.

The special features of the $\text{Ln}(\text{HBPz}_3)_3$ complexes which will be described in this chapter facilitate the detailed analysis of their NMR spectra. Several of the assumptions, outlined by Horrocks,⁷⁴ that are commonly used in NMR structural studies of lanthanide complexes can be made here

with complete confidence. The validity or lack thereof of the remaining assumptions can be verified in almost every case by experimental results.

The success of the approach, used for the $\text{Ln}(\text{HBPz}_3)_3$ series hinges largely on the solid state molecular structure of the prototype complex, $\text{Yb}(\text{HBPz}_3)_3$. The initial aim of this work was to compare the solution structure of this complex, derived from analysis of its NMR spectrum, with its known solid state structure. The NMR spectra do indeed provide quite precise information about the solution structures of the complexes but probably more importantly the series provides a model system with which to test the applicability of equations (7) and (8) and to compare the values of the magnetic susceptibility anisotropies, D_1 and D_2 , for a series of isostructural complexes. In addition, successful modeling of the pseudocontact shifts may allow a separation of contact from pseudocontact shifts and thereby a comparison of the contact shifts observed for a series of complexes and their relative magnitude within each complex for at least three different nuclei, ^1H , ^{13}C and ^{11}B .

^1H , ^{13}C and ^{11}B Spectra of $\text{Lu}(\text{HBPz}_3)_3$ and $\text{Yb}(\text{HBPz}_3)_3$.

The ^1H NMR spectrum of $\text{Lu}(\text{HBPz}_3)_3$ is shown in Figure 11 and the resonances are listed in Table 17. The diamagnetic lutetium complex shows a pattern similar to that found for the free HBPz_3^- ligand¹²⁰ and the yttrium complex.³⁶ The 3-H and 5-H protons appear as doublets ($J=2\text{Hz}$) mostly between $\delta 6.5$ and 8.0 ppm and the 4-H protons as triplets ($J = 2 \text{ Hz}$) between $\delta 5.5$ and 6.5 ppm. The proton decoupled ^{13}C NMR spectrum is shown in Figure 12 and Table 17. The 3- and 5- carbons are found between 134 and 144 ppm and the 4- carbons between 103 and 105 ppm downfield from TMS. The shifts are similar to those found for pyrazole and HBPz_3^- ligand.³³ The carbons of the pyrazolyl rings exhibit a coupling of ~ 180 Hz with the proton to which they are directly bonded.

The ^{11}B spectrum shows a single resonance at -4.1 ppm relative to $\text{BF}_3(\text{OEt})_2$. By comparison the ^{11}B nuclei in $\text{Zn}(\text{HBPz}_3)_2$ ¹²¹ and KHBPz_3 ¹²⁰ appear at -4.9 and -1.5 ppm respectively.

The complicated nature of the $\text{Lu}(\text{HBPz}_3)_3$ ^1H and ^{13}C NMR spectra suggests that the structure in solution is one of rather low symmetry which is not rapidly rearranging by intramolecular or intermolecular exchange processes.

The ^1H NMR spectrum of $\text{Yb}(\text{HBPz}_3)_3$ is shown in Figure 13. The most striking feature of the NMR spectrum is

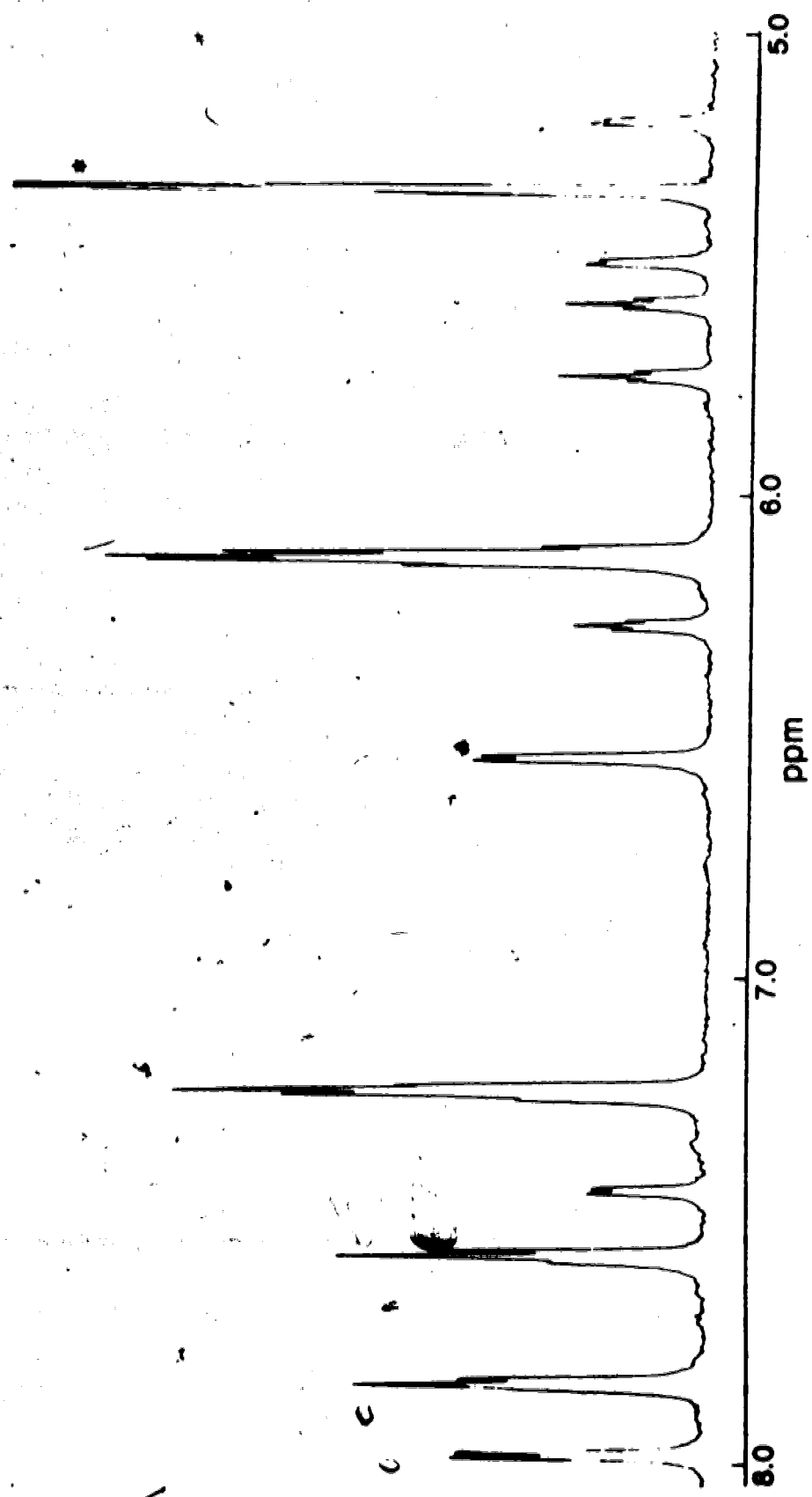


FIGURE 11. 200 MHz ¹H NMR Spectrum of Lu(HBPz)₃, * CDCl₂.

(

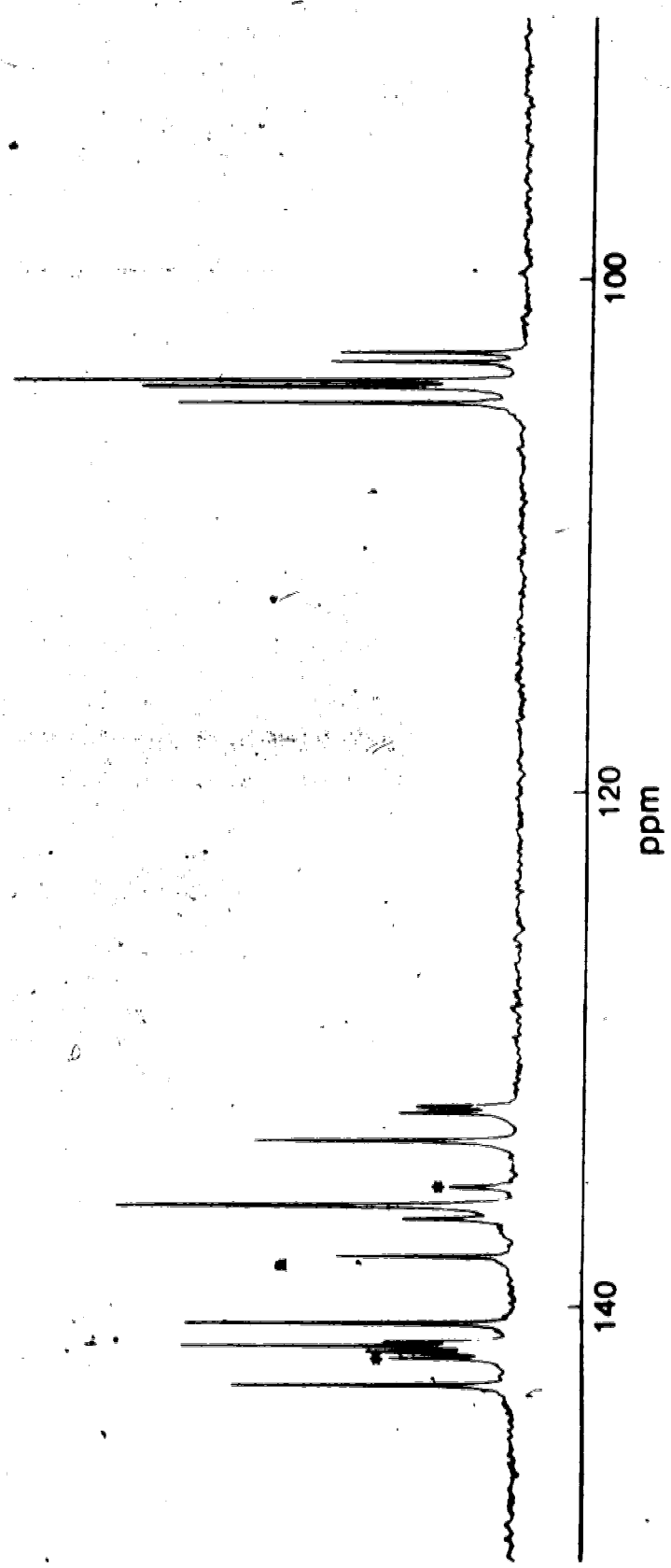


FIGURE 12. 50.33 MHz ^{13}C NMR Spectrum of $\text{Lu}(\text{HBPz}_3)_3$, * Impurities.

Table 17. ^1H , ^{13}C and ^{11}B Chemical Shifts of
 $\text{Lu}(\text{HBPz}_3)_3$ ^{a,b,c}

^1H	^{13}C	^{11}B
7.92 d(2)	143.45(2)	-4.1
7.79 multiplet(3)	142.16(1)	
7.52 multiplet(3)	141.92(2)	
7.38 d(1)	141.73(1)	
7.19 multiplet(5)	141.02(2)	
6.49 d(2)	138.42(1)	
6.22 t(1)	136.92(1)	
6.07 multiplet(6)	136.43(4)	
5.70 t(1)	133.93(2)	
5.55 t(1)	132.84(1)	
5.47 d(1)	132.56(1)	
5.18 d(1)	105.32(2)	
4.5 very broad(3)	104.67(2)	
	104.45(3)	
	103.72(1)	
	103.36(1)	

^a ^1H spectrum recorded with CD_2Cl_2 as solvent, ^{13}C and ^{11}B with $\text{CH}_2\text{Cl}_2/10\% \text{CD}_2\text{Cl}_2$ solvent.

^bShifts in ppm relative to TMS or BF_3OEt_2 . Measured using internal standards $^1\text{H}(\text{CHDCl}_2)$ and $^{13}\text{C}(\text{CD}_2\text{Cl}_2)$ at 65.32 ppm and 653.8 ppm, respectively.

^cd = doublet, t = triplet, relative intensities in parentheses.

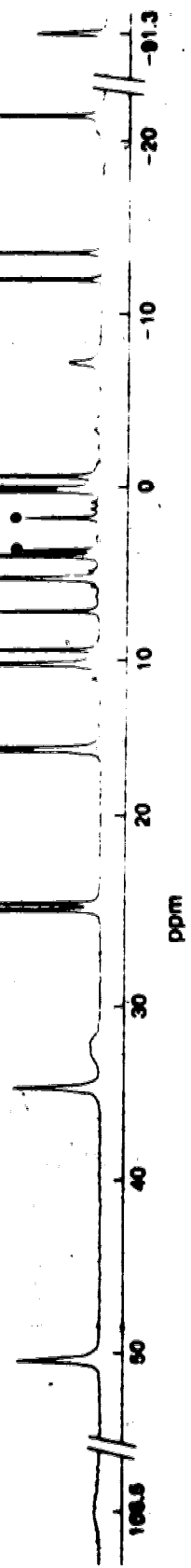


FIGURE 13. 200 MHz ¹H NMR Spectrum of Yb(HBPz₃)₃, *CHDCl₂, †silicone grease, °THF.

the large isotropic shifts caused by the paramagnetic ytterbium ion and exemplified by the range of the proton chemical shifts which is ~200 ppm. The spectrum like that of $\text{Lu}(\text{HBPz}_3)_3$ is complicated and implies that the molecule has a rigid solution structure. However, because of the much increased chemical shift range compared to the diamagnetic lutetium complex the presence of a large number of well separated resonances invites the use of the NMR spectrum to determine the solution structure of the complex. A close examination of the ^1H NMR spectrum reveals that the 27 pyrazolyl protons give rise to only 18 resonances. The relative intensity of nine of the resonances is one while the remaining peaks have relative intensity of two. In addition, there are three resonances that arise from the B-H protons. Similarly, the ^{13}C NMR spectrum exhibits 18 resonances with the same intensity distribution as the pyrazolyl hydrogens. Figure 14 shows a partially decoupled ^{13}C NMR spectrum. The C-H coupling ($J = -180$ Hz) is not "washed out" by the paramagnetic ytterbium ion and the large shifts in the ^1H spectrum makes it impossible to decouple the entire spectrum. The ^{11}B NMR spectrum shown in Figure 15 has three well separated resonances integrating with a 1:1:1 ratio.

The number and the relative intensity of the peaks indicate the presence of a mirror plane in the solution

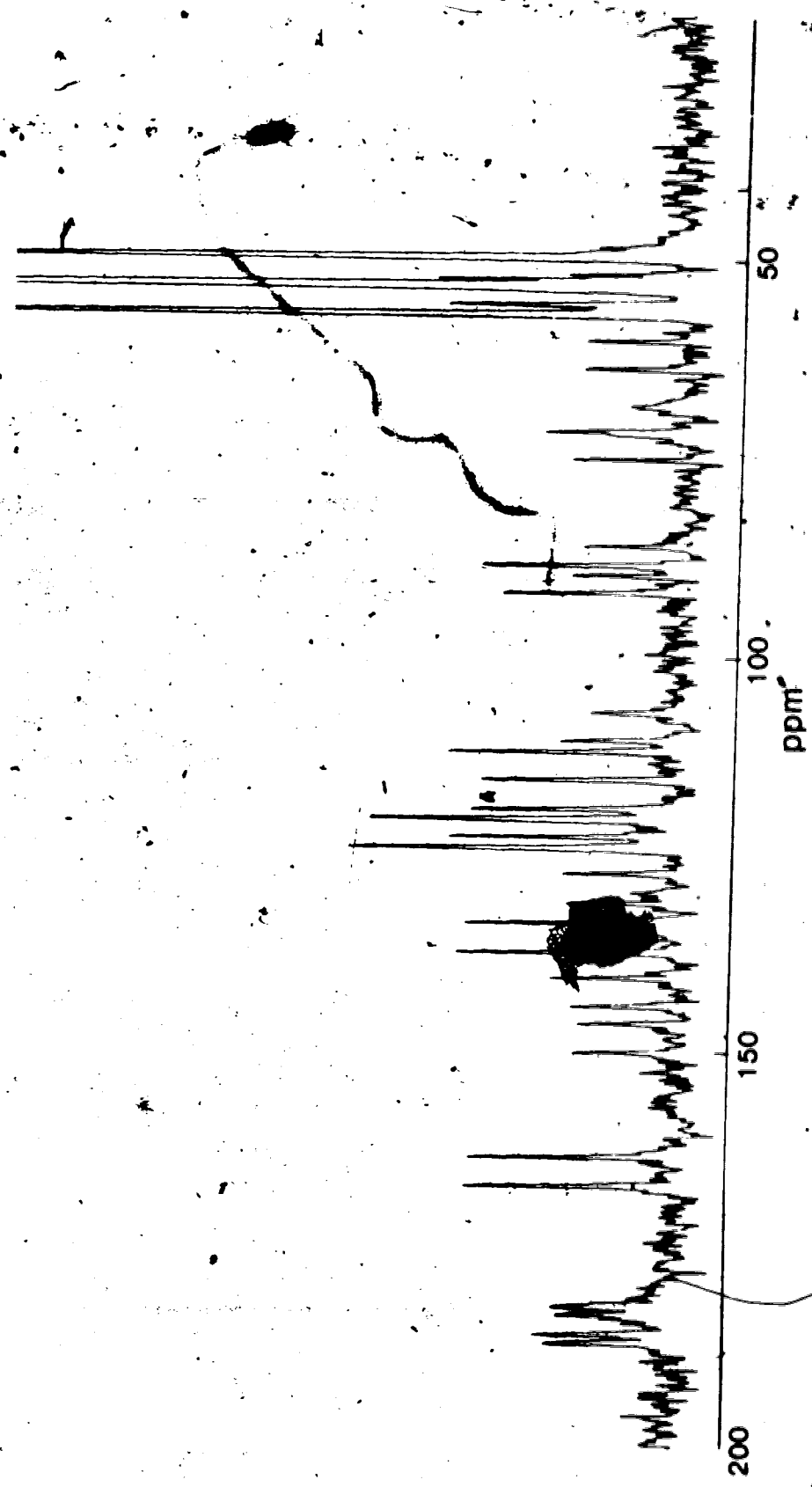


FIGURE 14. 50.33 MHz ^{13}C NMR Spectrum of $\text{Yb}(\text{HBPz})_3$.

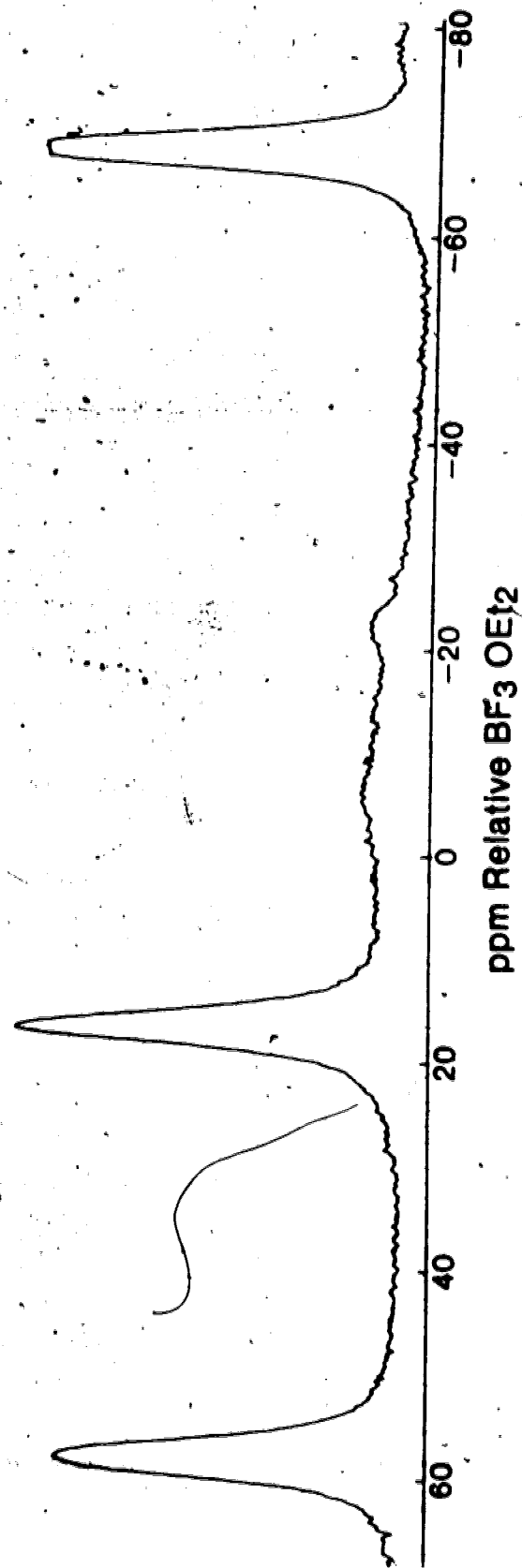


FIGURE 15. 64.23 MHz ^{11}B NMR Spectrum of $\text{Yb}(\text{HBPz}_3)_3$.

structure which causes the equivalence of six pyrazolyl rings in a pairwise fashion while maintaining the other three and the boron atoms distinct. Reference to Figure 6 and Figure 8 shows that only slight modification of the approximate C_3 solid state structure is required to account for the solution NMR features. One may conclude therefore that the ytterbium complex is rigid and its solution structure is very close to that found in the solid state. The known solid state structure, the rigid nature and the large number of unique NMR nuclei (42 in total) make $Yb(HBPz_3)_3$ an extremely interesting complex with regard to NMR studies of lanthanide complexes.

It has been noted that amongst the lanthanides Yb^{III} complexes will exhibit the largest relative pseudocontact contribution to the isotropic shift.^{80,84,119} Thus, starting with the twin assumptions that the structure observed in the solid state is maintained in solution and that, at least for the $Yb(HBPz_3)_3$ 1H NMR spectrum, Fermi contact contributions to the isotropic shifts will be negligible, a fit of the observed isotropic shifts to the X-ray structural data should be possible.

The full expression for the pseudocontact shift must be used (equation (7)) as the number of resonances in the NMR spectra indicate that complex is not axially symmetric. Fortunately, the C_3 symmetry of the molecule

fixes the z magnetic axis perpendicular to the mirror plane containing Yb, B(1), B(2) and B(3). The magnetic x, y plane coincides with this plane and it is now useful to redefine the angle Ω in equation (7) in terms of the magnetic parameter ϕ , the angle between the x magnetic axis and the Yb-B(1) vector, and the geometric variable k , the angle between the Yb-B(1) vector and the projection of the Yb-nucleus vector on the magnetic x,y plane, Figure 16. Thus, $\Omega = \phi + k$ and the calculable geometrical variables for each NMR observed nucleus become r , θ and k . These are obtained from the X-ray crystallographic data using the program ORFFE,⁵⁴ and are listed in Table 18. In the case of the hydrogen atoms instead of using the X-ray positions the values of r , θ and k were produced by repositioning the hydrogen atoms with C-H and B-H bond lengths 1.08 Å and 1.20 Å, respectively. The errors in the positions of the atoms are assumed to be isotropic. Those for the carbon and boron atoms are taken as 0.01 Å and those for the hydrogen atoms are assumed to be 0.05 Å. The errors in r , θ and k are calculated using these isotropic errors.

When two sets of geometric variables are available for one type of nucleus, (this arises from the mirror plane being a non-crystallographic mirror plane in the X-ray structure) the average value is used and the

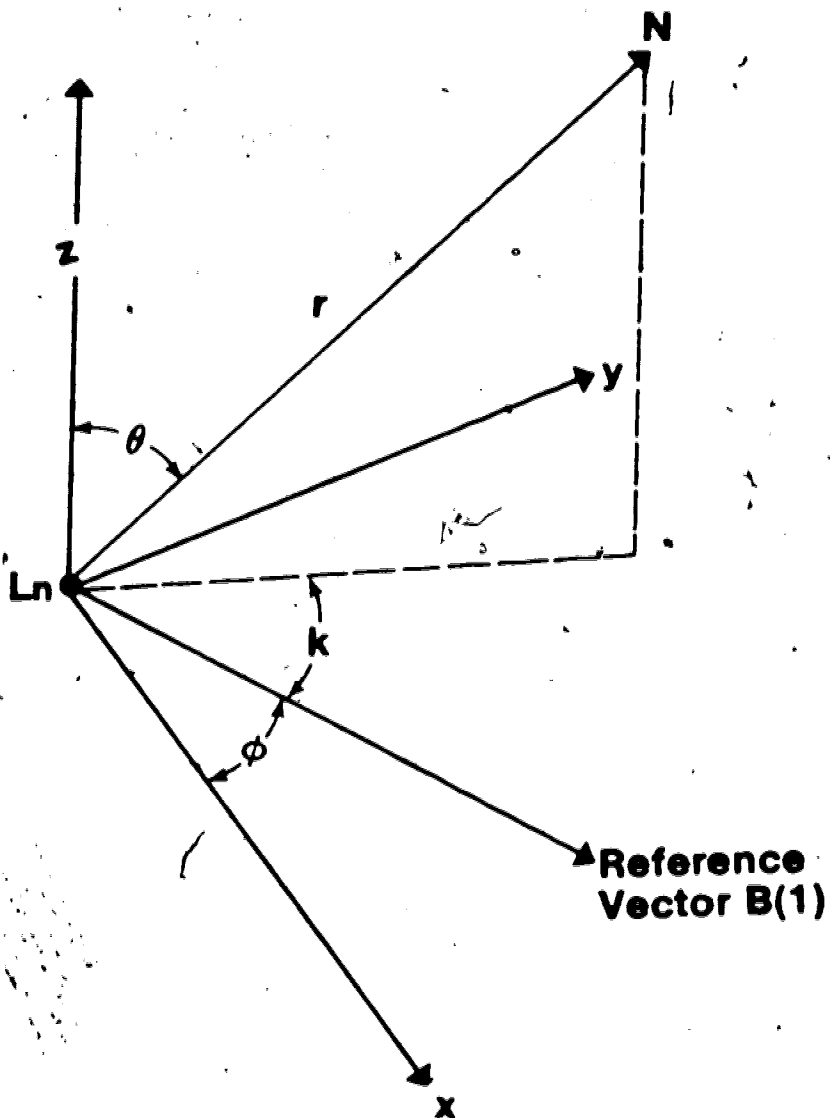


FIGURE 16. Coordinate System Defining Geometric Variables r , θ and k , for a nucleus N .

Table 18. Geometric Variables for $\text{Yb}(\text{HBPz}_3)_3^a$

Nucleus	r	θ	k	$\frac{3\cos^2\theta-1}{r^3}$	$\frac{\sin^2\theta}{r^3}$
	\AA	deg.	deg.	$\text{\AA}^{-3} \times 10^{-2}$	\AA^{-3}
i) Hydrogens					
H(13)	3.65(5)	24.3(12)	62.8(15)	3.08(16)	8.0(16)
H(43)	3.74(5)	28.7(12)	-165.9(15)	2.51(16)	
H(73)	3.62(5)	30.0(12)	-65.1(15)	2.63(16)	
H(14)	5.60(5)	42.3(6)	35.4(18)	0.364(20)	
H(44)	5.68(5)	42.4(6)	162.6(18)	0.347(20)	
H(74)	5.61(5)	43.0(6)	-97.0(18)	0.241(20)	0.66(10)
H(15)	5.48(5)	65.5(5)	16.9(6)	-0.295(15)	0.18(15)
H(45)	5.56(5)	65.4(5)	144.3(6)	-0.279(15)	1.8(15)
H(75)	5.50(5)	65.3(5)	-117.4(6)	-0.285(15)	4.4(15)
H(33)	3.85(5)	^b	-76.3(8)	-1.76(7)	1.76(7)
H(63)	3.74(5)	-	52.7(8)	-1.92(7)	1.92(7)
H(93)	8.07(5)	-	-127.2(5)	-0.190(4)	0.190(4)
H(34)	5.80(5)	-	-54.1(5)	-0.513(15)	0.513(15)
H(64)	5.72(5)	-	75.0(5)	-0.533(15)	0.533(15)
H(94)	8.08(5)	-	-145.9(5)	-0.190(4)	0.190(4)
H(35)	5.66(5)	-	-27.6(5)	-0.551(16)	0.551(16)
H(65)	5.62(5)	-	101.8(5)	-0.563(16)	0.563(16)
H(95)	5.82(5)	-	-157.6(5)	-0.509(12)	0.509(12)
H(1)	4.79(5)	-	1.1(8)	-0.911(30)	0.911(30)
H(2)	4.80(5)	-	130.3(8)	-0.904(30)	0.904(30)
H(3)	3.23(5)	-	-154.4(9)	-2.96(14)	2.96(14)

continued...

Table 18 (continued)

Nucleus	r Å	θ deg.	k deg.	$\frac{3\cos^2\theta-1}{r^3}$ Å ⁻³ x10 ⁻²	$\frac{\sin^2\theta}{r^3}$ Å ⁻³ x10 ⁻²
ii) Carbons and Borons					
H(13)	3.43(1)	36.0(7)	37.1(15)	2.39(9)	0.855(30)
C(43)	3.52(1)	38.3(7)	169.9(15)	1.94(9)	0.881(30)
C(73)	3.42(1)	39.1(7)	-91.4(15)	2.01(9)	0.994(30)
C(14)	4.61(1)	45.6(4)	30.2(10)	0.476(20)	0.520(8)
C(44)	4.68(1)	46.2(4)	158.6(10)	0.427(20)	0.508(8)
C(74)	4.62(1)	46.6(4)	-101.3(10)	0.421(20)	0.535(8)
C(15)	4.52(1)	60.0(2)	19.0(8)	-0.271(9)	0.811(6)
C(45)	4.60(1)	60.4(2)	147.3(8)	-0.276(9)	0.776(6)
C(75)	4.54(1)	60.4(2)	-114.3(8)	-0.266(9)	0.806(6)
C(33)	3.64(1)	^b -	-60.0(2)	-2.08(2)	2.08(2)
C(63)	3.54(1)	-	69.5(2)	-2.25(2)	2.25(2)
C(93)	7.12(1)	-	-131.0(2)	-0.277(1)	0.277(1)
C(34)	4.80(1)	-	-49.6(2)	-0.904(6)	0.904(6)
C(64)	4.73(1)	-	79.8(2)	-0.943(6)	0.943(6)
C(94)	7.14(1)	-	-142.0(2)	-0.275(1)	0.275(1)
C(35)	4.71(1)	-	-33.3(2)	-0.955(6)	0.955(6)
C(65)	4.67(1)	-	96.3(2)	-0.984(6)	0.984(6)
C(95)	5.89(1)	-	-147.0(2)	-0.489(3)	0.489(3)
B(1)	3.59(1)	-	0.0(2)	-2.16(2)	2.16(2)
B(2)	3.60(1)	-	130.0(2)	-2.14(2)	2.14(2)
B(3)	3.53(1)	-	-134.5(3)	-2.28(2)	2.28(2)

^aNumbers in parentheses represent the estimated errors in the least significant digits.

^bNuclei H(33) to H(3) and C(33) to B(3) are assumed to lie in the plane formed by Yb, B(1), B(2) and B(3). The value of θ for these nuclei is therefore 90.0°.

errors are adjusted to reflect the ranges in the two sets of observed values.

A problem arises in extracting the observed isotropic shifts from the NMR spectra using the chemical shifts of the diamagnetic lutetium complex, see equation (4). A rigorous assignment of the complicated $\text{Lu}(\text{HBPz}_3)_3$ NMR spectra is not possible. The resonances in the ^1H spectrum can be classified into two groups based on proton-proton coupling information - the 3-H and 5-H (doublets) and the 4-H (triplets). Further classification within each group can be made from relative integrations (either 2 or 1).

The ^{13}C NMR spectrum similarly can only be assigned in groups using the large chemical shift differences between the 3-carbons and 5-carbons, and the 4-carbons, and the relative peak integrations. Within most of these assigned groups there is a range of chemical shifts and consequently an average value has to be used as the diamagnetic zero for a group of nuclei. The ranges and average values are given in Table 19. The ranges are incorporated into the observed isotropic shifts as an uncertainty.

Specific assignment of the $\text{Lu}(\text{HBPz}_3)_3$ spectra is not essential to obtaining a fit of calculated to observed isotropic shifts for $\text{Yb}(\text{HBPz}_3)_3$. However, in the $\text{Yb}(\text{HBPz}_3)_3$ spectra each resonance must be assigned

Table 19. Diamagnetic Reference Shifts

		Range ^a	Average	Uncertainty
<u>¹H</u>	d(2)	7.92 - 6.49	7.2	±0.7
	d(1)	7.79 - 5.18	6.5	±1.3
	t(2)	6.09 - 6.05	6.07	±0.02
	t(1)	6.22 - 5.55	5.9	±0.3
	BH		4.5	±0.5
<u>¹³C</u>	3-C } (2)	143.45 - 133.93	138.7	±4.8
	5-C }			
	4-C (2)	105.32 - 104.45	104.9	±0.4
	3-C } (1)	142.16 - 132.56	137.4	±4.8
	5-C }			
	4-C (1)	104.45 - 103.36	103.9	±0.5
<u>¹¹B</u>			-4.1	±1.0

^aShifts in ppm taken from Table 17.

to a definite nucleus with geometrical variables, r , θ and k . The large number of resonances and the lack of a coupling handle (the proton-proton coupling is "washed out" by line broadening caused by the paramagnetic metal ion) makes an assignment of the ^1H NMR spectrum merely by inspection impossible. However, selective heteronuclear decoupling experiments allows the matching of all the ^{13}C and ^{11}B resonances to the resonances of the protons to which they are directly bonded.

Selective decoupling was extremely useful in the assignment of the spectra and was facilitated by the large differences in chemical shifts of the protons and the nuclear Overhauser effect which appears to be unaffected by the presence of the paramagnetic ion.

Consideration of the line widths and relative integrations allows the assignment of some of the resonances into groups. The three resonances due to the three equivalent pairs of nuclei H(13) (H23), H(43) (H53) and H(73) H(83) constitute one such group. These protons are closer to the ytterbium than the others on the same pyrazolyl group by at least 1.5 \AA . Their NMR signals have correspondingly greater line widths¹²² and the resonances are easily recognizable in the spectrum. Similarly, the two resonances due to H(33) and H(63) form another group and can be readily picked out in the

spectrum. The B-H protons also form a group and can be identified by their large "inhomogeneously broadened" line widths. Additionally from Figure 7 it can be seen that H(3) is much closer to the ytterbium than both H(1) and H(2). Thus H(3) can be definitely assigned while H(1) and H(2) form a group. The selective hetero-nuclear decoupling experiments allow the assignment of the resonances in the ^{11}B spectrum in a corresponding fashion.

There are six ways of assigning the 3 resonances arising from H(13), H(43) and H(73) which lead to the six sets of values of D_1 , D_2 and ϕ shown in Table 20.

Table 20. The Six Sets of Magnetic Parameters Obtained from the Observed Shifts of H(13), H(43) and H(73)

Solution	$D_1/\text{\AA}^3 \times 10^2$	$D_2/\text{\AA}^3 \times 10^2$	$\phi/\text{deg.}$
1	8.8	46.8	-23.3
2	11.2	63.6	33.7
3	7.4	-61.7	11.8
4	11.2	65.3	17.5
5	8.9	-47.6	-12.9
6	7.3	-59.2	39.8

^aParameters calculated with average values of $(3\cos^2\theta-1)/r^3$ and $\sin^2\theta/r^3$ of $2.7 \times 10^{-2} \text{\AA}^{-3}$ and $0.44 \times 10^{-2} \text{\AA}^{-3}$ respectively (see Table 18).

These are exact solutions of equation (7). Only one of these solutions (solution 1) gives calculated shifts which successfully account for the observed shifts for H(33); H(63), H(1), H(2), H(3) and the three ^{11}B nuclei. This solution also gave reasonable shifts for the remaining ^1H nuclei and a full assignment of the spectrum was then made using calculated shifts from the preliminary model together with information from hetero nuclear decoupling experiments and relative integrations.

A fit of calculated to observed pseudocontact shifts was carried out using a weighted non-linear least-squares¹²³ computer program adapted to combine the uncertainties in the observed shifts and the geometric variables r , ϕ and k as an effective variance¹²⁴ (σ_{eff}). The weight assigned to each isotropic shift is $1/(\sigma_{\text{eff}})^2$. Appendix 3 contains a listing of the program.

The values of the observed shifts, and the calculated pseudocontact shifts from the least-squares fit for the protons in $\text{Yb}(\text{HBPz}_3)_3$ are listed in Table 21. The magnetic parameters D_1 , D_2 and ϕ , and the reliability factor R_w from this refinement are given in Table 22. The goodness of fit as represented by the value of 8.4% for R_w confirms the view that the complex has the same structure in both the solid and solution states.

Interestingly, 12 of the NMR unique ^1H nuclei lie in the magnetic x, y plane defined by the 3 boron atoms

Table 21. Observed and Calculated ¹H Shifts for Yb(HBPz)₃

Chemical ^a Shift ppm	$\left(\frac{\Delta\nu}{\nu}\right)_{\text{iso}}^{\text{b}}$ obsd ppm	$\left(\frac{\Delta\nu}{\nu}\right)_{\text{pc}}^{\text{c}}$ calc ppm	$\left(\frac{\Delta\nu}{\nu}\right)_{\text{iso}} - \left(\frac{\Delta\nu}{\nu}\right)_{\text{pc}}$ ppm
H(13)	34.8	27.6(8)	4.4
H(43)	50.4	43.2(8)	2.0
H(73)	10.3	3.1(8)	-0.2
H(14)	15.3	9.15(2)	-1.2
H(44)	15.1	9.00(2)	-0.3
H(74)	-0.6	-6.70(2)	-0.2
H(15)	24.4	17.3(8)	-1.5
H(45)	4.0	-3.2(8)	-0.2
H(75)	0.3	-7.0(8)	1.2
H(33)	-91.3	-97.8(13)	-6.3
H(63)	-7.3	-13.8(13)	-3.7
H(93)	7.2	0.7(13)	1.7
H(34)	-12.0	-17.9(3)	-0.5
H(64)	-13.5	-19.4(3)	0.2
H(94)	10.3	4.4(3)	0.5
H(35)	9.4	2.9(13)	1.7
H(65)	-21.4	-27.9(13)	1.5
H(95)	24.1	17.6(13)	1.9
H(1)	32.5	28.0(8)	-1.7
H(2)	-21.0	-25.5(8)	1.9
H(3)	106.5	102.0(10)	17.7

^a Shift relative to TMS. Measured with internal standard CHCl₃; 65.32 ppm.

^b Calculated using equation (4) and data in Table 19.

^c Number in parentheses after the calculated pseudocontact shift represents the effective variance (see reference 124) in the least significant digit.

Table 22. Magnetic Parameters From Least-Squares Refinements of Pseudocontact Shifts of $\text{Yb}(\text{HBPz}_3)_3$.

Number and Type of Resonances	$\frac{D_1}{\text{Å}^3 \times 10^2}$	$\frac{D_2}{\text{Å}^3 \times 10^2}$	$\frac{\phi}{\text{deg.}}$	$\frac{R_w}{\%}$
21^1H	8.8(5)	43.6(9)	-10.1(5)	8.4
$18^{13}\text{C}, 3^{11}\text{B}$	8.8(7)	42.3(11)	-11.2(7)	10.1
$21^1\text{H}, 18^{13}\text{C}, 3^{11}\text{B}$	8.9(5)	42.6(8)	-10.9(4)	9.9

and the ytterbium. Figure 17 shows a map of the magnitude of the pseudocontact shifts in this plane and the orientation of the x axis with respect to the complex. The contours shown are for shifts ± 10 , ± 20 , ± 50 and ± 100 ppm, which are calculated from equation (7) and the D_1 and D_2 values listed in Table 22. The view of the complex is the same as that in Figure 8 but all the atoms not in the x,y plane have been removed for clarity.

Figure 17 provides a visual description of the sensitivity of the various nuclei to small changes in their positions, particularly H(3) and H(33) which lie in regions of high shift and H(63) and B(3) which lie close to the nodal surface.

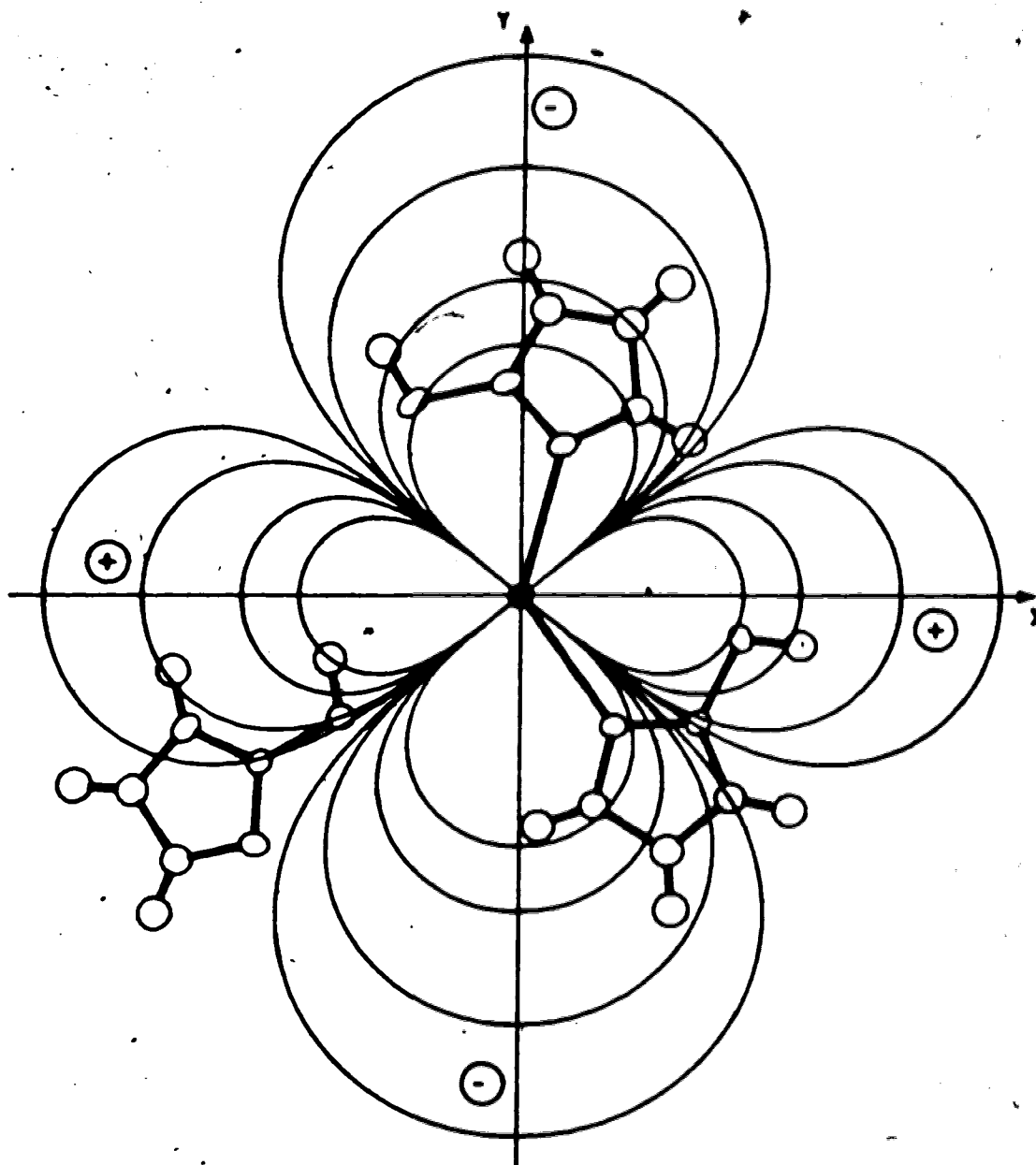


FIGURE 17. Contour Map of Pseudocontact Shifts in $\text{Yb}(\text{HBPz}_3)_3$ Molecule. Contours at ± 100 , ± 50 , ± 20 and ± 10 ppm.

Figure 17 is useful in determining the conformation adopted by the bidentate ligand in solution. The six membered metal chelate ring which is in the boat conformation in the solid state may either be undergoing a "ring flip" process, shown in Figure 18, which has been observed for bidentate polypyrazolyl borate ligands¹²⁵ or may favour the other boat conformation, in solution. Additionally rotation of the uncoordinated pyrazolyl group N(91)...C(95) about the N(91)—B(3) bond is also possible. Examination of the observed and calculated shifts of protons H(3) (bonded to B(3)) and H(95) (attached to C(95) in the uncoordinated pyrazolyl group) in conjunction with the dipolar surface map of Figure 17, indicates that the boat conformation found in the crystal structure is maintained in solution and that the uncoordinated pyrazolyl group is similarly locked into the rotational conformation seen in the X-ray structure.

The observed isotropic shift for H(3) is already 18 ppm farther downfield than the value calculated by the model. Any movement away from the particular boat conformation observed would change the position of H(3) such that the calculated shift for the new position would be even smaller than the observed isotropic shifts. By similar argument it can be seen from Figure 17 that rotation of the free pyrazolyl group away from the solid

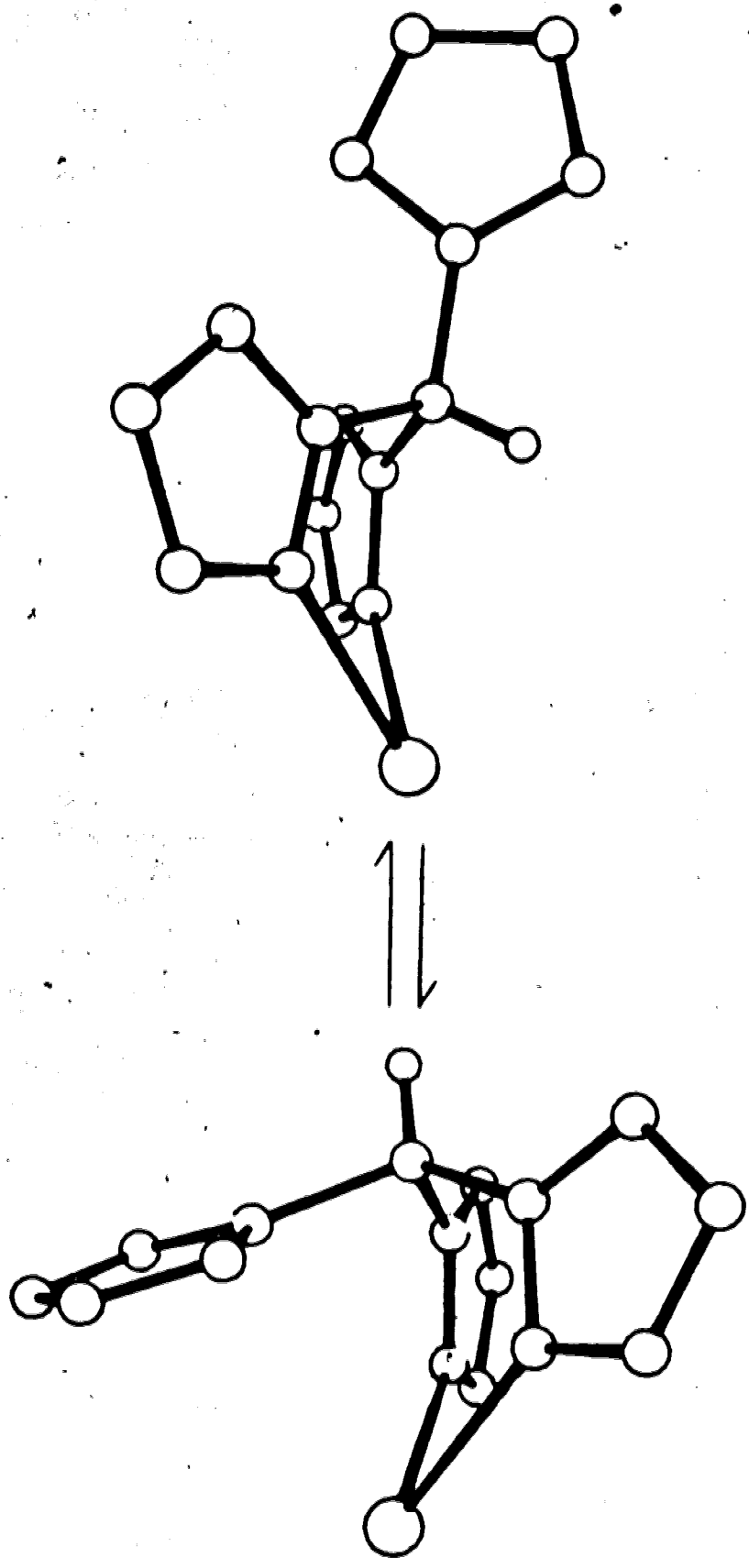


FIGURE 18. Scheme showing interconversion of two possible conformations of the bidentate ligand in $\text{Yb}(\text{HBPz}_3)_3$.

state conformation would result in a new position for R(95) which would have a much smaller calculated shift.

The good agreement between observed and calculated shifts also demonstrates that the second initial assumption, that there is no detectable contribution to ^1H isotropic shifts from a Fermi contact mechanism, is also valid. Table 23 contains the isotropic shifts of the ^{13}C and ^{11}B nuclei in $\text{Yb}(\text{HBPz}_3)_3$. The calculated shifts in Table 23 are those from the least-squares fit of only the 18 ^{13}C and 3 ^{11}B isotropic shifts. The values of D_1 , D_2 , and ϕ from this refinement and those from a refinement with 21 ^1H , 18 ^{13}C and 3 ^{11}B nuclei are contained in Table 22.

The close agreement between the observed shifts and calculated pseudocontact shifts indicates that the contact contributions to the ^{13}C and ^{11}B isotropic shifts are so small as to be essentially undetectable in the present analysis of the $\text{Yb}(\text{HBPz}_3)_3$ system. However, it should be noted that although the shifts are adequately accounted for solely by a pseudocontact mechanism, the rather large uncertainties in the observed isotropic shifts for some ^{13}C nuclei (up to 5 ppm) make it difficult to completely rule out a small contact contribution to the ^{13}C shifts.

Table 23. Observed Isotropic and Calculated Pseudocontact ^{13}C and ^{11}B Shifts for $\text{Yb}(\text{HBPz})_3$.

Chemical ^a Shift ppm	$(\frac{\Delta\nu}{\nu})_{\text{O}}^{\text{b}}$ iso ppm	$(\frac{\Delta\nu}{\nu})_{\text{O}}^{\text{c}}$ calc ppm	$(\frac{\Delta\nu}{\nu})_{\text{O}}^{\text{c}}$ iso - $(\frac{\Delta\nu}{\nu})_{\text{O}}^{\text{b}}$ ppm
C(13)	184.4	45.7(48)	43.5(52)
C(43)	183.3	44.6(48)	44.6(51)
C(73)	123.0	-15.7(48)	-20.4(51)
C(14)	121.2	16.3(4)	21.55(70)
C(44)	114.0	9.1(4)	21.6(7)
C(74)	90.9	-14.0(4)	12.8(8)
C(15)	164.7	26.0(48)	-12.3(8)
C(45)	135.9	-2.8(48)	-1.1(49)
C(75)	123.0	-15.7(48)	-13.5(49)
C(33)	56.1	-81.3(48)	-88.2(49)
C(63)	71.0	-66.4(48)	-62.8(49)
C(93)	142.7	5.3(48)	0.5(48)
C(34)	74.4	-29.5(5)	-28.0(6)
C(64)	63.0	-40.9(5)	-37.7(6)
C(94)	109.1	5.2(5)	4.5(5)
C(35)	129.8	-7.6(48)	-7.7(48)
C(65)	89.4	-48.0(48)	-49.8(48)
C(95)	148.4	11.0(48)	10.7(48)
B(1)	57.7	61.8(10)	65.7(13)
B(2)	-69.1	-65.0(10)	-67.4(12)
B(3)	16.3	20.4(10)	15.0(14)

^aShifts in ppm relative to TMS or BF_3OEt_2 . ^{13}C shifts measured with internal standard CH_2Cl_2 δ 53.8 ppm.

^bCalculated using equation (4) and data in Table 19.

^cNumber in parentheses after the calculated pseudocontact shift represents the effective variance (see reference 124) in the least significant digit.

^1H Spectra of $\text{Ln}(\text{HBPz}_3)_3$, $\text{Ln} = \text{Dy, Ho, Er, Tm}$.

The tris(hydrotrispyrazol-1-yl borate) complexes of the four metals that precede Yb in the lanthanide series Dy, Ho, Er, Tm appear from their solution infrared spectra and their solubility properties to be isostructural with $\text{Yb}(\text{HBPz}_3)_3$.

Application of the techniques used in the analysis of the $\text{Yb}(\text{HBPz}_3)_3$ NMR spectra to these complexes provides a sensitive structural probe and allows a comparison of magnetic parameters within a series of presumably isostructural lanthanide complexes. Moreover the method should allow a separation of contact and pseudocontact contributions to the isotropic shifts, the relative magnitudes of which are expected to change considerably across the series from dysprosium to ytterbium (see Table 16).

The ^1H NMR spectra of the complexes $\text{Ln}(\text{HBPz}_3)_3$ ($\text{Ln} = \text{Dy, Ho, Er, Tm}$) show the same number and pattern of resonances as the $\text{Yb}(\text{HBPz}_3)_3$ spectrum. The Dy, Ho and Er spectra have additional resonances arising from another species in solution which will be described in a subsequent section. The observed isotropic shifts are calculated using the $\text{Lu}(\text{HBPz}_3)_3$ ^1H chemical shifts. As a first approximation the complexes are assumed to be isostructural with $\text{Yb}(\text{HBPz}_3)_3$ and the geometric variables

r , θ and k are those used in the analysis of the NMR spectra of the ytterbium complex. No attempt was made to include the change in ionic radius between Yb^{3+} and Dy^{3+} as the difference is only -0.04 \AA (see Table 1) which is very much less than the range in the Yb-N bond lengths and less than the 0.05 \AA estimated error in the geometrical variable, r , for the protons. Assignments of the spectra are made by employing the method described for $\text{Yb}(\text{HBPz}_3)_3$, utilizing rough preliminary values of D_1 , D_2 and ϕ , decoupling information and relative intensities.

The observed ^1H chemical shifts in the $\text{Ln}(\text{HBPz}_3)_3$ ($\text{Ln} = \text{Tm}, \text{Er}, \text{Ho}, \text{Dy}$) complexes are listed in Tables 24, 25, 26 and 27 along with the calculated dipolar shifts from the least-squares fit. The observed shifts illustrate the mirror relationship of the spectra between Dy, Ho and Er, Tm, Yb. This is caused by the change in sign of $\langle J || \alpha || J \rangle^{84}$ between the two sets of Ln^{3+} ions and indicates that the isotropic shifts are dominated by dipolar effects. The later observation is confirmed by the generally good agreement between the observed isotropic and the calculated pseudocontact shifts. The values of the magnetic parameters and R_w are given in Table 28.

Table 24. Observed and Calculated ¹H Shifts for Tm(HBPz)₃

Chemical ^a Shift ppm	$(\frac{\Delta\nu}{\nu})_{\text{O}}^{\text{b}}$ iso ^b obsd ppm	$(\frac{\Delta\nu}{\nu})_{\text{O}}^{\text{c}}$ calc ppm	$(\frac{\Delta\nu}{\nu})_{\text{O}}^{\text{c}}$ iso - $(\frac{\Delta\nu}{\nu})_{\text{O}}^{\text{b}}$ ppm
H(13)	98.5	80.4(49)	10.9
H(43)	143.8	124.5(70)	12.1
H(73)	7.3	3.3(69)	-3.2
H(14)	39.2	36.7(17)	-3.6
H(44)	27.8	21.2(20)	0.5
H(74)	-9.0	-14.2(19)	-0.9
H(15)	60.5	58.4(22)	-5.1
H(45)	-19.0	-23.9(16)	-2.3
H(75)	0.3	-9.2(16)	2.3
H(33)	-291.9	-276.4(94)	-22.0
H(63)	23.5	28.4(76)	-11.4
H(93)	11.8	2.7(14)	2.6
H(34)	-59.4	-66.7(18)	1.4
H(64)	-38.8	-45.1(15)	0.4
H(94)	21.8	15.5(6)	0.4
H(35)	-2.9	-13.4(19)	4.0
H(65)	-80.0	-87.8(25)	1.3
H(95)	62.1	52.1(21)	3.5
H(1)	78.5	77.7(39)	-3.7
H(2)	-94.6	-105.3(38)	6.2
H(3)	335.0	292(18)	38.4

^a Shift relative to TMS. Measured with internal standard CHDCl₂, 65.32 ppm.

^b Calculated using equation (4) and data in Table 19.

^c Number in parentheses after the calculated pseudocontact shift represents the effective variance (see reference 124) in the least significant digit.

Table 25. Observed and Calculated ^1H Shifts for $\text{Er}(\text{HBPz}_3)_3$

Chemical ^a Shift ppm	$(\frac{\Delta\nu}{\nu})_{\text{O}}$ iso ^b Obsd ppm	$(\frac{\Delta\nu}{\nu})_{\text{O}}$ pc ^c calc ppm	$(\frac{\Delta\nu}{\nu})_{\text{O}}$ iso - $(\frac{\Delta\nu}{\nu})_{\text{O}}$ pc ppm
H(13)	57.6	46.3(30)	4.1
H(43)	85.8	75.1(43)	3.5
H(73)	1.9	-1.6(43)	-3.7
H(14)	24.0	22.6(11)	-4.7
H(44)	16.5	13.0(13)	-2.6
H(74)	-6.3	-9.5(12)	-2.9
H(15)	37.9	37.3(15)	-6.6
H(45)	-11.0	-14.6(12)	-3.6
H(75)	0.3	-5.5(12)	-1.4
H(33)	-178.5	-172.1(60)	-12.9
H(63)	20.2	20.1(49)	-6.4
H(93)	10.9	1.9(13)	2.5
H(34)	-36.2	-41.3(11)	-0.8
H(64)	-22.6	-27.9(10)	-0.6
H(94)	16.6	10.0(4)	0.7
H(35)	-1.0	-7.5(15)	0.0
H(65)	-48.1	-54.6(13)	0.1
H(95)	42.7	36.2(13)	2.6
H(1)	52.6	48.1(8)	-2.4
H(2)	-55.3	-59.8(8)	5.2
H(3)	214.0	209.5(20)	21.2

^aShift relative to TMS. Measured with internal standard CHCl_3 , $\delta 5.32$ ppm.

^bCalculated using equation (4) and data in Table 19.

^cNumber in parentheses after the calculated pseudocontact shift represents the effective variance (see reference 124) in the least significant digit.

Table 26. Observed and Calculated ¹H Shifts for Ho(HBPz₃)₃

Chemical ^a Shift ppm	$(\frac{\Delta\nu}{\nu})_{\text{O}}^{\text{iso}} \text{ obsd}$ ppm	$(\frac{\Delta\nu}{\nu})_{\text{O}}^{\text{pc}} \text{ calc}$ ppm	$(\frac{\Delta\nu}{\nu})_{\text{O}}^{\text{iso}} - (\frac{\Delta\nu}{\nu})_{\text{O}}^{\text{pc}}$ ppm
H(13)	-100.0	-90.0(53)	-17.2
H(43)	-127.6	-114.4(61)	-20.4
H(73)	-37.2	-44.4(60)	-0.4
H(14)	-23.2	-25.5(13)	-3.8
H(44)	-21.0	-21.7(13)	-5.4
H(74)	9.3	6.6(12)	-3.4
H(15)	-28.2	-31.1(15)	-4.3
H(45)	15.9	11.6(12)	-2.9
H(75)	17.6	17.6(13)	-7.2
H(33)	220.5	197.9(62)	16.1
H(63)	58.5	40.0(51)	12.0
H(93)	11.6	4.0(13)	1.1
H(34)	142.9	43.5(11)	-4.5
H(64)	144.3	43.0(11)	-2.6
H(94)	99.1	-4.9(4)	0.1
H(35)	7.9	7.9(16)	-6.5
H(65)	67.0	63.5(19)	-3.0
H(95)	-18.1	-22.5(17)	-2.1
H(1)	-30.0	-41.0(27)	6.5
H(2)	72.4	67.5(25)	0.4
H(3)	-171.0	-120(12)	-56.0

^aShift relative to TMS. Measured with internal standard CHCl₃; δ 5.32 ppm

^bCalculated using equation (4) and data in Table 19.

^cNumber in parentheses after the calculated pseudocontact shift represents the effective variance (see reference 124) in the least significant digit.

Table 27. Observed and Calculated ^1H Shifts for Dy(HBPz_3) $_3$

Chemical ^a Shift ppm	$(\frac{\Delta\nu}{\nu})_{\text{O}}$ iso ^b Obsd ppm	$(\frac{\Delta\nu}{\nu})_{\text{O}}$ pc ^c calc ppm	$(\frac{\Delta\nu}{\nu})_{\text{O}}$ iso - $(\frac{\Delta\nu}{\nu})_{\text{O}}$ pc ppm
H(13)	-183.9	-158.5(96)	-32.6
H(43)	-250.5	-220(12)	-37.3
H(73)	-49.1	-55(12)	-1.1
H(14)	-53.0	-54.0(27)	-5.1
H(44)	-43.9	-41.9(29)	-8.1
H(74)	19.8	19.0(27)	-5.3
H(15)	-72.6	-76.6(30)	-3.2
H(45)	30.5	26.5(22)	-3.2
H(75)	26.3	30.7(23)	-11.6
H(33)	466.9	424(13)	36.4
H(63)	74.5	41(11)	26.6
H(93)	10.9	4.2(15)	0.2
H(34)	192.4	94.5(24)	-6.0
H(64)	185.3	85.1(23)	-3.7
H(94)	88.4	-15.6(8)	0.1
H(35)	10.9	14.3(24)	-9.9
H(65)	136.8	135.7(34)	45.4
H(95)	-59.5	-61.5(26)	-4.5
H(1)	-84.7	-105.2(57)	16.0
H(2)	149.8	146.6(53)	-1.3
H(3)	-438.5	-334(26)	-108.8

^aShift relative to TMS. Measured with internal standard CH_2Cl_2 , δ 5.32 ppm

^bCalculated using equation (4) and data in Table 19.

^cNumber in parentheses after the calculated pseudocontact shift represents the effective variance (see reference 124) in the least significant digit.

Table 28. Magnetic Parameters from Least-Square Refinements of ^1H Isotropic Shifts of $\text{Ln}(\text{HBPz}_3)_3$

Lanthanide	$g_J^2 \frac{J(J+1)}{(2J-1)}$ (2J+3) <J α J>	D_1 $\text{A}^3 \times 10^2$	D_2 $\text{A}^3 \times 10^2$	ϕ deg	R_w %
Yb	39.2	8.8(5)	43.6(9)	-10.1(5)	8.4
Tm	95.3	26.6(13)	131.4(24)	-16.9(5)	7.2
Er	58.8	15.4(11)	82.9(22)	-16.8(7)	10.2
Ho	-71.2	-31.3(20)	-81.5(34)	-11.4(10)	14.4
Dy	-181.0	-55.1(33)	-186(6)	-12.9(8)	11.6

The angle ϕ which describes the orientation of the magnetic axes with respect to the complex is not a constant for the series. In the case of Ln = Yb, Ho, Dy ϕ is -11° while for Ln = Tm, Er it is -17° . The 6° difference is much larger than estimated standard deviation in ϕ which is calculated by the least-squares program to be less than 1° .

The weighted reliability factors R_w from the unrestrained least-squares in which ϕ is refined and the values of R_w from least-squares where ϕ is fixed at -11.0° or -17.0° and not refined are shown in Table 29.

Table 29. Restrained and Unrestrained Least-Squares Refinements ^1H Pseudocontact Shifts.

	R_w % ϕ refined	R_w % $\phi = -11.0^\circ$	R_w % $\phi = -17.0^\circ$
Yb	8.4		24.2
Tm	7.2	22.5	
Er	10.2	22.8	
Ho	14.4		21.9
Dy	11.6		18.3

The results clearly demonstrate that the 6° difference in the values of ϕ for the two sets Tm, Er and Yb, Ho, Dy are real and significant.¹²⁶

The separation of the complexes into two distinct sets depending on the value of ϕ appears at first to be inconsistent with the general results of the least-squares fits and the values of D_1 and D_2 which indicate that the complexes are isostructural. The anomaly can be rationalized if the geometry of the coordination polyhedron is considered. In solution the molecular point symmetry of the complex is C_s . The symmetry of the coordination polyhedron (see Figure 10) formed by the lanthanide and the eight ligating nitrogen atoms is close to C_{2v} . If

the geometry of the polyhedron had rigorous C_{2v} symmetry, the magnetic axes would be fixed by this symmetry point group and ϕ would disappear as a magnetic parameter. The x axis would lie at the intersection of the mirror planes formed by Yb, B(1), B(2), B(3) and Yb, N(12), N(22) and be coincident with the C_2 axis of the coordination polyhedron. The y and z axes would be normal to these mirror planes. In this model ϕ would be -20° (the angle between Yb—B(1) vector and the Yb, N(12), N(22) plane).

The values of D_1 , D_2 and ϕ , which are functions of the crystal field splittings of the lanthanide orbitals, are principally determined by the type of ligating atoms, the metal-ligand bond lengths and the symmetry of the coordination polyhedron. Taking an idealised C_{2v} , BCTP, polyhedron as a starting point, then distortion of this idealised geometry to that observed for $Yb(HBPz_3)_3$ in the solid and solution states requires only small changes in the metal-nitrogen bond lengths and ligand arrangement. These small changes are most probably the cause of the -10° ϕ angle observed for $Yb(HBPz_3)_3$ as opposed to the -20° value expected for the complex if it possessed a coordination polyhedron with C_{2v} point symmetry. The changes are small and subtle and it is not surprising therefore that the thulium and erbium complexes may lie closer to C_{2v} symmetry as evidenced by

the values of ϕ of -16.9° and -16.8° , respectively.

It is difficult to ascribe these small changes in coordination geometry to a simple monotonic change in ionic size of the lanthanide ion in view of the similarities in ϕ angle for the Yb, Ho and Dy complexes. The differences in structure between the Yb, Ho, Dy complexes and those of Tm and Er while producing a significant change in ϕ , do not affect the magnetic susceptibility anisotropies nearly so much. The D_1 terms for all five lanthanides when plotted against $g_J^2 J(J+1)(2J-1)(2J+3) \langle J || \alpha || J \rangle$ fit a single straight line (Figure 19). The D_2 terms also can be fitted to a single straight line (Figure 19), but a slightly better agreement can be found if the two sets of complexes are treated separately (Figure 20).

Examination of Tables 21, 24, 25, 26 and 27 reveal that the differences between observed isotropic and calculated pseudocontact shifts increases as the values of D_1 and D_2 increase. Particularly in error are the shifts predicted for H(13), H(43), H(33), H(63) and H(3). The discrepancies for the latter nucleus being apparently quite gross, at 38, -56 and -109 ppm for the thulium holmium and dysprosium complexes, respectively. However, at the same time it should be noted that the effective variances¹²⁴ for this nucleus are also large.

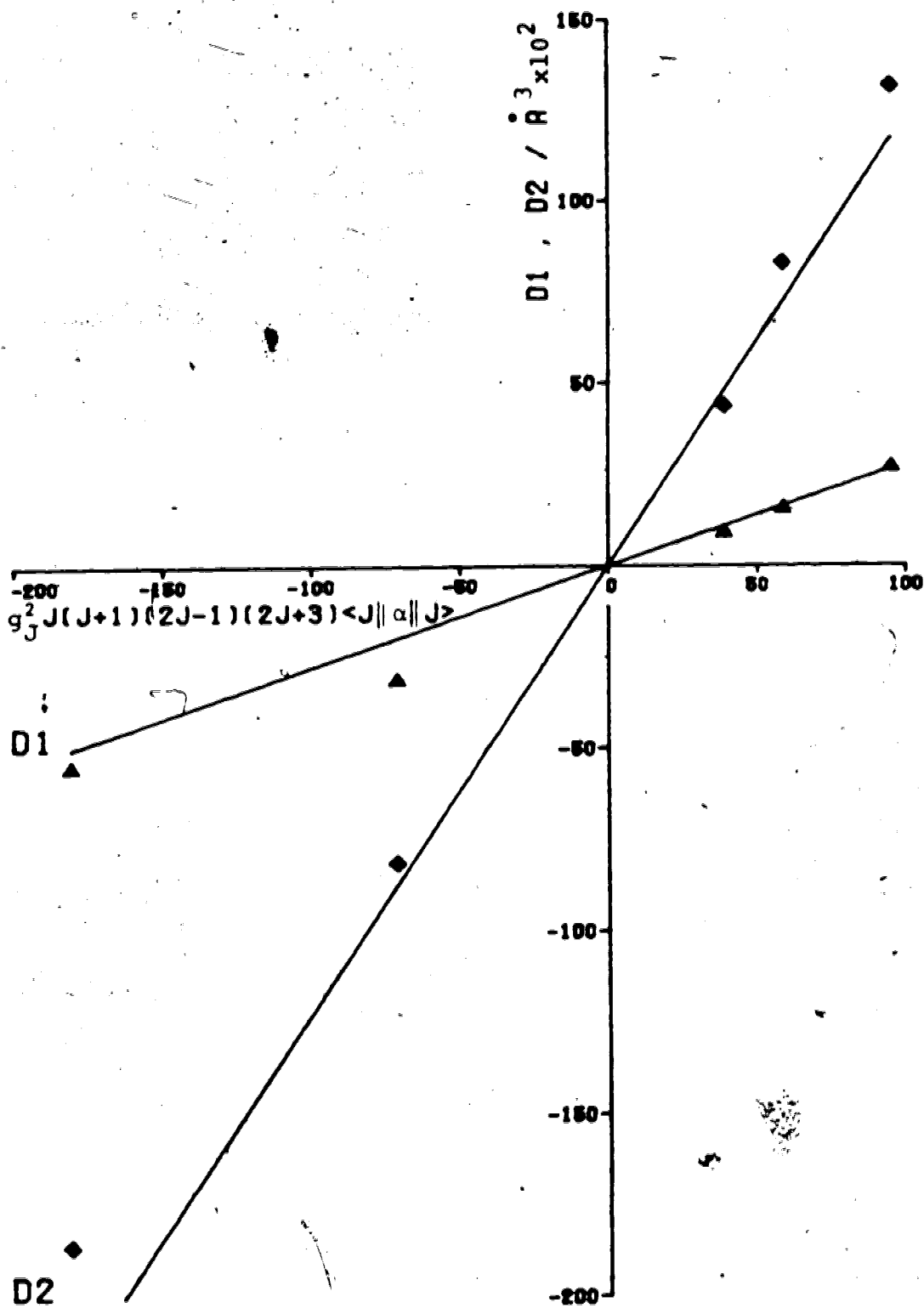


FIGURE 19. Plot of Observed vs. Theoretical Magnetic Susceptibility Anisotropies, D_1 and D_2 .

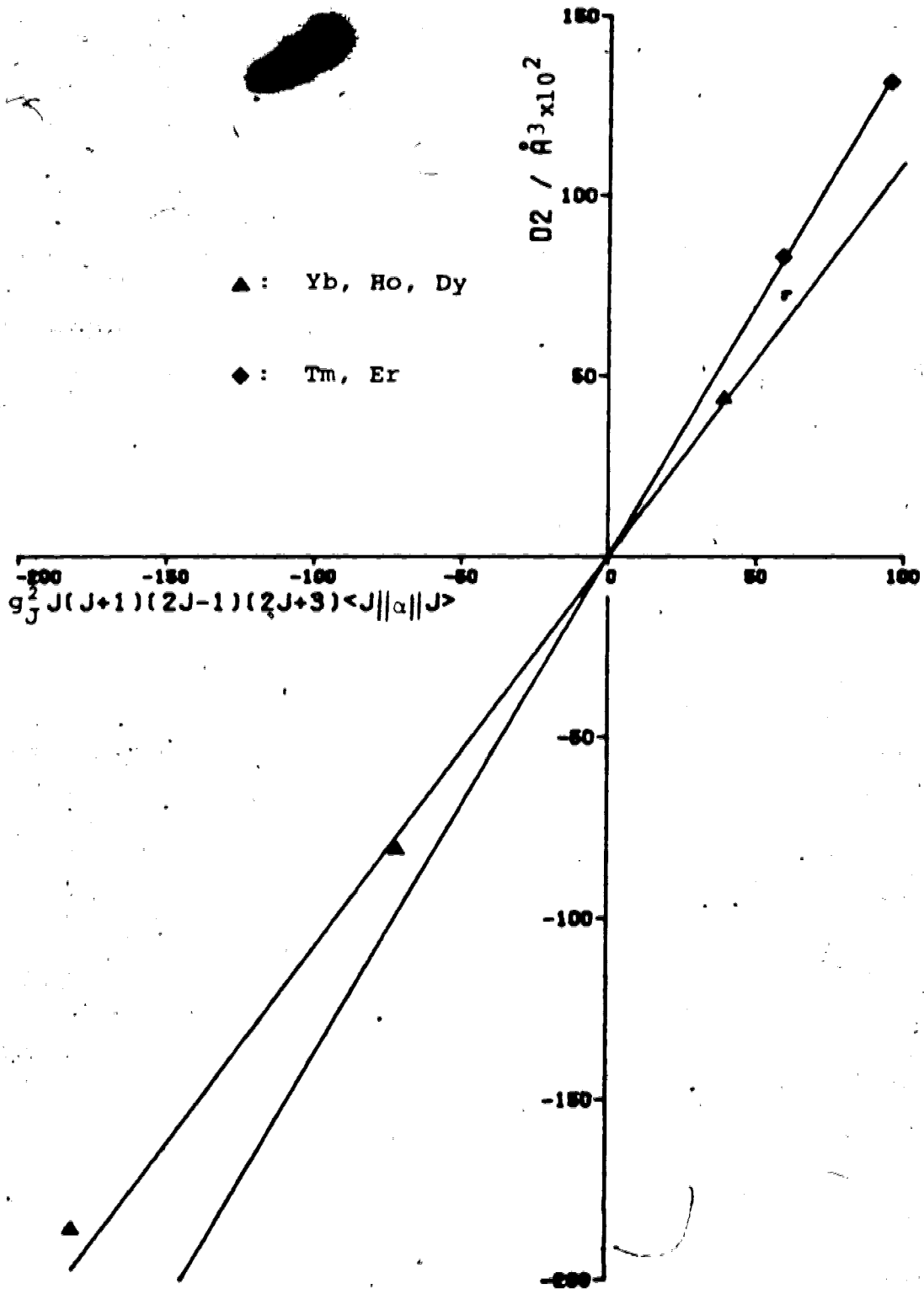


FIGURE 20. Plot of Observed vs. Theoretical Magnetic Susceptibility Anisotropies, D_2 .

It might be tempting, following common practice to ascribe the differences to contact contributions. That this is not the case can be seen from the following considerations. The discrepancies systematically change sign with a change in sign of D_1 and D_2 . This can be verified, for instance, by comparing the thulium and dysprosium data. However, the values of the contact shift parameter, $g_J(g_J-1)J(J+1)$, listed in Table 16 show that a contact shift would have the same sign for all the lanthanides in the series Dy-Yb. Furthermore, it is clear that a contact shift in the erbium complex should be greater than in the corresponding isostructural thulium complex.

The differences between observed and calculated shifts may thus be ascribed with some degree of certainty to errors in the geometrical model rather than to the presence of ^1H contact shifts. It is gratifying to see that the largest differences are associated with those shifts with large effective variances in the calculated dipolar shift.

In conclusion it is quite clear that the ^1H isotropic shifts in the series of complexes Dy-Yb are dominated by the pseudocontact effect and that contact shifts, are but a minor component of the large induced shifts.

The differences between observed and calculated chemical shifts clearly invites the search for a better

geometrical model. The fitting of an improved geometrical model to the observed shifts has not been carried out in the present investigation but it is obviously a worthwhile goal for future research on these complexes.

^{13}C and ^{11}B Spectra of $\text{Ln}(\text{HBPz}_3)_3$, $\text{Ln} = \text{Tm, Er, Ho, Dy}$.

The ^{13}C NMR spectra of $\text{Tm}(\text{HBPz}_3)_3$ and $\text{Er}(\text{HBPz}_3)_3$ are shown in Figure 21 and Figure 22, respectively. The ^{13}C pseudocontact shifts can be calculated using the geometrical variables from the $\text{Yb}(\text{HBPz}_3)_3$ solid state structure and the magnetic parameters derived from the proton isotropic shifts (Table 28). The results of these calculations for the Tm, Er, Ho and Dy complexes are given in Tables 30, 31, 32 and 33. The observed isotropic shifts are again calculated from the $\text{Lu}(\text{HBPz}_3)_3$ ^{13}C shifts. The differences between observed and calculated shifts are given in Table 34 and represent the values of possible contact shifts. However, it is important at this point to note that the difference between the observed and calculated shifts may be accounted for in some cases by errors in the geometrical model as was found for the nuclei H(13), H(43), H(33), H(63) and H(3) in the analysis of the ^1H spectra.

Initial inspection shows that the carbons of the free pyrazolyl group C(93), C(94) and C(95), which are at least 5 bonds distant from the metal, have negligible contact shifts. The difference between observed and calculated shifts are never greater than the effective variance of the calculated dipolar shift. On the other hand, the carbon nuclei at the 4 and 5 positions of the

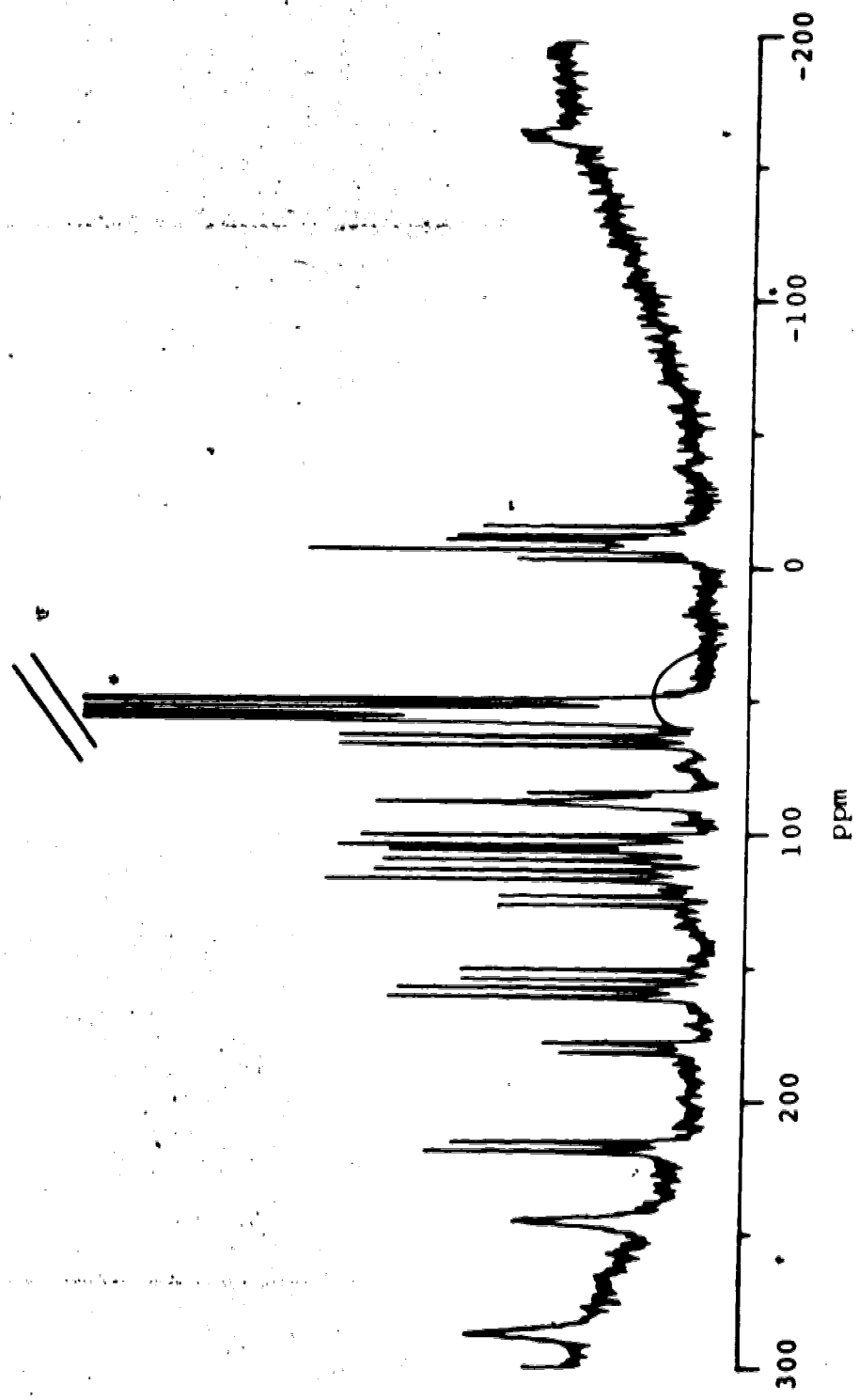


FIGURE 21. 50.33 MHz ¹³C NMR Spectrum of Tm(HBPz₃)₃. *CH₂Cl₂ solvent.

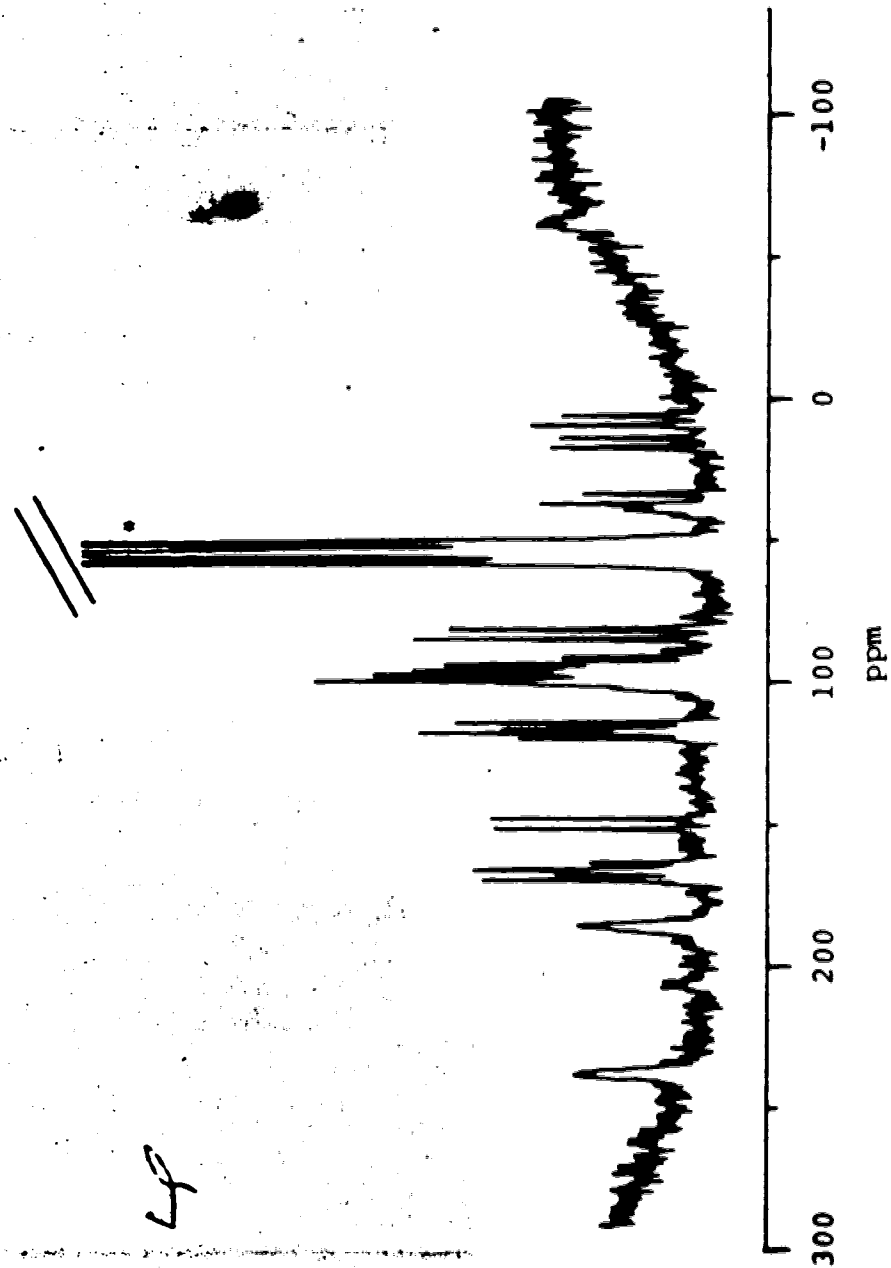


FIGURE 22. 50.33 MHz ¹³C NMR Spectrum of Er(HBPz)₃. *CH₂Cl₂ solvent.

Table 30. Observed Isotropic and Calculated Pseudocontact ^{13}C and ^{11}B Shifts for $\text{Tm}(\text{HBPz}_3)_3$.

Chemical ^a Shift ppm	$(\frac{\Delta\nu}{\nu})_{\text{O}}^{\text{b}}$ iso ^b Obsd ppm	$(\frac{\Delta\nu}{\nu})_{\text{O}}$ pc calc ppm	$(\frac{\Delta\nu}{\nu})_{\text{O}}^{\text{b}}$ iso - $(\frac{\Delta\nu}{\nu})_{\text{O}}$ pc ppm
C(13)	287.0	149.1(72)	-0.8
C(43)	244.7	119.7(76)	-13.7
C(73)	87.9	-51.3(74)	0.5
C(14)	158.7	73.8(16)	-20.0
C(44)	114.9	26.9(24)	-16.9
C(74)	65.0	-27.7(22)	-12.2
C(15)	216.9	99.0(49)	-20.8
C(45)	102.2	-23.6(56)	-12.9
C(75)	107.6	-21.1(56)	-10.0
C(33)	-161.7	-300.7(53)	1.6
C(63)	-9.4	-137.7(53)	-9.1
C(93)	151.8	8.5(48)	5.9
C(34)	-13.9	-105.0(10)	-12.8
C(64)	-5.0	-97.5(10)	-11.4
C(94)	124.5	19.5(5)	1.1
C(35)	86.1	-48.0(49)	-3.3
C(65)	-8.6	-146.8(49)	0.8
C(95)	179.5	41.4(48)	0.7
B(1)	161.1	178.6(25)	-13.4
B(2)	-263.1	-251.7(24)	-7.3
B(3)	120.1	101.7(32)	22.5

^a Shifts in ppm relative to TMS or BF_3OEt_2 . ^{13}C shifts measured with internal standard CH_2Cl_2 ; $\delta_{53.8}$ ppm.

^b Calculated using equation (4) and data in Table 19.

Table 31. Observed Isotropic and Calculated Pseudocontact ¹³C and ¹¹B Shifts for Et(HBPz)₃.

Chemical ^a Shift ppm	$(\frac{\Delta\nu}{\nu})_{\text{iso}}^{\text{b}}$ ppm	$(\frac{\Delta\nu}{\nu})_{\text{pc}}^{\text{calc}}$ ppm	$(\frac{\Delta\nu}{\nu})_{\text{iso}} - (\frac{\Delta\nu}{\nu})_{\text{pc}}$ ppm
C(13)	237.5	90.6(59)	8.2
C(43)	185.0	73.0(61)	-26.7
C(73)	99.0	-35.4(60)	-4.3
C(14)	115.5	45.8(10)	-35.2
C(44)	82.6	16.5(15)	-38.8
C(74)	54.9	-18.2(14)	-31.8
C(15)	166.8	62.9(48)	-34.8
C(45)	94.8	-14.2(51)	-29.7
C(75)	97.1	-13.2(51)	-28.4
C(33)	-62.1	-186.7(50)	-12.8
C(63)	38.2	-84.5(50)	-14.7
C(93)	149.0	5.7(48)	5.9
C(34)	7.1	-64.8(7)	-32.0
C(64)	15.0	-60.5(7)	-28.4
C(94)	117.6	12.6(5)	1.1
C(35)	92.4	-28.7(48)	-16.3
C(65)	34.8	-91.4(48)	-11.2
C(95)	164.5	26.7(48)	0.4
B(1)	96.3	116.2(18)	-15.8
B(2)	-166.1	-155.4(17)	-6.6
B(3)	96.3	66.8(21)	33.6

^a Shifts in ppm relative to TMS or BF₃OEt₂. ¹³C shifts measured with internal standard CH₂Cl₂ δ53.0 ppm.

^b Calculated using equation (4) and data in Table 19.

Table 32. Observed Isotropic and Calculated Pseudocontact ¹³C and ¹¹B Shifts for Ho(HBPz₃)₃.

Chemical ^a Shift ppm	($\frac{\Delta\nu}{\nu}$) iso ^b obsd ppm	($\frac{\Delta\nu}{\nu}$) pc calc, ppm	($\frac{\Delta\nu}{\nu}$) iso - ($\frac{\Delta\nu}{\nu}$) pc ppm
C(13)	42.4	-118.3 (64)	22.0
C(43)	-6.1	-113.2 (64)	-31.6
C(73)	154.9	10.1 (64)	6.1
C(14)	9.6	-48.5 (13)	-46.8
C(44)	15.4	-30.5 (15)	-59.0
C(74)	73.9	17.4 (14)	-48.4
C(15)	45.5	-55.3 (49)	-37.9
C(45)	99.6	6.6 (51)	-45.7
C(75)	122.2	29.3 (51)	-45.8
C(33)	303.5	200.3 (50)	-34.2
C(63)	271.5	151.7 (50)	-17.6
C(93)	144.2	2.9 (48)	3.9
C(34)	116.4	67.3 (7)	-54.8
C(64)	139.6	85.5 (7)	-49.8
C(94)	99.0	-4.8 (5)	-0.1
C(35)	133.9	29.1 (48)	-32.6
C(65)	217.9	109.8 (48)	-29.3
C(95)	121.6	-13.8 (48)	-2.0
B(1)	-106.9	-94.9 (18)	-7.9
B(2)	140.8	161.6 (17)	-16.7
B(3)	28.6	2.3 (22)	30.4

^a Shifts in ppm relative to TMS or BF₃OEt₂. ¹³C shifts measured with internal standard CH₂Cl₂; 653.8 ppm.

^b Calculated using equation (4) and data in Table 19.

Table 33. Observed Isotropic and Calculated Pseudocontact ^{13}C and ^{11}B Shifts for $\text{Dy}(\text{HBPz})_3$.

Chemical ^a Shift ppm	$(\frac{\Delta\nu}{\nu})_{\text{O}}^{\text{iso}}$ ^b Obsd ppm	$(\frac{\Delta\nu}{\nu})_{\text{O}}^{\text{pc}}$ ^c Calc ppm	$(\frac{\Delta\nu}{\nu})_{\text{O}}^{\text{iso}} - (\frac{\Delta\nu}{\nu})_{\text{O}}^{\text{pc}}$ ppm
C(13)	-C	-237(10)	-C
C(43)	-	-220(10)	-
C(73)	-	51.6(96)	-
C(14)	-69.8	-105.9(26)	-68.8
C(44)	-37.0	-58.1(33)	-83.8
C(74)	76.5	42.9(30)	-71.3
C(15)	-44.2	-132.5(50)	-50.4
C(45)	93.7	18.1(63)	-63.1
C(75)	130.2	55.0(63)	-63.5
C(33)	533.0	435.0(58)	-39.4
C(63)	417.0	289.5(58)	-9.9
C(93)	139.2	-0.5(48)	2.3
C(34)	177.6	146.2(13)	-72.5
C(64)	208.1	173.4(13)	-69.2
C(94)	84.8	-17.6(6)	-1.5
C(35)	152.2	60.0(50)	-45.2
C(65)	328.0	232.5(49)	-41.9
C(95)	90.1	-42.6(48)	-4.7
B(1)	-240.6	-243.2(35)	6.7
B(2)	322.9	351.0(33)	-24.0
B(3)	-26.5	-52.5(45)	30.1

^aShifts in ppm relative to TMS or BF_3OEt_2 . ^{13}C shifts measured with internal standard CH_2Cl_2 ; 653.8 ppm.

^bCalculated using equation (4) and data in Table 19.

^cResonances due to C(13), C(43) and C(73) could not be identified in the spectrum.

Table 34. Differences Between Observed Isotropic and Calculated Pseudocontact. ^{13}C and ^{11}B Shifts for $\text{Ln}(\text{HBPz}_3)_3$ Ln = Yb, Tm, Er, Ho, Dy - Possible Contact Shifts.

	Yb	Tm	Er	Ho	Dy	A/h ^b
$9_J(9_J-1)J(J+1)$	2.6	8.2	15.3	22.5	28.3	
C(14)	-5.2	-20.0	-35.2	-46.8	-68.8	-3.2(1)
C(44)	-4.7	-16.9	-38.8	-59.0	-83.8	-3.7(2)
C(74)	-0.6	-12.2	-31.8	-48.4	-71.3	-3.1(2)
C(15)	-5.2	-20.8	-34.8	-37.9	-50.4	-2.7(2)
C(45)	-3.0	-13.0	-29.7	-45.7	-63.1	-3.0(1)
C(75)	-0.6	-10.0	-28.4	-45.8	-63.5	-2.9(2)
C(34)	-2.2	-12.8	-32.0	-54.8	-72.5	-3.3(2)
C(64)	-1.4	-11.4	-28.4	-49.8	-69.2	-3.1(2)
C(35)	-1.5	-3.3	-16.3	-32.6	-45.2	-2.0(2)
C(65)	3.2	0.8	-11.2	-29.3	-42.0	-1.8(3)
C(93)	5.2	5.9	5.9	3.9	2.3	
C(94)	0.9	1.1	1.1	-0.1	-1.5	
C(95)	0.5	0.7	0.4	-2.0	-4.7	
C(13)	2.7	-0.8	8.2	22.0	-	
C(43)	-1.8	-13.7	-26.7	-31.6	-	
C(73)	6.4	0.5	-4.3	6.1	-	
C(33)	6.7	1.6	-12.8	-34.2	-39.4	
C(63)	0.9	-9.1	-14.7	-17.6	-9.9	
B(1)	-7.5	-13.4	-15.8	-7.9	6.7	
B(2)	0.8	-7.3	-6.6	-16.7	-24.0	
B(3)	7.9	22.5	33.6	30.4	30.1	

^aShifts in ppm. ^bA/h, coupling constant in units of 1×10^4 Hz.

pyrazolyl groups coordinated to the metal clearly have upfield contact shifts.

The magnitude of the contact shifts observed for the 4 and 5 positions correlate with the values of $g_J(g_J-1)J(J+1)$. This is shown graphically in Figure 23 and Figure 24. The straight line behaviour confirms that the hyperfine coupling constants, A/h , are independent of the lanthanide ion. The values of A/h calculated using equation (5) are given in Table 34. They are of the same order of magnitude, $\sim 10^4$ Hz, as those found for the ^{13}C nuclei in the $[\text{Ln}(\text{dpa})_3]^{3-}$ complexes¹¹³ and much smaller than -1.15 MHz, the coupling constant for the ^{13}C nuclei of the C_5H_5 groups in $(\text{C}_5\text{H}_5)_3\text{EuCNC}_6\text{H}_{11}$.¹²⁷ However, the carbon atoms in this complex are directly bonded to the metal. Large two bond couplings have been observed in $[\text{Ln}\{\text{S}_2\text{P}(\text{OEt})_2\}_4]^-$ complexes (^{31}P -lanthanide coupling constant is 1.52 MHz for the early, Ce-Dy, and 0.86 MHz for the late, Ho-Yb, lanthanides) and were attributed to the enhanced Ln-S bonding in these complexes.⁹

The small values of the coupling constant in the present complexes indicate that as with most lanthanide compounds, the bonding is mostly ionic with very little covalent character. The observed upfield contact shifts nevertheless reveal that there is negative spin density on the 4-C and 5-C nuclei of the pyrazolyl group. The

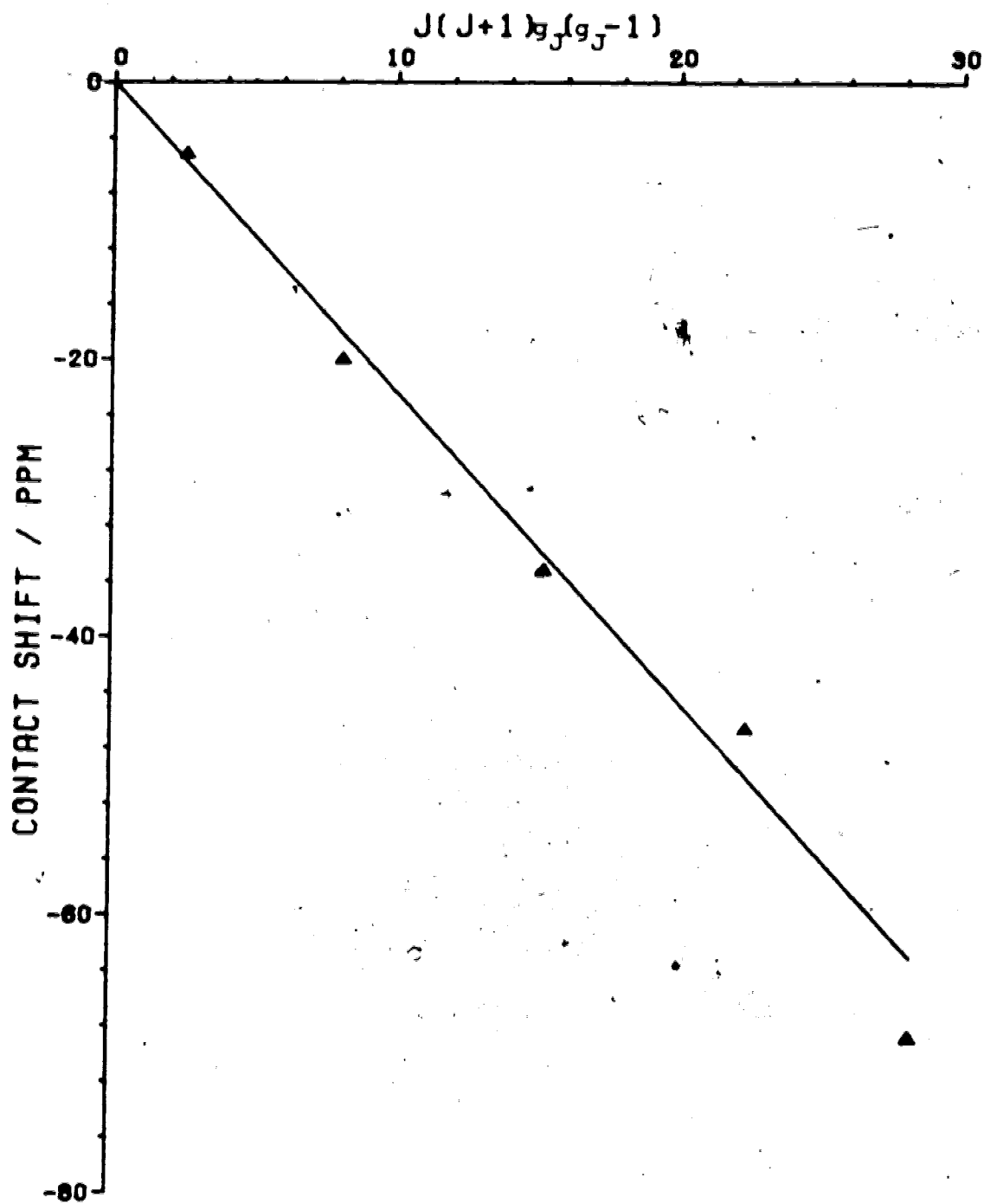


FIGURE 23. Plot of Observed Contact Shift vs.
 $g_J(g_J-1)J(J+1)$ for C(14) of $\text{Ln}(\text{HBPz}_3)_3$.

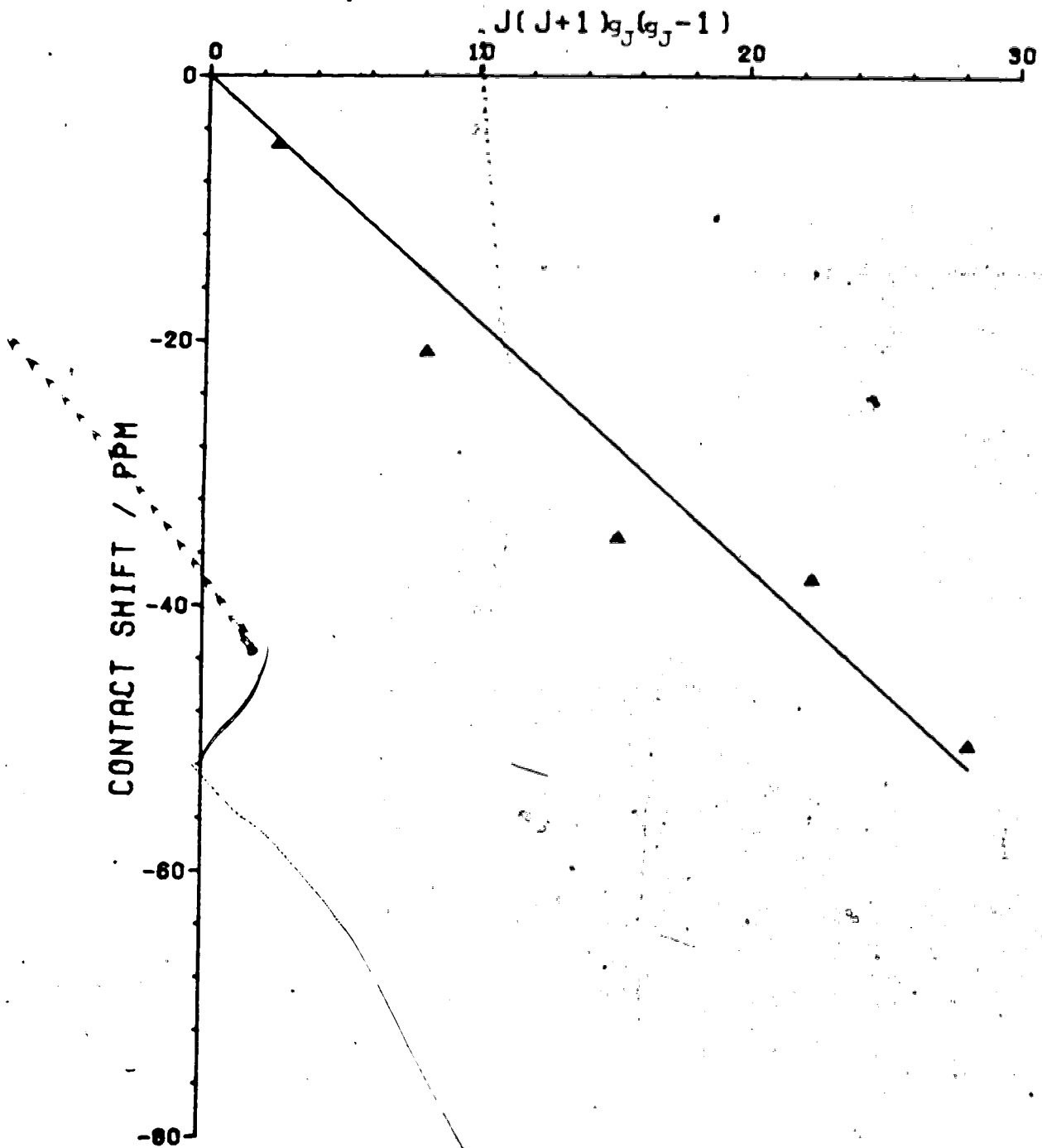


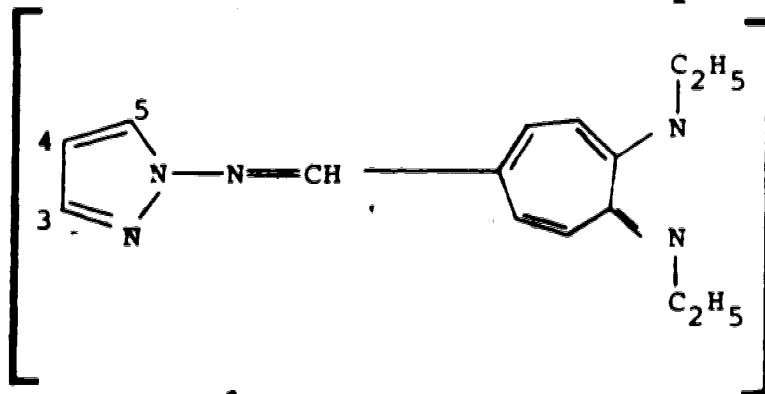
FIGURE 24. Plot of Observed Contact Shift vs.
 $g_J(g_J-1)J(J+1)$ for C(15) of $\text{Ln}(\text{HBPz}_3)_3$.

4f electrons of the lanthanide ion may produce spin density on the ligand by either direct transfer of an electron from ligand to metal or vice-versa, or by the spin polarization mechanism of Watson and Freeman.⁸¹ For the lanthanide ions with the electronic configurations $4f^n > 4f^7$ the former mechanism will result in positive spin density on the ligating atom while the latter will produce negative spin. The view that the spin polarization mechanism is operative in lanthanide complexes is confirmed by the signs of the coupling constants which are observed for the ^{14}N , ^{17}O ⁸⁰ and ^{13}C ¹²⁷ nuclei bonded directly to the metal.

There are several mechanisms¹²⁸⁻¹³⁰ that can account for the delocalization of spin density on the ligand. It is not our intention here to rationalize the observed shifts in terms of one particular mechanism but rather we shall confine the discussion to the important features of the results listed in Table 34.

It is noteworthy that there is no sign change in the coupling constant for the 4-C and 5-C nuclei. Successive sign inversions have been observed in the $\text{Ln}(\text{dpm})_3$ shift reagent studies of borneol, isoborneol, norbornylamine,¹³¹ isoquinoline¹³² and norbornenol,¹³² and the $[\text{Ln}(\text{dpa})_3]^{3-}$ complexes.¹¹³ However, Jesson⁸⁵ has observed that the 3-H, 4-H and 5-H protons in $\text{Co}(\text{HBPz}_3)_2$ all have the same

sign for A/h. Eaton et al.¹³³ have found that in the Ni(II) aminotroponeimineate complex, NiL_2 , where L is:



the protons in the 3, 4 and 5 positions of the pyrazolyl moiety similarly have the same sign for the nuclear hyperfine coupling constant. It appears that the compounds of the present study follow the same trend as established by other complexes containing the pyrazolyl moiety.

Several studies have noted that the ^{13}C contact shifts are attenuated with the number of bonds between the metal and the NMR nucleus.^{131,132} However, this is not always the case.¹³⁴

Perhaps surprisingly in the $Ln(HBPz_3)_3$ case the differences between observed isotropic and calculated pseudo-contact shifts for 3-carbons are in general much smaller than for 4-C and 5-C. The differences do not follow an obvious dependence on $g_J(g_J-1)J(J+1)$. It is most probable that the contact shifts here are small and that the major part of the differences in Table 34 are due to errors in the geometrical model which are expected to be large

for the 3-carbons as was found in the case of the 3-hydrogens. We have no rationale for the lack of a readily detectable contact shift for the 3-carbons except to note that in $[\text{Ln}(\text{dpa})_3]^{3-}$ complexes it is also the carbon atom immediately adjacent to the coordinated nitrogen which has the smallest contact shift.¹¹³

The ^{11}B data in Table 34, like the 3-C show smaller differences than 4-C and 5-C.

The differences listed in Table 34 for ^{11}B nuclei are considerably larger than the effective variances (see Tables 30 to 33). However, the direction of the possible contact shifts is different for B(2) and B(3) while those for B(1) are much smaller and most probably can be assigned to errors in the geometrical model. We can find no easy explanation for these observations.

Detection and Characterization of a Second Isomer of
 $\text{Ln}(\text{HBPz}_3)_3$ Ln = Er, Ho, Dy.

The ^1H NMR spectrum of $\text{Ho}(\text{HBPz}_3)_3$ in CD_2Cl_2 over the range $\delta 250$ to -200 ppm is shown in Figure 25. Figure 26 shows the spectrum in the region $\delta 25$ to -25 ppm. The spectrum has six extra resonances, three of relative intensity one at $\delta 35.0$, $\delta 21.4$ and $\delta 19.8$ ppm and three of relative intensity two at $\delta 10.1$, $\delta -10.5$ and $\delta -109.0$ ppm. These resonances do not arise from the major species in

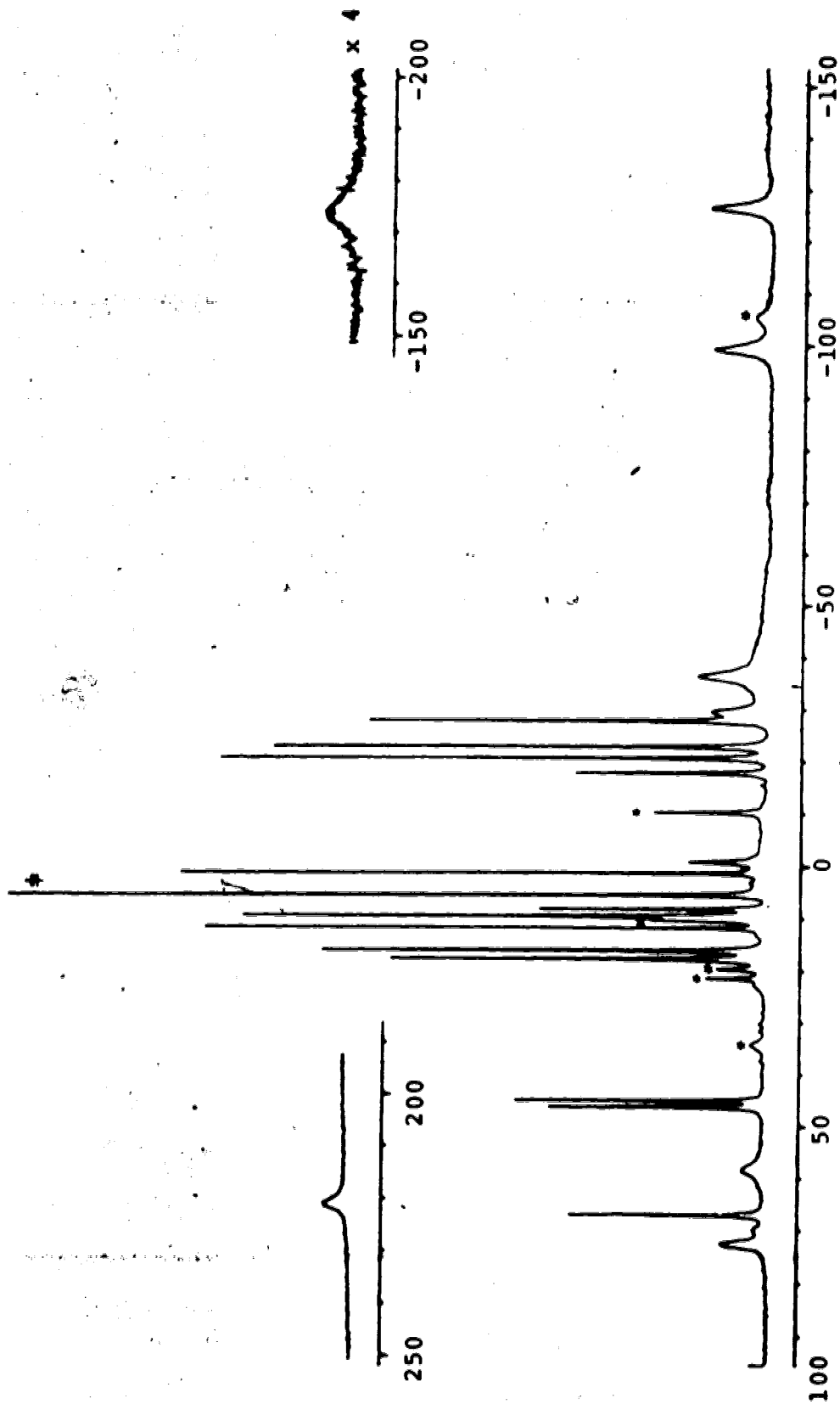


FIGURE 25. 200 MHz ${}^1\text{H}$ NMR Spectrum $\text{Ho}(\text{HBPz})_3$ ($\delta 250$ to -200 ppm). Signals arising from second isomer labelled with *. † Solvent CH_2Cl_2 .

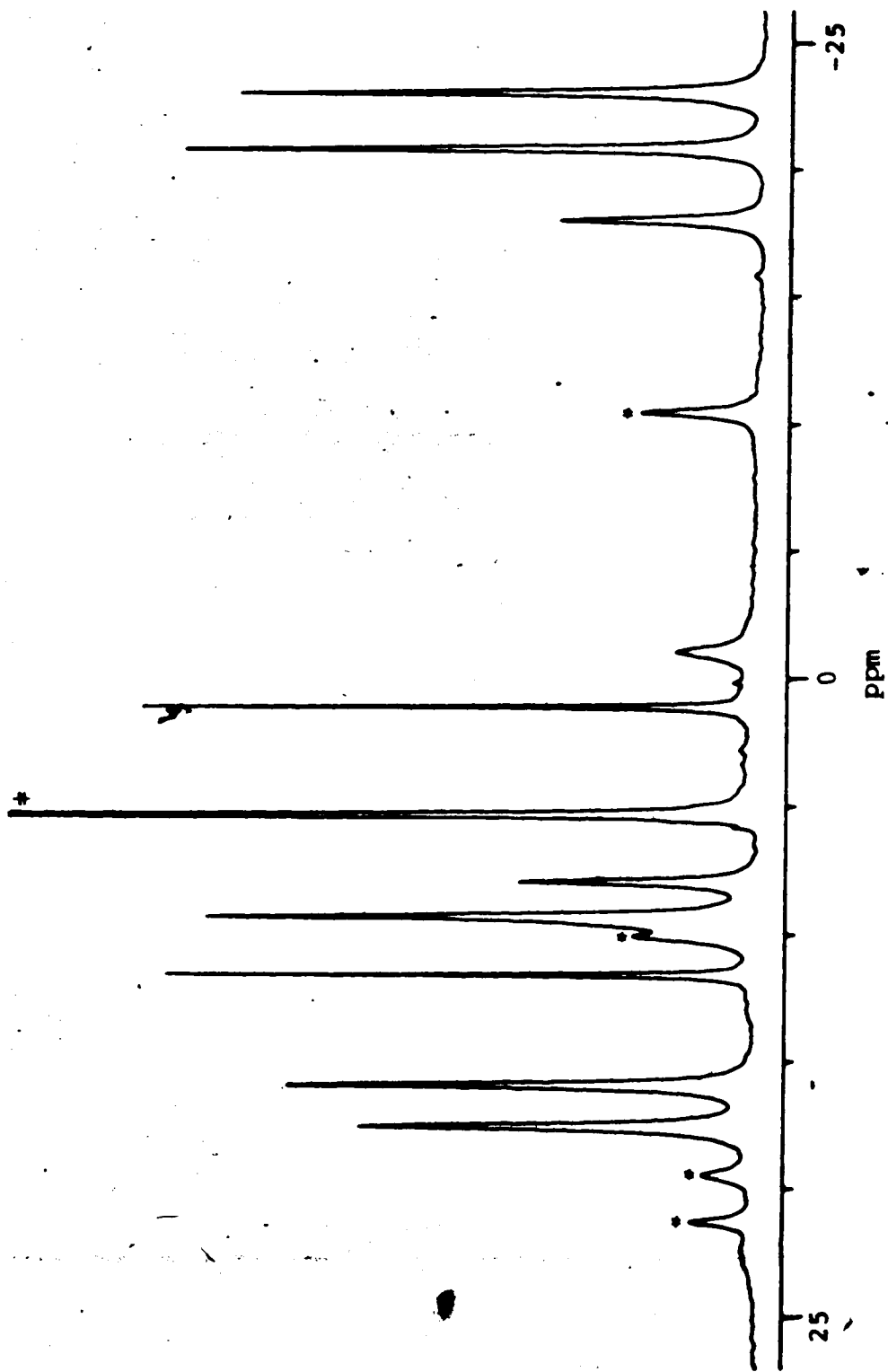


FIGURE 26. 200 MHz ^1H NMR Spectrum $\text{Ho}(\text{HBPz}_3)_3$ (δ 25 to $-\delta$ 25 ppm). Signals arising from second isomer labelled with *. \dagger Solvent CH_2Cl_2 .

the sample, the $\text{Ho}(\text{HBPz}_3)_3$ complex with bicapped trigonal prismatic geometry. Similar patterns of resonances are also found in the $\text{Er}(\text{HBPz}_3)_3$ and $\text{Dy}(\text{HBPz}_3)_3$ ^1H NMR spectra. Seven extra resonances are observed in the spectrum of the dysprosium complex while only four resonances can be seen in the erbium spectrum. Both the Ho and Dy ^{11}B spectra have an additional resonance. The crude products and samples recrystallized from $\text{CH}_2\text{Cl}_2/\text{hexane}$, THF/hexane and toluene showed no difference in the relative amounts of the two species in solution. This indicates that the extra resonances do not arise from impurity or decomposition product. Changing the temperature of the NMR probe changes the intensity ratio of the signals arising from the two species. Variable temperature NMR studies between 25° and -60°C suggest that there is a slow equilibrium between two isomers of $\text{Ln}(\text{HBPz}_3)_3$ ($\text{Ln} = \text{Er}, \text{Ho}$ and Dy). One of these isomers has the BCTP structure of which $\text{Yb}(\text{HBPz}_3)_3$ is prototypical. The equilibrium constants are also solvent dependent, the second isomer being almost undetectable in THF-d_8 and toluene-d_8 at room temperature.

The chemical shifts and relative integrations of these additional peaks are listed in Table 35. The almost constant ratio between the shifts in the different spectra suggests that the complexes are isostructural and that only the shifting characteristics of the lanthanide

Table 35. ^1H Chemical Shifts and Isotropic Shifts for Second Isomer Ln(HBPz₃)₃
Ln = Er, Ho, Dy.^a

Assignment and Relative Intensity	Chemical Shift ^b			$(\frac{\Delta\nu}{\nu_0})_{\text{iso}}$			Normalised Isotropic Shift ^c			$\frac{(\frac{\Delta\nu}{\nu_0})_{\text{Dy}}}{r^3} \frac{3\cos^2\theta-1}{r^3}$ ^d	$\frac{(\frac{\Delta\nu}{\nu_0})_{\text{Ho}}}{A^3} \times 10^{-2}$ ^e	$\frac{D_1}{A} \times 10^2$
	Er	Ho	Dy	Ho	Dy	Ho	Dy	Ho	Dy			
H3A (2)	-	-109.0	-198.8	-116.2	-206.0	-100	-100	1.77	2.74	1.77	2.74	-75.2
H4A (2)	14.5	-10.5	-22.5	-16.6	-28.6	-14.3	-13.9	1.72	0.35	1.72	0.35	-81.7
H5A (2)	-4.2	10.1	15.4	2.9	8.2	2.5	4.0	2.83	-0.28	2.83	-0.28	-29.3
H3E (1)	-	-	123.5	-	117.0	-	56.8	-	-1.84	-	-1.84	-63.6
H4E (1)	-16.5 ^e	19.8	32.2	13.9	26.3	12.0	12.8	1.89	-0.52	1.89	-0.52	-50.6
H5E (1)	-20.8 ^e	21.4	35.5	14.9	29.0	12.8	14.1	1.95	-0.56	1.95	-0.56	-51.8
BH (1)	-	35.0	58.3	30.5	53.8	26.2	26.1	1.76	-0.91	1.76	-0.91	-59.1
B	-	45.2	92.9	49.3	97.0	42.4 ^e	47.1	1.96	-2.15	1.96	-2.15	-45.1

^a Shifts in ppm. ^b Relative to TMS. ^c Normalised to $(\Delta\nu/\nu_0)_{\text{iso}}$ H3A = -100 ppm.

^d Calculated using equation (8).

^e Resonances detected at -40°C. Reported shifts are at this temperature.

ion changes.

The pattern of the resonances and relative integrations of the seven ^1H and one ^{11}B signals for $\text{Dy}(\text{HBPz}_3)_3$ on initial inspection suggest that the species possesses a rigid nine coordinate tricapped trigonal prismatic, TCTP, geometry.^{39,41} Such a structure would be axially symmetric with three equivalent capping pyrazolyl groups and six equivalent pyrazolyl groups coordinating at the apices of the prism and would be in accord with the spectral observations. There are however two principal reasons for believing that the complex is almost certainly not a nine coordinate species with C_{3h} symmetry but an eight coordinate complex which must then undergo rapid intramolecular rearrangement to give the experimental ^1H NMR spectra. First, the shifts calculated for the axially symmetric TCTP structure do not fit the observed isotropic shifts. The geometric factors, $(3\cos^2\theta - 1)/r^3$, are given in Table 35. They are calculated by assuming that the appropriate average values of the tridentate ligands in the $\text{Yb}(\text{HBPz}_3)_3$ BCTP structure would give a reasonable approximation for an axially symmetric TCTP arrangement.

The values of D_1 , calculated from these geometric factors and the observed isotropic shifts using equation (8) are listed in Table 35. The value of D_1 is not

constant for all the protons as would be expected for the axially symmetric TCTP structure. Second, although the rectangular face of the BCTP of the $\text{Yb}(\text{HBPz}_3)_3$ structure may be described as being uncapped, one implication of such a statement is that there is almost enough room to accommodate the ninth coordinating ligand. This is not the case, and use of molecular models and ORTEP⁵⁴ plots show that changing the configuration at the boron atom of the bidentate ligand B(3) by switching H(3) and the uncoordinated pyrazolyl ring in order to allow N(92) to coordinate to the lanthanide ion results in a very unfavourable nonbonded interaction between H(93) and B(2). Therefore, on the basis of the observed isotropic shifts and steric considerations the nine coordinate TCTP must be rejected as a possible structure for the second $\text{Ln}(\text{HBPz}_3)_3$ species in solution.

The second isomer is most probably eight coordinate and is undergoing an intramolecular exchange process which averages the pyrazolyl rings in exclusive sets of three and six.

A possible structural model is shown in Figure 27. The structure has bicapped trigonal prismatic geometry and is designated BCTP(2), to distinguish it from the $\text{Yb}(\text{HBPz}_3)_3$ type structure which will henceforward be called BCTP(1). Indeed, BCTP(2) is conceived from BCTP(1)

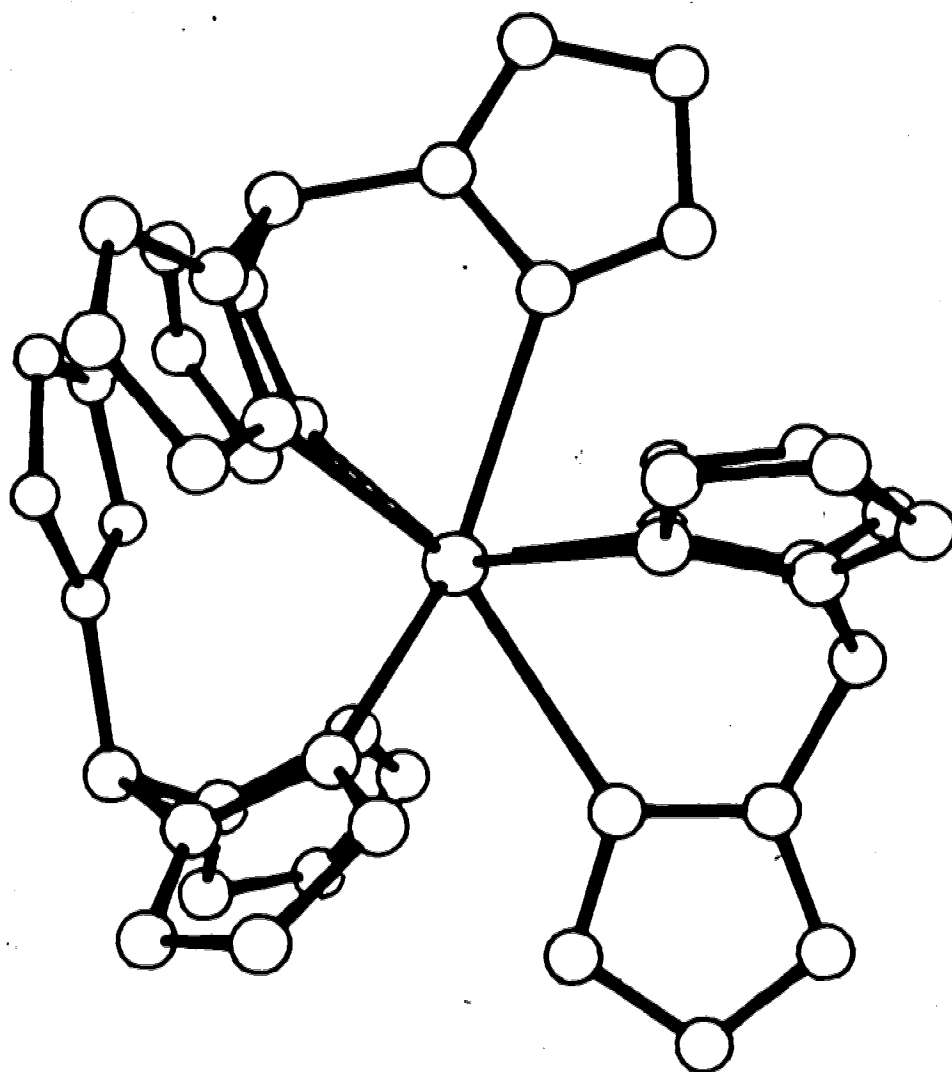
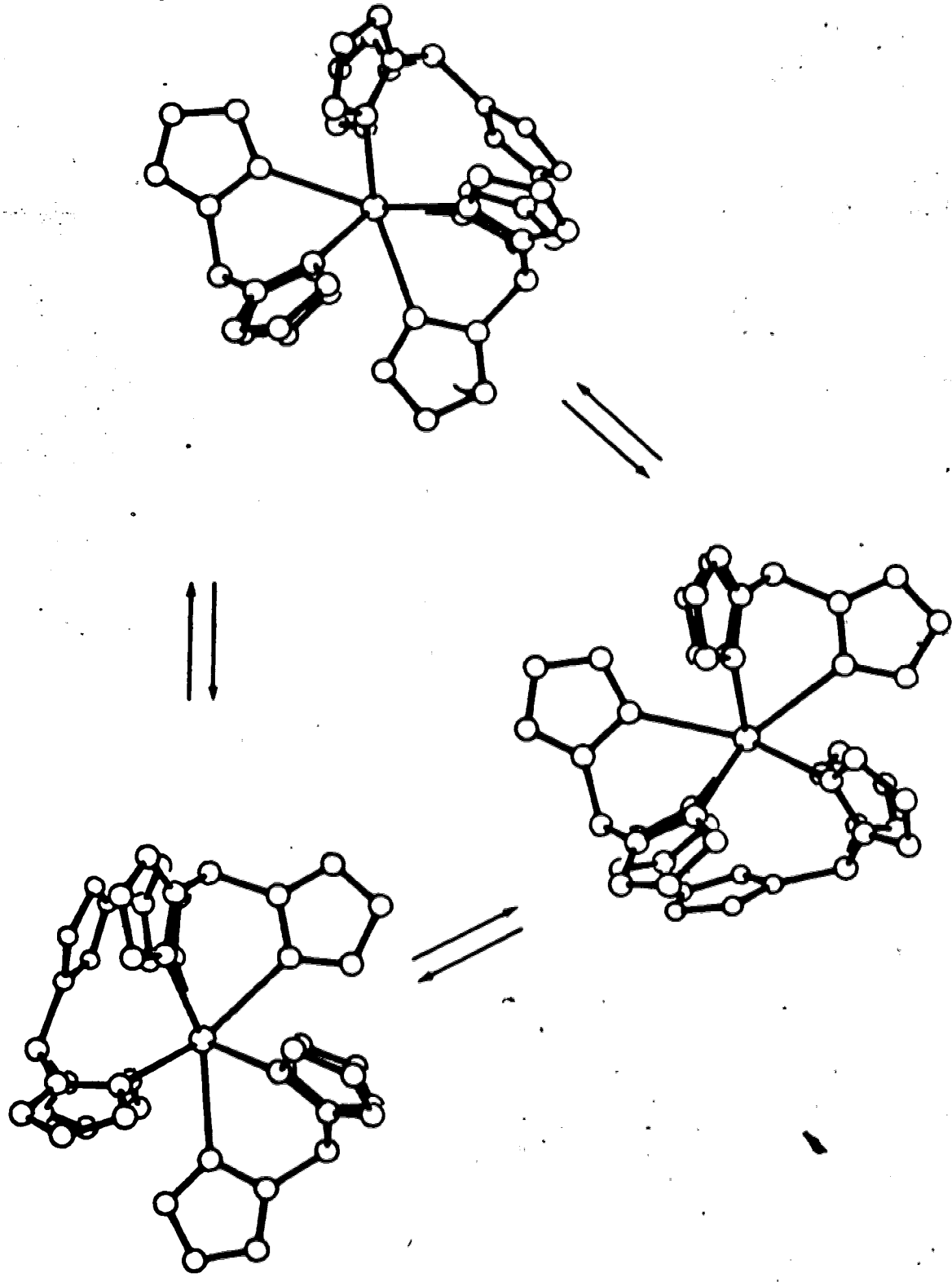


FIGURE 27. BCTP(2) Structural Model for Second Isomer of $\text{Ln}(\text{HBPz}_3)_3$ with Bicapped Trigonal Prismatic Geometry.

but differs from it in that the uncoordinated pyrazolyl group is now over the uncapped rectangular face and is rotated such that the plane of the ring is perpendicular to the equatorial plane containing the metal and the boron atoms. The exchange process in this structure would involve the rotation of the free pyrazolyl ring to coordinate to the lanthanide concomitant with the rotation of the next pyrazolyl group away from the metal to become the uncoordinated moiety. The process is shown in Scheme 2 and separately averages the six groups at the apices of the prism and the three groups that lie in or close to the equatorial plane.

Many authors, using lanthanide ions as structural probes have suggested that the effective axial symmetries observed in their systems stem from just such rapid ligand rotations and intra- or intermolecular exchange processes. Thus, taking this view very little difference would be expected between the spectrum generated from the BCTP(2) model and that arising from a rigid, axially symmetric, TCTP structure. That the isotropic shifts do not fit either axial symmetry or effective axial symmetry implies that either the structural model chosen is incorrect or that equation (8) is not applicable for this system. The model geometry could indeed be wrong but the lack of an obvious alternative structure suggests that the full equation, (7),

SCHEME 2:



for the isotropic shift complete with terms arising from the nonaxial symmetry of the instantaneous structure shown in Figure 27 must be used.

In applying equation (7) to the problem the exchange process is assumed to be a simple three site exchange. The observed isotropic shift of a particular resonance is regarded as the average of the three isotropic shifts expected in the frozen instantaneous structure (Figure 27). The twenty-one unique ^1H resonances expected for the complex shown in Figure 27 are reduced to seven by the exchange process. The geometric variables listed in Table 36 are from the $\text{Yb}(\text{HBPz}_3)_3$ crystal structure data except for the uncoordinated pyrazolyl group for which r , θ and k are found by using molecular models. The values of D_1 , D_2 and ϕ which are then obtained from a least-squares fit apply to the instantaneous structure.

As in the case of $\text{Yb}(\text{HBPz}_3)_3$ spectra, resonance assignment is not a trivial problem. Resonances arising from the six exchanging apical (A) groups can be distinguished from those due to the three equatorial (E) groups by peak integrals. The 3-H resonances can be distinguished from the 4-H and 5-H by peak widths. The 3-H protons are close to the metal and consequently have greater line widths. The linewidth of the BH resonance, unlike the other resonances, decreases with decreasing

Table 36. Geometric Factors for BCTP(2) Model of Ln(HBPz₃)₃^a

Nucleus	r (1) A°	r (2) A°	r (3)	θ (1) deg.	θ (2) deg.	θ (3)	k (1)	k (2) deg.	k (3)
H3A	3.65	3.74	3.62	24.3	28.7	30.0	62.8	-165.9	-65.10
H4A	5.60	5.68	5.61	42.3	42.4	43.0	35.4	162.6	-97.0
H5A	5.48	5.56	5.50	65.5	65.4	65.3	16.9	144.3	-117.4
H3E	3.85	3.74	4.68	90.0	90.0	70.0	-76.3	52.7	188.5
H4E	5.80	5.72	4.25	90.0	90.0	78.0	-54.1	75.0	161.5
H5E	5.66	5.62	3.76	90.0	90.0	60.0	-27.6	101.8	158.0
BH	4.78	4.80	4.79	90.0	90.0	90.0	1.0	130.0	-134.5
B	3.59	3.60	3.53	90.0	90.0	90.0	0.0	130.0	-134.5

^aThe subscripts 1, 2, and 3 appearing with r, θ and k refer to the three different sites in the BCTP(2) structure. Site (1) positions correspond to those atoms in the HBPz₃ ligand, in the Yb(HBPz₃)₃ structure which contains B(1). Thus, the three sites for H3A, 1, 2 and 3, correspond to H(13), H(43) and H(73), respectively. The uncoordinated pyrazolyl protons are H3E, H4E, H5E at Site (3).

temperature. This effect is caused by the quadrupolar boron nuclei and thus the BH resonance can be differentiated from the H3E resonance. The exchange process averages the term $\cos 2\Omega$ in equation (7) almost to zero. Thus, the relative importance of the second term, $D_2(\sin^2\theta/r^3)\cos 2\Omega$, is greatly diminished and H4A and H5A can be assigned on the basis of the signs of their respective geometric factors $(3\cos^2\theta-1)/r^3$. Unfortunately, the ambiguity in the assignment of H4E and H5E cannot be resolved.

The least-squares program used for the analysis of the $\text{Yb}(\text{HBPz}_3)_3$ system was modified to include the averaging process. The results of the Dy and Ho data are given in Table 37 and Table 38, respectively. Two separate refinements were carried out for each. One using five resonances H3A, H4A, H5A, BH and B and the other using all the data. The agreement between observed and calculated shifts is good for those nuclei that do not have large differences in the values of the geometric factors $(3\cos^2\theta-1)/r^3$ and $\sin^2\theta/r^3$ between the three different sites in the instantaneous structure; r and θ are almost constant for H3A, H4A, H5A, and B in the three sites, only k varies appreciably. The difference between observed and calculated shift is large for the BH resonance in the Dy case. At 13 ppm it is much larger than the 2 ppm effective variance in the calculated shift.

Table 37. Results of Least Squares Fit For BCTP(2) Model Ho(HBPz₃)₃.^a

Nucleus	$(\frac{\Delta\nu}{\nu_0})_{obs}$	$(\frac{\Delta\nu}{\nu_0})_{calc}$	$(\frac{\Delta\nu}{\nu_0})_{obs} - (\frac{\Delta\nu}{\nu_0})_{calc}$	SITE(1)	SITE(2)	SITE(3)	$\frac{D_1(3\cos^2\theta-1)}{r^3}$	$\frac{D_2\sin^2\theta\cos 2(\phi+k)}{r^3}$
H3A	-116.2	-106(4)	-11	-109	-122	-86	-109	3
H4A	-16.6	-14(1)	-2	-18	-27	2	-14	-0.4
H5A	2.9	6(1)	-3	-13	-0.1	30	11	-5
H3E		84		161	114	-24	57	27
H4E	13.9	20(1)	-6	28	51	-18	29	-9
H5E	-14.9	2(2)	13	1	53	-47	21	-19
BH	30.5	21(1)	9	-19	42	41	36	-15
B	49.3	52(1)	-3	-45	99	103	87	-35
H3A	-116.2	-112(4)	-4	-125	-137	-75	-115	2
H4A	-16.6	-17(1)	1	-29	-23	0	-15	-3
H5A	2.9	3(1)	-0.4	-24	17	17	12	-9
BH	30.5	22(1)	9	-22	78	9	38	-17
B	49.3	52(1)	-3	-49	184	22	92	40

^a Shifts in ppm. ^b Calculated shifts for 3 nonequivalent sites in frozen instantaneous structure.

Table 38. Results of Least Squares Fit for BCTP(2) Model Dy(HBPz₃)₃.^a

Nucleus	$(\frac{\Delta\nu}{\nu_0})_{obs}$	$(\frac{\Delta\nu}{\nu_0})_{calc}$	$(\frac{\Delta\nu}{\nu_0})_{obs} - (\frac{\Delta\nu}{\nu_0})_{calc}$	SITE(1)	SITE(2)	SITE(3)	r^3	$D_1(3\cos^2\theta-1)$	$D_2\sin^2\theta\cos 2(\phi+\kappa)$	r^3
H3A	-206.0	-172(6)	-34	-182	-187	-148	-176	4		4
H4A	-28.6	-23(1)	-5	-28	-38	-4	-23	-0.4		-0.4
H5A	8.2	12(1)	-4	-9	5	41	18	-6		-6
H3E	117.0	124(4)	-7	219	169	-16	92	32		32
H4E	26.3	36(1)	-10	42	69	-2	47	-11		-11
H5E	29.0	12(2)	17	11	72	-47	34	-22		-22
BH	53.8	41(2)	13	-6	65	65	59	-17		-17
B	97.0	100(1)	-3	-14	153	162	141	-41		-41
H3A	-206.0	-200(7)	-6	-219	-236	-146	-204	4		4
H4A	-28.6	-30(1)	1	-46	42	-1	-26	-3		-3
H5A	8.2	8(1)	-0.2	-33	22	36	21	-13		-13
BH	53.8	41(2)	13	-30	118	35	68	-27		-27
B	97.0	100(2)	-3	-67	279	88	164	-64		-64

^a Shifts in ppm.^b Calculated shifts for 3 nonequivalent sites in frozen instantaneous structure.

As would be intuitively expected the averaging process greatly diminishes the contribution to the isotropic shift from the second term of equation (7), which involves $\cos^2(\phi+k)$, as compared to its importance to the shifts of the BCTP(1) isomer. This contribution is negligible for H3A and H4A, but significant for H5A and the boron nuclei. Reference to Table 35 shows that these non-axial contributions are most probably the cause of the apparently anomalous values of D_1 , calculated using equation (8), for H5A and B.

The improved agreement between calculated and observed shifts when those protons which are postulated to have greater changes in r , θ and k during the exchange process are removed from the fit may be due in large part to refinement of three parameters in a weighted least-squares with only five observations.

The values of the magnetic parameters and R factors from the least-squares fits of the Dy and Ho data are given in Table 39. Implicit in the BCTP(2) model is the assumption that the coordination polyhedron for the second isomer is essentially the same as that found in the BCTP(1) isomer. The values of the two sets of magnetic parameters for the two isomers should therefore be comparable in sign and magnitude and the values of the orienting angle ϕ should be almost the same. This is

Table 39. Magnetic Parameters and R_w Factors from Least Squares Fit BCTP(2) model $\text{Ln}(\text{HBPz}_3)_3$ Ln = Ho, Dy.

Number of Resonances	D_1 $\text{A}^3 \times 10^2$	D_2 $\text{A}^3 \times 10^2$	ϕ deg.	R_w %
<u>Holmium</u>				
7	-40 ± 7	-61 ± 30	2 ± 6	21
5	-42 ± 7	-73 ± 22	-14 ± 24	12
<u>Dysprosium</u>				
8	-64 ± 8	-71 ± 32	2 ± 8	17
5	-75 ± 11	-112 ± 35	-10 ± 20	9

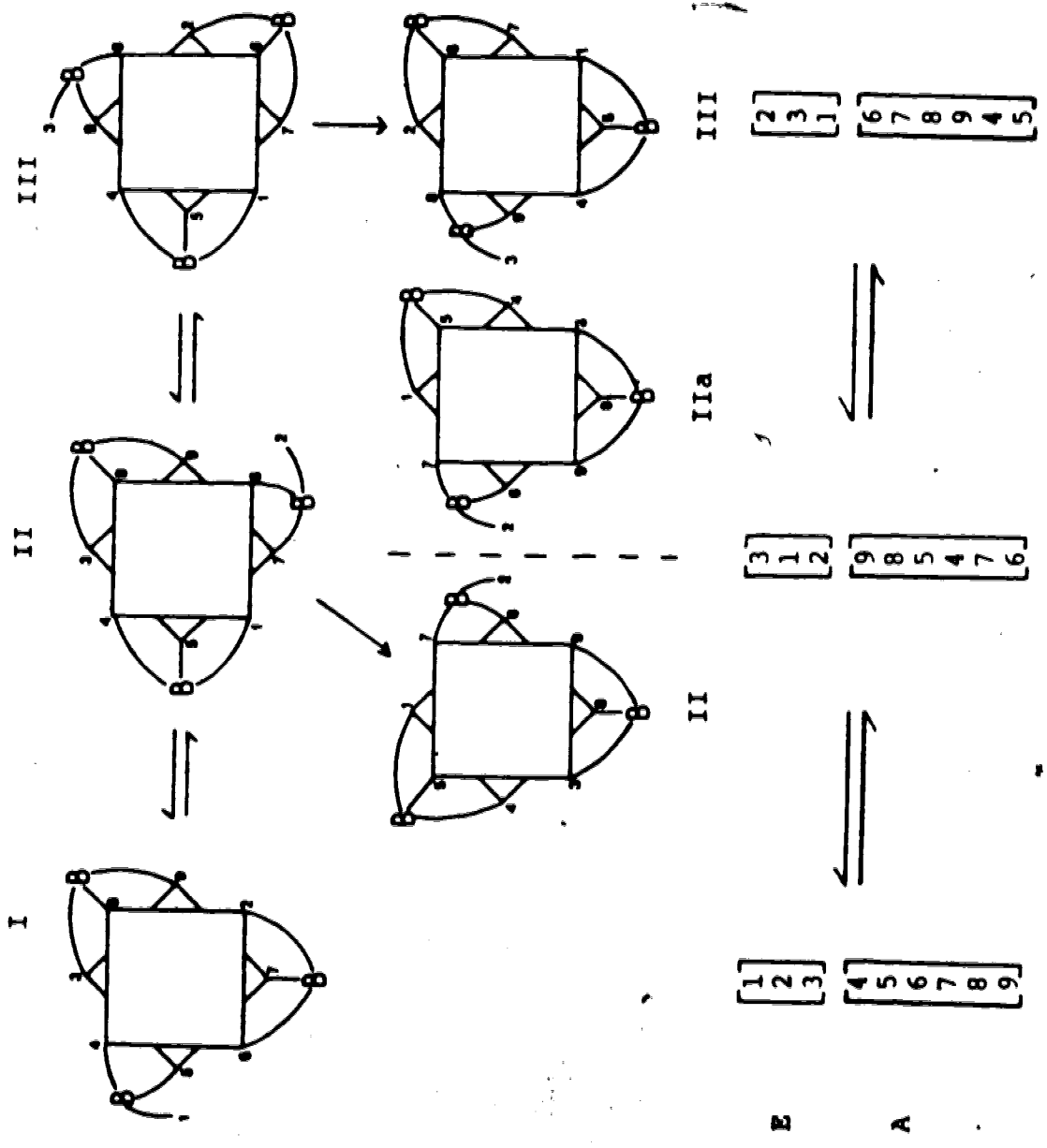
found to be the case when Table 39 is compared with Table 28.

The agreement between observed and calculated shifts for H4E, H5E and BH resonances is not good. The free pyrazolyl group is in a rather sterically congested position which from molecular models appears to be much less energetically favourable than the position which it adopts in the BCTP(1) isomer (see Figure 8). Additionally, the mechanism of the slow equilibrium between the two isomers which are postulated to differ only in the configuration at the boron atom of the bidentate ligand would require the breaking and making of metal nitrogen bonds and would involve a seven coordinate intermediate.

For the reasons above it seemed reasonable to postulate an alternative structure for the second isomer which would be based on a different coordination polyhedron. The choice of another polyhedron rests between the DOD and SAP. Of the two, the DOD is the more unlikely. In this geometry at least one ligand would have to bridge a b edge (see Figure 4) which in the idealised polyhedral shape has a length 1.25 times longer than the other edges and consequently would support with more difficulty the rigid chelating "tripod" HBPz_3^- ligand than a geometry based on the SAP.

A structure with SAP geometry is shown in Scheme 3. The requirements of the ligand preclude the spanning of

SCHEME 3:



FOOTNOTE for Scheme 3:

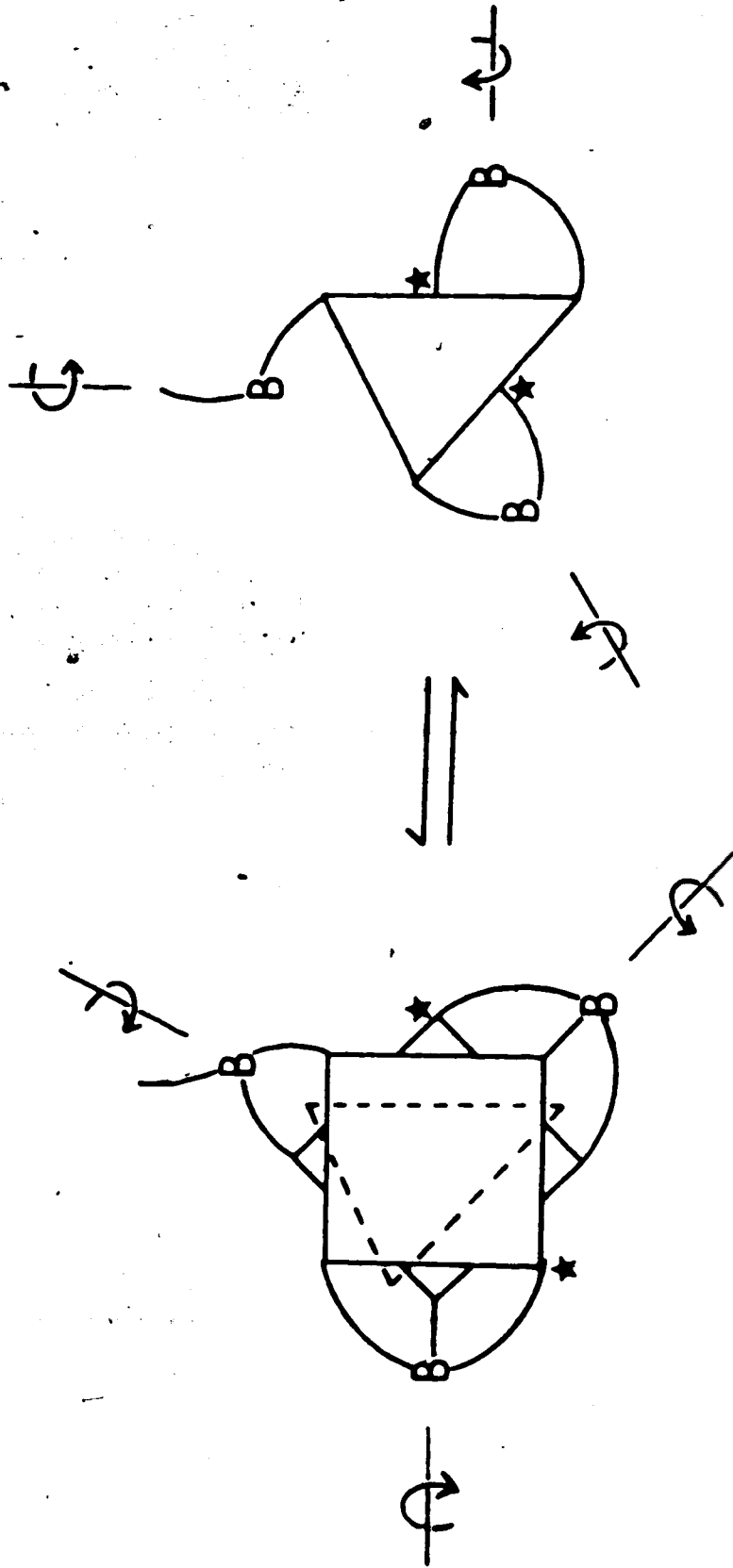
- a) Pyrazolyl positions after the 1st, II, and 2nd steps, III, of the rearrangement in the $\text{Ln}(\text{HBPz}_3)_3$ SAP isomer. The pyrazolyl groups are numbered 1 through 9. Structures II and III have been redrawn to facilitate the identification of the exchanging groups. II was rotated anticlockwise by 45° about the " S_8 " axis of the SAP, followed by 180° flip about an axis along the 4-6 vector. IIa is the mirror image of II. III was rotated 90° anticlockwise about the " S_8 " axis.

the diagonals of the square faces and results in only one possible isomer (*lls, lls, l*).

Scheme 3 also describes the intramolecular rearrangement process that the complex must undergo to be consistent with the observed ^1H NMR spectrum. The free uncoordinated pyrazolyl groups attacks the backside of a tridentate ligand with the concomitant release of the coordinated pyrazolyl group of that ligand, across from the site of attack. Of importance is that in the exchange process, only the schematic pyrazolyl groups 1, 2 and 3 may be or become uncoordinated and exchange amongst themselves in a closed set. They produce three resonances H3E, H4E and H5E. The remaining six pyrazolyl groups equivalent to the A set in the discarded BCTP(2) and TCTP models are similarly averaged only amongst themselves. The complex is asymmetric and each step shown in Scheme 3 takes the complex into its enantiomer. The exchange vectors are also shown in Scheme 3 and demonstrate, as would be intuitively expected, that the E set are permuted in three steps while the A set require six steps to be completely averaged.

The advantage of regarding the second isomer as having SAP rather than BCTP(2) coordination geometry becomes evident in Scheme 4 which shows a possible route between the BCTP(1) isomer and the SAP isomer.

SCHEME 4



SAP

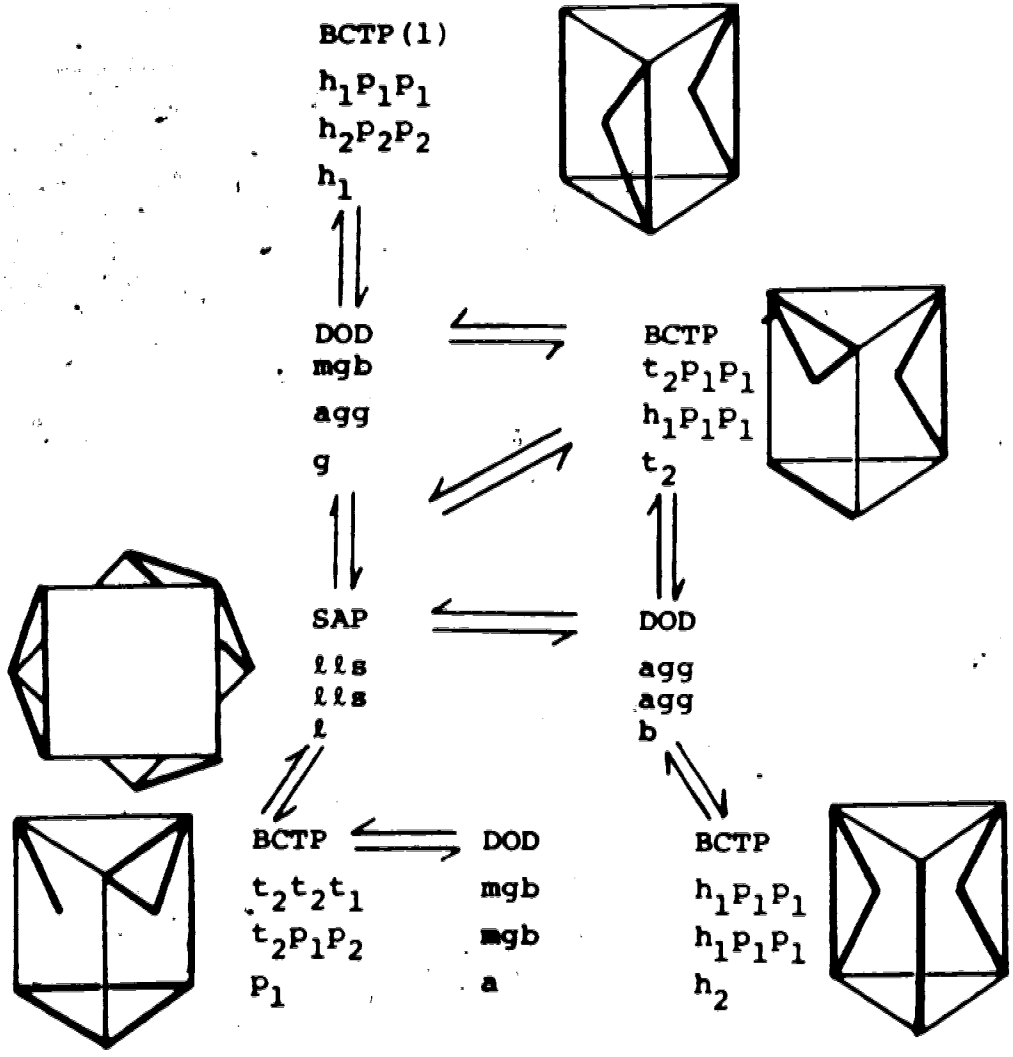
BCTP(I)

This involves rotation of the ligands about the boron - lanthanide vectors. The rotations are "disrotatory" between ligands at faces of the trigonal prism that are capped while the uncapped face has a "conrotatory" motion which cannot occur at the capped faces because of the orientation of the pyrazolyl rings.

An alternative view of the BCTP-SAP isomerization is shown in Scheme 5. This is the classical deformation mode that interconverts the SAP, BCTP and DOD. The trail from the BCTP(1) ($h_1P_1P_1, h_2P_2P_2, h_1$) isomer (using the nomenclature of Porai-Koshits and Aslanov, the tridentate ligands span the faces with edges $h_1P_1P_1$ and $h_2P_2P_2$) goes by way of DOD (mgb, agg, g) isomer which is reached by reforming the diagonal of the uncapped face as a b edge. From here the SAP can be then formed directly by the stretching and deforming of the b edges of the DOD and their eventual disappearance as edges.

Scheme 5 also shows the other possible isomers with different ligand wrapping patterns. The interconversion pathways are by means of the b edge - square face diagonal interchange. The accessible isomers are shown merely for completeness. Although the interconversion of BCTP(1) and SAP (tts, tts, t) could go via another route involving the BCTP ($t_2P_1P_2, h_1P_1P_1, t_2$) isomer, the ligand wrapping pattern in BCTP(1) requires that the pathway involve the

SCHEME 5:



intermediacy of the DOD (mgb, agg, g) isomer from which there is a direct route to the SAP.

The aspect of the proposed pathway between the SAP and BCTP(1) isomers of $\text{Ln}(\text{HBPz}_3)_3$ that makes it particularly attractive is that it does not require metal ligand bond breaking but rather a concerted deformation along the well known BCTP-DOD-SAP route.

Improved Structural Modeling of the Second Isomer -
Solid State Structure of $\text{Dy}(\text{HBPz}_3)_3$?

For the SAP isomer detailed solid state structural information would seem to be a prerequisite for a successful fit of calculated shifts, as was found in the case of the BCTP(1) isomer; especially so in view of the dramatic reduction by the averaging process in the number of observed resonances.

The appearance of a second isomer in the NMR spectra of the holmium and dysprosium complexes can be correlated with the results described in Chapter II where the two complexes exhibit slightly different physical properties than those of the heavier lanthanide derivatives. If this view is indeed correct and the complementary results are not merely coincidental, then there is the definite implication that the terbium and dysprosium complexes have the square antiprismatic structure in the solid state.

Speculation on this subject will remain academic until a single crystal X-ray structure determination of the dysprosium complex is made. The infrared spectra in Chapter II show that unlike the holmium complex, $\text{Dy}(\text{HBPz}_3)_3$ precipitates from CH_2Cl_2 with $\text{Tb}(\text{HBPz}_3)_3$ type structure. Slow crystallization from organic solvents could therefore provide suitable crystals for a structural determination. The X-ray structure information could then possibly provide a model for the frozen instantaneous structure in the exchange process.

Variable Temperature NMR Studies

A typical variable temperature study with $\text{Ho}(\text{HBPz}_3)_3$ is shown in Figure 28. On lowering the temperature of the NMR probe the relative proportion of the SAP isomer (H4A) to BCTP(1) isomer (H(95)) increases. The relative concentrations of the two isomers are easily extracted using peak integrations of these and other appropriate resonances.

The so obtained average values of the equilibrium constant, K , for the slow isomerization



at temperatures between 25°C and -60°C are tabulated in Table 40.

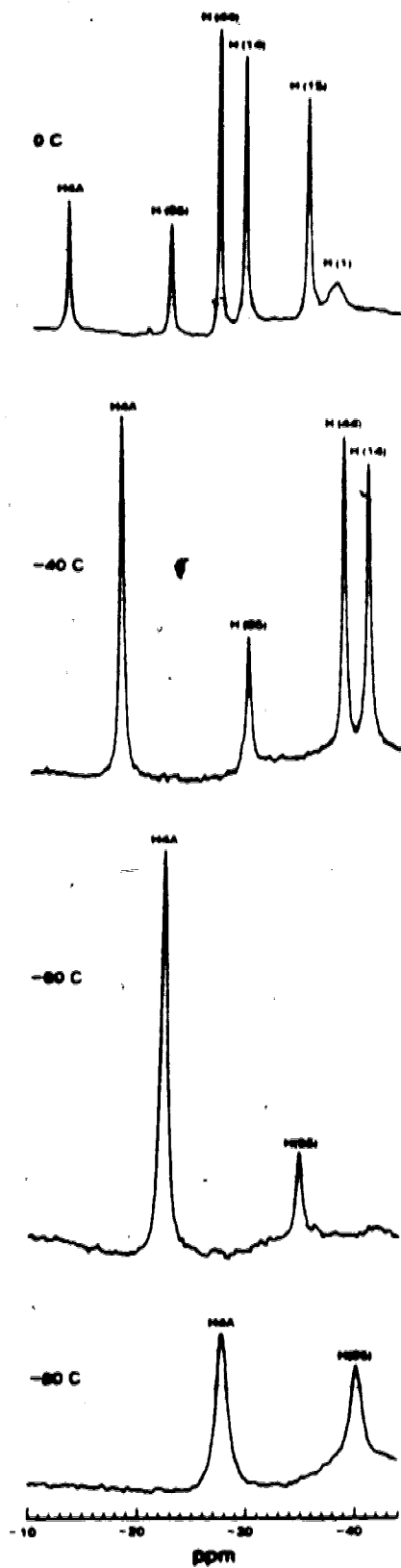


FIGURE 28. Variable Temperature 200 MHz ^1H NMR Spectra of $\text{Ho}(\text{HBPz}_3)_3$.

Table 40. Equilibrium Constants For Isomerisation of
 $\text{Ln}(\text{HBPz}_3)_3$ Ln = Ho, Dy.^a

T °K	K	
	Ho	Dy
298	8.94 (33)	3.88 (12)
273	6.08 (32)	2.18 (7)
253	4.17 (17)	1.52 (12)
233	2.49 (14)	0.78 (5)
223	1.54 (8)	0.59 (8)
213	1.28 (11)	0.54 (7)

^aIn CD_2Cl_2 solution.

Plots of $\ln K$ vs $1/T$ are shown in Figure 29 and give values of $\Delta H^\circ = 12.4 \pm 0.7 \text{ kJ mole}^{-1}$ and $\Delta S^\circ = 60 \pm 3 \text{ J K}^{-1}$, and $\Delta H^\circ = 13.3 \pm 0.6 \text{ kJ mole}^{-1}$ and $\Delta S^\circ = 56 \pm 2 \text{ J K}^{-1}$ for the holmium and dysprosium complexes, respectively. ΔH° for the isomerization is small and this is consistent with the small differences in energy calculated for the various coordination geometries.⁴⁴⁻⁴⁸ The values of ΔS° are large and this may appear a little surprising as the isomerization is unimolecular.

A possible explanation involves consideration of the positions of the free pyrazolyl group in the two complexes. It is difficult to estimate exactly where this uncoordinated group would lie in the SAP isomer. However, molecular models indicate that it may approach closer to the metal than in BCTP(1) case and fit more closely into the sphere roughly defined by the three boron atoms. This view receives support from the rapid intramolecular ligand exchange which the SAP isomer undergoes. In the BCTP(1) isomer the free pyrazolyl group juts out quite sharply from the complex (see Figure 8) and the consequent disruption of the solvent sheath around the complex would result in a higher entropy state for this complex in solution than for the SAP isomer.

The importance of solvent effects is also evident from the solvent dependent behaviour of the equilibrium

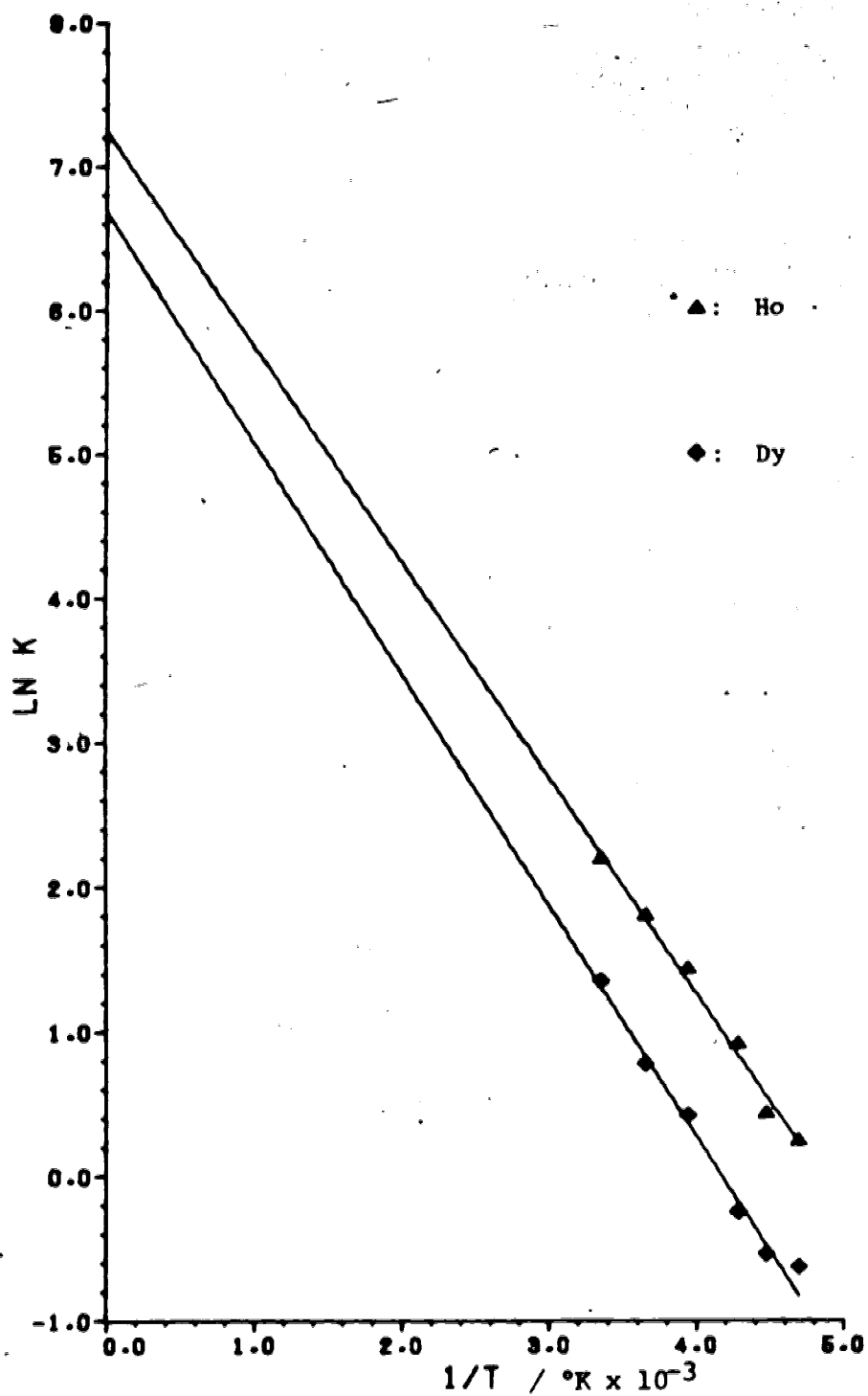


FIGURE 29. Plot of $\ln K$ vs. $1/T$ for the Isomerisation of $\text{Ho}(\text{HBPz}_3)_3$ and $\text{Dy}(\text{HBPz}_3)_3$.

constant. The SAP isomer is very nearly undetectable at room temperature in toluene or THF. It may be that the projecting free pyrazolyl group of the BCTP(1) isomer may have more energetically favourable interactions with these solvents resulting in the observed shift of the equilibrium.

In toluene- d_8 at 80°C the SAP isomer is undetectable in the NMR spectrum. The resonances arising from the BCTP(1) isomer are much broader at this temperature than at 25°C . This broadening is not due to the presence of the lanthanide ion as the rapid paramagnetic electron relaxation should become even faster at higher temperatures thus decreasing the efficiency of the nuclear relaxation mechanism and giving a sharper NMR signal. Therefore, the broadening observed at elevated temperature could possibly be attributed to the collapse of the spectrum as the interconversion of the SAP and BCTP(1) isomers becomes more rapid.

Reference to Figure 28 shows that whereas from 0°C to -60°C the relative amount of the SAP isomer increases, below -60°C the trend appears to be reversed. It seems unlikely that the equilibrium constant should decrease down to -60°C and then below -60°C start to increase. No precipitation of solid was observed in the NMR samples at -80°C . The apparent reversal of the trend below -60°C therefore may be due to incipient collapse of the spectrum

caused by the slowing down of the intramolecular rearrangement process shown in Scheme 3. Similar behaviour was found for the dysprosium complex below -60°C . Line shape analysis at temperatures below -80°C was not attempted. Even if the postulated rearrangement process is correct the results of the previous section show that the fit of calculated to observed shifts of the SAP isomer leaves much to be desired. We therefore have only a vague idea of the chemical shifts for the three (perhaps six in the case of the A type protons) sites in the frozen instantaneous structure. The extreme temperature dependence of the shifts also compounds the problem. The shifts do not all have the same temperature dependence and do not exhibit either a simple T^{-1} or T^{-2} dependence. For these reasons line shape analysis of the spectrum of the SAP isomer at temperatures below -60°C does not seem to be a particularly fruitful area of investigation at present. However, if the observed shifts can be modeled successfully, using more detailed information about the solid state structure of $\text{Dy}(\text{HBPz}_3)_3$, and the exact nature of the temperature dependence of the shifts is known it may be possible to obtain kinetic parameters for the intramolecular rearrangement process as well.

Conclusion

The importance of the non-axial term in equation (7) is seen in the NMR spectra of the $\text{Ln}(\text{HBPz}_3)_3$ complexes. This is expected for the BCTP(1) isomer which is rigid and possesses only C_3 point symmetry. However, in the case of the non rigid SAP isomer the ligand exchange process does not result in effective magnetic axial symmetry.

The intramolecular exchange process is quite specific, the pyrazolyl groups are not permuted as a complete set of nine and the evidence, although far from conclusive, indicates a three (perhaps six) site exchange process. The "large ensemble of rapidly interconverting geometrical isomers" model described by Horrocks¹⁰⁰ or the free rotation model of Briggs *et al.*⁹⁹ would therefore both appear to be inapplicable here.

Our simple model of a three site exchange meets with some success but obviously lacks the detailed information necessary for a full accounting of the observed isotropic shifts. The analysis of the observed shifts clearly demonstrates that although the number and pattern of resonances on cursory inspection suggests effective axial symmetry (the normalised shifts for the two complexes shown in Table 35 are virtually the same) the lanthanide induced shifts still retain significant non-axial character.

Observations of constant shift ratios are frequently invoked as evidence indicating that the system can be treated as though it possessed axial symmetry. As a converse to this argument observation of variation in shift ratios is often attributed to the presence of contact shifts or structural changes within the series of complexes. The possibility of non-axial contributions to the pseudocontact shifts being responsible for the variation is only rarely considered.

In conclusion we itemise the two salient features of the $\text{Ln}(\text{HBPz}_3)_3$ complexes which are particularly relevant to the use of lanthanide ions as structural probes.

- 1) ^1H contact shifts can be satisfactorily ignored for complexes of the lanthanide ions Dy^{3+} to Yb^{3+} . The large magnetic anisotropies for Ln^{3+} heavier than Tb^{3+} cause the pseudocontact shifts to be dominant.
- 2) A ligand exchange process, intra- or intermolecular, does not a priori average out non-axial contributions to the pseudocontact shifts to zero. Non-axial contributions may become significant especially if the number of geometrical isomers or the number of nonequivalent sites amongst which the ligands exchange is small.

Thus conclusions regarding the geometry of substrate molecules or the magnitude of contact contribution to the isotropic shift reached on the basis of effective axial symmetry due to molecular rearrangement must be viewed with caution.

CHAPTER V

EXPERIMENTAL PROCEDURES

General

Solvents were purified according to standard procedures.¹³⁵ Lanthanide chloride hydrates were obtained from the American Potash and Chemical Corporation, and Research Chemicals.

Synthesis of Ln(HBPz₃)₃

KHBPz₃ was synthesized by the method described by Trofimenko.¹²⁰ The complexes Ln = Dy, Ho, Er, Tm, Yb, Lu were prepared by the same general procedure which is outlined below for Ho(HBPz₃)₃.

HoCl₃·6H₂O (1.50 g, 3.95 mmol) was dissolved in H₂O (15 mL) and filtered, to remove a small amount of undissolved material, into a solution of KHBPz₃ (3.00 g, 11.90 mmol) in water (30 mL). A pale pink precipitate formed immediately. The slurry was stirred for 5 minutes and then filtered. The pale pink solid was washed with two 15 mL portions of water and two 10 mL portions of ethanol and dried overnight under vacuum, yield 2.39 g, 75%.

The syntheses are effectively quantitative, however, some product is lost with the ethanol washings. Analytical

samples were obtained by recrystallization from CH_2Cl_2 /hexane. The latter procedure was carried out under a dry nitrogen atmosphere using dry solvents.

The terbium complex was prepared by a similar procedure. The insolubility of this compound in common organic solvents precluded purification by recrystallization.

The samples for C, H and N analyses were combusted with W_2O_3 because of the boron content of the samples. The analyses were carried out in the microanalytical laboratory of this department. Table 41 contains the analytical data for the complexes. The analysis reported for the terbium complex is that of the crude product. Attempted purification of this compound by soxhlet extraction with CH_2Cl_2 under a dry nitrogen atmosphere was unsuccessful.

Infrared Spectra

Infrared spectra were recorded on a Nicolet MX-1 Fourier transform spectrometer. Solid samples were recorded as mineral oil mulls between KBr plates. Solution spectra were recorded in 0.5 mm NaCl cells.

X-ray Powder Diffraction

The powder diffraction patterns were recorded on a Phillips XRD diffractometer using CuK_α radiation

Table 41. Analyses of Ln(HBPz₃)₃ Complexes.

Ln	Colour	Calculated			Found		
		C	H	N	C	H	N
Sm ^a	Colourless	41.08	3.83	31.93	40.95	3.88	32.37
Tb	Colourless	40.64	3.79	31.59	39.67	3.77	30.76
Dy	Colourless	40.46	3.77	31.45	40.10	3.88	31.10
Ho	Pink	40.34	3.76	31.36	39.89	3.79	30.96
Er ^a	Pink	40.22	3.75	31.27	40.43	3.83	30.66
Tm	Colourless	40.14	3.74	31.20	39.62	3.80	30.83
Yb	Colourless	39.93	3.72	31.04	39.58	3.73	30.73
Lu	Colourless	39.84	3.72	30.97	40.52	3.75	30.80

^aData from reference 36.

($\lambda = 1.5418 \text{ \AA}$). The samples were backpacked.

NMR Spectra

CD_2Cl_2 was dried over P_2O_5 . THF- d_8 and toluene- d_8 were distilled from potassium. All deuterated solvents were stored under nitrogen over Linde 4A molecular sieves.

All spectra were recorded with a Bruker WH-200 spectrometer. Deuterated solvents and 5 mm sample tubes were used for the 200 MHz ^1H spectra. The ^{13}C 50.33 MHz and ^{11}B 64.23 MHz spectra were recorded using a multi-nuclear probe and a 20 mm sample tube fitted with a vortex plug. The solvent was CH_2Cl_2 with 10% CD_2Cl_2 . The volume of the sample was typically 12 mL. Sample concentrations were $\sim 0.08 \text{ M}$ for the Lu, Yb and Tm complexes. The reduced solubility of the Ho and Dy complexes necessitated the use of almost saturated solutions.

Chemical shifts for the ^1H and ^{13}C spectra were measured with respect to internal standards: CHDCl_2 , $\delta 5.32 \text{ ppm}$, and CH_2Cl_2 , $\delta 53.8 \text{ ppm}$, respectively. The ^{11}B shifts were measured relative to external BF_3OEt_2 and were corrected for bulk magnetic susceptibility effects. The chemical shifts in this work are reported with respect to TMS or BF_3OEt_2 , downfield shifts positive.

CHAPTER VI

CRYSTAL AND MOLECULAR STRUCTURES OF $\text{Fe}(\text{CO})_3(\text{PPh}_3)$ (DIETHYLFUMARATE) AND $\text{Fe}(\text{CO})_3(\text{PPh}_3)$ (DIETHYLMALEATE).

Introduction

The elucidation of the coordination geometry of five coordinate transition metal complexes and the distribution of ligands on the coordination sphere has formed the basis of several theoretical studies^{136,137} and a multitude of physical, mainly X-ray diffraction, investigations.¹³⁸ It is now well established that for d^8 metal complexes containing nominally monodentate ligands the geometry is based overwhelmingly on the trigonal bipyramid.

In a very broad treatment Hoffmann and Rossi¹³⁶ have established the electronic site preference of ligands and their influence on the metal-ligand bond distances in five coordinate molecules. However, these authors readily recognized that the geometry of metal complexes are not only influenced by electronic factors but by steric effects as well.

In another study in these laboratories¹³⁹ a series of complexes of the type $\text{Fe}(\text{CO})_3(\text{PR}_3)(\text{olefin})$ ($\text{PR}_3 = \text{PPh}_3, \text{PMe}_2\text{Ph}, \text{P}(\text{OMe})_3$; olefin = diethylfumarate and

diethylmaleate) were prepared and characterized by spectroscopic techniques. Since the compounds contain significantly different ligands, their structures could in principle shed light on the relative importance of steric and electronic factors in determining the positioning of ligands on pentacoordinate, trigonal bipyramidal molecules. Furthermore, infrared spectroscopy seemed to indicate that the fumarate and maleate complexes belonged to different isomeric classes and this gave added impetus to determine the solid state structure of a member of each class.

This chapter reports the single crystal X-ray structure determination of $\text{Fe}(\text{CO})_3(\text{PPh}_3)(\text{diethylfumarate})$ and $\text{Fe}(\text{CO})_3(\text{PPh}_3)(\text{diethylmaleate})$.

Experimental

Diethylfumarate and (diethylmaleate)(triphenylphosphine)tricarbonyliron, $\text{Fe}(\text{CO})_3(\text{PPh}_3)(\text{fum})$ and $\text{Fe}(\text{CO})_3(\text{PPh}_3)(\text{mal})$, were prepared by prolonged photolysis of $\text{Fe}(\text{CO})_4(\text{PPh}_3)$ in the presence of excess olefin. Chromatography on alumina followed by crystallization from $\text{CH}_2\text{Cl}_2/\text{pentane}$ affords the pure complexes as yellow crystals suitable for single-crystal X-ray diffraction studies. ¹³⁹

Data Collection⁵⁴

A crystal of the diethylfumarate complex was mounted in a thin-walled glass capillary. Preliminary Weissenberg and precession photographs revealed systematic absences of hkl , $h + k = 2n + 1$, and $h0l$, $l = 2n + 1$, consistent with space groups $C2/c$ or Cc . The centrosymmetric space group was chosen and later verified by the successful refinement of the structure.

A crystal of the diethylmaleate complex was similarly mounted in a glass capillary. Preliminary photographs showed no systematic absences. A cell reduction failed to show the presence of higher symmetry. The centrosymmetric space group $P\bar{1}$ was chosen and later verified by successful refinement of the structure.

Data collection for the two title compounds was carried out by the same general procedures described in Chapter III for the $Yb(HBPz_3)_3$ crystal structure. A summary of the crystal data and other details of the data collection are given in Table 42.

Solution and Refinement of the Structures⁵⁴

The structures of the fumarate and maleate complexes were solved by the same general procedure which is described below.

Table 42. Summary of Crystal Data and Intensity Data Collection for $\text{Fe}(\text{CO})_3(\text{PPh}_3)_3$ (olefin) (olefin = fum, mal).

Compound	$\text{Fe}(\text{CO})_3(\text{PPh}_3)\{\text{trans-}\text{C}_2\text{H}_2(\text{CO}_2\text{Et})_2\}$	$\text{Fe}(\text{CO})_3(\text{PPh}_3)\{\text{cis-}\text{C}_2\text{H}_2(\text{CO}_2\text{Et})_2\}$
Formula	$\text{FePO}_7\text{C}_{29}\text{H}_{27}$	$\text{FePO}_7\text{C}_{29}\text{H}_{27}$
Space Group	C2/c (C_{2h}^6 No.15) 60	$\text{P}\bar{1}$ (C_i^1 No.2) 60
Cell Parameters		
a, Å	17.674(4)	14.792(2)
b, Å	16.551(4)	10.420(1)
c, Å	19.491(6)	10.807(2)
α , deg	90.0	112.41(1)
β , deg	91.98(2)	65.89(1)
γ , deg	90.0	90.51(1)
Z	8	2
Crystal faces and distance from an arbitrary origin within the crystal, in mm.	1 0 0 0.15 $\bar{1}$ 0 0 0.15 0 1 0 0.16 0 $\bar{1}$ 0 0.16 0 0 1 0.23 0 0 $\bar{1}$ 0.23	0 0 1 0.2 0 0 $\bar{1}$ 0.2 1 1 0 0.1 1 $\bar{1}$ 0 0.1 1 0 0 0.25 $\bar{1}$ 0 0 0.25 1 0 1 0.20 $\bar{1}$ 0 $\bar{1}$ 0.24

(continued....)

Table 42 (continued)

Temperature, °C	22	22	1	1	0.12
Radiation	Mo K α graphite monochromated	MoK α Zr filtered.	1	1	0.12
Receiving aperture	6mm x 6mm, 30 cm from crystal	5.5mm x 5.5mm, 30 cm from crystal	2	0	0.25
Take Off Angle, deg.	2.45	2.4	2	0	0.20
Scan Speed	2° min ⁻¹	2° min ⁻¹ (2.5° ≤ 2θ ≤ 40°), 1° min ⁻¹ (40° < 2θ ≤ 49°).			
Scan Range	1.0° below K α_1 to 1.0° above K α_2	1.0° below K α_1 to 1.0° above K α_2			
Background Counting	at each scan limit, 10s (2.5 < 2θ < 40°); 20s (40 < 2θ < 51°)	at each scan limit, 10s (2.5° < 2θ < 36°); 20s (36° < 2θ < 49°)			
2θ Limits, deg	2.5-51.0	2.5-49.0			
P-factor ⁵⁶	0.05	0.05			
μ , cm ⁻¹	6.24	5.86			
Unique Data collected	5486	4926			

(continued...)

Table 42 (continued)

Unique Data Used ($F_i \geq 3\sigma(F_0)^2$)	3541	3119
Final Number of Parameters varied	225	226
Error In Observation of Unit Weight	1.852	1.513
R	0.056	0.053
R_w	0.073	0.064

The position of the iron atom was found from a three-dimensional Patterson synthesis. The remaining non-hydrogen atoms were located by successive difference Fourier, least-squares cycles. Atomic scattering factors were taken from Cromer and Waber's tabulations⁶² for all atoms except hydrogen for which the values of Stewart et al.⁶³ were used. Anomalous dispersion terms were included for the iron atom.⁶⁴ The carbon atoms of the phenyl rings of the phosphine ligand were refined as rigid bodies under D_{6h} symmetry with C-C distances of 1.392 Å and individually assigned isotropic temperature factors. All other non-hydrogen atoms were refined with anisotropic thermal parameters. The olefinic hydrogen atoms were located from a difference Fourier map and were refined isotropically. The remaining hydrogen atoms, with the exception of the methyl hydrogens, were included at their idealized positions calculated by a local positioning program and a C-H distance of 0.95 Å. These atoms were assigned thermal parameters 1 Å² greater than the atom to which they were attached, but were not refined. The final models converged to $R = 0.056$ and $R_w = 0.073$ for the fumarate complex and $R = 0.053$ and $R_w = 0.064$ for the maleate complex. The final difference Fourier maps showed the highest 20 residual peaks (0.54-0.32 e/Å³) to be close to the phenyl rings of the

triphenylphosphine and the methyl groups of the olefinic ligands.

The final positional and thermal parameters of the refined nongroup atoms for the fumarate and maleate complexes are given in Tables 43 and 44, respectively. The positional and thermal parameters of the rigid phenyl groups and the remaining hydrogen atoms and a listing of the observed and calculated structure amplitudes are contained in Appendix 4.

Description of the Structures

The crystal packing diagrams for the two structures are shown in Figure 30 and Figure 31. The crystal structures of $\text{Fe}(\text{CO})_3(\text{PPh}_3)(\text{fum})$ and $\text{Fe}(\text{CO})_3(\text{PPh}_3)(\text{mal})$ consist of discrete molecular units with no unusual intermolecular contacts. The molecular structures of the two complexes are shown in Figure 32 and Figure 33 and are based on the expected trigonal bipyramidal coordination geometry about the central iron atom. In both compounds the olefin is coordinated in an equatorial position and is tilted such that the carbon-carbon double bond makes an angle of 7.3° and 6.0° , for the maleate and fumarate respectively, with the plane formed by the remaining equatorial ligands and the iron atom. Similar tilting of the olefinic ligand is commonly found in structures

Table 43. Positional and Thermal Parameters for Non-group Atoms of $\text{Fe}(\text{CO})_3(\text{PPh}_3)(\text{fum})$.

Atom	x ^a	y	z	U ₁₁ ^b	U ₂₂	U ₃₃	U ₁₂	U ₁₃	U ₂₃
Fe	0.1818(3)	0.00122(4)	-0.14563(3)	5.18(4)	4.32(3)	3.68(3)	-0.16(3)	-0.17(2)	-0.06(3)
P	0.26807(7)	-0.02345(6)	-0.22702(6)	4.81(6)	3.73(6)	3.87(6)	0.13(5)	-0.31(5)	-0.14(4)
C(11)	0.0985(3)	-0.0549(3)	-0.1635(3)	6.8(4)	7.8(4)	5.3(3)	-1.5(3)	0.6(3)	-0.8(3)
C(2)	0.1464(3)	0.0823(3)	-0.1992(3)	6.2(3)	6.8(3)	4.5(3)	1.1(3)	-0.1(2)	-0.1(2)
C(3)	0.2167(3)	-0.0834(3)	-0.0954(3)	8.2(4)	4.9(3)	4.8(3)	-0.6(3)	-0.2(3)	-0.1(2)
O(1)	0.0432(2)	-0.0896(3)	-0.1719(2)	7.6(3)	13.7(4)	9.1(3)	-4.7(3)	-0.1(2)	-1.3(3)
O(2)	0.1234(3)	0.1312(3)	-0.2353(2)	11.6(3)	9.9(3)	6.5(3)	4.8(3)	-0.1(2)	2.3(2)
O(3)	0.2331(3)	-0.1389(2)	-0.0636(2)	14.7(4)	5.3(2)	7.3(3)	0.3(2)	-1.8(3)	1.2(2)
C(4)	0.2315(3)	0.0862(3)	-0.0788(2)	5.8(3)	3.5(2)	3.8(2)	-0.5(2)	-0.3(2)	-0.0(2)
C(5)	0.1608(3)	0.0594(3)	-0.0543(2)	6.2(3)	4.6(2)	3.9(3)	-0.3(2)	0.7(2)	0.2(2)
C(41)	0.3013(3)	0.0612(3)	-0.0418(2)	6.7(3)	5.1(3)	4.1(3)	0.0(2)	-0.6(2)	-0.5(2)
C(51)	0.0944(3)	0.1121(3)	-0.0580(2)	5.6(3)	5.0(3)	4.6(3)	-0.6(2)	0.7(2)	-0.7(2)
O(41)	0.3078(2)	0.0075(2)	-0.0007(2)	8.8(3)	7.5(2)	5.6(2)	-0.1(2)	-1.7(2)	1.6(2)
O(42)	0.3601(2)	0.1076(2)	-0.0593(2)	5.0(2)	6.7(2)	6.0(2)	-0.4(2)	-1.1(2)	-0.0(2)
O(51)	0.0896(2)	0.1772(2)	-0.0851(2)	6.6(2)	4.7(2)	8.3(3)	0.4(2)	1.5(2)	0.9(2)
O(52)	0.0373(2)	-0.0778(2)	-0.0248(2)	5.3(2)	6.8(2)	7.2(2)	-0.5(2)	1.1(2)	1.3(2)
C(42)	0.4328(3)	0.0885(4)	-0.0252(3)	6.7(4)	11.6(5)	7.3(4)	0.7(3)	-2.9(3)	-0.7(4)
C(43)	0.4880(4)	0.1494(6)	-0.0486(5)	6.2(4)	17.9(8)	14.5(8)	-4.0(5)	-1.1(4)	0.7(6)
C(52)	-0.0357(3)	0.1180(4)	-0.0282(3)	6.0(3)	8.5(4)	8.1(4)	-0.3(3)	1.2(3)	0.8(3)
C(53)	-0.0608(4)	0.0882(4)	-0.0900(4)	9.2(5)	8.9(5)	9.6(5)	-1.5(4)	-2.3(4)	0.8(4)

Atom	x	y	z	B(A ³)	Atom	x	y	z	B(A ³)
H(4)	0.235(2)	0.137(2)	-0.094(2)	3.0(8)	H(5)	0.161(2)	0.026(2)	-0.016(2)	2.7(8)

^aEstimated standard deviations in the least significant figure(s) are given in parentheses in this and all subsequent tables.

^bThe form of the thermal ellipsoid is:

$$\exp[-2\pi^2(a^2U_{11}h^2 + b^2U_{22}k^2 + c^2U_{33}l^2 + 2a^*b^*U_{12}hk + 2a^*c^*U_{13}hl + 2b^*c^*U_{23}kl)].$$

The quantities given in the table are the thermal coefficients $\times 10^2$.

Table 44. Positional and Thermal Parameters for Non-group Atoms of $\text{Fe}(\text{CO})_3(\text{PPh}_3)_3$ (mal).

Atom	x	y	z	U ₁₁	U ₂₂	U ₃₃	U ₁₂	U ₁₃	U ₂₃
Fe	0.20929(6)	0.06026(7)	0.45766(8)	4.25(5)	3.64(4)	4.28(5)	-1.00(3)	-1.81(4)	1.75(3)
P	0.24286(9)	0.2710(1)	0.4462(1)	3.41(7)	3.69(7)	3.46(8)	-0.86(5)	-1.54(6)	1.63(6)
C(1)	0.0870(4)	0.1501(5)	0.6004(6)	5.1(3)	4.7(3)	5.9(4)	-1.7(3)	-2.4(3)	2.9(3)
C(2)	0.2069(4)	-0.0072(5)	0.2802(6)	5.9(3)	4.4(3)	4.8(3)	1.2(3)	-2.4(3)	1.3(3)
C(3)	0.1673(4)	-0.0919(6)	0.4884(7)	5.8(4)	4.7(3)	7.4(4)	-1.5(3)	-3.2(3)	2.7(3)
O(1)	0.0056(3)	0.1894(5)	0.6911(5)	4.7(3)	9.0(3)	7.2(3)	-0.4(2)	-0.3(2)	3.5(3)
O(2)	0.2076(4)	-0.0535(5)	0.1658(5)	10.9(4)	7.9(3)	5.5(3)	-1.8(3)	-4.4(3)	1.4(2)
O(3)	0.1299(4)	-0.1795(5)	0.5150(6)	9.2(4)	6.4(3)	12.7(4)	-4.1(3)	-4.8(3)	5.8(3)
C(4)	0.3190(4)	0.0630(6)	0.5315(6)	4.8(3)	4.2(3)	5.7(4)	-1.2(2)	-2.8(3)	2.5(3)
C(5)	0.3573(4)	-0.0246(6)	0.3776(7)	4.2(3)	4.6(3)	5.5(4)	-0.7(2)	-1.5(3)	2.6(3)
C(11)	0.2940(4)	0.0088(6)	0.6476(7)	6.0(3)	4.5(3)	6.4(4)	0.5(3)	-3.5(3)	2.8(3)
C(51)	0.3877(5)	-0.1806(6)	0.3122(7)	6.6(4)	5.1(3)	6.0(4)	0.3(3)	-1.7(3)	2.3(3)
O(42)	0.2938(3)	0.1142(4)	0.6267(5)	9.2(3)	4.8(2)	7.3(3)	-0.8(2)	-3.2(3)	3.3(2)
O(51)	0.3416(4)	0.1153(4)	0.7816(5)	10.3(3)	5.4(2)	6.4(3)	-2.4(2)	-5.0(3)	3.3(2)
O(52)	0.4796(4)	-0.2696(5)	0.2736(7)	9.7(4)	4.6(3)	15.3(6)	-0.7(3)	-5.3(4)	1.3(3)
C(42)	0.2223(6)	-0.2124(5)	0.2937(6)	7.3(3)	6.2(3)	12.9(5)	1.8(2)	-2.6(3)	2.7(3)
C(43)	0.1132(6)	0.0744(8)	0.9117(8)	12.9(7)	7.0(4)	6.4(4)	-2.7(4)	-5.5(5)	3.6(4)
C(52)	0.5244(8)	-0.3650(8)	0.9580(9)	8.5(5)	10.4(6)	7.3(5)	-1.9(5)	-2.6(4)	3.1(4)
C(53)	0.6026(8)	-0.4032(9)	0.228(1)	13.3(8)	6.6(5)	13.8(9)	3.6(5)	-3.0(7)	3.0(5)
Atom	x	y	z	B(A ²)	Atom	x	y	z	B(A ²)
H(4)	C.359(4)	0.149(6)	0.554(6)	4(1)	H(5)	0.402(4)	0.007(6)	0.325(7)	3(2)

^a Estimated standard deviations in the least significant figure(s) are given in parentheses in this and all subsequent tables.

^b The form of the thermal ellipsoid is:

$$\exp[-2\pi^2(a^2U_{11}h^2 + b^2U_{22}k^2 + c^2U_{33}l^2 + 2a*b*U_{12}hk + 2a*c*U_{13}hl + 2b*c*U_{23}kl)].$$

The quantities given in the table are the thermal coefficients $\times 10^2$.

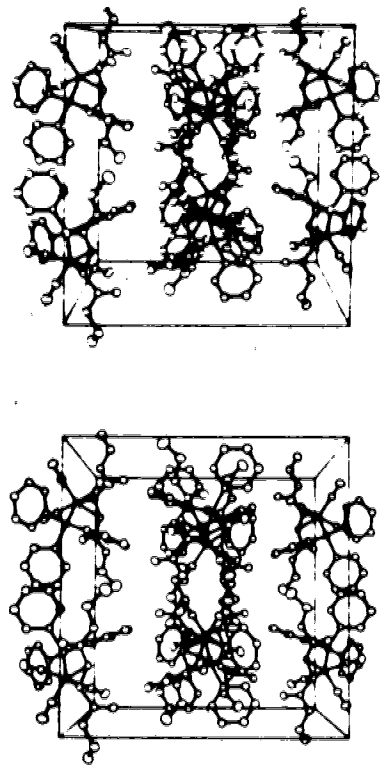


FIGURE 30. Cell packing diagram for $\text{Fe}(\text{CO})_3(\text{PPh}_3)_3$ (fum). The crystallographic a axis runs horizontal from left to right, the b axis runs from top to bottom and the c axis goes into the page.

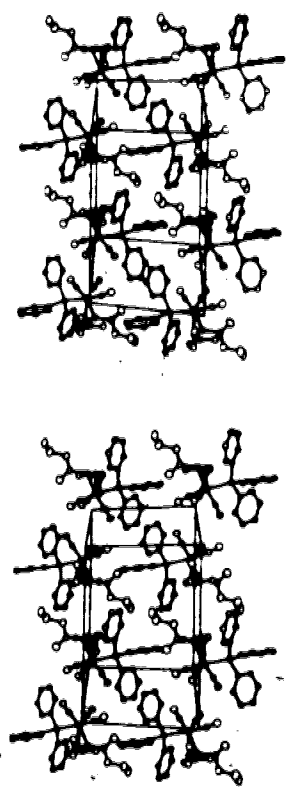


FIGURE 31. Cell packing diagram for $\text{Fe}(\text{CO})_3(\text{PPh}_3)_3$ (mal). The crystallographic a axis runs horizontal from left to right, the b axis runs from top to bottom and the c axis goes into the page.

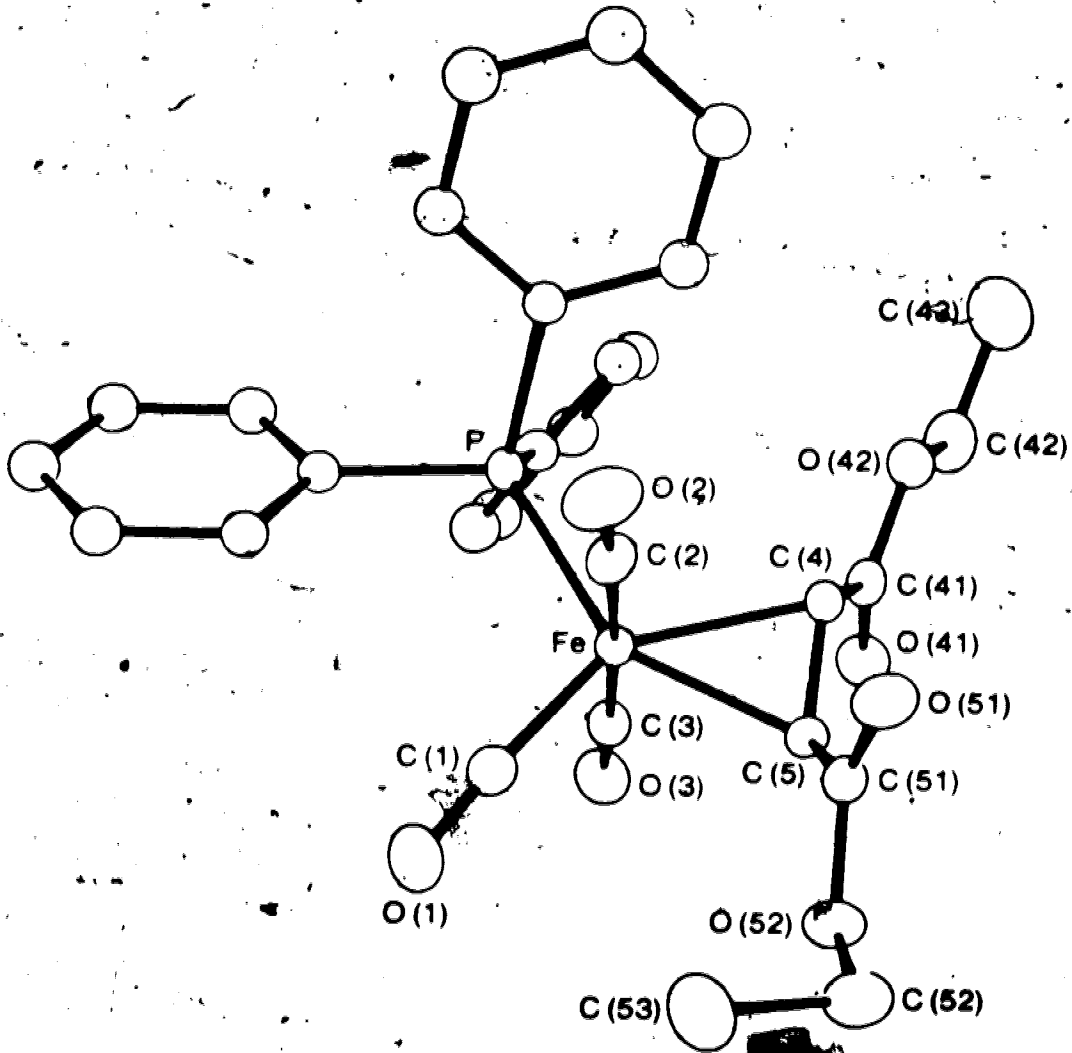


FIGURE 32. Perspective View of $\text{Fe}(\text{CO})_3(\text{PPh}_3)$ (fum).

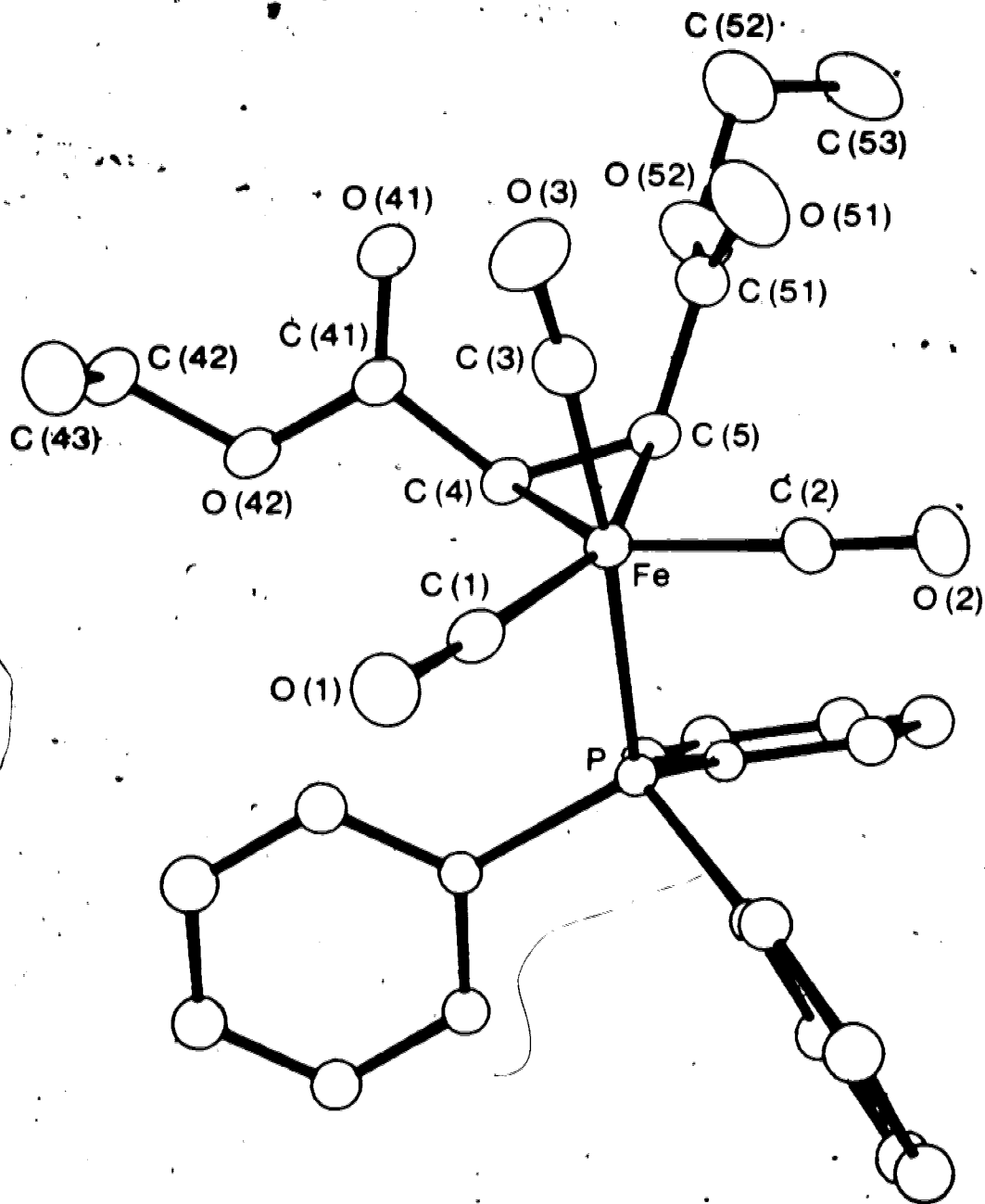


FIGURE 33. Perspective View of $\text{Fe}(\text{CO})_3(\text{PPh}_3)(\text{mal})$.

of metal olefin complexes (for references see Table 49).

The most interesting feature of the two molecular structures is the site occupied by the triphenyl phosphine ligand. The maleate complex has the phosphine in an axial position while in the fumarate complex it is coordinated in an equatorial site.

The bond lengths and interbond angles for the two complexes are listed in Tables 45 and 46.

Site Preference in $\text{Fe}(\text{CO})_3(\text{PR}_3)(\text{olefin})$ Complexes

Primarily on the basis of symmetry and overlap arguments, Rossi and Hoffmann¹³⁶ have shown that for d^8 trigonal bipyramidal transition metal complexes the stronger σ -donor ligand would preferentially occupy an axial site while the stronger π -acceptor ligand would be found in an equatorial position. These conclusions have received ample experimental verification mainly from X-ray crystallographic studies on numerous five coordinate molecules. Thus, in $\text{Fe}(\text{CO})_4\text{L}$ complexes where L is a stronger σ -donor and weaker π -acceptor than CO, such as PPh_3 ,¹⁴⁰ pyridine¹⁴¹ or CN^- ¹⁴² axial coordination of L is observed.

The relative σ -donor and π -acceptor strength of an olefin with respect to CO clearly depends on the type of olefin under investigation. Nevertheless, structural

Table 45. Bond Lengths and Bond Angles in $\text{Fe}(\text{CO})_3(\text{PPh}_3)(\text{fum})$

i) Bond Lengths (Å)			
Fe-P	2.274(1)		
Fe-C(1)	1.766(5)	C(1)-O(1)	1.141(6)
Fe-C(2)	1.800(5)	C(2)-O(2)	1.137(6)
Fe-C(3)	1.805(5)	C(3)-O(3)	1.140(6)
C(4)-C(5)	1.423(6)		
Fe-C(4)	2.088(4)	Fe-C(5)	2.069(5)
C(4)-C(41)	1.467(6)	C(5)-C(51)	1.462(7)
C(4)-H(4)	0.90(4)	C(5)-H(5)	0.92(4)
C(41)-O(41)	1.201(5)	C(51)-O(51)	1.202(5)
C(41)-O(42)	1.345(6)	C(51)-O(52)	1.343(5)
O(42)-C(42)	1.462(6)	O(52)-C(52)	1.452(6)
C(42)-C(43)	1.486(9)	C(52)-C(53)	1.504(8)
P-C(11)	1.841(2)	P-C(31)	1.838(3)
P-C(21)	1.838(2)		
ii) Bond Angles (deg)			
P-Fe-C(1)	110.0(2)	C(2)-Fe-C(3)	177.2(2)
P-Fe-C(2)	87.6(2)	C(2)-Fe-C(4)	89.4(2)
P-Fe-C(3)	90.8(2)	C(2)-Fe-C(5)	94.7(2)
P-Fe-C(4)	106.2(1)	C(3)-Fe-C(4)	93.2(2)
P-Fe-C(5)	146.0(1)	C(3)-Fe-C(5)	87.8(2)
C(1)-Fe-C(2)	90.4(2)	C(4)-Fe-C(5)	40.0(2)
C(1)-Fe-C(3)	88.0(2)	Fe-C(1)-O(1)	176.4(5)
C(1)-Fe-C(4)	143.7(2)	Fe-C(2)-O(2)	177.0(5)
C(1)-Fe-C(5)	103.9(2)	Fe-C(3)-O(3)	174.7(5)
Fe-C(4)-C(5)	69.3(2)	Fe-C(5)-C(4)	70.7(3)
Fe-C(4)-C(41)	116.4(3)	Fe-C(5)-C(51)	113.8(3)
Fe-C(4)-H(4)	118(3)	Fe-C(5)-H(5)	114(3)
C(5)-C(4)-C(41)	118.7(4)	C(4)-C(5)-C(51)	120.7(4)
C(5)-C(4)-H(4)	118(2)	C(4)-C(5)-H(5)	118(2)
C(41)-C(4)-H(4)	111(2)	C(51)-C(5)-H(5)	112(2)
C(4)-C(41)-O(41)	126.6(5)	C(5)-C(51)-O(51)	126.9(4)
C(4)-C(41)-O(42)	111.1(4)	C(5)-C(51)-O(52)	109.8(4)
O(41)-C(41)-O(42)	122.4(5)	O(51)-C(51)-O(52)	123.3(4)
C(41)-O(42)-C(42)	115.9(4)	C(51)-O(52)-C(52)	117.7(4)
O(42)-C(42)-C(43)	106.8(5)	O(52)-C(52)-C(53)	109.4(5)
C(11)-P-C(21)	102.1(1)	Fe-P-C(11)	116.5(10)
C(11)-P-C(31)	102.2(1)	Fe-P-C(21)	115.0(10)
C(21)-P-C(31)	104.6(1)	Fe-P-C(31)	114.7(12)

Table 46. Bond Lengths and Bond Angles in $\text{Fe}(\text{CO})_3(\text{PPh}_3)(\text{mal})$

i) Bond Lengths (Å)			
Fe-P	2.286 (1)		
Fe-C(1)	1.783 (6)	C(1)-O(1)	1.157 (6)
Fe-C(2)	1.788 (6)	C(2)-C(2)	1.139 (6)
Fe-C(3)	1.796 (6)	C(3)-O(3)	1.134 (6)
C(4)-C(5)	1.415 (8)		
Fe-C(4)	2.077 (5)	Fe-C(5)	2.056 (5)
C(4)-C(41)	1.479 (7)	C(5)-C(51)	1.490 (7)
C(4)-H(4)	0.92 (5)	C(5)-H(5)	0.83 (6)
C(41)-O(41)	1.214 (6)	C(51)-O(51)	1.194 (7)
C(41)-O(42)	1.340 (6)	C(51)-O(52)	1.318 (7)
O(42)-C(42)	1.462 (7)	O(52)-C(52)	1.498 (8)
C(42)-C(43)	1.493 (11)	C(52)-C(53)	1.380 (11)
P-C(11)	1.842 (3)	P-C(31)	1.846 (3)
P-C(21)	1.826 (3)		
ii) Bond Angles (deg)			
P-Fe-C(1)	87.8 (2)	C(2)-Fe-C(3)	91.7 (3)
P-Fe-C(2)	91.9 (2)	C(2)-Fe-C(4)	135.4 (2)
P-Fe-C(3)	172.2 (2)	C(2)-Fe-C(5)	95.7 (2)
P-Fe-C(4)	88.2 (1)	C(3)-Fe-C(4)	94.1 (2)
P-Fe-C(5)	94.7 (2)	C(3)-Fe-C(5)	91.7 (2)
C(1)-Fe-C(2)	109.6 (3)	C(4)-Fe-C(5)	40.0 (2)
C(1)-Fe-C(3)	84.5 (2)	Fe-C(1)-O(1)	175.3 (5)
C(1)-Fe-C(4)	114.9 (2)	Fe-C(2)-O(2)	177.9 (5)
C(1)-Fe-C(5)	154.5 (2)	Fe-C(3)-O(3)	172.5 (5)
Fe-C(4)-C(5)	69.2 (3)	Fe-C(5)-C(4)	70.8 (3)
Fe-C(4)-C(41)	114.2 (4)	Fe-C(5)-C(51)	119.4 (4)
Fe-C(4)-H(4)	110 (4)	Fe-C(5)-H(5)	119 (4)
C(5)-C(4)-C(41)	123.7 (5)	C(4)-C(5)-C(51)	124.1 (5)
C(5)-C(4)-H(4)	115 (4)	C(4)-C(5)-H(5)	113 (4)
C(41)-C(4)-H(4)	114 (4)	C(51)-C(5)-H(5)	108 (4)
C(4)-C(41)-O(41)	125.2 (5)	C(5)-C(51)-O(51)	128.3 (6)
C(4)-C(41)-O(42)	110.6 (4)	C(5)-C(51)-O(52)	110.0 (6)
O(41)-C(41)-O(42)	124.1 (5)	O(51)-C(51)-O(52)	121.7 (6)
C(41)-O(42)-C(42)	117.4 (5)	C(51)-O(52)-C(52)	118.1 (6)
O(42)-C(42)-C(43)	112.3 (6)	O(52)-C(52)-C(53)	110.5 (8)
C(11)-P-C(21)	103.3 (2)	Fe-P-C(11)	115.9 (11)
C(11)-P-C(31)	103.3 (2)	Fe-P-C(21)	113.9 (15)
C(21)-P-C(31)	103.9 (2)	Fe-P-C(31)	115.1 (11)

studies on $\text{Fe}(\text{CO})_4(\text{olefin})$ type complexes have invariably found the olefinic ligand to occupy an equatorial site with the carbon-carbon double bond approximately in the equatorial plane (for references see Table 49). This mode of coordination for an olefin is that found for all pentacoordinate d^8 transition metal complexes and has been predicted also by Hoffmann *et al.*^{136,143} and Veit *et al.*¹³⁷ for olefins and other "single-faced" π -acceptor ligands. The ostensible reason for such ligand arrangement is that it provides for optimum π back-bonding interactions.

The electronically preferred arrangement of ligands for a complex of the type $\text{Fe}(\text{CO})_3(\text{phosphine})(\text{olefin})$ would therefore be axial phosphine, equatorial olefin. This disposition of ligands has been found for $\text{Fe}(\text{CO})_3(\text{PPh}_3)(\text{acry})$ ¹⁴⁴ (acry = methylacrylate) and it is that observed for $\text{Fe}(\text{CO})_3\text{PPh}_3(\text{mal})$. However, the equatorial coordination of the phosphine in the fumarate complex is surprising.

The anomaly can be satisfactorily rationalized if the importance of steric effects upon coordination geometry and the arrangement of the ligands are also recognised and taken into consideration. The olefin being a single-faced π -acceptor ligand is coordinated equatorially with its double bond lying roughly in the

equatorial plane. If the phosphine ligand were now to be coordinated in either axial site the trans arrangement of the substituents in the diethyl fumarate ligand would give rise to severe unfavourable steric interactions with the bulky phosphine. To avoid this situation the phosphine prefers to occupy an equatorial position. Clearly, in this instance, steric effects dominate the electronic site preference in determining the final ligand arrangement in the molecule. It should be noted that in both the acrylate and maleate complexes the olefin substituents are directed towards the other side of the molecule away from the triphenyl phosphine ligand as to minimize steric repulsions in the compounds.

Bond Distances in the $\text{Fe}(\text{CO})_3(\text{PPh}_3)$ Molecular Fragment

In addition to the site preference of ligands, Rossi and Hoffmann¹³⁶ have also evaluated the relative strength of the axial and equatorial bonds in trigonal-bipyramidal complexes. Their conclusions concerning d^8 metal compounds can be summarized as follows: metal-ligand σ -bonding results in stronger axial bonds; π -donation will weaken the metal-ligand bonds but greater weakening of the equatorial bonds is anticipated, on the other hand, π -acceptor ligands strengthen the metal-ligand bonding and do so more when the ligand occupies an equatorial

site. As expected the conclusions parallel the site preference arguments.

In organometallic complexes where the ligands are both σ -donors and π -acceptors, the opposing nature of σ and π effects on bonding indicate that the observed distances are determined by the relative σ and π bonding capabilities of the ligands. Not surprisingly the relative lengths of axial and equatorial Fe-CO bonds in $\text{Fe}(\text{CO})_5$ and its derivative have generated considerable, if not always harmonious, debate.

The metal-carbonyl bond lengths for several trigonal bipyramidal iron carbonyl complexes are given in Table 47.

In $\text{Fe}(\text{CO})_5$ the axial metal-carbonyl bond is shorter than the equatorial one, this would be consistent with the σ effect being dominant. Replacement of an axial CO with a better σ -donor and weaker π -acceptor ligand such as pyridine,¹⁴¹ pyrazine¹⁴¹ or CN^- ¹⁴² shortens both axial and equatorial bonds, as expected from the greater amount of back bonding to the carbonyl ligands in these complexes. However, this trend is not universally observed since in $\text{Fe}(\text{CO})_4\text{L}$ (L = PPh_2 ,¹⁴⁷ PPh_3 ¹⁴⁰) the equatorial bonds appear to exhibit greater contraction. Preferential back bonding to the equatorial carbonyl moieties, vide supra, was invoked to account for the observed distances. In $\text{Fe}(\text{CO})_4$ (olefin) complexes the metal-carbonyl distances

Table 47. Metal Carbonyl Bond Lengths (Å) for Some
Trigonal Bipyramidal Iron Carbonyl Complexes

Compound	Fe-C _{axial}	Fe-C _{equatorial}	Reference
Fe(CO) ₅ X-ray		1.82(2)	145
Electron diff.	1.806(3)	1.833(2)	146
[Fe(CO) ₄ (CN)] ⁻	1.723(8)	1.768(8)	142
Fe(CO) ₄ (py)	1.772(7)	1.805(8)	141
Fe(CO) ₄ (pyr)	1.774(4)	1.810(4)	141
Fe(CO) ₄ (PPh ₂)	1.792(8)	1.793(9)	147
Fe(CO) ₄ (PPh ₃)	1.795(2)	1.795(4)	140
[Fe(CO) ₄] ₂ (C ₈ H ₁₂)	1.805(7)	1.782(8)	148
Fe(CO) ₄ (C ₁₂ H ₈)	1.812(3)	1.793(10)	149
[Fe(CO) ₄] ₂ (dppf)	1.816(6)	1.783(6)	150
Fe(CO) ₄ (C ₂ F ₄)	1.823(10)	1.846(10)	151
Fe(CO) ₃ (PPh ₃)- (acry)	1.784(2)	1.781(2)	144
Fe(CO) ₃ (PPh ₃)(mal)	1.796(6)	1.786(6)	this work
Fe(CO) ₃ (PPh ₃)(fum)	1.803(5)	1.766(5)	this work

reflect the relative π -acidity of the olefinic ligands. Since the olefin occupies an equatorial position it is the equatorial metal-carbonyl distances which are not affected by olefin substitution. In general, olefinic ligands are weaker π -acids than carbon monoxide and it is the equatorial carbonyls which are more tightly bonded to iron (cf. structures of $\text{Fe}(\text{CO})_4$, 1,5-cyclooctadiene, C_8H_{12} ,¹⁴⁸ acenaphthylene, C_{12}H_8 ,¹⁴⁹ and diphenylfulvene, dpf ¹⁵⁰); only with the very strong π -acceptor, tetrafluoroethylene, does the converse appear to be true.

In discussing the metal-carbonyl bond distances in $\text{Fe}(\text{CO})_3(\text{PPh}_3)(\text{olefin})$ complexes, the distribution of ligands must also be considered. Ligand arrangement in the acrylate and maleate complexes is consistent with the electronic site preference arguments and as a result the molecules can be considered to be derivatives of $\text{Fe}(\text{CO})_4\text{PPh}_3$. Therefore in going from $\text{Fe}(\text{CO})_4\text{PPh}_3$ to $\text{Fe}(\text{CO})_3(\text{PPh}_3)(\text{olefin})$ (olefin = mal, acry) little change would be expected in the axial metal-carbonyl bond lengths and the equatorial bonds would be expected to change dependent on the relative π -acidity of the olefin compared to CO. The expectations are borne out by the observed distances and indicate that diethylmaleate is comparable in π -acidity to CO. The marginal increase in the metal-carbonyl distance between the acrylate and maleate

derivative confirms the view^{152,153} that the latter olefin is a better π -acid than the former.

In considering the fumarate complex our point of reference is an $\text{Fe}(\text{CO})_4(\text{olefin})$ complex in which the equatorial bonds are almost always shorter than axial bonds. Substitution of an equatorial carbonyl in a $\text{Fe}(\text{CO})_4(\text{olefin})$ complex by PPh_3 a weaker π -acceptor than CO should strengthen the π interaction between the metal and the sole remaining equatorial carbonyl and thus further shorten this bond length with respect to the axial metal-carbonyl distance. This is indeed what is observed.

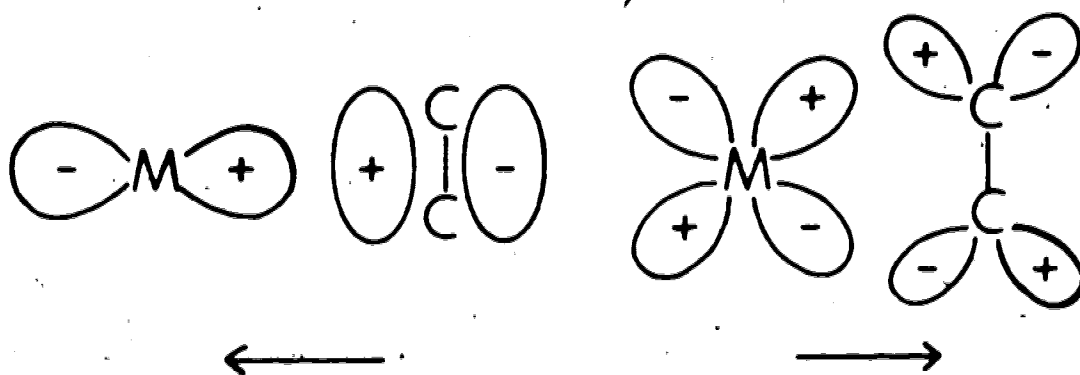
Finally, we note that the Fe-P distances in these complexes are similar to those found in $\text{Fe}(\text{CO})_4\text{PPh}_3$ ¹⁴⁰ (2.244(11) Å) and $\text{Fe}(\text{CO})_3(\text{PPh}_3)(\text{acry})$ ¹⁴⁴ (2.275(1) Å). Surprisingly the equatorially substituted phosphine in the fumarate derivative has a marginally shorter Fe-P bond (2.274(1) Å) than the phosphine ligand in the maleate complex which occupies an axial site (2.286(1) Å).

Geometry and Bond Distances in the Fe-olefin Molecular Fragment

Bonding between an olefinic ligand and a metal atom was first successfully described by Dewar¹⁵⁴ and later applied to the description of the bonding in Zeise's salt by Chatt and Duncanson.¹⁵⁵ This so called

Dewar-Chat-Duncanson model is now the most widely accepted qualitative description for metal-olefin bonding and the bonding to other unsaturated organic ligands as well. The bonding arrangement is shown in Scheme 6. It involves

SCHEME 6:



formation of a σ -bond by donation of π -electrons from the olefin to the metal and the formation of a π -bond by back-donation from filled metal d-orbitals into the empty π^* -orbital of the olefin.

Population of the π^* orbital reduces the bond order of the olefin double bond and results in a bending back of the olefinic substituents out of the plane of the olefin and away from the metal.

Consideration of a limiting case of the bonding scheme in which two electrons are donated in the forward σ -bond and two electrons are returned in the π -back bond

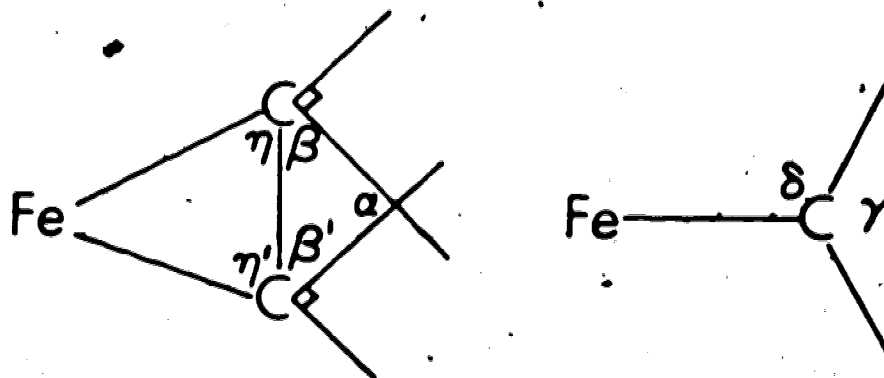
gives the metallocyclopropane model of olefin coordination.

In both models the carbon atoms may be considered to undergo a rehybridization from sp^2 towards sp^3 : The metal-carbon bonds having more p character than the external olefin-substituent bonds.

Although the relative importance of σ and π contributions to the metal-olefin bonding is difficult to assess, as the electronegativity of the unsaturated ligand increases back-bonding becomes more important. Since it has been shown that with electron rich $Fe(O)^{152,153}$ and $Ni(O)^{156,157}$ olefin complexes the π component is the most important bonding factor, the nonplanarity of the olefinic ligand and the metal-carbon distances are expected to reflect the π -acidity of the olefin.

The dihedral angles and interbond angles that have been used to describe the degree of deformation of the coordinated olefin are shown in Scheme 7. The angle β is

SCHEME 7:



is the angle between the olefin carbon-carbon double bond and the normal to the plane defined by the substituent atoms, α is the angle between the plane normals. Because of the larger errors normally associated with the positions of the hydrogen atoms in X-ray structures an alternative measure of bending back are the torsion angles, δ and γ , of the substituent groups about the olefin double bond.

Reference to the tabulation of olefin complexes by Ittel and Ibers¹⁵⁸ shows that, as predicted, the bending is least for hydrogen atoms, increases for ester and cyano groups and is greatest for halogen substituents. The values of α , β , γ and δ for $\text{Fe}(\text{CO})_3(\text{PPh}_3)(\text{fum})$ and $\text{Fe}(\text{CO})_3(\text{PPh}_3)(\text{mal})$ are listed in Table 48. For the fumarate complex the δ angles are not too dissimilar for the two carboethoxy substituents, $109.6(4)^\circ$ and $106.8(4)^\circ$ for C(41) and C(51), respectively. Both carboethoxy groups are oriented in the same manner with respect to the olefin and the slightly larger angle at C(41) may be due to steric interactions with the adjacent triphenylphosphine ligand. The value of γ for the fumarate complex is $142(3)^\circ$, slightly smaller than the average value of $150(4)^\circ$ found in $\text{Fe}(\text{CO})_4$ (fumaric acid),¹⁵⁹ and taken together with the other angles in Table 48 indicates that the degree of bending back of the olefin is about the same

Table 48. Angles describing the geometry of the coordinated olefin.

		MALEATE	FUMARATE
δ^a	C(41)	105.9(5)	109.6(4)
	C(51)	113.0(6)	106.8(8)
	H(4)	103(4)	111(3)
	H(5)	113(4)	108(3)
γ^a	C(4)	151(4)	139(3)
	C(5)	133(4)	145(3)
β	C(4)	66(3)	57(2)
	C(5)	54(3)	62(2)
α		60(4)	61(3)
η	C(4)	69.2(3)	69.3(2)
	C(5)	70.8(3)	70.7(2)

^a δ and γ are torsion angles about the C(4)-C(5) bond. δ for the substituent atom C(41) is the torsion angle between the Fe-C(4) bond and the C(4)-C(41) bond. The idealized value of δ for no bending back of the olefin is therefore 90°. γ for C(4) is the torsion angle between the C(4)-C(41) and C(4)-H(4) bonds about the C(4)-C(5) bond. The idealized value of γ for no bending back is 180°.

as that observed¹⁵⁸ in the tcne complexes Ni (^tBuNC)₂(tcne)¹⁶⁰ and Pt(PPh₃)₂(tcne)¹⁶¹, but not as great as that found for the olefin in Pt(PPh₃)₂(Cl₂CCl₂).¹⁶²

The maleate derivative has δ angles of 105.9(5) and 113.0(6) for C(41) and C(51), respectively. This difference between the two is clearly due to the distinctly different orientations of the two ester substituents. The orientations of the olefin substituents observed in the maleate and fumarate complexes are the result of both steric and electronic influences.

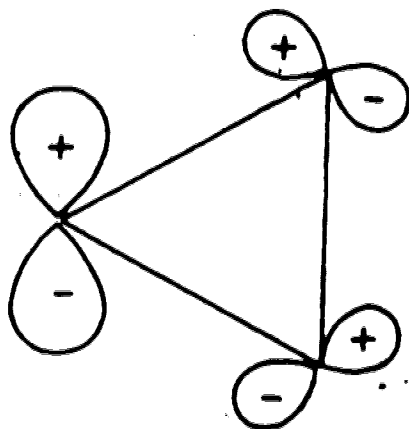
Steric interactions between the carboethoxy groups and the axial carbonyl ligands in the fumarate complex are minimized in the conformation observed where the planes formed by atom O(41), C(41), O(42), C(4) and O(51), C(51), O(52), C(5) are close to being coplanar with the olefin planes C(41), C(4), C(5) and C(51), C(5), C(4), respectively. This conformation is observed for the ester group in the acrylate complex, Fe(CO)₃(PPh₃)(acry) as well.

For the maleate complex both substituents cannot adopt such a conformation because the cis arrangement of the olefin makes such an arrangement sterically very unfavourable. The maleate therefore has one carboethoxy group oriented as those in the fumarate complex while the other is approximately perpendicular to this. The

observed orientations minimize both intraligand (olefin) and interligand steric interactions.

The metallocyclopropane model of metal olefin bonding can be used to predict the electronically preferred conformation of the carboethoxy groups which are π withdrawing substituents. The similarity between the orbitals involved in the conventional Dewar-Chatt-Duncanson concept, Scheme 6, and the highest occupied molecular orbital, HOMO, of cyclopropane capable of interacting with π -substituents in the Walsh model, Scheme 8, is evident.¹⁶³ Thus, the Walsh model which

SCHEME 8:



has been used successfully to explain the conjugation of cyclopropane with π -bonding substituents can also be applied to investigate the effect of π interaction in metal-olefin complexes.

Reference to the Scheme shows that conjugation of the HOMO with the π^* orbital of the carbonyl group of

the carboethoxy substituent has a stabilizing influence on the newly formed molecular orbital. Maximum interaction between the π^* orbital of the ester carbonyl and the metallocyclopropane HOMO occurs when the O(41), C(41), C(4), O(42) and O(51), C(51), C(5), O(52) planes are perpendicular to the Fe, C(4), C(5) plane.

The angles between these planes for substituents at C(4) and C(5) are 79° and 76° , respectively for the fumarate and 78° and 54° for the maleate derivatives. The corresponding angle in the acrylate complex is 81° .

The torsion angles about the C(41)-C(4) bond and C(51)-C(5) bond (the dihedral angle between planes O(41), C(41), C(4) and C(41), C(4), C(5), and O(51), C(51), C(5) and C(51), C(5), C(4)) are $16.1(7)^\circ$ and $6.1(7)^\circ$, respectively for the fumarate. The corresponding values for the maleate are $7.5(9)^\circ$ and $79.5(9)^\circ$. For the acrylate the torsion angle is 10° .

These angles are directly dependent on the degree of bending back of the olefin substituents, which is described by the angle β . As the substituents are bent back more the plane of the substituent must rotate, increasing the torsion angle, in order to remain perpendicular to Fe C(4) C(5) plane. The hypothetical torsion angles where substituent planes would be perpendicular to the Fe, C(4), C(5) plane are 33° and 28° for C(41) and C(51), respectively.

Thus both olefin substituents of the fumarate and one of the maleate complex have conformations intermediate between being coplanar with the olefin and perpendicular to the Fe, C(4), C(5) plane. The remaining ester group of the maleate moiety is grossly distorted from the preferred orientation for π -stabilization, this has already been attributed to steric congestion in this ligand system. Nevertheless, it appears that the metallocyclopropane model presents an oversimplified picture for the bonding of olefin to iron in these complexes.

Another test for the metallocyclopropane bonding model are the angles at the bonded carbon atom. The anticipated tetrahedral geometry for these atoms cannot be achieved because of severe strain imposed by the three membered ring. A geometrical model has been proposed by Guggenberger and Cramer¹⁶⁴ to account for the simplest of steric considerations. In this model α_T and β_T are calculated using η , the internal angle at the carbon atom of the olefin, and represent the hypothetical values of α and β if a true metallocyclopropane structure were found. The planes containing the substituents in this situation would contain the bisectors of the internal ring angles at the coordinated olefin. Thus

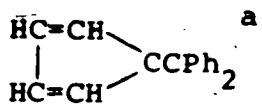
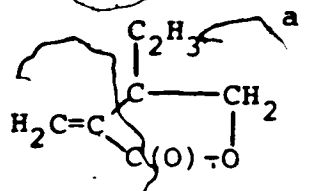
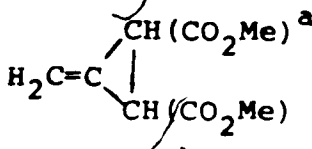
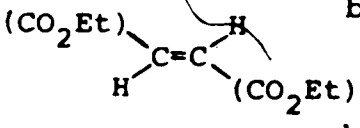
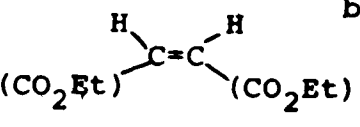
$$\alpha_T = \frac{\eta}{2} + \frac{\eta'}{2}, \quad \beta_T = 90 - \frac{\eta}{2}, \quad \beta_T = 90 - \frac{\eta'}{2}.$$

The calculated values are: $\text{Fe}(\text{CO})_3(\text{PPh}_3)$ (fumarate)
 $\alpha_{\text{T}} = 70^\circ$, $\beta_{\text{T,C}(4)} = 55.3^\circ$, $\beta_{\text{T,C}(5)} = 54.6^\circ$;
 $\text{Fe}(\text{CO})_3(\text{PPh}_3)$ (maleate) $\alpha_{\text{T}} = 70^\circ$, $\beta_{\text{T,C}(4)} = 55.4^\circ$,
 $\beta_{\text{T,C}(5)} = 54.5^\circ$. Reference to Table 48 show that α_{T}
 is consistently larger, and β_{T} is, with the exception
 of the sterically congested ester group of the maleate
 complex, consistently smaller than the experimental
 values. Thus, excessive bending back is predicted based
 on the "pure" metallocyclopropane model. This seems to
 be a general result for the majority of olefinic ligands
 and only halogen-substituted olefins produce bending
 back of the substituents greater than predicted.¹⁵⁸

The iron-olefin carbon bond lengths of several
 $\text{Fe}(\text{CO})_2(\text{olefin})$ and $\text{Fe}(\text{CO})_3(\text{PPh}_3)(\text{olefin})$ complexes are
 listed in Table 49. The general trend in the metal-carbon
 distances reflects the π -acidity of olefinic ligands;
 the shortest distances are found with the strongly π -
 accepting olefin, tetrafluoroethylene. The trend
 corroborates the contention that in these molecules the
 π -back bonding is the more important component of the
 metal-olefin interaction. As expected, it also parallels
 the trend observed for the bending back of the substituents
 on the olefinic ligands.

Concentrating on the $\text{Fe}(\text{CO})_3(\text{PPh}_3)(\text{olefin})$ complexes
 it can be seen that the greater π -acidity of the disub-
 stituted olefins results in shorter metal-carbon bond

Table 49. Fe-C(olefin) and C-C Double Bond Lengths in Fe(CO)₄(olefin)^a and Fe(CO)₃(PPh₃)(olefin)^b Complexes.^c

Olefin	Fe-C(5), Å	Fe-C(4), Å	C(5)-C(4) Å	Ref.
C ₁₂ H ₈ ^a	2.146(3)	2.156(4)	1.421(5)	149
	2.147(3)	2.160(4)	1.404(4)	150
F ₂ C=CF ₂ ^a	1.989(10)	1.989(10)	1.530(16)	151
	2.098(5)	2.127(4)	1.408(7)	166
	2.092(7)	2.024(5)	1.401(9)	167
H ₂ C=CHCO ₂ Me ^b	2.092(2)	2.106(2)	1.413(3)	144
	2.069(5)	2.088(4)	1.423(6)	this work
	2.056(5)	2.077(5)	1.415(8)	this work

^aFe(CO)₄(olefin) complexes.

^bFe(CO)₃(PPh₃)(olefin) complexes.

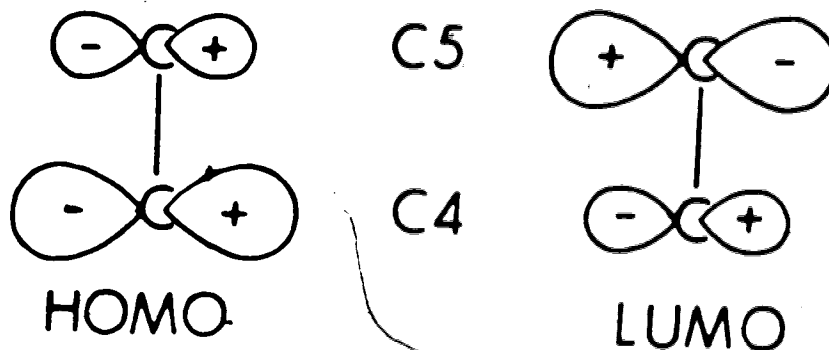
^cIn the complexed olefin the first olefinic carbon atom as written is labeled C(5) and the second C(4).

lengths in the fumarate and maleate derivatives than in the acrylate substituted compound. However, this greater π -acidity is not reflected in significantly different carbon-carbon double bond lengths. This lack of sensitivity of the coordinated double bond to the nature of the olefin substituents has been noted previously^{158,165} and this is also evident from Table 49, where only the $F_2C=CF_2$ distance is significantly different from the other values.

Closer examination of the data listed in the table also reveals that the complexes containing unsymmetrically substituted olefins possess unequal metal-olefin carbon bond lengths. It is seen that, with the exception of, Feist's acid ($H_2CC(CHCO_2Me)_2$), the metal-carbon bond length to the carbon carrying the π -withdrawing substituent (C(4)) is longer than the other distance. The fumarate and maleate derivatives represent somewhat special cases and will be treated separately.

This bonding asymmetry can be explained successfully when the polarization of the olefin π and π^* orbitals by π -acceptor substituents is also taken into account. Libit and Hoffmann¹⁶⁸ have shown that the polarization is in the sense illustrated in Scheme 9. Since in these Fe(O)-olefin complexes the back-bonding into the π^* orbital of the olefin is more important than the forward

SCHEME 9:



σ -donation, it is clear from Scheme 9 that a shortening of the metal-carbon bond opposite to the site of π -acceptor substituent should and does result.

The differences between the two bond lengths in the acrylate complex is significant but small and this is a little surprising in view of the large asymmetry of the olefin. In the fumarate complex the olefin is symmetrically substituted and the ester functionalities are oriented in the same fashion, the two ends of the olefin are rendered inequivalent by the phosphine ligand occupying an equatorial site of the trigonal bipyramid. The difference in the bond lengths is small and at the limit of being significant. Nevertheless, it is gratifying to see that it is the metal-carbon bond adjacent to the phosphine ligand which is longer. Steric repulsion from the bulky triphenyl phosphine is expected to lengthen this bond. Further, since the phosphine is a weaker π -acceptor than carbon monoxide it makes more electron density on the iron available for back bonding to C(5) which is trans to the

phosphine. Both these effects act to shorten the Fe-C(5) bond relative to the Fe-C(4).

In the maleate derivative the situation of having one ester group in a conformation in which it can act as a π -withdrawing group and the other effectively orthogonal to this orientation yields a truly asymmetric olefinic ligand. The difference in metal-carbon distances is again small, but the shorter Fe-C(5) bond is, as predicted, across from the π -accepting ester substituent. The fact that differences in substituent orientation, and the so produced subtle electronic changes, can produce detectable changes in iron-olefin carbon bond lengths which follow the predictions of Hoffmann's polarization model is a clear vindication of the theory.



REFERENCES

1. Cotton, F.A.; Wilkinson, G. "Advanced Inorganic Chemistry. A Comprehensive Text", 3rd ed.; International Science Publishers: New York, 1972; p 1056.
2. Cotton, S.A.; Hart, F.A. "The Heavy Transition Elements"; Macmillan: London, 1975; p 188.
3. Moeller, T. In "MTP International Review of Science, Inorganic Chemistry, Series One"; Emeleus, H.J.; Bagnall, K.W., Ed.; University Park Press, Baltimore, Md., 1972; Vol 7, p 275.
4. Shannon, R.D. Acta Crystallogr. Sect. A, 1976, 32, 751.
5. Watkins, E.D.; Cunningham, J.A.; Phillips, T.; Sands, D.E.; Wagner, W.F. Inorg. Chem. 1969, 8, 29.
6. Wasson, S.J.S.; Sands, D.E.; Wagner, W.F. Inorg. Chem. 1973, 12, 187.
7. Cunningham, J.A.; Sands, D.E.; Wagner, W.F. Inorg. Chem. 1967, 6, 499.
8. Horrocks, W.DeW.; Sipe, J.P.; Luber, J.R. J. Am. Chem. Soc. 1971, 93, 5258.
9. Pinkerton, A.A.; Earl, W.L. J. Chem. Soc. Dalton, 1978, 267.
10. Arhland, S.; Chatt, J.; Davies, N.R., Quart. Rev. Chem. Soc., 1958, 12, 265.
11. Pearson, R.G. J. Am. Chem. Soc. 1963, 85, 3533.

12. Koppikar, D.K.; Sivapullaiah, P.V.; Ramakrishnan, L.; Soundararajan, S. Structure and Bonding, 1978, 34, 135.
13. Forsberg, J.H. Coord. Chem. Rev. 1973, 10, 195.
14. Forsberg, J.H.; Moeller, T. Inorg. Chem. 1969, 8, 883.
15. Charpentier, L.J.; Moeller, T. J. Inorg. Nucl. Chem. 1970, 32, 3575.
16. Durham, D.A.; Frost, G.H.; Hart, F.A. J. Inorg. Nucl. Chem. 1969, 31, 833.
17. Frost, G.H.; Hart, F.A.; Heath, C.; Hursthouse, M.B. Chem. Comm. 1969, 1421
18. Siddall, T.H.; Stewart, W.E. J. Inorg. Nucl. Chem. 1970, 32, 1147.
19. Ciampolini, M.; Nardi, N.; Lamaino, P.; Orioli, P. J. Chem. Soc. Dalton, 1977, 379.
20. Pinkerton, A.A.; Meseri, Y.; Reider, C. J. Chem. Soc. Dalton 1978, 85.
21. Kanellakopoulos, B.; Bagnall, K.W. In "MTP International Review of Science, Series One"; Emeleus, H.J.; Bagnall, K.W., Ed.; University Park Press: Baltimore, Md., 1972; Vol 7, p 229.
22. Baker, E.C.; Halstead, G.W.; Raymond, K.N. Structure and Bonding, 1976, 25, 23.
23. Marks, T.J. Prog. Inorg. Chem. 1978, 24, 51.

24. Marks, T.J.; Fischer, R.D., Ed.; "Organometallics of the f-elements, Proc. NATO Advanced Study Inst., Sogesta, Italy, 1978"; D. Reidel: Dordrecht, Holland, 1979.
25. Raymond, K.N.; Eigenbrot, Jr., C.W. Accts. Chem. Res. 1980, 13, 276.
26. Trofimenko, S. J. Am. Chem. Soc. 1966, 88, 1842.
27. Trofimenko, S. Accts. Chem. Res. 1971, 4, 17.
28. Trofimenko, S. Chem. Rev. 1972, 72, 497.
29. Shaver, A. J. Organometal. Chem. Libr. 1977, 3, 157.
30. Manzer, L.E. J. Organometal. Chem. 1975, 102, 167.
31. Burchill, P; Wallbridge, M.G.H. Inorg. Nucl. Chem. Lett. 1976, 12, 93.
32. Bagnall, K.W.; Edwards, J.; du Preez, J.G.H.; Warren, R.F. J. Chem. Soc. Dalton 1975, 140.
33. Bagnall, K.W.; Edwards, J.; Heatley, F. In "Transplutonium Elements", Müller, W; Lindner, R., Ed.; North Holland, 1976.
34. Bagnall, K.W.; Behestiti, A.; Edwards, J.; Heatley, F.; Tempest, A.C. J. Chem. Soc. Dalton 1979, 1241.
35. Bagnall, K.W.; Tempest, A.C.; Takats, J.; Masino, A.P. Inorg. Nucl. Chem. Lett. 1976, 12, 555.
36. Masino, A.P. Ph.D. Dissertation, University of Alberta, 1978.

37. Moseley, P.T. In "MTP Int. Review of Science, Inorg. Chem. Series Two"; Emeleus, H.J.; Bagnall, K.W., Ed.; University Park Press: Baltimore, Md., 1975; Vol 7, p 65.
38. Sinha, S.P. Structure and Bonding 1976, 25, 69.
39. Muetterties, E.L.; Wright, C.M. Quart. Rev. 1967, 21, 109.
40. Lippard, S.J. Prog. Inorg. Chem. 1967, 8, 109.
41. Drew, M.G.B. Coord. Chem. Rev. 1977, 24, 179.
42. Hoard, J.L.; Silvertorn, J.V. Inorg. Chem. 1963, 2, 235.
43. Al-Karaghoul, A.R.; Day, R.O.; Wood, J.S. Inorg. Chem. 1978, 17, 3702.
44. Kepert, D.L. J. Chem. Soc. 1965, 4736.
45. Parish, R.V.; Perkins, P.G. J. Chem. Soc. A 1970, 345.
46. King, R.B. J. Am. Chem. Soc. 1970, 92, 6455.
47. Kepert, D.L. Prog. Inorg. Chem. 1978, 24, 179.
48. Blight, D.G.; Kepert, D.L. Theor. Chim. Acta 1968, 11, 51.
49. Porai-Koshits, M.A.; Aslanov, L.A. Zh. Strukt. Khim. 1972, 13, 266.
50. Muetterties, E.L.; Guggenberger, L.J. J. Am. Chem. Soc. 1974, 96, 1748.
51. Lippard, S.J.; Russ, B.J. Inorg. Chem. 1968, 7, 1688.
52. Dollase, W.A. Acta Crystallogr., Sect. A 1974, 30, 513.

53. Steffen, W.L.; Fay, R.C. Inorg. Chem. 1978, 17, 779.
54. The computer programs used in the data collection solution and refinement are listed in Appendix 1.
55. The error in observation of unit weight is $[\sum w(|F_o| - |F_c|)^2 / (N_o - N_v)]^{1/2}$ where N_o is the number of observations and N_v the number of variables.
56. Doedens, R.J.; Ibers, J.A. Inorg. Chem. 1967, 6, 204.
57. Stout, G.H.; Jensen, L.H. "X-ray Structure Determination"; Macmillan: London, 1968.
58. Buerger, M.J. "Crystal Structure Analysis"; Wiley: New York, 1960.
59. Buerger, M.J. "Vector Space"; Wiley: New York, 1959.
60. "International Tables for X-ray Crystallography", 3rd ed.; The Kynoch Press: Birmingham, England, 1974.
61. Patterson, A.L. Z. Krist. 1935, A90, 517.
62. Reference 60, Vol IV, Table 2.2A.
63. Stewart, R.F.; Davidson, E.R.; Simpson, W.T. J. Chem. Phys. 1965, 42, 3175.
64. Cromer, D.T.; Liberman, D.J. J. Chem. Phys. 1970, 53, 1891.
65. Albertson, J. Acta Chem. Scand. 1972, 26, 1023 and references therein.
66. Churchill, M.R.; Gold, K.; Maw, Jr, C.E. Inorg. Chem. 1970, 9, 1597.
67. Holt, E.M.; Holt, S.L.; Cavalito, F.; Watson, K.J. Acta Chem. Scand. 1976, A30, 225.

68. Guggenberger, L.J.; Prewitt, C.T.; Meakin, P.; Trofimenko, S.; Jesson, J.P. Inorg. Chem. 1973, 12, 508.
69. Hinckley, C.C. J. Am. Chem. Soc. 1969, 91, 5160.
70. Reuben, J. Progr. Nucl. Magn. Reson. Spectrosc. 1973, 9, 1.
71. Sievers, R.E., Ed. "Nuclear Magnetic Resonance Shift Reagents"; Academic Press: New York, 1973.
72. Mayo, B.C. Chem. Soc. Rev. 1973, 2, 49.
73. Flockhart, B.D. CRC Crit. Rev. Anal. Chem. 1 6, 69.
74. Horrocks, W.Dew. In "NMR of Paramagnetic Molecules", LaMar, G.N.; Horrocks, W.Dew.; Holm, R.H., Ed.; Academic Press: New York, 1973; p 479.
75. von Ammon, R.; Fischer, R.D. Angew. Chem., Int. Ed. Engl. 1972, 11, 675.
76. Wilcott, M.R.; Davis, R.E. Science 1975, 190, 850.
77. Glasel, J.A.; Prog. Inorg. Chem. 1973, 18, 383.
78. Fermi, E. Z. Phys. 1930, 60, 320.
79. Lewis, W.B.; Jackson, J.A.; Lemons, J.F.; Taube, H. J. Chem. Phys. 1962, 36, 694.
80. Golding, R.M.; Halton, M.P. Aust. J. Chem. 1972, 25, 2577.
81. Watson, R.E.; Freeman, A.J. Phys. Rev. Lett., 1961, 6, 277.

82. McGarvey, B.R.; Kurland, R.J. In "NMR of Paramagnetic Molecules", Lammi, J.N.; Horrocks, W.DeW.; Holm, R.H. Ed.; Academic Press: New York, 1973; p 559.
83. McConnell, H.M.; Robertson, R.E. J. Chem. Phys. 1958, 29, 1361.
84. Bleaney, B. J. Magn. Reson. 1972, 8, 91.
85. Jesson, J.P. J. Chem. Phys. 1967, 47, 582.
86. Briggs, J.; Hart, F.A.; Moss, G.P. Chem. Comm. 1970. 1506.
87. Briggs, J.; Hart, F.A.; Moss, G.P.; Randall, E.W. Chem. Comm. 1971, 364.
88. Barry, C.D.; Dobson, C.M.; Williams, R.J.P.; Xavier, A.V. J. Chem. Soc. Dalton, 1974, 1765.
89. Birdsall, B.; Birdsall, W.J.M.; Feeney, J.; Thornton, J. J. Am. Chem. Soc. 1975, 97, 2845.
90. Geraldès, C.F.G.C. J. Magn. Reson. 1979, 36, 89.
91. Levine, B.A.; Williams, R.J.P. Proc. R. Soc. Lond. A 1975, 345, 5.
92. Barry, C.D.; North, A.C.T.; Glasel, J.A., Williams, R.J.P.; Xavier, A.V. Nature 1971, 232, 236.
93. Hawkes, G.E.; Leibfritz, D.; Roberts, D.W.; Roberts, J.D. J. Am. Chem. Soc. 1973, 95, 1659.
94. Wilcott, M.R.; Lenkinski, R.E.; Davis, R.E. J. Am. Chem. Soc. 1972, 94, 1742.

95. Sullivan, G.R. J. Am. Chem. Soc. 1976, 98, 7162.
96. Cramer, R.E.; Seff, K. Acta Crystallogr. Sect. B 1972, 28, 3281.
97. Uebel, J.J.; Wing, R.M. J. Am. Chem. Soc. 1972, 94, 8910.
98. Horrocks, W.Dew.; Sipe, J.P. Science 1972, 177, 994.
99. Briggs, J.M.; Moss, G.P.; Randall, E.W.; Sales, K.D. J.C.S. Chem. Comm. 1972, 1180.
100. Horrocks, W.Dew. J. Am. Chem. Soc. 1974, 96, 3022.
101. DeBoer, J.W.M.; Sakker, P.J.D.; Hilber, C.W.; DeBoer, E. J. Magn. Reson. 1977, 25, 455.
102. Marinetti, T.D.; Snyder, G.H.; Sykes, B.D. J. Am. Chem. Soc. 1975, 97, 6562.
103. Cramer, R.E.; Dubois, R.; Seff, K. J. Am. Chem. Soc. 1974, 96, 4125.
104. Cramer, R.E.; Maynard, R.B. J. Magn. Reson. 1978, 31, 295.
105. Catton, G.A.; Harman, M.E.; Hart, F.A.; Hawkes, G.E.; Moss, G.P. J. Chem. Soc. Dalton 1978, 181.
106. Agresti, D.G.; Lenkinski, R.E.; Glickson, J.D. Biochem. Biophys. Res. Commun. 1977, 76, 711.
107. Campbell, I.D.; Dobson, C.M.; Williams, R.J.P. Proc. R. Soc. Lond. A 1975, 345, 41.
108. Lee, L.; Sykes, B.D. Biophys. J. 1980, 32, 193.
109. Lee, L. Ph.D. Dissertaion, University of Alberta, 1980.

110. Dobson, C.M.; Williams, R.J.P.; Xavier, A.V. J. Chem. Soc. Dalton, 1973, 2662.
111. Reilley, C.N.; Good, B.W.; Desreux, J.F. Analyt. Chem. 1975, 47, 2110.
112. Reilley, C.N.; Good, B.W.; Allendoerfer, R.D. Analyt. Chem. 1976, 48, 1446.
113. Desreux, J.F.; Reilley, C.N. J. Am. Chem. Soc. 1976, 98, 2105.
114. Sherry, A.D.; Yang, P.P.; Morgan, L.O. J. Am. Chem. Soc. 1980, 102, 5755..
115. Horrocks, W.DeW. J. Magn. Reson. 1977, 26, 333.
116. Stout, E.W.; Gutowsky, H.S. J. Magn. Reson. 1976, 24, 389.
117. McGarvey, B.R. J. Magn. Reson. 1979, 33, 445.
118. Lee, L.; Sykes, B.D. J. Magn. Reson. 1980, 41, 512.
119. Reuben, J. J. Magn. Reson. 1973, 11, 103.
120. Trofimenko, S. J. Am. Chem. Soc. 1967, 91, 3170.
121. Jesson, J.P.; Trofimenko, S.; Eaton, D.R. J. Am. Chem. Soc. 1967, 89, 3148.
122. Swift, T.J. In "NMR of Paramagnetic Molecules", LaMar, G.N.; Horrocks, W.DeW.; Holm, R.H., Ed.; Academic Press: New York, 1973; p 53.
123. Marquadt, D.W. J. Soc. Indust. Appl. Math. 1963, 11, 431.
124. Barker, D.R.; Diana, D.M. AJP 1974, 42, 224.

125. See page 158 reference 29 and references therein.
126. Hamilton, W.C. Acta Crystallogr. 1965, 18, 502.
127. von Ammon, R.; Kanellakopoulos, B.; Fishcer, R.D.;
Formacek, V. Z. Naturforsch. 1973, 28B, 200.
128. LaMar, G.N. In "NMR of Paramagnetic Molecules",
LaMar, G.N.; Horrocks, W.DeW.; Holm, R.H., Ed.;
Academic Press: New York, 1973; p 85.
129. Horrocks, W.Dew. In "NMR of Paramagnetic Molecules",
LaMar, G.N.; Horrocks, W.DeW.; Holm, R.H., Ed.;
Academic Press: New York, 1973; p 127.
130. Eaton, D.R. In "NMR of Paramagnetic Molecules",
LaMar, G.N.; Horrocks, W.DeW.; Holm, R.H., Ed.;
Academic Press: New York, 1973; p 179.
131. Hawkes, G.E.; Marzin, C.; Johns, S.R.; Roberts, J.D.
J. Am. Chem. Soc. 1972, 95, 1661.
132. Gansow, O.A.; Loeffler, P.A.; Davis, R.E.; Lenkinski,
R.E.; Willcott, M.R. J. Am. Chem. Soc. 1976, 98,
4250.
133. Eaton, D.R.; Benson, R.E.; Bottomley, C.J.; Josey,
A.D. J. Am. Chem. Soc. 1972, 94, 5996.
134. Sherry, A.D.; Pascual, E. J. Am. Chem. Soc. 1977,
99, 5871.
135. Perrin, D.D.; Armarego, W.L.F.; Perrin, D.F.
"Purification of Laboratory Chemicals", 2nd ed.
Pergamon Press: Oxford 1980.

136. Rossi, A.R.; Hoffmann, R. Inorg. Chem. 1973, 14, 365.
137. Demuynck, J.; Strich, A.; Veillard, A. Nouveau. J. Chimie 1977, 1, 217.
138. Wood, J.S. Progr. Inorg. Chem. 1972, 16, 227.
139. Gittawong, S.; LiShingMan, L.K.K.; Takats, J.
Unpublished results.
140. Riley, P.E.; Davis, R.E. Inorg. Chem. 1980, 19, 159.
141. Cotton, F.A.; Troup, J.M. J. Am. Chem. Soc. 1974, 96, 3438.
142. Gadfield, S.A.; Raymond, K.N. Inorg. Chem. 1974, 13, 770.
143. Albright, T.A.; Hoffmann, R.; Thibeault, J.C.; Thorn, D.L. J. Am. Chem. Soc. 1979, 101, 3807.
144. Krüger, C.; Tsay, Y.-H. Cryst. Struct. Comm. 1976, 5, 219.
145. Hanson, A.W. Acta Crystallogr. 1962, 15, 930.
146. Beagley, B.; Cruickshank, D.W.J.; Pinder, P.M.; Robiette, A.G.; Sheldrick, G.M.; Acta Crystallogr. Sect. B. 1969, 25, 737.
147. Kilbourn, B.T.; Raeburn, K.N.; Thompson, D.T. J. Chem. Soc. A 1969, 1966.
148. Kruger, C. J. Organometal. Chem. 1970, 22, 697.
149. Cotton, F.A.; Lahuerta, P. Inorg. Chem. 1975, 14, 116.
150. Behrens, U. J. Organometal. Chem. 1976, 107, 103.

151. Beagley, B.; Schmidling, D.G.; Cruickshank, D.W.J.
Acta Crystallogr. Sect. B 1973, 29, 1499.
152. Grevels, F.-W.; Koerner von Gustorf, E. Justus
Liebig's Ann. Chem. 1973, 1821.
153. Van Dam H.; Oskam, A. J. Electron Spectrosc. Relat.
Phenom. 1979, 16, 307.
154. Dewar, M.J.S. Bull. Soc. Chim. Fr. 1951, 18, C71.
155. Chatt, J.; Duncanson, L.A. J. Chem. Soc. 1953, 2939.
156. Tolman, C.A.; English, A.D.; Manzer, L.E. Inorg.
Chem. 1975, 14, 2353.
157. Ittel, S.D. Inorg. Chem. 1977, 16, 2589.
158. Ittel, S.D.; Ibers, J.A. Adv. Organometal. Chem.
1976, 14, 33.
159. Pedone, C.; Sirigu, A. Inorg. Chem. 1968, 7, 2614.
160. Stalick, J.K.; Ibers, J.A. J. Am. Chem. Soc. 1970,
92, 5333.
161. Bombieri, G.; Forsellini, E.; Panattoni, C.;
Graziani, R.; Bandoli, G. J. Chem. Soc. A 1970, 1313.
162. Francis, J.N.; McAdam, A.; Ibers, J.A. J. Organometal.
Chem. 1971, 29, 131.
163. Dewar, M.J.S.; Ford, G.P. J. Am. Chem. Soc. 1979, 101,
783.
164. Guggenberger, L.J.; Cramer, R. J. Am. Chem. Soc.
1972, 94, 3779.
165. Baraban, J.M.; McGinnety, J.A. J. Am. Chem. Soc.
1975, 97, 4232.

166. Chisnall, B.M.; Green, M.; Hughes, R.P.; Wells, A.J.
J. Chem. Soc. Dalton 1976, 1899.
167. Whitesides, T.H.; Slaven, R.W.; Calabrese, J.C.
Inorg. Chem. 1974, 13, 1995.
168. Libit, L.; Hoffmann, R. J. Am. Chem. Soc. 1974, 96,
1370.

Appendix 1: Programs Used in Crystal Structure Solution,
Refinement and Analysis.

<u>Author</u>	<u>Program</u>	<u>Description</u>
Northwestern University Version	AGNOST	Absorption correction program using Gaussian integration.
J.A. Ibers A.P. Gaughan	CELREF	Refines crystal alignment and cell parameters.
S.K. Dwight	DATABL	Outputs tables of position and thermal parameters for publication.
A. Zalkin	FORDAP	Fourier summation for Patterson or Fourier maps.
P.D. Cradwick	HATOM	Calculates positions of hydrogen atoms attached to atoms which are sp^3 or sp^2 hybridized.
M.J. Bennett B. Foxman	MMMR	Calculates starting parameters for rigid bodies and hindered rotors.
G. Germain P. Main M.M. Woolfson	MULTAN	General direct methods program.
P. Main C.T. Grainger	NORMAL	Calculates E's, does Wilson statistics. For input to MULTAN.
M.E. Pippy F.R. Ahmed	NRC-22	Calculated least-squares planes.
W. Busing H.A. Levy	ORFPE	Calculates bond lengths, angles and associated standard devia- tions. Modified by W.L. Brooks and M. Elder for hindered rotors and rigid bodies.
C. Johnson	ORTEP	Thermal ellipsoids plotting program.

Appendix 1: (continued).

<u>Author</u>	<u>Program</u>	<u>Description</u>
M.J. Bennett	PMMO	Transforms raw data to intensities, applying corrections.
A.P. Gaughan	PRCNTA	Molecular weight, % composition, density, absorption coefficient calculations from formula and cell.
M. Cowie	PUBE	Sorts data according to any desired sequence of h, k or l.
R.C. Elder	PUBTAB	Prints structure factor amplitude tables, modified by S.K. Dwight for use on the page printer.
S.K. Dwight	RIGIDH	Calculated rigid body parameters for hydrogen atoms.
C.T. Prewitt	SFLS5	Structure factor calculation and least-squares refinement of parameters. Modified by B.M. Foxman and M.J. Bennett for rigid body routine, and by W.L. Hutcheon and M.J. Bennett for the hindered rotor.
S.L. Lawton	TRACERA	General Cell Reduction Program.

[The page contains approximately 25 lines of extremely faint, illegible text, likely a scan of a document with low contrast or significant fading. The text is arranged in a standard left-aligned format.]

Handwritten scribble or signature in the top left corner.

Main body of the document containing dense, mostly illegible text, possibly a list or a series of entries.

[The page contains approximately 25 lines of extremely faint, illegible text, possibly a form or a list. The text is too light to be transcribed accurately.]



Appendix 3: Least-Squares Programs Used in the Analysis of NMR Spectra.

```

C
C      GRUB 4007FIV  PAR=SIZE=50
C      /COMPILE 80LIST 80WARD 80BET
C
C
C      REQUIRES A FUNCTION SUBPROGRAM 'FCALC(BETA,X,DER)' APPROPRIATE
C      TO THE SPECIFIC MODEL  FCALC COMPUTES THE VALUE OF THE MODEL
C      FUNCTION AT THE VALUE OF THE INDEPENDENT VARIABLE X ( X MAY BE
C      A VECTOR IF THERE ARE SEVERAL INDEPENDENT VARIABLES) WITH THE
C      MODEL PARAMETERS BETA  IT ALSO COMPUTES THE DERIVATIVES OF THE
C      MODEL FUNCTION WITH RESPECT TO EACH OF THE PARAMETERS, AND
C      RETURNS THEM IN THE VECTOR DER
C
C
C      NPTS=NUMBER OF POINTS (ISOTROPIC SHIFTS)
C
C      NVAR=NUMBER OF VARIABLES (GEOMETRIC VARIABLES R , THETA , KAPPA )
C
C      NPAR=NUMBER OF PARAMETERS ( B1 ,B2 AND PHI )
C
C      ERR'S AND ERRORS ARE BY(1) ,BX(1,J)
C
C      BY(1) ERROR OR UNCERTAINTY IN ISOTROPIC SHIFT Y(1)
C      BX(1,J) E S D IN GEOMETRIC VARIABLE X(1,J)
C      BEFF(1) = CALCULATED EFFECTIVE VARIANCE OF CALCULATED
C      SHIFT YCALC(1)
C
C      IMPLICIT REAL*8(A-H,O-Z)
C      DATA 10/' '
C      REAL*4 BY
C      CHARACTER*8 NCB(200)
C      COMMON /IMAG/DT,L,ITEST,ERRR,ILINE(100)
C      INTEGER*2 ILINE
C      REAL*8 BETA(10),C(10),D(10,10),DER(10)
C      1 V(200),PSAVE(200),STDEV(10),DEL(10),K(10,200)
C      2 ,PMT(10),BEFF(200),BX(10,200),BY(200),PPRIME(10)
C
C
C      3 ,DIA(200)
C      LOGICAL 80BET:
C      READ,NPAR,NPTS,NVAR,NMAX,EPS,ERRR
C
C      NMAX= MAX NUMBER OF ITERATIONS
C
C      EPS CONVERGENCE TEST PARAMETER
C
C      ERRR = USED IN SUBROUTINES 80NT AND 80BOUT
C      MAXIMUM VALUE OF E S D OR CALCULATED ERROR THAT WILL
C      BE PRINTED AS 1 OR 2 DIGIT NUMBER IN PARENTHESES AFTER
C      A NUMERICAL VALUE IN THE OUTPUT
C      PRINT 1000,NPAR,NPTS,NVAR,NMAX,EPS,ERRR
C      READ,(BETA(1),1),NPAR)
C      PRINT 1010,(BETA(K),K),NPAR)
C      READ,(NCB(1),X(1,1),BX(1,1),J+1,NVAR),V(1),BY(1)
C      1 ,DIA(1),1),NPTS)
C
C      A RUN-TIME FORMAT IS USED HERE TO OUTPUT THE TABLE OF
C      E, Y, YCALC, Y-YCALC AT LINE 51
C
C      READ(5,1005) PMT
C      PRINT 1015
C      DO 10 J = 1 , NPTS
C      10 WRITE(6,PMY) NCB(1),X(1,J),BX(1,J),J+1,NVAR),V(1),BY(1)
C      1YER = 0
C
C      GET THE C-VECTOR AND THE D-MATRIX TO ZERO
C
C      20 DO 20 K = 1 , NPAR
C      C(K) = 0.000
C      DO 20 IS = 1 , NVAR
C      D(IS,K) = 0.000
C      20 CONTINUE
C      DO 30 J = 1 , NPTS
C
C      GET VALUE OF FUNCTION AND DERIVATIVES AT THE J-TN POINT
C      D1=V(1)-FCALC(BETA,X(1,J),DER,PPRIME)
C
C      USE THESE VALUES TO COMPUTE APPROPRIATE TERMS IN SUMMATIONS
C      AND STORE THE RESULTS IN THE C-VECTOR AND THE LOWER HALF OF
C      THE D-MATRIX
C
C      S10 = BY(1)**2
C      DO 25 JVAR = 1 , NVAR
C      25 S10 = S10 + PPRIME(JVAR)*(BX(JVAR,1))**2
C      DO 40 K = 1 , NPAR
C      C(K) = C(K) + D1*DER(K)
C      DO 40 IS = 1 , NVAR
C      40 D(IS,K)=D(IS,K) + DER(IS)*DER(K)/S10
C      50 CONTINUE

```

```

C
C
C      COPY LOWER OFF-DIAGONAL ELEMENTS ACROSS TO UPPER OFF-DIAGONAL
C
      DO 50 K = 1, NPAR
      DO 50 IS = K, NPAR
      DO 50 I(K, IS) = D(I, K)
C
C      INVERT D
C
      CALL EJMIV(NPAR, 10, 0, DRY)
C
C      COMPUTE THE INCREMENTS TO THE PARAMETERS
C
      DO 50 K = 1, NPAR
      S1 = 0.000
      DO 70 IS = 1, NPAR
      TO S1 = S1 + D(K, IS)*C(IS)
      DO DEL(K)=0
      IYER = IYER + 1
      PRINT 1020, IYER, (DEL(K), K+1, NPAR)
      DONE = .TRUE.
C
C      ADD INCREMENTS TO PARAMETERS AND TEST FOR CONVERGENCE
C
      DO 50 K = 1, NPAR
      BETA(K) = BETA(K) + DEL(K)
      IF (DABS(BETA(K) - BPS) LT DABS(DEL(K))) DONE = .FALSE.
      DO CONTINUE
      PRINT 1030, (BETA(K), K+1, NPAR)
      IF ((NOT DONE) AND (IYER LT NMAX)) GO TO 50
      SIGY = 0.000
C
C      COMPUTE THE VARIANCE AND STANDARD DEVIATION IN Y
C
      COMPUTE R FACTORS
      RW = WEIGHTED RELIABILITY FACTOR PERCENT
      R1 BASED ON (Y(I) - PSAVE(I))
      R2 BASED ON SQUARE OF (Y(I) - PSAVE(I))
C
      R1+R2=0
      R1+R2=0
      R2+R2=0
      DO 55 I = 1, NPTS
      PSAVE(I) = FCALC(BETA, K(1:3), DER, PPRIME)
      S1 = SY(I)**2
C
      DO 55 JVAR = 1, NVAR
      S2 = S1 + PPRIME(JVAR)*(S2(JVAR, I))**2
      SEFF(I) = DSORT(S1)
      RSW+RWS = [(Y(I) - PSAVE(I))/SEFF(I)]**2
      R2+R22 = (Y(I) - PSAVE(I))**2
      R2+R22 = Y(I)**2
      R1+R1+DABS(Y(I) - PSAVE(I))
      R1+R1+DABS(Y(I))
      DO 55 SIGY = SIGY + [(Y(I) - PSAVE(I))**2]/S1
      SIGY = SIGY/DFLAGAT(NPTS - NPAR)
      RW = DSORT(RWS/RW) * 100
      R2 = DSORT(R22/R2) * 100
      R1 = (R1/R2) * 100
C
C      COMPUTE STANDARD DEVIATIONS IN EACH OF THE PARAMETERS
C
      DO 55 K = 1, NPAR
      STDEV(K) = DSORT(SIGY)*D(K, K)
      PRINT 1040, NPAR, NPTS, IYER
      PRINT 1050, (BETA(K), STDEV(K), K+1, NPAR)
      PRINT 1060, R-FACTOR 1, R1
      PRINT 1070, R-FACTOR 2, R2
      PRINT 1080, WEIGHTED R, RW
      PRINT 1090
      DO 102 I=1, NPTS
      DO 103 J=1, 70
      ILINE(J)=10
      DO 101 J=1, NVAR
      L=12*(J-1)+3
      ST*BX(J, I)
      CALL EBMV(K, J, I)
      CALL EBMOUT
      L=44
      ST*BY(I)
      CALL EBMV(Y(I))
      CALL EBMOUT
      L=50
      ST*SEFF(I)
      CALL EBMV(PSAVE(I))
      CALL EBMOUT
      WRITE(6, 1100) R2(I), (ILINE(K), K+1, 57), Y(I) - PSAVE(I)
      DO CONTINUE
      STOP
1100 FORMAT(' ', AT, STAB, F8.1)
1000 FORMAT('1000 LINEAR LEAST SQUARES ANALYSIS USING A MODEL '
1 ' WITH 12 PARAMETERS /// THERE ARE 14 DATA POINTS '
2 ' AND 12 INDEPENDENT VARIABLES /// ITERATIONS ARE '
3 ' CONTINUED UNTIL 13 ITERATIONS HAVE BEEN PERFORMED '
4 ' OR THE RELATIVE CORRECTIONS TO THE PARAMETERS '
5 ' FALL BELOW 1PB12 4. / .015)
1010 FORMAT('/// THE INITIAL VALUES OF THE PARAMETERS ARE '
1 ' [(1PB12 4)])

```

```

1015 FORMAT(//// DATA TO BE FIT TO THIS MODEL BY LEAST SQUARES ROUTINE
1// LISTED BY COLUMNS IN THE ORDER X(1,1),SX(1,1),X(2,1),SX(2,1),
2// Y(1),SY(1)///)
1020 FORMAT(/// ITERATION #, IZ// CORRECTIONS TO PARAMETERS
3// (10(IPD12 4))
1030 FORMAT(/// NOW PARAMETERS (10(IPD12 4))
1040 FORMAT(/// RESULTS OF NON-LINEAR LEAST-SQUARES ANALYSIS WITH
4// A MODEL CONTAINING IZ PARAMETERS ON A DATA SET OF
5// IZ POINTS/// IZ ITERATIONS PERFORMED )
1050 FORMAT(/// TABLE OF OBSERVED AND CALCULATED Y-VALUES
6// LISTED BY COLUMNS IN THE ORDER X(1,1), SX(1,1),
7// X(IYAR,1), SX(IYAR,1), YOBS(I), SY(I), YCALC(I),
8// DIFF(I), (YOBS(I)-YCALC(I))//)
1060 FORMAT(1046)
END

```

/OPTIONS NOLIST

C
C
C
C
C
C
C
C
C
C
C

SUBROUTINE ESDDUT AND TOUT ADJUSTS ESD'S AND ERRORS
IN LEAST SIGNIFICANT FIGURE IN X(I,J),Y(I),ETC
TO A 1 OR 2 DIGIT NUMBER IN PARENTHESES

```

SUBROUTINE ESDDUT
COMMON /IMAGE/ST,J,ITEST,NERR,ILINE(100)
INTEGER*2 ILINE,IS(2),IM(10)
DATA IS/'0','1','2','3','4','5','6','7','8','9'//
J,J+1
ILINE(J)=IS(1)
IF(ITEST.LE 100) GO TO 10
ITV=ITEST/10
ITEST=ITEST-ITV*10
ILINE(J+1)=IM(ITV+1)
ILINE(J+2)=IM(ITEST+1)
J,J+2
GO TO 11
10 J,J+1
ILINE(J)=IM(ITEST+1)
J,J+1
11 ILINE(J)=IS(2)
RETURN
END

```

C
C

C
C
C
C

```

SUBROUTINE ESUT(X)
REAL*8 XX,X
COMMON /IMAGE/ST,J,ITEST,NERR,ILINE(100)
INTEGER*2 ILINE,IS(2),IM(10)
DATA IS/'0','1','2','3','4','5','6','7','8','9'//
JCOB=0
DO 10 I=1,6
ITEST=ST+0.5
IF(ITEST.GT.NERR)GO TO 11
ST=ST+10
10 JCOB=1
ITEST=100
RETURN
11 ITEST=ITEST*0.10
IPER=2
JCOB=1
XX=X
20 IF(DABS(XX)*0.5*10**(-1-JCOB).LT.10*0.100) GO TO 12
XX=XX/10.0
IPER=IPER+1
J,J+1
GO TO 20
12 IF(X.LT.0.0)ILINE(J)=IS(2)
XX=DABS(XX)*0.5*10**(-1-JCOB)
DO 12 I=1,JCOB
ITV=XX
XX=XX-DPLBAT(ITV)*10.0
ITV=ITV+1
J,J+1
IF(IPER.NE.100) GO TO 13
ILINE(J)=IS(1)
J,J+1
13 ILINE(J)=IM(ITV)
RETURN
END

```

C
C
C
C
C
C
C
C
C
C
C
C

GAUSS-JORDAN MATRIX INVERSION SUBROUTINE

THE MATRIX A IS INVERTED BY THE GAUSS-JORDAN ELIMINATION
PROCEDURE USING A DOUBLE PIVOTING STRATEGY

IF THE PIVOT ELEMENT ON ANY ELIMINATION STEP IS LESS THAN
1.0E-10 TIMES THE PRODUCT OF THE PREVIOUS PIVOTS, THE
MATRIX IS DEEMED SINGULAR, AND THE VALUE OF THE DETERMINANT
IS SET TO ZERO BEFORE CONTROL IS RETURNED TO THE CALLING
PROGRAM


```

C
C
100 WRITE(0,1000)
DET = 0.000
RETURN
1000 FORMAT('MATRIX IS SINGULAR')
END
/OPTIONS SOLIST
C
C FUNCTION PCALC
C CALCULATES PSEUDOCONTACT SHIPT
C
C BETA(1)=B1 BETA(2)=B2 BETA(3)=PNI
C
C X(1,1)=(DCOSB+STNSYA-1)/R+*3
C X(1,2)=(B1B+2TNSYA)/R+*3
C X(1,3)=0
C
C DERIV(J)=DERIVATIVE OF PCALC WRT BETA(J)
C PPRIME(J)=DERIVATIVE OF PCALC WRT X(1,J)
C
FUNCTION PCALC(BETA,X,DERIV,PPRIME)
IMPLICIT REAL*8(A-H,O-Z)
REAL*8 BETA(3),DERIV(3),PPRIME(3),X(3)
DERIV(1) = X(1)
DERIV(2) = DCOS(0.034904595*(BETA(3)+X(2)))
DERIV(3) = -0.034904595*BETA(2)*X(2)+DBIN(0.034904595*(BETA(3)
+ X(2)))
PPRIME(1) = BETA(1)+*2
PPRIME(2) = (BETA(2)+DERIV(2))+2
PPRIME(3) = DERIV(3)+*2
DERIV(2) = X(2)+DERIV(2)
PCALC = BETA(1)+DERIV(1) + BETA(2)+DERIV(2)
RETURN
END
/EXECUTE
C
C FORMAT FREE INPUT DATA
C
C
3 31 3 10 0.01 0
0 40 -10
*C(12) 2.292 0 00 0 8847 0 03 37 1 1 6 45 7 4 8 128 7
*C(13) 1 824 0 00 0 8813 0 03 100 0 1 6 44 8 4 8 128 7
*C(12) 2 010 0 00 0 8827 0 03 -51 4 1 6 -15 7 4 8 128 7
*C(14) 0 478 0 02 0 8205 0 005 30 2 1 0 16 3 0 4 104 0
*C(44) 0 4250 0 02 0 8070 0 005 100 0 1 0 0 1 0 4 104 0

*C(74) 0 4215 0 02 0 8283 0 005 -101 2 1 0 -14 0 0 4 104 0
*C(15) -0 271 0 005 0 8108 0 002 10 0 0 2 20 0 4 0 128 7
*C(45) -0 2787 0 005 0 7784 0 005 147 3 0 4 -2 0 4 0 128 7
*C(75) -0 288 0 005 0 8064 0 005 -114 3 0 4 -10 7 4 0 128 7
*C(23) -2 082 0 017 2 082 0 017 -60 0 0 3 -51 3 0 0 127 4
*C(23) -2 254 0 018 2 254 0 018 80 0 0 2 -50 4 4 0 127 4
*C(23) -0 2778 0 001 0 2778 0 001 -121 0 0 2 5 3 4 0 127 4
*C(24) -0 8027 0 008 0 8027 0 008 -48 0 0 2 -20 0 0 0 103 0
*C(24) -0 8428 0 008 0 8428 0 008 70 0 0 2 -40 0 0 0 103 0
*C(24) -0 2701 0 001 0 2701 0 001 -102 0 0 2 5 2 0 0 103 0
*C(25) -0 8552 0 008 0 8552 0 008 -23 3 0 2 -7 0 4 0 127 4
*C(25) -0 8844 0 008 0 8844 0 008 80 2 0 2 -48 0 4 0 127 4
*C(25) -0 4880 0 002 0 4880 0 002 -147 0 0 2 11 0 4 0 127 4
*E1] -2 142 0 018 2 142 0 018 0 0 0 2 0 1 0 1 0 -4 1
*E2] -2 142 0 018 2 142 0 018 120 0 0 2 -85 0 1 0 -4 1
*E3] -2 201 0 018 2 201 0 018 -124 0 0 3 20 0 1 0 -4 1
[AT,11P10 3]
/PTCHEND

```

```

C FUNCTION TO CALCULATE PSEUDOCONTACT SHIFTS FOR
C 3 SITE EXCHANGE PROBLEM - SCTP(2) MODEL
C
C THERE ARE 6 SYMMETRIC VARIABLES 3 FOR EACH SITE
C
C R1(J) (J=1,2) ARE DISTANCES R
C R1(J) (J=4,5) ARE ANGLES THETA
C R1(J) (J=7,8) ARE ANGLES X
C
C FUNCTION PCALC(BETA,X,DERIV,PPRIME)
C IMPLICIT REAL*8(A-N,O-Z)
C REAL*8 BETA(3),DERIV(3),PPRIME(3),X(3)
C TANG(3),THETA(3),COS(3),ARRIV(3),SERIV(3)
C DO 10 J=1,3
C ARR(J)=0.0240000000*(BETA(3)+X(J+3))
C TANG(J)=0.01745329*X(J+3)
C COS(J)=1.0/X(J)+.2
C ARRIV(J)=(3.0*(DCOS(THETA(J))+2)-1.0)*COS(J)
C SERIV(J)=DCOS(ANG(J))*(DSIN(THETA(J))+2)*COS(J)
C DERIV(J)=BETA(3)*(DSIN(THETA(J))+2)*COS(J)+(-0.0240000000*
C 1 TANG(J))
C 10 CONTINUE
C PPRIME(1)=[(BETA(1)+ARRIV(1))*(BETA(2)+DERIV(1))]+(-3.0/X(1)
C 1 )+1.0/3.0)+.2
C PPRIME(2)=[(BETA(1)+ARRIV(2))*(BETA(2)+DERIV(2))]+(-3.0/X(2)
C 1 )+1.0/3.0)+.2
C PPRIME(3)=[(BETA(1)+ARRIV(3))*(BETA(2)+DERIV(3))]+(-3.0/X(3)
C 1 )+1.0/3.0)+.2
C PPRIME(4)=[(2.0*DCOS(THETA(1))+DSIN(THETA(1)))+(-3.0
C 1 *BETA(1)+BETA(2)*DCOS(ANG(1)))+COS(1)+0.01745329)
C 2 *1.0/3.0)+.2
C PPRIME(5)=[(2.0*DCOS(THETA(2))+DSIN(THETA(2)))+(-3.0
C 1 *BETA(1)+BETA(2)*DCOS(ANG(2)))+COS(2)+0.01745329)
C 2 *1.0/3.0)+.2
C PPRIME(6)=[(2.0*DCOS(THETA(3))+DSIN(THETA(3)))+(-3.0
C 1 *BETA(1)+BETA(2)*DCOS(ANG(3)))+COS(3)+0.01745329)
C 2 *1.0/3.0)+.2
C PPRIME(7)=[(SERIV(1)+1.0/3.0)+.2
C PPRIME(8)=[(SERIV(2)+1.0/3.0)+.2
C PPRIME(9)=[(SERIV(3)+1.0/3.0)+.2
C DERIV(1)=(ARRIV(1)+ARRIV(2)+ARRIV(3))+1.0/3.0
C DERIV(2)=(SERIV(1)+SERIV(2)+SERIV(3))+1.0/3.0
C DERIV(3)=(ARRIV(1)+ARRIV(2)+ARRIV(3))+1.0/3.0
C PCALC =1.0*BETA(1)+DERIV(1) + BETA(2)+DERIV(2)
C RETURN
C END

```

/EXECUTE

C FORMAT FREE INPUT

```

C
C
C
C 3 5 8 10 0 01
C -5000 -10000 -1 25
C -12A 3 05 0 05 8 74 0 05 2 02 0 05 24 3 1 2 20 7 1 2 20 0 1 2 02 0 1 5
C -105 0 1 5 -55 1 1 5 -205 0 7
C -14A 3 05 0 05 5 55 0 05 5 51 0 05 42 2 0 0 42 4 0 0 42 0 0 0 20 0 1 0
C 102 0 1 5 -57 0 1 5 -205 0 02
C -105A 3 0 45 0 05 5 55 0 05 5 50 0 05 55 5 0 0 55 4 0 0 55 2 0 0 15 0 0 0
C 144 3 0 5 -117 4 0 5 2 0 7
C -10B 3 0 75 0 05 4 50 0 05 4 70 0 05 55 0 0 001 50 0 0 001 50 0 0 001 1 0 1 0
C 120 1 0 -124 5 1 0 52 2 0 5
C 10 3 20 0 01 3 20 0 01 3 22 0 01 20 0 0 001 50 0 0 001 50 0 0 001 0 0 0 2
C 120 0 2 -124 5 0 2 57 1 0
C (A7,1279,2)
C /BYCARD

```

Appendix 4. Supplementary Data for Crystal Structures of $\text{Fe}(\text{CO})_3(\text{PPh}_3)$ (olefin) (olefin = fum, mal).

Table 51. Rigid Group Parameters $\text{Fe}(\text{CO})_3(\text{PPh}_3)$ (fum).

Atom	x	y	z	B(A ²)	Atom	x	y	z	B(A ²)
C(11)	0.2376(2)	-0.0910(2)	-0.2978(2)	3.45(8)	C(24)	0.3481(2)	0.2040(2)	-0.3414(2)	5.6(1)
C(12)	0.2904(2)	-0.1368(2)	-0.3322(2)	4.51(9)	C(25)	0.3489(2)	0.2023(2)	-0.2700(2)	5.5(1)
C(13)	0.2672(2)	-0.1844(2)	-0.3879(1)	4.8(1)	C(26)	0.3249(2)	0.1334(2)	-0.2360(1)	4.43(9)
C(14)	0.1912(2)	-0.1927(2)	-0.4092(2)	4.7(1)	C(31)	0.3558(2)	-0.0721(2)	-0.1949(2)	4.01(9)
C(15)	0.1384(2)	-0.1405(2)	-0.3748(2)	4.45(9)	C(32)	0.4228(2)	-0.0288(1)	-0.1844(2)	4.7(1)
C(16)	0.1616(2)	-0.0929(2)	-0.3191(1)	3.87(8)	C(33)	0.4881(2)	-0.0883(2)	-0.1605(1)	5.6(1)
C(21)	0.3001(2)	0.0663(2)	-0.2734(2)	3.40(8)	C(34)	0.4855(2)	0.1508(2)	-0.1471(2)	6.4(1)
C(22)	0.2992(2)	0.0690(2)	-0.3449(2)	4.26(9)	C(35)	0.4195(2)	-0.1940(1)	-0.1575(2)	6.6(1)
C(23)	0.3232(2)	0.1368(2)	-0.3789(1)	5.5(1)	C(36)	0.3941(2)	-0.1547(2)	-0.1814(1)	5.7(1)

Rigid Group Parameters

	^a Xc	Yc	Zc	Delta	Epsilon	Eta
Ring1	0.2144(1)	-0.1386(1)	-0.3535(1)	-0.875(2)	2.900(3)	2.040(3)
Ring2	0.3241(1)	0.1351(1)	-0.3074(1)	0.366(2)	1.590(2)	4.211(2)
Ring3	0.4211(1)	-0.1115(1)	-0.1710(1)	0.189(2)	2.890(2)	0.487(2)

^a Xc, Yc and Zc are the fractional coordinates of the centroid of the rigid group.

^b The rigid group orientation angles Delta, Epsilon and Eta (radians) are the angles by which the rigid body is rotated with respect to a set of axes X, Y and Z. The origin is the centre of the ring; X is parallel to a^c, Z is parallel to c and Y is parallel to the line defined by the intersection of the plane containing a^c and b^c with the plane containing b and c.

Table 52. Rigid Group Parameters Fe(CO)₃(PPh₃) (mal).

Atom	X	Y	Z	B(A ²)	Atom	X	Y	Z	B(A ²)
C(11)	0.1774(3)	0.3389(3)	0.3648(3)	3.01(9)	C(24)	0.5797(6)	0.2443(4)	0.1608(5)	5.1(1)
C(12)	0.2149(2)	0.4349(3)	0.3038(3)	3.8(1)	C(25)	0.5169(6)	0.1921(3)	0.0931(8)	5.1(1)
C(13)	0.1602(3)	0.4923(3)	0.2529(3)	4.3(1)	C(26)	0.4147(4)	0.2042(4)	0.1789(5)	4.2(1)
C(14)	0.0680(3)	0.4536(3)	0.2630(3)	4.3(1)	C(31)	0.2116(3)	0.4197(3)	0.6274(4)	2.87(8)
C(15)	0.0304(2)	0.3576(3)	0.3240(3)	4.4(1)	C(32)	0.1761(3)	0.3968(3)	0.7567(3)	4.0(1)
C(16)	0.0852(3)	0.3002(3)	0.3749(3)	3.6(1)	C(33)	0.1483(3)	0.5099(4)	0.8941(3)	5.0(1)
C(21)	0.3752(6)	0.2685(4)	0.3345(5)	2.98(9)	C(34)	0.1561(3)	0.6458(3)	0.9021(4)	4.6(1)
C(22)	0.4379(6)	0.3207(3)	0.4023(8)	3.9(1)	C(35)	0.1916(7)	0.6686(3)	0.7728(3)	4.1(1)
C(23)	0.5402(4)	0.3086(4)	0.3155(5)	5.0(1)	C(36)	0.2194(6)	0.5556(4)	0.6354(3)	3.51(8)

Rigid Group Parameters.

	X ^a	Y ^c	Z ^c	Delta ^b	Epsilon	Eta
Ring1	0.1227(2)	0.3963(2)	0.3139(2)	3.893(2)	2.455(3)	2.712(3)
Ring2	0.4774(2)	0.2564(2)	0.2477(3)	4.193(2)	0.954(4)	2.962(4)
Ring3	0.1839(2)	0.5327(2)	0.7648(3)	3.106(2)	1.208(2)	0.827(2)

^a Xc, Yc and Zc are the fractional coordinates of the centroid of the rigid group.

^b The rigid group orientation angles Delta, Epsilon and Eta (radians) are the angles by which the rigid body is rotated with respect to a set of axes X, Y and Z. The origin is the centre of the ring; X is parallel to a^c, Z is parallel to c and Y is parallel to the line defined by the intersection of the plane containing a^c and b^c with the plane containing b and c.

Table 53. Hydrogen Atom Positions Fe(CO)₃(PPh₃)₃ (fum)

Atom	X	Y	Z	B(A ³)	Atom	X	Y	Z	B(A ³)
H(42a)	0.4481	0.0346	-0.0365	7.90	H(22)	0.3223	0.1380	-0.4277	6.46
H(42b)	0.4279	0.0904	0.0239	7.90	H(23)	0.3641	0.2510	-0.3647	6.58
H(52a)	-0.0288	0.1759	-0.0304	6.93	H(24)	0.3658	0.2480	-0.2445	6.46
H(52b)	-0.0629	0.1076	0.0130	6.93	H(25)	0.3256	0.1321	-0.1873	5.41
H(11)	0.3421	-0.1359	-0.3176	5.50	H(31)	0.4239	0.0276	-0.1934	5.61
H(12)	0.3032	-0.2158	-0.4115	5.85	H(32)	0.5337	-0.0386	-0.1529	6.67
H(13)	0.1754	-0.2186	-0.4475	5.68	H(33)	0.5309	-0.1775	-0.1302	7.31
H(14)	0.0866	-0.1416	-0.3896	5.44	H(34)	0.4182	-0.2502	-0.1478	7.48
H(15)	0.1256	0.0617	-0.2957	4.88	H(35)	0.3084	-0.1840	-0.1883	6.58
H(21)	0.2821	0.0221	-0.3704	5.23					

Table 54. Hydrogen Atom Positions Fe(CO)₃(PPh₃)₃ (mal)

Atom	X	Y	Z	B(A ³)	Atom	X	Y	Z	B(A ³)
H(42a)	0.2320	0.1522	0.9929	7.19	H(22)	0.5828	0.3448	0.3628	6.00
H(42b)	0.2591	-0.0059	0.8892	7.19	H(23)	0.6496	0.2359	0.1024	6.18
H(52a)	0.4714	-0.4229	0.2229	10.88	H(24)	0.5442	0.1477	-0.0120	6.18
H(52b)	0.5446	-0.3845	0.2954	10.88	H(25)	0.3721	0.1685	0.1337	5.31
H(11)	0.2779	0.4613	0.2962	4.86	H(31)	0.1700	0.3045	0.7522	5.02
H(12)	0.1852	0.5583	0.2117	5.31	H(32)	0.1226	0.4950	0.9839	6.01
H(13)	0.0300	0.4933	0.2293	5.40	H(33)	0.1360	0.7236	0.9968	5.63
H(14)	-0.0327	0.3312	0.3314	5.45	H(34)	0.1968	0.7615	0.7786	5.30
H(15)	0.0600	0.2342	0.4159	4.67	H(35)	0.2483	0.5710	0.5474	4.58
H(21)	0.4107	0.3655	0.5082	4.88					

Table 55. $10 \times (F_O \text{ vs. } F_C) \text{ Fe}(\text{CO})_3(\text{PPh}_3) (\text{fum})$.

[The page contains approximately 35 lines of extremely faint, low-contrast text. The characters are small and difficult to distinguish, appearing as a series of horizontal rows of dots and dashes. There are several instances of vertical lines or gaps in the text, possibly indicating paragraph breaks or specific formatting. The overall appearance is that of a heavily degraded or low-quality scan of a document.]

[The page contains several paragraphs of extremely faint, illegible text, likely a scan of a document with low contrast or a very faded print. The text is organized into approximately 10 distinct blocks, separated by blank lines. A large, hand-drawn scribble is present on the right side of the page, overlapping the text in the middle section.]

[The page contains dense, illegible text, likely a scan of a document with very small font or significant noise. The text is organized into several paragraphs, with some lines appearing to be indented or separated by small gaps. The overall appearance is that of a high-resolution scan of a printed page where the characters are too small to be read accurately.]

✓

1. The first part of the document discusses the importance of maintaining accurate records of all transactions. It emphasizes that every entry must be supported by a valid receipt or invoice. This ensures that the financial statements are reliable and can be audited without any discrepancies.

2. The second part of the document outlines the procedures for handling cash payments. It states that all cash receipts should be deposited into the company's bank account immediately. This helps in maintaining a clear trail of the company's cash flow and prevents any misappropriation of funds.

3. The third part of the document describes the process of issuing invoices to customers. It highlights that invoices should be issued promptly after the goods or services are delivered. This not only helps in accelerating the payment cycle but also serves as a legal document in case of any disputes.

4. The fourth part of the document discusses the importance of regular reconciliation of the company's accounts. It advises that the general ledger should be reconciled with the bank statements and the subsidiary ledgers at least once a month. This helps in identifying any errors or irregularities in a timely manner.

5. The fifth part of the document concludes by stating that maintaining good financial records is essential for the long-term success of any business. It encourages the management to adopt a systematic and disciplined approach to financial management.

Table 56. $10 \times (F_0 \text{ vs. } F_C) \text{ Fe}(\text{CO})_3(\text{PPh}_3)_3 \text{ (mal)}$.

[The page contains approximately 25 lines of extremely faint, illegible text, likely a scan of a document with very low contrast or a very poor quality scan. The text is too light to be transcribed accurately.]

[The page contains approximately 25 lines of extremely faint, illegible text, likely a scan of a document with very low contrast or a very poor quality scan. The text is arranged in a standard left-aligned paragraph format.]

9